UNIVERSITAT DE BARCELONA

Molecular Self-Assembly for the preparation of novel nanostructured materials

Jorge Rodrigo Magaña Rodríguez

UNIVERSITAT DE BARCELONA

FACULTAT DE FARMÀCIA I CIÈNCIES DE L’ALIMENTACIÓ

MOLECULAR SELF-ASSEMBLY FOR THE PREPARATION OF NOVEL NANOSTRUCTURED MATERIALS

JOSÉ RODRIGO MAGAÑA RODRÍGUEZ, 2017

UNIVERSITAT DE BARCELONA

FACULTAT DE FARMÀCIA I CIÈNCIES DE L'ALIMENTACIÓ

PROGRAMA DE DOCTORAT: NANOCIÈNCIES

MOLECULAR SELF-ASSEMBLY FOR THE PREPARATION OF NOVEL NANOSTRUCTURED MATERIALS

Memòria presentada per Jose Rodrigo Magaña Rodriguez per optar al títol de doctor per la universitat de Barcelona

Directors:

Dra. Conxita Solans Marsá

Dr. Carlos Rodríguez Abreu

Doctorando: Jose Rodrigo Magaña Rodríguez

Tutora: Dra. Mª José García-Celma

JOSÉ RODRIGO MAGAÑA RODRIGUEZ, 2017

Table of Contents

RESUMEN EN CASTELLANO

En las últimas décadas, el auto-ensamblaje molecular ha ganado importancia debido a su potencial tecnológico. El estudio de nuevas moléculas con capacidad de formar agregados funcionales es un área de investigación relevante en la ciencia de materiales. Los tensioactivos son los ejemplos más representativos de moléculas auto-ensambladas. Los tensioactivos están formados por una cadena hidrocarbonada (hidrófoba) y un grupo polar (hidrófilo). Los tensioactivos se auto-agregan en solución debido a segregación entre el solvente y las cadenas hidrofóbicas formando un amplio rango de nanoestructuras, desde micelas esféricas hasta cristales líquidos. No obstante, el auto-ensamblaje molecular no es una propiedad que está restringida a los tensioactivos. Algunas moléculas planas y aromáticas, como las llamadas cromónicas, pueden también auto-organizarse en solución. Las propiedades de las moléculas cromónicas son diferentes de aquellas mostradas por los tensioactivos. El estudio de las propiedades de auto-agregación de las moléculas cromónicas está restringida a unos pocos sistemas. Es por eso que se conoce muy poco sobre la relación entre su estructura molecular y su comportamiento de auto-agregación en solución.

Los nanomateriales han sido una de las áreas de mayor enfoque científico y tecnológico de los últimos años debido a que estos presentan propiedades únicas. Estas propiedades dependen en gran medida de la composición química, tamaño y morfología, es por eso que controlar estos parámetros es fundamental. Principalmente hay dos metodologías de síntesis de nanomateriales: aquellas que parten de un material en el estado masivo (“bulk”) para obtener unidades más pequeñas (“top-down”) y aquellas que consisten en partir de átomos y moléculas para construir nanomateriales (“bottom-up”). La metodología “bottom-up” produce estructuras estables y robustas; adicionalmente es económico, versátil y fácil. Entre los métodos de bottom-up quizás los que están más ampliamente estudiados son aquellos que utilizan auto-agregados (especialmente tensioactivos) en solución como plantillas. En este caso la morfología y tamaño del material final están determinados por el tipo de agregado utilizado. Desde un punto de vista industrial, se prefiere el uso de tensioactivos de grado técnico (disponibles comercialmente) debido a que son más económicos; no obstante, las propiedades de auto-ensamblaje de tensioactivos pueden cambiar por la presencia de impurezas y es por ello que el estudio del efecto de dichas impurezas es relevante. Por otra parte, es de interés el uso de otro tipo de agregados con morfologías distintas a aquellas presentadas por sistemas tensioactivos. A este respecto, las moléculas cromónicas son atractivas ya que poseen propiedades ópticas que, combinadas con materiales inorgánicos, pueden usarse en un amplio rango de aplicaciones.

En este contexto, el objetivo principal de este trabajo de tesis es el de estudiar y caracterizar el comportamiento de auto-ensamblaje molecular de tensioactivos de grado comercial y moléculas cromónicas en medio acuoso y utilizar estos agregados para sintetizar nanomateriales funcionales.

Para ello el plan de trabajo se dividió en tres partes:

- Estudio del comportamiento fásico de las moléculas seleccionadas en medio acuoso.
- Preparación de materiales usando los agregados identificados en el estudio del comportamiento fásico como plantillas.
- Estudio de las posibles aplicaciones de los materiales preparados en liberación controlada de fármacos, almacenaje de energía y tecnología de sensores.

Se determinó el comportamiento fásico mediante determinación de diagramas de fase en función de la concentración y temperatura de los distintos compuestos elegidos. Los límites de las distintas fases se determinaron mediante microscopia de luz polarizada (**POM**) con control de temperatura. La estructura de los agregados se caracterizó por técnicas de dispersión de radiación, tales como dispersión de rayos X a ángulo pequeño (**SAXS**/**WAXS**) y dispersión dinámica de luz (**DLS**).

Para los tensioactivos derivados de di-glicerol poli-isostearatos, se demostró que el di-glicerol mono-isostearato (**C41V**) en medio acuoso se autoagrega formando estructuras de cristal líquido hexagonal inverso ($\mathbf{H_2}$). Este cristal líquido $\mathbf{H_2}$ se dispersó en agua mediante distintos métodos formando los denominados ‘’hexosomas’’. El método de evaporación de solvente proporcionó los mejores resultados, obteniéndose tamaños de hexosomas más pequeños y con baja polidispersidad. Se encapsuló en los hexosomas obtenidos un fármaco hidrófobo (ketoprofeno)se estudió su liberación a un medio gastrointestinal simulado. Estos estudios pusieron de manifiesto que puede controlarse la difusión del fármaco a una solución receptora. Adicionalmente los hexosomas formados por **C41V** se degradan en condiciones gastro-intestinales, lo cual evita que estos se acumulen en los órganos corporales.

El glicerol y los tensioactivos con grados de esterificación más altos presentes en **C41V** se separaron y se estudió la influencia de las impurezas en el comportamiento fásico del tensioactivo. Se encontró que el glicerol produce una segregación de fases a altas concentraciones de **C41V**. Adicionalmente se demostró que variando la cantidad de tensioactivo con mayor grado de esterificación en **C41V** se pueden obtener distintos cristales líquidos en coexistencia con un exceso de agua.

En los sistemas acuosos de colorantes estudiados, se evidenció que todas las moléculas seleccionadas (Quinaldine red, Pyronin Y, Tiacarbocianinas, Oxacarbocianinas, Alcian Blue) se auto-agregan formando columnas moleculares apiladas cara-a-cara. Estas columnas crecen a medida que la concentración del colorante aumenta. A concentraciones suficientemente altas se forma una fase cristal líquido nemático (Fase N) y una fase de cristal líquido hexagonal (Fase M). En el sistema de agua/Quinaldine Red se identificó una estructura a concentraciones altas en la cual las columnas moleculares están ordenadas en una estructura rectangular. Los estudios con las Tiacarbocianinas y Oxacarbocianinas pusieron de manifiesto que las fuerzas inter-moleculares se pueden modular cambiando el tamaño de cadena de las cadenas alquílicas laterales o la cadena de metinos que separa los grupos aromáticos. Los estudios con Alcian Blue muestran que este colorante se auto-agrega en solución, pero se disocia poco en agua por lo cual no forma cristales líquidos. Alcian Blue en medio acido forma cristales líquidos debido que su disociación aumenta al disminuir el pH.

Los agregados de los colorantes se han utilizado como plantillas para sintetizar nano-fibras de sílice con una nano-estructura determinada y una elevada superficie específica (230 m^2/g). Los materiales derivados se han estudiado mediante diferentes técnicas tales como **SEM**, **SAXS** y adsorción/desorción de gases. Las nano-fibras de sílice se usaron como plantillas para obtener fibras de carbono Se exploraron aplicaciones de las fibras de carbono obtenidas en súper-capacitores mediante técnicas electroquímicas y se encontró que los materiales muestran un excelente rendimiento (capacitancias de hasta 300 F/g). Adicionalmente se estudió el uso de las fibras de carbono como sensores de vapores orgánicos, obteniéndose una alta sensibilidad respecto a compuestos aromáticos.

ABSTRACT

In this thesis, the phase behavior in water of a technical grade diglycerol-based surfactant (**C41V**) and a group of dyes (Quinaldine Red, Pyronin Y, N-Alkylthiacarbocyanines, Oxacarbocyanines, Pinacyanol and Alcian Blue) was studied. Several experimental techniques such as polarized optical microscopy, small and wide X-ray scattering, dynamic light scattering, **UV-Vis** and **NMR** spectroscopy, were used to characterize the different phases and get insight into the molecular self-assembly behavior.

The phase diagram of the water/**C41V** system is characterized by a wide region at temperatures lower than 70 ºC in which an inverse hexagonal liquid crystal (**H_2**) coexists with excess water. The **H_2** phase could be successfully dispersed in water in the form of nanoparticles (hexosomes). A hydrophobic drug (Ketoprofen) was encapsulated in the hexosomes and its release to a receptor solution showed a non-Fickian diffusion profile. Excess of glycerol and surfactants with higher degree of esterification were separated from **C41V**. It was found that glycerol causes phase segregation at high **C41V** concentrations. The spontaneous curvature of the surfactant system can be tuned by mixing the purified C41V with the surfactants with higher degree of esterification.

Structural characterization of dyes in water reveals that the molecules stack in columnar aggregates, which increase in size with concentration. At relatively high concentrations (ca. > 30 wt%) Quinaldine Red and Pyronin Y form a Nematic chromonic liquid crystal composed by columns with unimolecular cross-section. Additionally, at higher concentrations, Quinaldine Red forms a chromonic rectangular phase, which indicates that the columns cross-section is anisotropic. **UV-Vis** spectroscopy suggests that N-Alkylthiacarbocyanines stack face to face. The dimer model was used to fit the **UV-Vis** spectra and to estimate the dimeric constant and the intermolecular dissociation. The intermolecular interactions increase with the alkyl chain length (from 19.2 k_BT to 20.5 k_BT) suggesting that not only aromatic $\pi-\pi$ interactions but also the hydrophobic effect contribute to the aggregation process. From small angle X-ray scattering measurements it can be inferred that the molecular columns are hollow. By applying the exciton theory to the **UV-Vis** spectra of Oxacarbocyanines it was found that the stacking angle of these dyes is around 54.7 º. It was also found that the molecular interactions can also be tuned by varying the carbon atoms in the poly-methine spacer of cyanine dyes. Alcian Blue showed evidence of stacking in aqueous solution, however, due to the poor solubility of this dye in water no liquid crystal was formed; nevertheless, Alcian blue solubility increases at acidic pH and liquid crystals can be formed. Cyanine dye aggregates were used as templates for silica synthesis by a sol-gel reaction. Silica nanofibers with high surface area (i.e. 230 m^2/g) and hierarchical arranged mesopores were obtained. Furthermore, silica nanofibers were used as hard templates to produce carbon materials. The resulting templated carbon nanofibers were used as functional materials in energy storage and sensing applications. Carbon nanofibers showed superior performance as double layer capacitors (capacitance values of ca. 3000 F/g) and presented potential as sensing materials for aromatic compounds, especially pyridine.

The work described in this thesis is partially published in:

- **Magana, J.R.**; Homs, M.; Solans, C.; Obiols-Rabasa, M.; Salonen, L. M.; Rodriguez-Abreu, C. Self-assembly and Formation of Chromonic Liquid Crystals from the Dyes Quinaldine Red acetate and Pyronin Y. *J. Phys. Chem. B*, **2016**, 120, 250-258.
- **Magana, J.R.**; Kolen'ko, Y; Deepak, F; Solans, C; Shrestha, R; Hill, Jonathan; Katsuhiko, A; Shrestha, L; Rodriguez-Abreu, C. From Chromonic Self-Assembly to Hollow Carbon Nanofibers: Efficient Materials in Supercapacitor and Vapor Sensing Applications. *ACS Appl. Mater. Interfaces*, **2016**, 8 (45), 31231–31238

1. INTRODUCTION

1.1. BASIC ASPECTS OF MOLECULAR SELF-ASSEMBLY

Self-assembly is a process in which objects spontaneously arrange into stable and well-ordered structures due to non-covalent interactions. This process occurs at all length scales, from nanoscopic objects such as atoms or molecules (i.e. formation of crystals) to objects of cosmic size (i.e. formation of galaxies) (Figure 1.1). The resulting structure would depend on the shape, type of interactions and homogeneity of the assembling units.[1] Self-assemblies contain coded information about the assembling units, i.e. shape, charge, polarizability, magnetic dipole, mass, etc. as these properties determine the interactions among them.

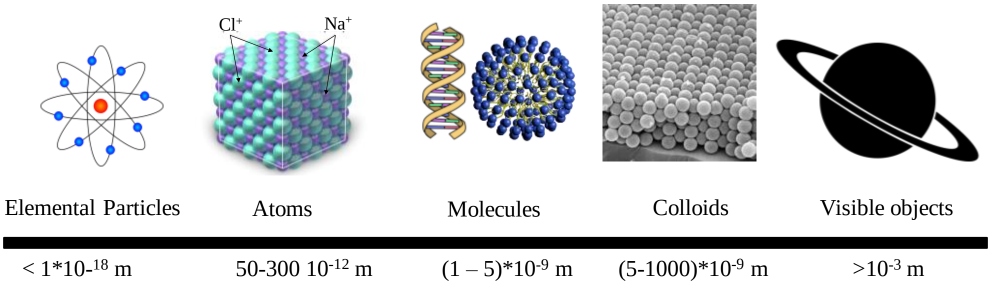

Figure 1.1. Schematic representation of self-assembly at all scales.

1.1.1. Intermolecular interactions

It has been stablished that there are four different forces in nature. Two of these are strong and weak interactions with a very short range of action (ca. 10^{-5} nm) that act between elementary particles (neutrons, electrons, etc.). The other two forces are the electromagnetic and gravitational interactions that act between all particles. These forces are effective over a much larger range of distances, from subatomic to practically infinite distances, and consequently are the forces that govern self-assembly.[2] Among self-assembly phenomena, molecular self-assembly studies are of great importance since their building units have chemical functionality with reactivity and directionality which can restrict and tune the products of self-assembly usually to thermodynamically stable forms, allowing to obtain tailor-made structures. The intermolecular forces can be controlled by chemically tuning the molecular architecture. For instance, the presence of hydrogens atoms in a molecule covalently bound to an electronegative atom (such as oxygen or halides) can be used to increase the molecular interactions (H-bonding) and produce stable assembled structures.

With the development of the quantum theory it was possible to understand the origin of intermolecular forces and derive interactions for their potentials. It was found that all the intermolecular forces are of electrostatic nature. This is reflected in the Hellmann-Feynman theorem which states that after determining the spatial distribution of electrons (i.e. by solving the Schrödinger equation) the intermolecular forces can be calculated using classical electrostatic theories;[3] however, exact solutions of the Schrödinger equation are practically impossible to obtain. In colloidal science it is useful to classify intermolecular interactions into different categories, such as:

- Electrostatic double layer forces (ionic bonds, $\pi - \pi$ interactions, dipole-dipole, hydrogen bonding, etc.)
- Van der Waals forces
- Hydration forces

It is noteworthy knowing the interaction between two isolated molecules does not give a complete understanding on how an ensemble of molecules will behave. For this purpose, thermodynamic and probabilistic concepts, such as entropy, enthalpy or free energy must be considered. The Gibbs free energy, G, is defined as a potential that measures the maximum reversible work that can be performed by a closed system at a constant volume and pressure. The Gibbs free energy of a process can be defined as:

$$\Delta G = \Delta H - T\Delta S_{int}$$

Equation 1.1

Where ΔG, ΔH and ΔS_{int} are the change in free energy, enthalpy and internal entropy between two states respectively, T refers to the absolute temperature of the system. As the equation is only for two states of an isolated system, the second law of thermodynamics can predict the spontaneity of the process:

- $\Delta G < 0$ favored process (spontaneous)
- $\Delta G = 0$ equilibrium
- $\Delta G > 0$ disfavored process (nonspontaneous)

Molecular self-assembly is a process that is driven by the minimization of the Gibbs energy. In principle, it would be plausible to assume that in a self-assembly process, the ordering increases and therefore $\Delta S_{int} < 0$, i.e. $-T\Delta S$ term in Equation 1.1 is larger than 0; hence, the enthalpy term, ΔH would define whether the process is spontaneous or not. In molecular self-assembly ΔH generally depends on the molecular interactions (molecule-molecule, solvent molecule interactions). However, for surfactants the hydrophobic effect implies $\Delta S_{int} > 0$, which is associated with the disruption of the hydrogen bonds between the water molecules by the formation of aggregates. Self-assembly always involves attractive and repulsive interactions.[4]

1.1.2. Formation of condensed mesophases: Liquid Crystals

All matter exists in one of several states such as, for example, solid, liquid or gas having different degree and type of positional and orientational order. In the isotropic liquid or gas phases, molecules without order occupy the whole space and have no long-range positional or orientational order. The solid state can be divided to several categories, such as glass or crystal. In a typical crystalline phase, molecules or atoms have three-dimensional long-range positional order and in molecular crystals there is also long-range orientational order. Liquid crystals are a special class of soft materials that can flow like an isotropic liquid yet possess a long-range orientational order and a complete or partial absence of positional order of building units which can be individual molecules or their aggregates. The two main types of liquid crystals are thermotropic and lyotropic liquid crystals

1.1.3. Thermotropic liquid crystals

Thermotropic liquid crystals are those which molecules self-assemble without the need of a solvent. At low temperatures, they are usually in a crystalline state. At higher temperatures, the thermal motion of the molecules induces a phase transition into a liquid crystal. Thermotropic liquid crystals are usually made of highly anisotropic organic molecules, either elongated (rod-like molecules) or disk-like (discotic molecules). As a rule, the inner part of molecules is rigid (e.g. phenyl groups) and the outer part flexible (aliphatic chains). This double character explains altogether the existence of steric interactions (between rod-like or disk-like cores) yielding orientation order and the fluidity of the phases. Typical examples are cyanobiphenyls.[5, 6] These produce thermotropic mesophases, i.e. phases with a single component, whose phase transitions can be induced by a change in temperature. A general phase behavior of thermotropic systems is shown in Figure 1.2. One of the most representative applications of thermotropic liquid crystals are the so-called LCD screens of Liquid Crystal Displays.

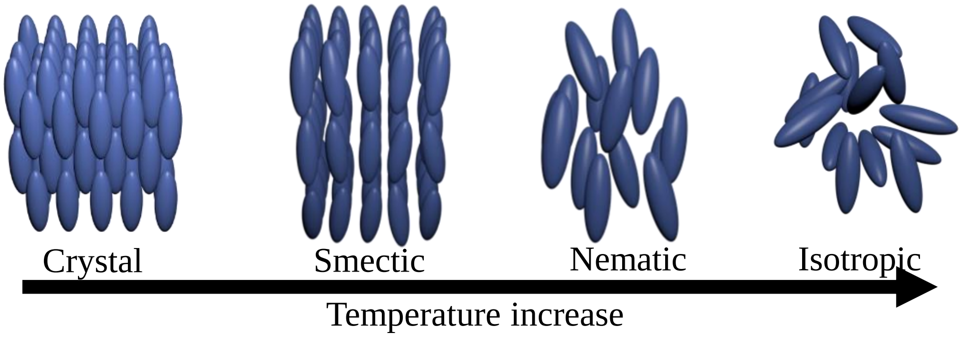

Figure 1.2. Schematic representation of the most common phase transitions in a thermotropic liquid crystal.

1.1.4. Lyotropic liquid crystals

Liquid crystals or mesophases can also form in the presence of a solvent when a certain concentration of molecular assemblies is reached. The size of aggregates and the effective volume fraction are the most important factors that influence mesophase formation. The effective volume of the aggregates includes the occupied volume plus the repulsive interactions between aggregates, such as electrostatic forces or steric interactions.[7] When the volume fraction reaches a certain value, the aggregates rearrange in an ordered assembly. Aggregates can also change in shape when the volume fraction is near the value of maximum packing. For instance, for spherical aggregates, the maximum volume fraction is 74% for a cubic lattice. For cylindrical aggregates in a hexagonal lattice it is 91%, while for a layered structure is about 100%. According to the dimensionality of the translational correlations of the building units, lyotropic liquid crystals can be divided in four types:

- Liquid crystals with no translational correlation: Nematic liquid crystal
- Liquid crystals 1-D correlation: Lamellar liquid crystal.
- Liquid crystals with 2-D correlation: Hexagonal and Rectangular liquid crystal.
- Liquid crystals with 3-D correlation: Cubic liquid crystals.

1.1.5. Methods for liquid crystal characterization.

The most widely used methods for characterizing liquid crystals are those involving X-ray radiation. Due to the long correlation lengths in these phases, it is necessary to use a small angle scattering equipment (**SAXS**). The identification of liquid crystalline phases is straightforward since it is based on the existence of sharp reflection lines corresponding to the spacing in the planes of the liquid crystalline structure.

- **Nematic liquid crystal**

A nematic liquid crystal is usually formed by molecules or aggregates that are elongated. They have no positional order, but they self-align to have a long-range orientational order along a director (Figure 1.3). The **SAXS** pattern is characterized by a broad band, with the maxima proportional to the inverse of the mean separation between aggregates.

- **Lamellar liquid crystals**

This phase is characterized by stacked layers with a series of diffraction spacings in the ratio 1:2:3:4… corresponding to a one-dimensional repetition of the planes with the Miller indexes of (1 0), (2 0), (3 0), etc. The first order spacing, d, is equivalent to the distance between layers (Figure 1.3). If the volume fraction, ϕ_f, of molecules is known then the thickness of the aggregates layer, d_L, can be calculated by:

$$d_L = \phi_f d$$

Equation 1.2

- **Hexagonal and rectangular liquid crystals**

The hexagonal phase is composed of long cylinders arranged in a hexagonal lattice (Figure 1.3). The **SAXS** pattern shows a series of diffraction spacing's in the ratio $1{:}\sqrt{3}{:}\sqrt{4}{:}\sqrt{7}$ ... corresponding to the planes with the Miller indexes: (1 0), (1 1), (2 0), (2 1) respectively. The unit cell dimension, *a*, can be calculated by:

$$a = \frac{2}{\sqrt{3}} d$$

Equation 1.3

Where *d* is the first order spacing. If the molecular volume fraction, ϕ_f, is known, then the radius of the cylinder, *r*, can be calculated from:

$$r = \left(\frac{2\phi_f d^2}{\sqrt{3}\pi} \right)^{\frac{1}{2}}$$

Equation 1.4

Rectangular liquid crystals are formed when the cross-sectional area of cylinders is anisotropic along one axis (Figure 1.3). The relative position of the diffraction peaks will depend on the dimensions of the cross section.

$$\frac{1}{d_{hk}^2} = \left[\frac{h^2}{a^2} + \frac{k^2}{b^2} \right]$$

Equation 1.5

Where *d* is the distance between layers, *h* and *k* are the Miller indices for the planes, and *a* and *b* are the dimensions of the unit cell ($b > a$). The first two peaks, generally correspond to the planes with the miller indices of (0 2) and (1 1). The cross-sectional area of the cylindrical aggregates can be calculated by:

$$A_c = \frac{1}{2} ab\phi_f$$

Equation 1.6

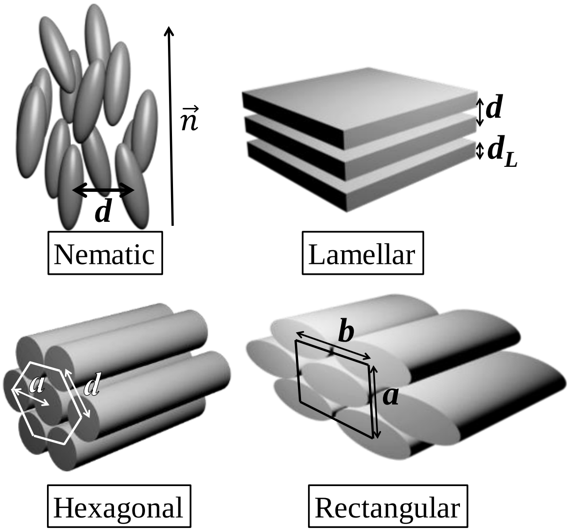

Figure 1.3. Liquid crystalline structures with the relevant structural parameters indicated.

- **Cubic liquid crystals**

Cubic phases are the most complex to characterize. Such phases show **SAXS** patterns presenting spacings in the ratios: $\sqrt{1}: \sqrt{2}: \sqrt{3}: \sqrt{4}: \sqrt{5}: \sqrt{6}: \sqrt{7}: \sqrt{8}$: ... Absent spacings in the **SAXS** pattern are related to the symmetry (space group) of the cubic lattice. Some of the most common cubic liquid crystal properties are presented in Table 1.1.

Table 1.1. Lattice planes and their respective spacing ratios for different space groups for a cubic lattice.

Space Group	Planes (h, k, j)	Spacing ratio
Im3m	(1 1 0), (2 0 0), (2 1 1), (2 2 0), (3 1 0), (2 2 2)	$\sqrt{2}: \sqrt{4}: \sqrt{6}: \sqrt{8}: \sqrt{10}: \sqrt{12}$
Pn3m	(1 1 0), (1 1 1), (2 0 0), (2 1 1), (2 2 0), (2 2 1)	$\sqrt{2}: \sqrt{3}: \sqrt{4}: \sqrt{6}: \sqrt{8}: \sqrt{9}$
Ia3d	(2 1 1), (2 2 0), (3 2 1), (4 0 0), (4 2 0), (3 3 2)	$\sqrt{6}: \sqrt{8}: \sqrt{14}: \sqrt{16}: \sqrt{20}: \sqrt{22}$
Fd3m	(1 1 1), (2 2 0), (3 1 1), (2 2 2), (4 0 0), (3 3 1)	$\sqrt{3}: \sqrt{8}: \sqrt{11}: \sqrt{12}: \sqrt{16}: \sqrt{19}$

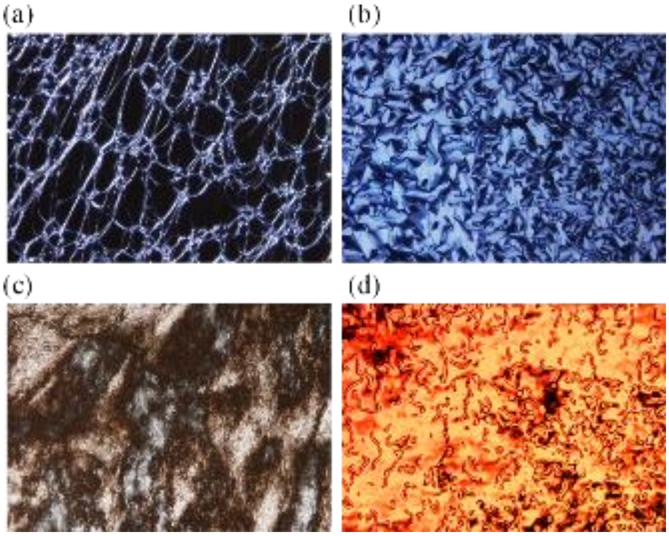

Figure 1.4. Polarized optical microscopy (**POM**) pictures of (a) oily streaks of a lamellar phase, (b) fan-shape conic texture of a hexagonal phase (c) smokey texture of a closely packed columnar mesophase and (d) schlieren texture of a nematic liquid crystal.

In addition to **SAXS**, the bulk properties of the phases formed can also serve as tools for determining the type of mesophases structures. For instance, most liquid crystals (with exception of the cubic phases) are optically anisotropic, therefore they can change the direction of polarized light. They present different optical textures under polarized light through a microscope. Some characteristic textures are shown in Figure 1.4. The microscopic textures from liquid crystals are mainly caused by defects on the crystalline network and depend only on the packing of the aggregates

1.2. SURFACTANT SELF-ASSEMBLY.

Surfactant molecules are one of the most representative examples for molecular self-assembly. Nowadays they are used in diverse applications including pharmaceutical, food and cosmetics. Surfactants are defined as amphiphilic, meaning that they have at least two differentiated hydrophobic (tail) and hydrophilic (head) parts (Figure 1.5). The hydrophobic moiety may be linear or branched and is usually a hydrocarbon chain, but it also may be a fluorinated or a siloxane chain.

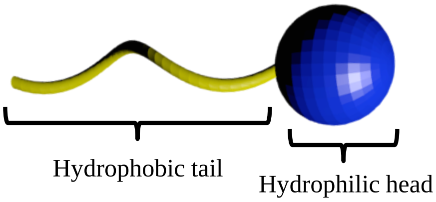

Figure 1.5. General representation of a surfactant molecule.

Surfactants can be classified according to the dissociation of the hydrophilic head in aqueous solution[8, 9] as:

- Ionic surfactants: Molecules with hydrophilic heads that ionize in a solvent. Anionic surfactants have a negatively charged hydrophilic head commonly composed by a carboxylate, sulfonate of sulfate group. The most common cationic surfactants have a quaternary ammonium halide salt on the hydrophilic head.
- Non-ionic surfactants: Molecules with no charge, with the hydrophilic head composed by highly polar groups, such as alcohols, ethers or amides. The most common non-ionic surfactants are those with a poly-oxyethylene chain as hydrophilic head.
- Zwitterionic surfactants: Molecules with both, positive and negative charges. The net charge of the molecule in solution can be dependent of pH.

The dual hydrophilic/hydrophobic nature of surfactants is one the main driving forces for self-assembly. In aqueous media, these properties are caused by the strong tendency of hydrophobic tails to avoid direct contact with water, consequently, they are first adsorbed at the interface between solvent and air (with the hydrophobic tails directed towards the air). Since the surface tension of a liquid depends on the number of adsorbed molecules per unit area, and surfactants occupy more area than a water molecule, the surface tension is decreased. When the surface is saturated, surfactants self-assemble in solution in a way that the hydrophilic domains become exposed to water and the hydrophobic parts are shielded (forming the so-called micelles). The concentration at which the surface is saturated and aggregates start to form is defined as the critical micellar concentration or **CMC**. A representative scheme of this aggregation process in solution is shown in Figure 1.6.

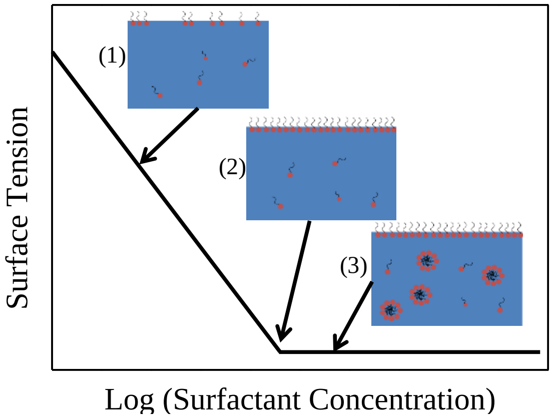

Figure 1.6. Representation of the variation of the surface tension with surfactant concentration. The insets show surfactant concentrations (1) < **CMC** (2) = **CMC** and (3) > **CMC**.

At higher surfactant concentration there is a first order phase transition driven by interactions between aggregates. Micelles assemble into hierarchically ordered structures, the so-called liquid crystals. This type of lyotropic liquid crystals can be regarded as arising from the interactions between micelles occurring at high surfactant concentrations.[10] The most common phases encountered in surfactant systems and their corresponding nomenclature used in this thesis are shown in Table 1.2.

Table 1.2. Structure and nomenclature of the phases found in surfactant systems.

Phase Structure	Nomenclature
Direct Micelles	$\mathbf{L_1}$
Inverse Micelles	$\mathbf{L_2}$
Sponge Phase	$\mathbf{L_3}$
Bicontinuous Structure	**D**
Lamellar	$\mathbf{L_\alpha}$
Gel Phase	$\mathbf{L_\beta}$
Hexagonal	$\mathbf{H_1}$
Inverse Hexagonal	$\mathbf{H_2}$
Direct Cubic (micellar)	$\mathbf{I_1}$
Inverse Cubic (micellar)	$\mathbf{I_2}$
Bicontinuous Cubic	**V**

The type of self-assemblies formed by surfactant systems can be (to some extent) predicted only by considering the effective surfactant geometries with the packing parameter:[11]

$$N = \frac{v_L}{L * a_s}$$

Equation 1.7

Where v_L and L represent the volume and the length of the hydrophobic chain in the core of the structure and a_s the cross-sectional area occupied by the hydrophilic head. a_s can be calculated by **SAXS** measurement of surfactant mesophases. v_L and L can be calculated using the equations reported by Tanford:[12]

$$v_L = 0.027(n_C + n_{CH3})$$

Equation 1.8

$$L = 0.15 + 0.127n_C$$

Equation 1.9

n_C and n_{CH3} correspond to the total number of carbon atoms and methyl groups present in the hydrophobic chain.

The packing parameter has two main limitations: one is that it is calculated from the molecular properties alone and these can vary depending on the solvent. The second is that the effects of the interactions between hydrophilic heads are not considered. A reviewed version of the packing parameter taking into account the hydrophilic head effect was reported by Kunieda et al.[13]

With the packing parameter, the surfactant can also be classified into hydrophilic ($N < 1$), hydrophobic ($N>1$) or balanced ($N=1$). Depending on the packing parameter, the self-assemblies will have a preferred structure (Figure 1.7).[9] Surfactants with $N< 1$ will prefer forming direct structures such as $\mathbf{L_1}$, $\mathbf{I_1}$ or $\mathbf{H_1}$, whereas surfactants with $N>1$ will form inverse structure (such as $\mathbf{H_2}$, $\mathbf{I_2}$ or $\mathbf{L_2}$), generally insoluble in water. Surfactants with balanced hydrophobic and hydrophilic parts (N close to 1) will favor the formation of layered or bicontinuous structures.

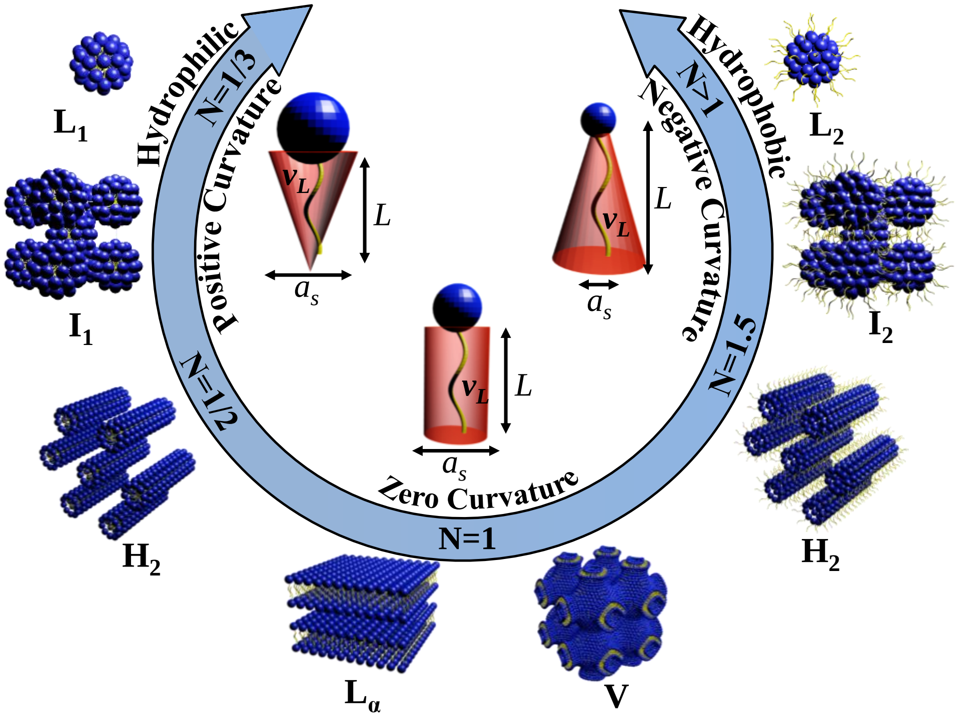

Figure 1.7. Critical packing parameters, N, of surfactant molecules and their preferred self-assembled structures.

1.2.1. Phase Behavior of Surfactant systems

The main objective of the study of phase behavior of surfactant systems is to answer tree fundamental questions: 1) How many phases are in equilibrium, 2) What composition they have? and 3) What structure do they have?

One of the most useful tools to study phase behavior are the phase diagrams. Generally, the phase diagrams are representations of the phases present at different compositions and temperatures and at a constant pressure.

All the aggregates formed are states of matter that satisfy the definition of a phase. The Gibbs phase rule determines the number of variables needed to specify the state of a system:

$$f = c + 2 - p$$

Equation 1.10

Where *f*, *c* and *p*, are the degrees of freedom, number of components and number of phases, respectively. The degrees of freedom correspond to the number of independent variables that must be fixed to specify the state of the system. Equilibrium phase diagrams must be consistent with the phase rule. Determining thermodynamically consistent phase diagram is in some cases not possible due to the high cost and low availability of pure substances.

As described in subsection 1.1.2 there is a maximum packing fraction for a given aggregate shape. For a binary system (water/surfactant) as the concentration is increased, surfactants can change their shape and curvature to enable a closer packing. Consequently, the phases present in a diagram as a function of concentration and temperature follow a certain sequence. A general binary aqueous phase behavior of a surfactant can be summarized in the phase diagram shown in Figure 1.8.[14] Note that it is not usual that a water/surfactant system presents all the structures described. This is limited by the nature of surfactants (i.e. molecular architecture, surfactant solubility, etc.)

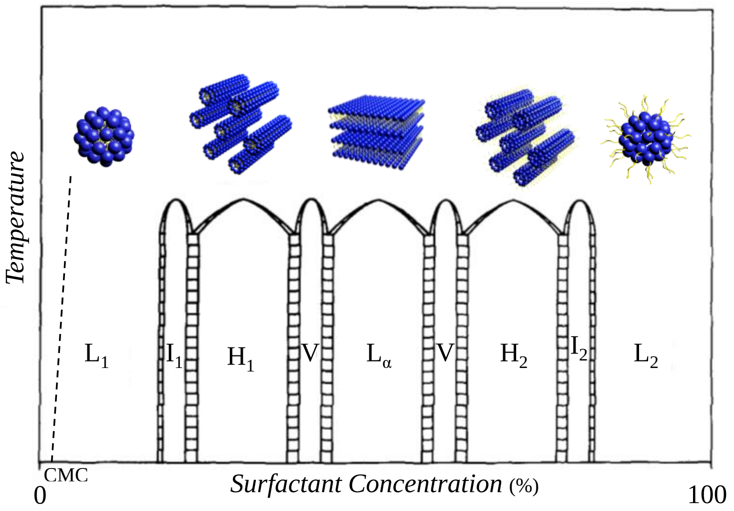

Figure 1.8. General representation of a phase diagram for a water/pure ionic surfactant system in which the transitions are driven by changes in the surfactant concentration. Adapted from [14]. The dashed regions represent a coexistence between two phases. The dashed line represents the boundary at which aggregates start forming (**CMC**).

For ternary systems, such as water/surfactant/oil mixtures the phase behavior is usually represented in the so-called ternary phase diagrams. As an example, the phase diagram of the water/Brijj 30/decane is shown in Figure 1.9 (Reproduced from [15]). Each vertex of the triangle represents a 100% pure component, points on the sides represent mixtures between two components. The mixtures inside the triangle are formed by the three components.

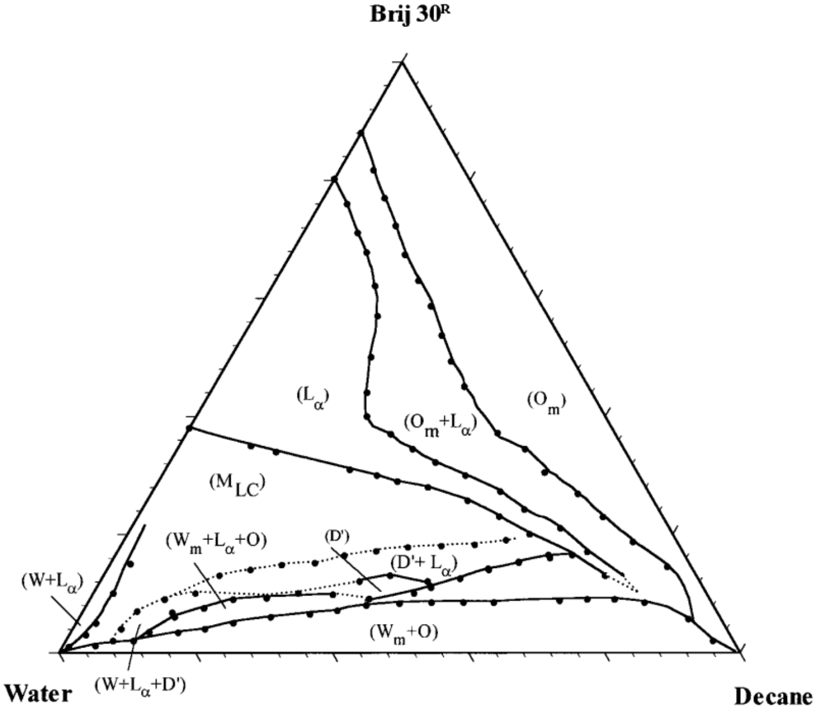

Figure 1.9. Phase behavior of water/Brijj 30/decane system at 25 ºC. O represents an oil liquid phase; W an aqueous phase; M_{LC} is a multiphase region including $\mathbf{L_\alpha}$ liquid crystals. Reproduced from [15].

1.2.2. Glycerol-based surfactants

From an environmental point of view, one interesting alternative to ethoxylated surfactants, is the use of natural glycerol as the hydrophilic part of a fatty acid based-surfactant[16]. Polyglycerol-based surfactants synthetized by partially hydrolyzing triglycerides represent the most widely used surfactants of this kind, found as emulsifiers in many food and cosmetic products. On the other hand, polyglycerol fatty acid esters produced through a condensation reaction have been the focus of many studies and applications.[17-21] However, this synthetic approach gives rise to a complex distribution of surfactants with various degrees of esterification.[22] According to EU regulations, the polyglycerol moiety should mainly be diglycerol, triglycerol, and tetraglycerol with a maximum of 10% of polyglycerols equal to or higher than heptaglycerol. In the United States, however, the U.S. Food and Drug Administration (FDA) regulation permits a polymerization degree up to decaglycerol.[23]. Technical grade glycerol-based surfactants may vary considerably in composition, depending on the degree of polymerization and degree of esterification. The composition of glycerol-based surfactants products is very complex, with a high number of positional isomers. The challenges of studying technical grade polyglycerol-based surfactants have been addressed.[24] Studies show that the phase behavior can be modified by varying the degree of esterification, which is a common situation in the industrial synthesis of these products. As an example Figure 1.10 shows the phase diagrams of two different technical grade decanoglycerol lauryl fatty acids with different degrees of esterification, $(G_{10}(C_{11})_x)$.[21] It can be observed that the phase behavior changes abruptly with the esterification degree.

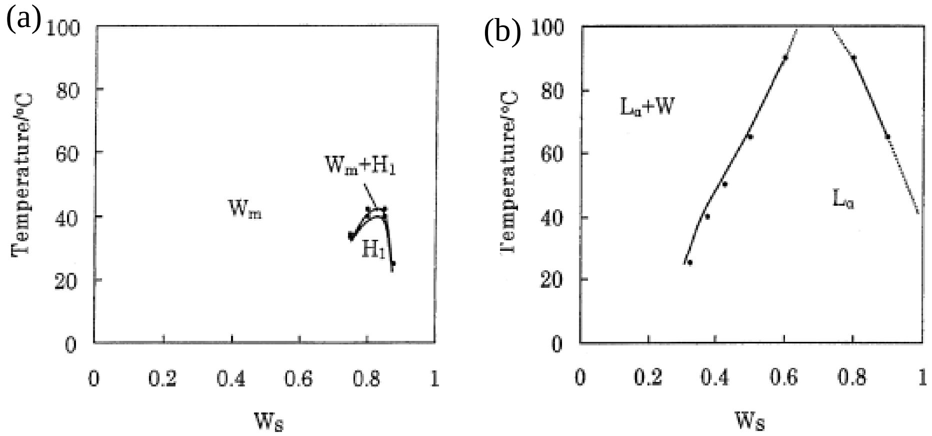

Figure 1.10. Phase diagrams as a function of weight fraction of surfactant, *Ws*, and temperature in water for: (a) $G_{10}(C_{11})_{1.9}$ and (b) $G_{10}(C11)_{3.4}$.Reproduced from [21]

1.3. CHROMONIC SELF-ASSEMBLY

Over the last 20 years since the work of Lydon, J., Atwood, T.K., Tiddy, G. and coworkers[25-27] there has been a growing interest in a type of lyotropic mesogens different from surfactants, the so-called chromonics. They are formed by a range of water-soluble multi-ring aromatic compounds. The self-assembly behavior and the structure of the chromonic molecules differ from those of conventional amphiphiles in many aspects: The chromonic molecules are rigid aromatic planks, rather than flexible aliphatic rods. The solubilizing groups in these molecules are located at the periphery rather that at one end, and they do not show a Krafft point or a definitive critical aggregate concentration.[25] The planar molecules in chromonic systems undergo $\pi - \pi$ stacking interactions forming columns in an isodesmic-type assembly.[28] Their aggregation is driven mainly by entropic contributions. Contrary to surfactant lyotropic liquid crystals, the behavior of chromonics is still not completely understood in terms of the effect of molecular architecture on their occurrence and properties. The knowledge of chromonic mesophases is still limited to a few drug molecules,[29-32] dyes[33-45] and biological relevant molecules.[46, 47]

In chromonics, the molecular aggregates are usually columnar although they can have different cross-sections. **SAXS** data shows evidence that some chromonic molecules, such as Pinacyanol or Acid Red 266 tend to form multimolecular cross-sectional columnar aggregates.[39, 40] Moreover, layered structures in which the molecules are arranged in a brick-wall like structure has also been found.[42] Some models of the most common aggregates are shown in Figure 1.11.

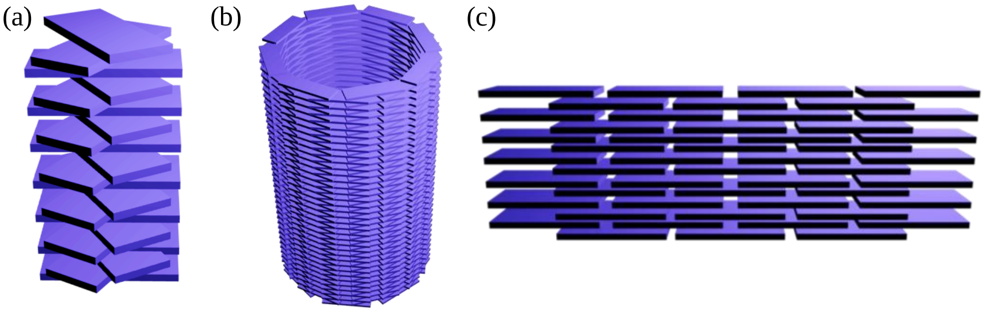

Figure 1.11. Schematic representation of chromonic aggregates with: (a) Unimolecular cross-section, (b) multimolecular cross-section and (c) brick-wall like layers.

As the concentration of chromonic molecules is increased, the columns grow in size and in concentration. When a certain volume fraction is reached, mesophases can form. Two mesophases are commonly found: at lower concentrations, a nematic array of molecular columns (**N** phase), and at higher concentrations, the **M** phase, in which the aggregates pack in a hexagonal lattice; in both cases the director is perpendicular to the molecular stacking planes. Both of this mesophases are anisotropic, meaning that they present characteristic textures under **POM. SAXS** patterns of different samples are characterized by a wide-angle axial reflection correspond to a *d* spacing of 3.4 Å which is ascribed to the distance between the center of two planar aromatic moieties. In addition, many reports of lamellar liquid crystals are also found [42, 44]. Chromonic rectangular liquid crystals are expected to exist by analogy to thermotropic systems.[26] Evidence of the rectangular phase is found in literature,[48, 49] however it has been poorly characterized. The phase properties of chromonic liquid crystal are influenced by many factors including molecular structure, concentration, temperature and presence of additives; however, some of these effects are far for being completely understood.

One of the first examples in literature of phase diagram determination of chromonic molecules are those from disodium chromoglycate (**DSCG**). **DSCG** was one of the first effective anti-asthmatic drugs, commercialized under the trade names INTAL in Britain and Chromolyn in the US. The study of the phase behavior of this dye was motivated by the hypothesis that the superior medical properties were consequence of the mesophases formed. The phase diagram of **DSCG** is shown in Figure 1.12.[50, 51]

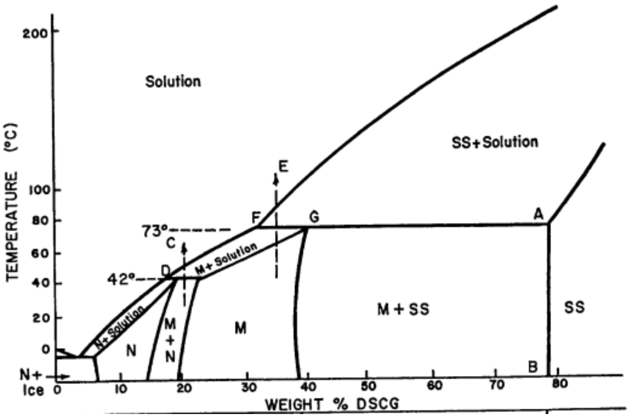

Figure 1.12. Phase diagram of the water/**DSCG** system as a function of **DSCG** concentration (in wt%) and temperature. [50, 51]

The coexisting region between chromonic liquid crystal and isotropic solution might be wide, which is caused by the isodesmic nature of the aggregation process.

Since some chromonic molecules are conjugated systems, they present concentration dependent absorption spectra in the **UV-Vis** range. These changes can be explained by the exciton theory

1.3.1. The exciton theory

Although chromonic liquid crystals are relatively new, dye aggregates in solution have been known for a long time and extensively studied as they play key roles in natural processes (i.e. light harvesting in photosynthesis). Attractive forces between dyes (usually planar molecules) induce self-assembly both in solution and on solid surfaces, causing changes in optical properties compared to those in the monomeric, non-aggregated state. The changes are reflected in a displacement of the bands in the absorption spectra: blue or hypsochromic shifts to shorter wavelengths are referred to as H-bands while bathochromic shifts to longer wavelengths are referred to as J-bands.[52] Research on H- and J-aggregates in dilute solutions, initially motivated by their relevance for spectral sensitization of the photographic process, is still very active nowadays, including both experimental[53] and theoretical studies[54] with potential impact in fields such as dye-sensitized solar cells, optoelectronics, and photodynamic therapy.

Kasha and McRae introduced their exciton theory for aggregated dimers based on the point dipole approximation.[55] In this theory the transition dipole moment of the molecules A and B are assumed to be classical oscillators and V_{ex} is the exciton splitting that can be calculated by:

$$V_{ex} = \frac{1}{4\pi\varepsilon_0 |d_m^3|}[\mu_A \cdot \mu_B - 3(\mu_A \cdot \hat{r})(\mu_B \cdot \hat{r})]$$

Equation 1.11

Where μ_A and μ_B are the transition dipole moments of the monomers A and B, $\varepsilon_0$the permittivity of vacuum, and d_m the distance between the centers of the molecules A and B. In the case of coplanar alignment of molecules, the Equation 1.11 simplifies to:

$$V_{ex} = \frac{|\mu_{AB}^2|}{4\pi\varepsilon_0 d_m^3}[1 - 3cos^2\theta]$$

Equation 1.12

The energy levels for ground (S_0) and excited (S_1) states for are illustrated in Figure 1.13. For both, H and J-dimers the possible dipole phase relations are depicted, with f_s being the oscillator strength to the exciton state, which is proportional to$|\mu_{AB}^2|$. The larger the value of f_s, the more likely is the transition to this energy level, transitions for f_s= 0 are forbidden.

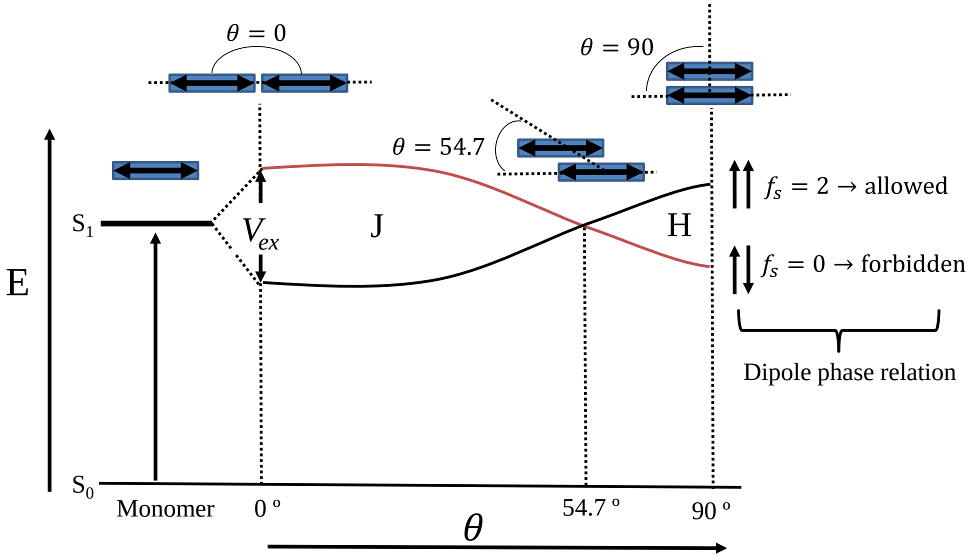

Figure 1.13. Energy diagram for aggregated dimers with coplanar inclined transition dipoles. The black and red line indicates allowed and forbidden transitions, respectively.

J-aggregates transitions are only allowed into lower energies, whereas H-aggregates are only allowed to high energies. Notice that although there is exciton coupling, no splitting is observed at staking angles of 54.7 °.

As a result of a rapid internal conversion of the excited state of H-aggregates into the forbidden state there is a decreasing transition probability for a radiative process from the forbidden state to the ground state; consequently, H-aggregates do not present fluorescence.

Chromonic applications are still far from being exploited. Some cationic chromonic molecules are known to be able to template silica growth.[33, 39] In both cases mesoporous high aspect ratio silica fibers were obtained, containing pores parallel to the fibers length. The **N** and **M** phase can be easily aligned and then dried down to produce a solid with the same degree of ordering. This property can be exploited to form polarizing films.[35] Another good example of chromonic applications is in sensors. Lavrentovich et al. [56, 57] studied a biosensor composed of a chromonic nematic liquid crystal cell between two polarizers oriented with their polarization axes orthogonal to each other. Microbes could be detected by the defects in the nematic liquid crystal. In order to exploit all possible applications of chromonic systems a deeper understanding of the molecular structure/condensed phase properties is needed for designing novel and functional mesogens, optimized for specific uses.[58]

1.4. MOLECULAR SELF-ASSEMBLIES AS TEMPLATES FOR NANOSTRUCTURED MATERIALS

Nanotechnology has drawn a great interest in the past decades due to its potential for generating novel materials with extraordinary physical and chemical properties. Considerable efforts have been invested in the research and development of these materials while a general list of properties has been identified through simulations of specific nanoscale architectures. As their potential in material science has become clear, there is a great interest in understanding and developing new synthetic routes.[59] Two strategies are commonly employed for generating nanostructures. The first is top-down, which uses various methods of lithography to pattern bulk materials.[60] Top-down methods of nanofabrication are expensive, and they usually have relatively low throughput and most of them are limited to two dimensional structures. The second strategy is bottom-up [61, 62] that consists in starting from atoms or molecules to generate a nanostructured material. Self-assembly stands out as one of most attractive bottom up synthesis methods since it is versatile and cost-effective. In the bottom-up synthesis of nanomaterials, self-assemblies can for example act as templates for the polymerization of a precursor, therefore the shape of the material obtained is usually the complementary of the aggregate. Interestingly, the bottom-up path using self-assembly can be observed in nature. For instance, organisms use organic macromolecules and microstructures to control the nucleation and growth of inorganic materials.[63-65] Similar approaches are used in material chemistry. Syntheses assisted by molecular self-assembly can take place in two ways. In the first one, self-assemblies act as directing agents in the synthesis. These can be in the form of discrete aggregates or condensed phases, such as liquid crystals. They self-assemble when the reaction starts (transcriptive synthesis) or co-assemble during synthesis (Synergistic synthesis).[59] In the second way, the growth of inorganic materials is spatially restricted by confining the reaction solutions within organized media (e.g. micelles, microemulsions). In both cases, the final material size and structure would depend on the type of self-assemblies formed. Surfactants are probably the most well-known molecular templates. For instance, amphiphilic copolymers and a silica precursor (**TEOS**) can produce nanoporous materials such as SBA-15, with high surface area and hierarchically arranged pores.[66, 67]

The discovery of new materials with novel properties to find solutions to increasing societal challenges makes nanotechnology one of the best alternatives for the future. Molecular self-assembly represents one of the most useful tools for generating nanomaterials; therefore the study of new self-assembled molecules is of uttermost importance.

1.4.1. Applications of functional materials

As explained in the previous sections, molecular self-assembly can serve as a tool for generating nanomaterials with well-defined structures, high porosity and functionality. Surfactants in solution can solubilize hydrophobic and hydrophilic drugs therefore show some promising applications as vehicles for controlled release of active molecules.[68-74] On the other hand, chromonics can template inorganic materials growth into high aspect ratio mesoporous fibers.[33, 39] These fibers can be further used to template other materials, such as carbon. The derived carbon materials can be used in several applications. Among them, energy storage is one of the most promising applications of carbon materials.[75, 76] The development of efficient energy storage devices (such as electrical double layer capacitors; **EDLCs**) with fast charging times, high power density and high stability to charge/discharge cycles is essential to address the growing demand for portable electronic devices. Porous carbon has also received considerable attention in sensor technology since their high surface area combined with their surface chemistry makes them selective towards aromatic volatile organic compounds (**VOCs**).[58, 77, 78]

1.4.1.1. **Drug delivery**

Lyotropic liquid crystalline phases from biocompatible glycerol-based surfactants are of special interest for a multitude of applications, such as food, cosmetic and pharmaceutics. Recently they have received increasing attention due to the growing need to create biocompatible material templates for drug encapsulation and release.[79-83] The systems that form inverse liquid crystal phases are of great interest in basic and applied research. Studies have shown that these phases have potential as drug delivery systems,[71, 84] as nano-vehicles for confining proteins, as well as for crystallizing membrane proteins.[85-87] However, it is important to mention that the use of these phases in the pharmaceutical and nutraceutical industry is still very limited. Their high viscosity makes them difficult to handle, and furthermore, these bulk phases might be problematic in contact with the biological epithelia, because the high amount of surfactant can cause irritation.[88, 89] There is a promising alternative to overcome these problems, which consist in dispersing these liquid crystals in excess water to form diluted non-viscous aqueous dispersions with internal nanostructures (**LCN's**).[90] This dispersion would retain the original structure of the mesophase and similar properties but with viscosities similar to water. Vesicles are one of the more known and used **LCN**, in contrast the non-lamellar **LCN**'s are less studied. Therefore, there is an increasing interest for studying and using nanostructured aqueous dispersions of non-lamellar soft structures with properties similar to their bulk non-dispersed phase.

Many glycerol-based surfactants are reported to form liquid crystal dispersions both in water and oil. Kunieda *et al* reported the phase behavior of pentaglycerol monostearate and monooleate in aqueous systems.[17] These surfactants form fine dispersions of lamellar liquid crystals on the dilute surfactant region and can be used to make highly stable aqueous foams.[91] Formation of inversed vesicles has been found in monoglycerol fatty acid esters in non-polar oils.[92] Probably the most representative example of glycerol-based surfactants forming liquid crystal phases in excess water are those corresponding to the monoolein[93] and monolinolein[94] (Figure 1.14) which presents a rich phase polymorphism:

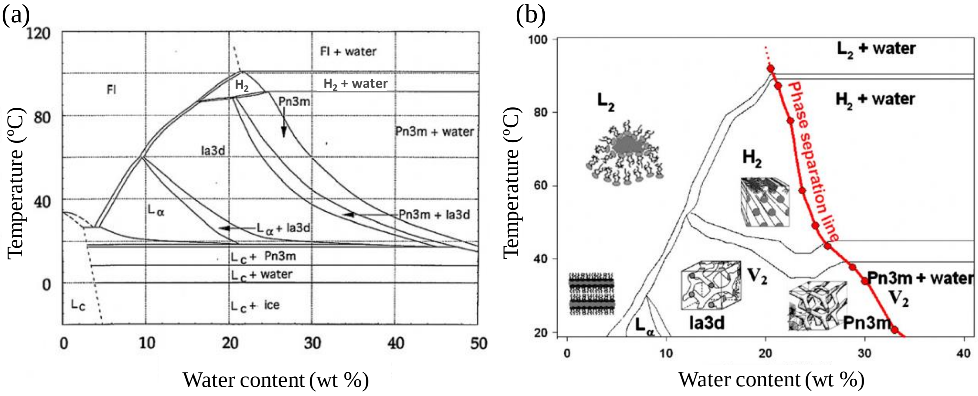

Figure 1.14. Phase diagram as a function of water content and temperature of (a) water/monolein[93] and (b) water/monolinolein[94] systems. L_C and FI represent liquid crystalline phase with unresolved structure and an isotropic fluid, respectively.

The regions at high water contents of the phase diagrams in Figure 1.14 can be used to form cubosomes (dispersions of bicontinuous liquid crystal) or hexosomes (dispersions of inverse hexagonal liquid crystals). Since they can solubilize active compounds in their structure, they have been widely used as drug delivery vehicles.

Representative examples of nanostructured dispersions as drug delivery vehicles are shown in Table 1.3

Table 1.3. Representative examples of the utilization of cubosomes and hexosomes as drug carriers.

Type of nanostructured dispersion	Active substance or material	Reference
Cubosomes	Indomethacin	[95]
Cubosomes	Magnetic Nanoparticles	[96]
Cubosomes	Docetaxel/Rhodamine	[97]
Cubosomes	Insulin	[98]
Hexosomes	Cyclosporin A	[99, 100]
Hexosomes	Nitroxide	[101]
Hexosomes	IIrrinotecan	[102]

1.4.1.2. **Electrical double layer capacitors**

EDLCs are energy storage devices based on charge storage within the electrical double layer. **EDLCs** can store energy due the polarization of an electrolyte solution by applying a voltage between two porous electrodes. The electrolytes are absorbed and retained in the surface of the electrode material, storing energy in the form of potential energy. In the process of returning to the initial state they create a current (Figure 1.15). It is obvious that the amount of energy that they can be stored is related to the surface and pore structure of the material, however the influence of the surface area on the amount of energy that **EDLCs** can store is still a matter of discussion. Another factor that increases the total energy that can be stored is the easy transport of electrons from the electrode to the solution. Materials with higher conductivity usually can storage more energy.

Several studies have demonstrated that activated carbon,[103-107] mesoporous carbon,[108-115] carbon nanotubes,[116-118] graphene,[119-122] etc. are potential candidates for **EDLCs**. Nowadays, the market for these devices (used for memory protection in electronics circuitry mainly) is about \$150-\$200 million annually.[75]

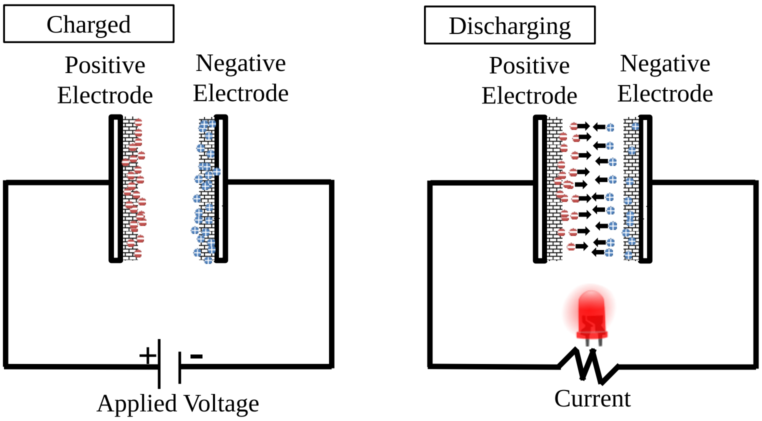

Figure 1.15. Schematic representation of a **EDLCs** mechanism of storing energy

EDLCs differ from normal batteries in many aspects. For instance, the kinetics of charging/discharging does not depend on a chemical reaction, consequently they can be charged in matter of milliseconds and they have long cycle life of more than 10,000 charge/discharge cycles (batteries usually reduce their storage capacity to 80% after 100 cycles). Additionally, they can supply high amounts of electricity in that same amount of time (power densities up to 10 kW/kg) and they generally exhibit an environmental friendly synthesis (no use of heavy metals). However, they cannot store high amounts of energy compared to normal batteries (low energy density), therefore, the improvement of this parameter is one of the main challenges in **EDLCs** technology. **EDLCs** are of importance in applications where high power densities are needed, e.g. starting an electrical car needs high amount of energy. The use energy from the wind or the sun is often limited to the long charging times of batteries (hours). The optical cyclic voltammetry responses for batteries and **EDLCs** is shown in Figure 1.16. The optimal response for a **EDLCs** is a rectangular profile since low internal resistance to charging is expected (no dependent of kinetic factors). In contrast the cyclic voltammetry’s of batteries contain oxidation/reduction peaks corresponding to a redox reaction, which limits the charging time.

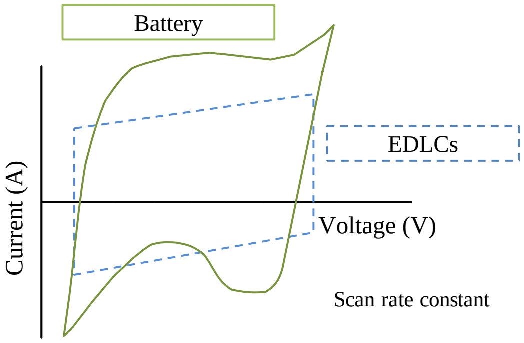

Figure 1.16. Characteristic cyclic voltammetry curves for batteries and **EDCLs**.

1.4.1.3. **Molecular sensing**

The demand of accurate and dedicated sensors to provide precise process control and safety in manufacturing processes has made sensor technology an active area of research.[77, 78], particularly focused on the development of sensing materials with new structures or morphologies to improve sensitivity, selectivity and stability of sensors.[123-125]

Piezoelectric sensors are based on mass detection using a quart crystal microbalance (**QCM**) and provide a versatile detection method for a wide range of guest substances because all adsorbates produce weight changes upon adsorption on a substrate. This kind of sensors usually reach nanogram-level sensitivities. The principle behind piezoelectric sensors is simple (

Figure 1.17). The frequency shift is measured as a function of time. If a substance is absorbed there is a frequency shift that is proportional to the mass absorbed. Mesoporous materials often provide appropriate materials for **QCM** sensing. For instance, carbon deposited on a **QCM** plate shows good selectivity towards adsorption of aromatic hydrocarbons, such as benzene or toluene.[124-129]

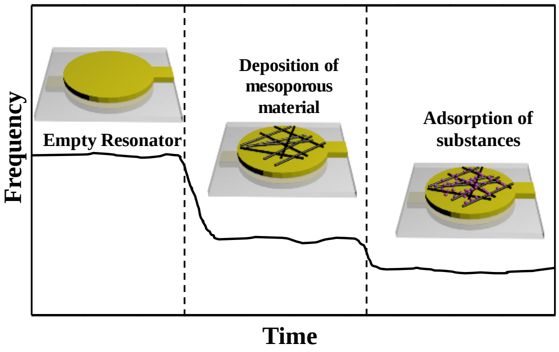

Figure 1.17. Schematic representation of a **QCM** vapor sensor.

2. OBJECTIVES

In the last decades, molecular self-assembly has gained increasing importance due to its great technological potential. The study of novel molecules with the ability to self-assemble into new structures with controlled properties has become an important area of research.

Surfactants are known for their self-assembly properties. These molecules are composed of polar and hydrophobic moieties. Their self-assembly in solution is driven by solvophobic segregation, consequently, they form a wide range of nanostructures, from simple micelles to liquid crystals such as lamellar, hexagonal or cubic phases. The molecular forces that drive self-assembly are non-covalent (electrostatic, Van der Waals, hydrophobic effect, etc.). Molecular self-assembly can be controlled by external stimuli such as temperature, pH etc.

Molecular self-assembly is not only a property of surfactants. Some aromatic molecules (including dyes), so-called chromonics, can also form self-organized structures. The properties of chromonics differ from those of conventional amphiphilic systems; moreover, the relationship between molecular structure of chromonics and bulk phase behavior is still poorly understood. Reported chromonics are restricted only to a few types of anionic dyes or polyaromatic planar molecules, and thus is of high interest to increase their availability by studying new compounds.

Nanomaterials have raised much attention during the last years due to their unique and special properties that are of interest to almost every field of science and industry. The properties of nanomaterials depend on their chemical composition, size and morphology; controlling accurately those parameters has been an active area of research in the past years. The bottom-up fabrication of nanostructures offers numerous attractive advantages: the process usually occurs towards thermodynamic minima, resulting in stable and robust structures, thus, it is cost-effective, versatile and facile. Among the bottom-up approaches found in literature, the most common methods to obtain nanomaterials with hierarchical ordered mesopores are those using molecular self-assemblies as templates.

In a typical bottom-up material synthesis, the final morphology and pore size distribution of the resulting material is determined by the starting molecular assemblies. Surfactant aggregates in aqueous media are probably the most used templates for synthetizing nanomaterials. From the industrial point of view technical grade surfactants are preferred because they are more cost-effective; however, molecular self-assembly can be highly influenced by the presence of impurities and only few studies are performed on technical grade products compared to those from pure surfactants. The study of the self-assembly behavior of technical grade surfactants and the influence of impurities is of uttermost importance for developing well defined materials. On the other hand, other types of self-assemblies with different morphologies than those formed by surfactant systems are interesting from a technological point of view. Among them, chromonics molecules are of special interest due to their special optical properties, that when combined with inorganic materials can be exploited in a wide range of application.

In this context, the main objective of this thesis was to characterize the molecular self-assembly of surfactants and chromonics in aqueous media for the synthesis of novel functional nanostructured materials for selected applications.

The achievement of that objective involved the following tasks:

a) Determination of the self-assembly behavior of technical grade diglycerol-based surfactants and dyes (with potential chromonic behavior) in aqueous media and its correlation with molecular architecture.

b) Preparation of soft and hard functional materials using self-assemblies as templates.

c) Exploration of applications of the obtained materials in drug delivery, energy storage and sensing technologies.

Tasks were addressed according to the following work plan:

1. Selection of the appropriate glycerol-based surfactants and chromonic compounds able to form liquid crystals.
2. Phase behavior study of the selected molecules.
    a. Phase diagram determinations as a function of composition and temperature.
    b. Characterization of the mesophases by using polarized optical microscopy (**POM**), small and wide angle x-ray scattering (**SAXS**/**WAXS**) and spectroscopic techniques.
3. Study of glycerol-based surfactant self-assemblies as drug delivery vehicles.
    a. Formation and stabilization of liquid crystal nanoparticles, and characterization by dynamic light scattering (**DLS**)
    b. Encapsulation of a model hydrophobic active molecule and determination of their release profile to a receptor solution.
4. Application of dye chromonic self-assemblies as templates for the formation of mesoporous silica.
    a. Determination of the capacity of different chromonic molecules for templating silicon oxide.
    b. Characterization of the obtained silica materials by electron microscopy, **SAXS** and gas sorption.
5. Formation of mesoporous carbon materials using mesoporous silica as a hard template.

    a. Synthesis of carbon materials from silica using furfuryl alcohol as carbon precursor.
    b. Characterization of carbon materials by X-ray techniques (**XPS**, **SAXS**, **XRD**), Raman, gas sorption, and electron microscopy.
6. Testing potential applications of the derived carbon materials in energy storage and molecular sensing.
    a. Capacitance estimation by voltammetry and charge/discharge curves
    b. Determination of vapor sensing capacity using the quartz crystal microbalance (**QCM**) technique.

3. EXPERIMENTAL

3.1. MATERIALS

3.1.1. Surfactants

- **Diglycerol polyisostearates: Isooctadecanoic acid esters with oxydi(propanediol).**

The diglycerol-isostearate-based surfactants (Figure 3.1) are a gift from Nisshin Oillio Group (Japan). This family of surfactants is produced through a condensation reaction of fatty acids with diglycerol at Diglycerol: Isostearic acid acid ($C_{18}H_{36}O_2$) ratios of 1:1 (Cosmol 41V), 1:2 (Cosmol 42V), 1:3 (Cosmol 43V) and 1:4 (Cosmol 44V). Some physical properties are summarized in Table 3.1.

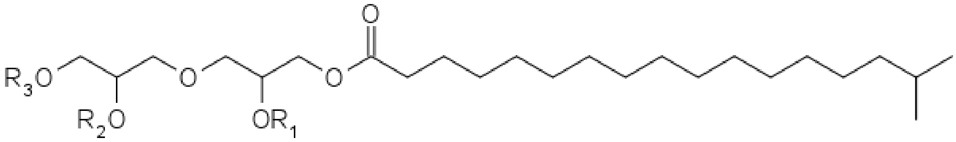

R_1, R_2 & R_3=H → Cosmol 41V

R_1=$C_{18}H_{35}O_2$, R_2 & R_3=H → Cosmol 42V

R_1 & R_2=$C_{18}H_{35}O_2$, R_3=H → Cosmol 43V

R_1, R_2 & R_3=$C_{18}H_{35}O_2$ → Cosmol 44V

Figure 3.1. General molecular structure of diglycerol isostearate esters.

Table 3.1. Physical properties of diglycerol isostearate esters.

Surfactant	HLB number	Dynamic viscosity (mm^2/s)	Acid Value (mg KOH/g Surfactant)
Cosmol 41V	8	6.540	< 0.1
Cosmol 42V	4	1.160	0.2
Cosmol 43V	2	0.448	0.5
Cosmol 44V	---	0.370	0.2

- **Pluronic F127 (F127, BASF)**

Pluronic **F127** or Poloxamer 407 is a high-molecular-weight surface active tri-block copolymer (Figure 3.2).

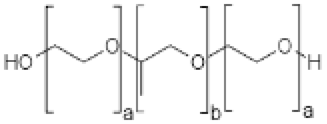

Figure 3.2. Molecular structure of Pluronic **F127**. The approximate block lengths are a=101 and b=56.

3.1.2. Dyes

- **Quinaldine Red Iodide (QR-I)**

QR-I (95%) was obtained from Across Organics and was purified by washing the powder with water and recovering the insoluble fraction by filtration; this process was repeated three times before drying the insoluble fraction (80% of yield).

- **Quinaldine Red Acetate (QR-Ac)**

QR-Ac (Figure 3.3) was prepared by adding silver acetate (1.1 equivalents) into a solution of **QR-I** in **EtOH** (2.5 mmol of **QR-I** in 20 mL of **EtOH**). After removal of precipitate by filtration, the solvent was evaporated under nitrogen flow to obtain the solid **QR-Ac** with 95% yield.

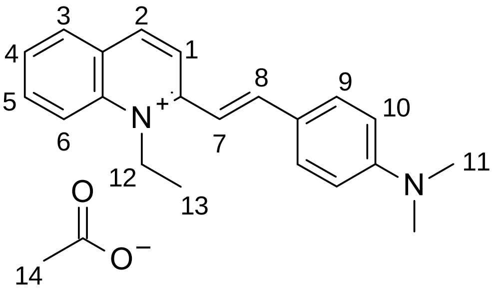

Figure 3.3. Molecular structure of **QR-Ac**.

^{1}H NMR (400 MHz, D_2O): 1.40 (t, J = 7.4 Hz, 3 H, H–C(13)), 1.93 (s, 3 H, H–C(14)), 2.35 (s, 6 H, H–C(11)), 4.27 (q, J = 8.0 Hz, 2 H, H–C(12)), 5.73 (d, J = 8.80 Hz, 2 H, H–C(10)), 6.43 (d, J = 15.6 Hz, 1 H, H–C(7)), 6.87 (d, J = 8.8 Hz, 2 H, H–C(9)), 7.33 (d, J = 15.2 Hz, 1 H, H–C(8)), 7.51–7.55 (m, 1 H, H–C(4)), 7.62 (d, J = 9.6 Hz, 1 H, H–C(1)), 7.70 (d, J = 8.0 Hz, 1 H, H–C(3)), 7.73–7.79 (m, 2 H, H–C(5) and H–C(6)), 8.00 (d, J = 8.8 Hz, 1 H, H–C(2));^{13}C NMR (100 MHz, D_2O): 12.9, 23.1, 38.4, 45.5, 108.0, 110.7, 116.9, 118.4, 120.4, 126.6, 127.4, 129.5, 130.7, 133.8, 137.4, 141.2, 147.9, 151.6, 153.4, 181.2.

^{1}H NMR (400 MHz, $(CD_3)_2SO$): 1.54 (t, J = 7.1 Hz, 3 H, H–C(13)), 1.55 (s, 3 H, H–C(14)), 3.09 (s, 6 H, H–C(11)), 5.05 (q, J = 7.1 Hz, 2 H, H–C(12)), 6.84 (d, J = 9.0 Hz, 2 H, H–C(10)), 7.47 (d, J = 15.4 Hz, 1 H, H–C(7)), 7.82–7.89 (m, 3 H, H–C(9) and H–C(4)), 8.09 (ddd, *J* = 8.8, 7.2, 1.6 Hz, 1 H, H–C(5)), 8.25 (dd, *J* = 8.0, 1.4 Hz, 1 H, H–C(3)), 8.32 (d, *J* = 15.4 Hz, 1 H, H–C(8)), 8.44 (d, *J* = 9.0 Hz, 1 H, H–C(6)), 8.54 (d, *J* = 9.3 Hz, 1 H, H–C(1)), 8.80 (d, *J* = 9.2 Hz, 1 H, H–C(2)); ^{13}C NMR (100 MHz, $(CD_3)_2SO$): 13.8, 24.8, 45.5, 110.7, 111.9, 118.4, 120.3, 122.4, 127.1, 128.0, 130.1, 132.1, 134.4, 138.1, 142.0, 149.7, 153.0, 155.4, 172.6 (one signal hidden under the carbon resonance of the solvent).

- **Pyronin Y (PyY)**

Pyronin Y (96%) (Figure 3.4) was obtained from Sigma Aldrich and used as received without further purification.

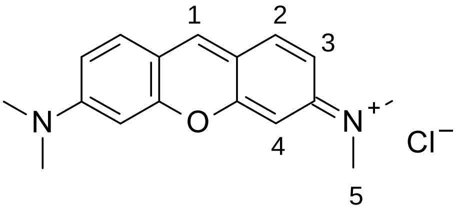

Figure 3.4. Molecular structure of **PyY**.

^{1}H NMR (400 MHz, D_2O): 3.03 (s, 12 H, H–C(5)), 6.16 (s, 2 H, H–C(4)), 6.67 (dd, *J* = 9.1, 1.6 Hz, 3 H, H–C(3)), 7.23 (d, *J* = 9.2 Hz, 2 H, H–C(2)), 7.82 (s, 1 H, H–C(1)).

- **3,3´-Diethylthiacarbocyanine iodide**

3,3´-Diethylthiacarbocyanine iodide (97%) was obtained from Sigma Aldrich and used without further purification.

- **3,3´-Diethylthiacarbocyanine Acetate (TCC-C_2)**

TCC-C_2 (Figure 3.5) was prepared by dissolving 120 mg of 3,3´-Diethylthiacarbocyanine iodide (0.24 mmol) in **MeOH** (30 mL). Silver acetate (41 mg, 0.24 mmol) was added, and the reaction mixture was stirred in the dark for 65 h. The mixture was then centrifuged (10 min, 4000 rpm) and passed through filter paper. The supernatant was collected and the remaining brown solid was resuspended in **MeOH** (5 mL), centrifuged, and filtered. The combined supernatants were evaporated to dryness under nitrogen flow and purified over C_{18}-reversed phase silica gel (Fluka, 40–63 μm, fully end-capped) with **MeOH** as eluent. **TCC-C_2** (96 mg, 94%) was obtained as dark purple solid.

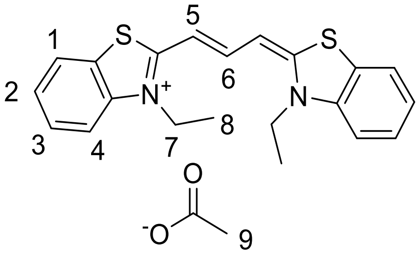

Figure 3.5. Molecular structure of **TCC-C$_2$**.

^{1}H NMR (400 MHz, (CD$_3$)$_2$SO): 8.01 (d, *J* = 8.0 Hz, 2 H, H–C(1/4)), 7.83–7.78 (m, H–C(1/4), H–C(6)), 7.59 (br t, *J* = 7.6 Hz, 2 H, H–C(2/3)), 7.44 (br t, *J* = 7.6 Hz, 2 H, H–C(2/3)), 6.62 (d, *J* = 12.8 Hz, 2H, H–C(5)), 4.40 (q, *J* = 6.8 Hz, 4 H, H–C(7)), 1.55 (s, 3 H, H–C(9)), 1.34 (t, *J* = 7.0 Hz, 6 H, H–C(8)); ^{1}H NMR (400 MHz, D$_2$O, 1 wt%): 7.21 (d, *J* = 7.7 Hz, 2H, H–C(1) or H–C(4)), 7.05 (t, *J* = 12.7 Hz, 1H, H–C(6)), 6.99–6.94 (m, 4H, H–C(1) or H–C(4) and H–C(2) or H–C(3)), 6.56–6.52 (m, 2H, H–C(2) or H–C(3)), 5.66 (d, *J* = 12.8 Hz, 2H, H–C(5)), 3.66–3.60 (m, 4H, H–C(7)), 1.95 (s, 3H, H–C(9)), 1.09 (t, *J* = 7.2 Hz, 6H, H–C(8)); ^{13}C NMR (100 MHz, (CD$_3$)$_2$SO): 172.3, 164.2, 146.7, 140.8, 128.1, 125.21, 125.15, 123.1, 113.4, 98.6, 41.4, 25.5, 12.6; ^{13}C NMR (100 MHz, D$_2$O, 1 wt%): 181.0, 163.5, 145.2, 139.9, 127.6, 124.7, 124.5, 122.2, 112.2, 96.4, 41.3, 23.1, 12.0. The signals of the protons were assigned based on two-dimensional **NMR** experiments. Due to signal overlapping complete assignment of the aromatic protons was not possible.

- **3,3´-Dipropylthiacarbocyanine iodide**

3,3´-Dipropylthiacarbocyanine iodide (98%) was obtained from Sigma-Aldrich and used without further purification.

- **3,3′-Dipropylthiacarbocyanine Acetate (TCC-C$_3$)**

TCC-C$_3$ (Figure 3.6) was prepared by dissolving 100 mg of 3,3´-Dipropylthiacarbocyanine iodide (0.19 mmol) in **MeOH** (15 mL). Silver acetate (35 mg, 0.21 mmol) was added, and the reaction mixture was stirred in the dark for 24 h. The mixture was then centrifuged and passed through filter paper. The supernatant was collected and the remaining solid was resuspended in **MeOH** (5 mL) and centrifuged. The resuspended solid was centrifuged and filtered. The combined supernatants were evaporated to dryness under nitrogen flux. **TCC-C$_3$** (75 mg, 85%) was obtained as dark purple solid, and used without further purification.

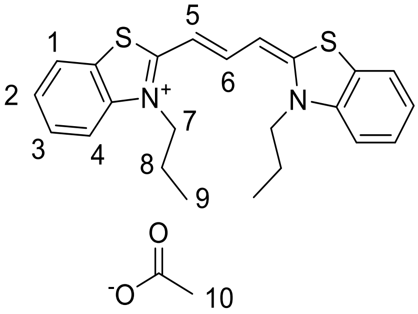

Figure 3.6. Molecular structure of **TCC-C$_3$**.

^{1}H NMR (400 MHz, $(CD_3)_2SO$): 7.99 (d, *J* = 7.8 Hz, 2 H, H–C(1/4)), 7.81–7.73 (m, 3 H, H–C(1/4), H–C(6)), 7.56 (br t, *J* = 7.8 Hz, 2 H, H–C(2/3)), 7.41 (br t, *J* = 7.8 Hz, 2 H, H–C(2/3)), 6.64 (d, *J* = 12.8 Hz, 2H, H–C(5)), 4.31 (t, *J* = 7.4 Hz, 4 H, H–C(7)), 1.78 (m, 4 H, H–C(8)), 1.58 (s, 3 H, H–C(10)), 1.00 (t, *J* = 7.4 Hz, 6 H, H–C(9)); ^{13}C NMR (100 MHz, $(CD_3)_2SO$): 172.6, 164.6, 146.6, 141.3, 128.0, 125.2, 125.0, 123.0, 113.7, 98.9, 47.4, 25.4, 20.7, 10.8. The signals of the protons were assigned based on two-dimensional **NMR** experiments. Complete assignment of the aromatic protons was not possible.

- **3,3´-Dibutylthiacarbocyanine iodide**

3,3´-Dibutylthiacarbocyanine iodide (98%) was obtained from Sigma-Aldrich and used without further purification.

- **3,3′-Dibutylthiacarbocyanine Acetate (TCC-C$_4$)**

TCC-C$_4$ (Figure 3.7) was prepared by dissolving 49 mg of 3,3´-Dibutylthiacarbocyanine iodide (0.09 mmol) in **MeOH** (20 mL), and stirred at room temperature in the dark for 1 h to solubilize the dye. Then, silver acetate (17 mg, 0.10 mmol) was added, and the reaction mixture was stirred in the dark for 96 h. The mixture was then passed through a filter paper (Whatman 42), filter was rinsed with **MeOH**, and the solvent was evaporated to dryness. Purification was performed in a C_{18}-reversed phase silica gel (Fluka, 40–63 μm, fully endcapped) using **MeOH** as eluent. Then, water (0.5 mL) was added and after freeze-drying **TCC-C$_4$** (35 mg, 80%) was obtained as purple solid.

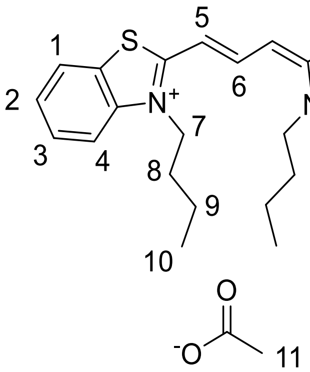

Figure 3.7. Molecular structure of **TCC-C₄**.

^{1}H NMR (400 MHz, $(CD_3)_2SO$): 8.00 (d, *J* = 7.9 Hz, 2 H, H–C(1/4)), 7.74–7.83 (m, 3 H, H–C(1/4), H–C(6)), 7.58 (br t, J = 7.7 Hz, 2 H, H–C(2/3)), 7.42 (br t, J = 7.6 Hz, 2 H, H–C(2/3)), 6.62 (d, J = 12.8 Hz, 2H, H–C(5)), 4.34 (t, J = 7.4 Hz, 4 H, H–C(7)), 1.80–1.69 (m, 4 H, H–C(8)), 1.64 (s, 3 H, H–C(11)), 1.49–1.38 (m, 4 H, H–C(9)), 0.95 (t, J = 7.4 Hz, 6 H, H–C(10)); 13C NMR (100 MHz, (CD3)2SO): 172.6, 164.6, 146.7, 141.2, 128.1, 125.2, 125.0, 123.0, 113.6, 98.8, 46.1, 29.4, 24.2, 19.4, 13.7. The signals of the protons were assigned based on two-dimensional **NMR** experiments. Complete assignment of the aromatic protons was not possible.

- **3,3´-Dipentylthiacarbocyanine iodide**

3,3´-Dipentylthiacarbocyanine iodide (96%) was obtained from Alfa Aesar and used without further purification.

- **3,3′-Dipentylthiacarbocyanine Acetate (TCC-C₅)**

TCC-C₅ (Figure 3.8) was prepared by dissolving 100 mg of 3,3´-Dipentylthiacarbocyanine iodide (0.17 mmol) in **MeOH** (20 mL). Silver acetate (31.5 mg, 0.19 mmol) were added, and the reaction mixture was stirred in the dark for 24 h. The mixture was then centrifuged (10 min, 4000 rpm) and passed through filter paper. The supernatant was collected and the remaining solid was resuspended in **MeOH** (5 mL), centrifuged and separated. The combined supernatants were passed through a C_{18} reversed phase silica gel (Fluka, 40–63 µm, fully endcapped) with **MeOH** as eluent. The final eluent was evaporated under nitrogen atmosphere to obtain **TCC-C₅** (83 mg, 94%) was as dark reddish solid.

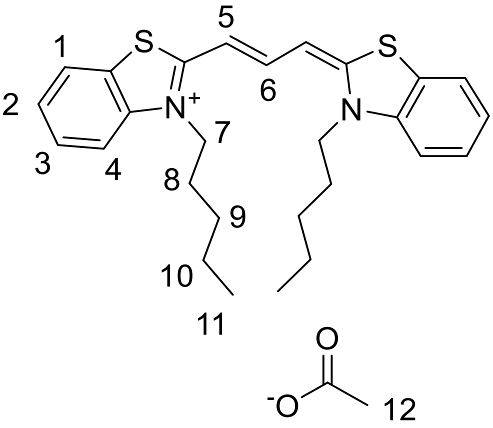

Figure 3.8. Molecular structure of **TCC-C$_5$**.

^{1}H NMR (400 MHz, $(CD_3)_2SO$): 8.00 (d, J = 7.9 Hz, 2 H, H–C(1/4)), 7.74–7.83 (m, 3 H, H–C(1/4), H–C(6)), 7.58 (br t, J = 7.7 Hz, 2 H, H–C(2/3)), 7.42 (br t, J = 7.6 Hz, 2 H, H–C(2/3)), 6.62 (d, J = 12.8 Hz, 2H, H–C(5)), 4.34 (t, J = 7.4 Hz, 4 H, H–C(7)), 1.80–1.69 (m, 4 H, H–C(8)), 1.64 (s, 3 H, H–C(11)), 1.47–1.33 (m, 4 H, H–C(9/10)), 0.98 (t, J = 7.4 Hz, 6 H, H–C(11)).

- **3,3′-Diethyloxacarbocyanine Iodide (Sigma-Aldrich, 98%)**

3,3′-Diethyloxacarbocyanine iodide (98%) was obtained from Sigma Aldrich and used without further purification.

- **3,3′-Diethyloxacarbocyanine Acetate (OXA-3C)**

OXA-3C (Figure 3.9) was prepared by adding silver acetate (1.1 equivalents) to a solution of 3,3′-Diethyloxacarbocyanine iodide (2.2 mmol) in 20 mL of **MeOH**. After 1 h the sample was centrifuged and filtrated to remove the precipitate, the solvent was evaporated under nitrogen flow to obtain the solid **OXA-3C** with 93% yield.

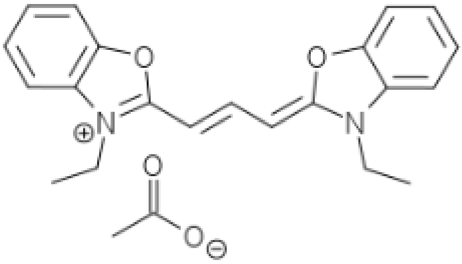

Figure 3.9. Molecular structure of **OXA-3C**.

- **3,3′-Diethyloxadicarbocyanine iodide (Sigma-Aldrich, >99%)**

3,3′-Diethyloxadicarbocyanine iodide (>99%) was obtained from Sigma Aldrich and used without further purification.

- **3,3′-Diethyloxadicarbocyanine Acetate (OXA-5C)**

OXA-5C (Figure 3.10) was prepared by adding silver acetate (1.1 equivalents) to a solution of 3,3′-Diethyloxadicarbocyanine iodide (0.50 mmol) in 10 mL of **MeOH**). After 1 h the sample was centrifuged and filtrated to remove the precipitate, the solvent was evaporated under nitrogen flow to obtain the solid **OXA-5C** with 91% yield.

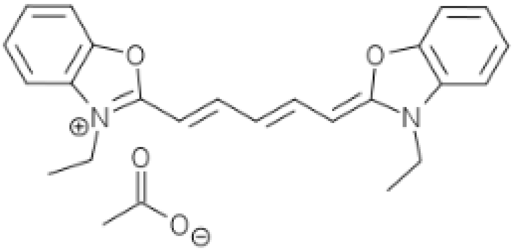

Figure 3.10. Molecular Structure of **OXA-5C**.

- **Pinacyanol Chloride**

Pinacyanol Chloride (95%) was obtained from Across Organics and purified by washing the powder with water and recovering the insoluble fraction by filtration; this process was repeated three times before drying the insoluble fraction (90% yield).

- **Pinacyanol Acetate (PiC)**

PiC (Figure 3.11) was prepared by adding silver acetate (1.1 equivalents) to a solution of pinacyanol chloride in **EtOH**. After separation of precipitate by filtration, the solvent was removed under nitrogen flow to obtain the solid pinacyanol acetate (**PiC**) in 95% yield.

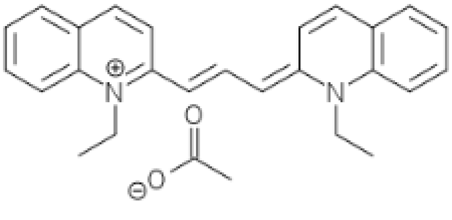

Figure 3.11. Molecular structure of **PiC**.

- **Alcian Blue Chloride (AB-Cl)**

Alcian Blue chloride (>85%) was obtained from Sigma Aldrich and was purified by dissolving AB in water (2 g of Alcian Blue in 100 g of water). The non-soluble part was separated by centrifugation followed by filtration. The supernatant was recovered and freeze dried to obtain purified Alcian Blue chloride (80 % yield).

- **Alcian Blue Acetate and p-Toluensulfonate (AB-Ac and AB-Toc)**

The acetate and p-toluensulfonate salts (**AB-Ac** and **AB-Toc,** Figure 3.12) were prepared by adding a 1:1 molar ratio of silver acetate or silver p-toluensulfonate into a solution of 1 g of **AB-Cl** in 50 mL of **MeOH**. This mixture was heated to 80 ºC under reflux for 3 h. The sample was centrifuged and filtrated to remove the precipitate and the solvent in the supernant was evaporated under nitrogen flow to obtain the solid **AB-Ac** or **AB-Toc**.

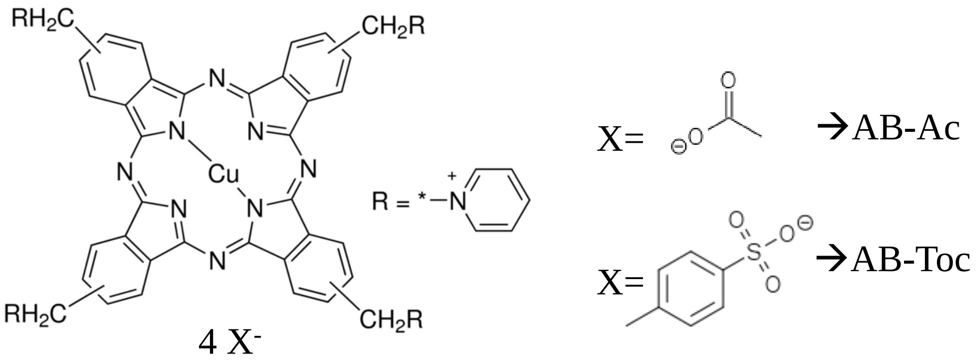

Figure 3.12. Molecular structure of **AB-Ac** and **AB-Toc.**

3.1.3. Aqueous Components

- **Milli-q ultra-pure water (18 µS/cm)**
- **HPLC aqueous phase (pH=3)**

HPLC aqueous phase is composed of: Citric acid (7.3 g/L), NaCl (3.8 g/L) and NaOH (0.15 g/L)

- **Phosphate Buffer Saline (0.16 M, pH=7.4**)

PBS 0.16M is composed of: NaCl (136.89 mM), $NaH_2PO_4 \cdot H_2O$ (0.93 mM) and $Na_2HPO_4 \cdot 2H_2O$ (16.76 mM)

- **Deuterated water (D_2O, Sigma Aldrich, >99.85 %)**
- **Simulated Stomach Fluid (Sigma Aldrich, pH=1.2)**
- **Aqueous Ammonia (Sigma Aldrich, 25 wt%)**

3.1.4. Organic Phases

- **Ethyl Acetate (EAc, Merck, 99.7 %)**
- **Deuterated dimethyl Sulfoxide (6d-DMSO, Sigma Aldrich, >99.9%)**
- **Acetonitrile (Fischer Scientific, HPLC grade)**

3.1.5. Active Molecules

- **Ketoprofen (KP)**

KP (98 %) (2-(3-benzoylphenyl)-propionic acid ($C_{16}H_{14}O_3$)) was obtained from Sigma Aldrich and used without further purification. **KP** is a propionic acid class of nonsteroidal anti-inflammatory drugs with analgesic and antipyretic effects. It acts by inhibiting the body's production of prostaglandin. The molecular structure is show in Figure 3.13.

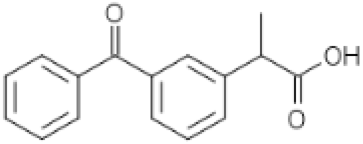

Figure 3.13. Molecular structure of **KP**.

3.1.6. Other chemicals

- **Tetraethylortosilicate (TEOS, Sigma-Aldrich, 98%)**
- **Furfuryl Alcohol (FA, Sigma-Aldrich, 98%)**
- **Silver acetate (Sigma-Aldrich, 99.99%)**
- **Silver p-toluenesulfonate (Sigma-Aldrich, >99%)**
- **NAFION solution (Sigma Aldrich, 0.5% solution in EtOH)**

3.2. INSTRUMENTATION

Otherwise stated, all of the instrumentation used belongs to the Nanostructured Liquid Characterization Unit of the Spanish Research Council (CSIC) and the Biomedical Networking Center (CIBER-BBN), located at IQAC, Barcelona.

- **Polarized optical microscope (POM)**

Olympus BX51TRF6 microscope coupled to an Olympus DP73 digital camera.

- **Small and wide angle X-ray Scattering system (SAXS)**

Two instruments were used:

- S3MICRO instrument (Hecus X-ray Systems) with point focalization, equipped with a GENIX micro-focus X-ray source (λ = 1.54 Å) operating at 50 kV and 1 mA. The scattered intensity was recorded using a position-sensitive detector (HECUS). The detector consists on an arrangement on channels with a finite width, W. The scattering vector, q, can be calculated from the position of the channel with the expression:

$$q = \frac{4\pi}{\lambda}\sin\left(\frac{W * (i - p_o)}{2d_d}\right)$$

Equation 3.1

Where λ, W, i, p_o and d_d are the X-ray wavelength, width of the channel, channel number, position of the primary beam and sample to detector distance respectively.

- SAXSLab Ganesha 300XL instrument (SAXSLAB ApS) (Lund University, Sweden). A pinhole collimated system equipped with a Genix 3D X-ray source (λ = 1.54 Å) operating at 50 kV and 1 mA. Data were collected with a Pilatus 300K detector placed at sample-to-detector distance that yielded an overall q range of 0.1–3 Å^{-1}.

The distance between planes in a liquid crystalline structure, d, is related to q by the Bragg's equation:

$$d = \frac{2\pi}{q}$$

Equation 3.2

For structural calculations, the solute volume fraction ϕ_f is defined as

$$\phi_f = \left(1 + \frac{(1-c)\rho_c}{c\rho_w}\right)^{-1}$$

Equation 3.3

Where c, ρ_c and ρ_w are the concentration and densities of the solute and water, respectively.

- **Spinning drop tensiometer**

Spinning drop Kruss GmbH site 04.

- **3D cross-correlated photon dynamic light scattering (DLS) spectrophotometer**

Dynamic light scattering (**DLS**) were performed on a 3D LS spectrometer (LS instruments) equipped with a 35 mW He-Ne laser light source (λ = 632.8 nm). The instrument uses two lasers to implement the so-called cross-correlation technology that suppress multiple scattering. Measuring cells are immersed in a decalin bath for refractive index matching.

- **Laser diffraction spectrophotometer**

Laser diffractometer Mastersizer 2000

- **High pressure liquid chromatography (HPLC)**

Waters 152 Series instrument using in an inverse C_{18} column (Water Spherisorb ODS3 C18) and with a UV detector at 256 nm.

- **Nuclear magnetic resonance (NMR) spectrometer**

^{1}H and ^{13}C **NMR** spectroscopy were collected in a Varian VNMRS spectrometer (400 MHz and 500 MHz). Proton chemical shifts are expressed in parts per million (δ scale) and are calibrated using residual non-deuterated solvent peak as an internal reference (**D_2O**: δ 4.79, **6d-DMSO**: δ 2.50). Carbon chemical shifts are expressed in parts per million (δ scale) and are calibrated using residual non-deuterated solvent peak as an internal reference (**6d-DMSO**: δ 39.51).

- **Ultraviolet-visible light spectrometer**

Varian Cary 300 instrument at 25 ºC with 2 mm path length quartz cuvettes.

- **Fluoresce spectrometer**

Varian Cary Eclipse 4000 instrument at 25 ºC with 2 mm path length quartz cuvettes

Micro-differential scanning calorimeter (DSC)

Setaram Micro-DSC III with hermetically sealed 850 µl hasteloid sample holders to avoid evaporation of solvent.

- **Thermo-gravimetric analysis (TGA)**

Hitachi HT-Seiko 6300 instrument (NIMS, Japan) with a heating rate of 10 ºC/min on air atmosphere (air flux of 30 cm^{3}/min).

- **Scanning Electron Microscope (SEM)**

Three instruments were used:

  - Low vacuum, tabletop Hitachi TM-1000, operating at 10 kV
  - High and low vacuum Quanta FEG-SEM, operating from 10 to 30 kV (INL, Portugal)
  - High vacuum SEM, Hitachi S-4800, operating at 10 kV and 15 kV (NIMS, Japan)

- **Transmission Electron Microscope (TEM)**

Three instruments were used:

  - TEM, JEOL Model JEM-2100F operated at 200 kV (NIMS, Japan)
  - Titan ChemiSTEM 80-200 kV microscope operated at 200 kV (INL, Portugal)
  - JEOL 1010 operated at 80 kV. (Hospital Clinic, Barcelona)

- **Nitrogen sorption**

Two instruments were used:

  - Quantachrome Instrument, Autosorb-1 (NIMS, Japan)
  - Quantachrome Instrument, Autosorb-IQ2 (INL, Portugal).

Before measurements, samples were degassed at high vacuum and temperature at the conditions below:

Silica: 1 hour at 80 ºC followed by 1 h at 100 ºC and finally 3 h at 250 ºC

Carbon: 10 h at 150 ºC

- **X-ray Photoelectron Spectrometer (XPS)**

Theta Probe spectrometer (Thermo Electron Co.) (NIMS, Japan). The instrument is equipped with a monochromatic Al−Kα radiation source (photon energy 15 KeV, energy resolution ≤ 0.47 eV, space resolution ≤ 15 μm). C 1s and O 1s core level **XPS** spectra are recorded in 0.05 eV steps. A built-in electron flood gun prevents sample charging.

- **X-Ray Diffraction (XRD)**

Two equipments were used:

  - Rigaku RINT2000 (NIMS, Japan)
  - PanAnalytical X Pert PRO MRD system (INL, Portugal)

- **Quartz Microbalance (QCM)**

Quartz Crystal Micro-balance (QCM) AT-cut (NIMS, Japan) working at 9 MHz

- **Potentiostat**

Electrochemical Analyzer, Model 850D, ALS/CH instrument (NIMS, Japan) in the potential range from 0 to 1.0 Volts (vs. Ag/AgCl) using a three-electrode system. Ag/AgCl in saturated KCl was used as a reference, platinum wire as a counter electrode, and the glassy carbon electrode coated with the active material was used as the working electrode. All samples were measured using aqueous 1 M H_2SO_4 solution as the electrolyte

3.3. METHODS

3.3.1. Qualitative Phase Behavior

Liquid crystalline phases were identified by water contact experiments. Briefly, a small quantity of surfactant or dye was placed between a glass slide and cover slip. A drop of water was added on one side of the cover. Water diffused through the sample creating a concentration gradient. The sample was observed under **POM** to detect any liquid crystal formation at 25 ºC.

3.3.2. Quantitative Phase Behavior: Phase Diagram Determination

Samples with selected compositions were prepared. Viscous samples were placed in test tubes (5 mm diameter) with a narrow constriction and flame-sealed. The samples were mixed by repeated centrifugation at 40 ºC. Surfactant samples were kept at -20 ºC for at least 2 days to reach equilibrium before phase diagram determinations. Dye samples were kept in a 25 ºC water bath for at least 1 day to reach equilibrium before determining the phase diagram.

Binary phase diagrams were constructed by heating the samples from 10 ºC to 100 ºC and observing bulk properties. As all binary phase diagrams in this work showed turbid aspect or absorbed light, birefringence could not be observed by placing the samples between two crossed polarizers, therefore polarized optical microscopy was used to define the transition temperatures.

For the ternary phase diagrams determinations of surfactant systems, samples were kept in a constant temperature bath (25 ºC) for several days. Visual assessment was used as a first tool for determining the phase boundaries in surfactant systems. Viscosity and birefringence were observed by tilting the tubes or placing them between cross polarizers respectively. The flowchart to assign a phase to region by visual observation is presented in Figure 3.14. Further characterization was performed using **POM** and **SAXS**.

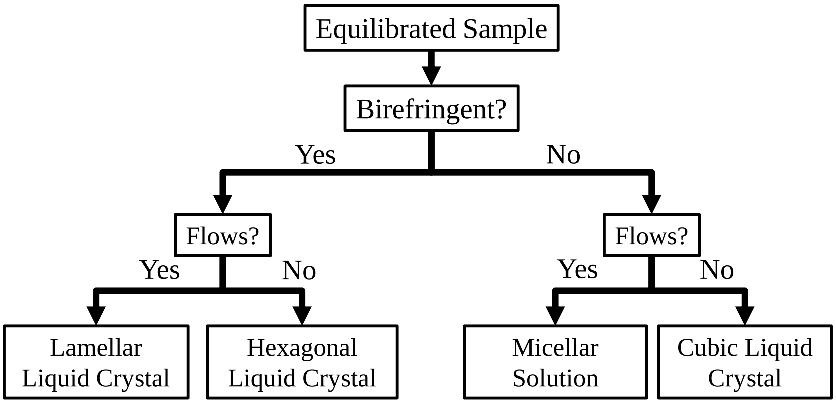

Figure 3.14. Flowchart used to assign phases to the phase diagram regions.

3.3.3. Phase identification by polarized optical microscopy (POM)

A drop of sample was placed between a glass slide and a cover slip and sealed using silicone oil to avoid solvent evaporation. Samples were heated using a peltier hot stage with a precision of ±1 ºC. The texture of the sample under **POM** was assessed as a function of temperature. Loss in birefringence or change in the texture was taken as phase transitions.

3.3.4. Structural determination of self-assemblies by small and wide X-ray scattering (SAXS/WAXS)

Samples were placed into 1 mm capillary tubes (Hilgenberg, Germany) made of glass (0.01 wall thickness) and sealed using wax. More viscous samples were placed between two mica covers separated by a rubber O-ring. These samples were introduced in a vacuum chamber. The sample was heated to a specific temperature with a peltier hot-stage and the amount of X-ray counts per second was measured as a function of the scattering vector, q.

3.3.5. Determination of the size of particles by dynamic light scattering (DLS)

Samples were placed in 5 mm cylindrical borosilicate tubes, and kept in a 25 ºC bath and measured at a scattering angle of 90 º. The decay rate (derived from the second-order cumulant analysis of the normalized autocorrelation function) was used to calculate the mean diffusion coefficient, D, of the nanoparticles. The hydrodynamic radius, R_H, was calculated using the Stokes-Einstein equation:

$$R_H = \frac{k_B T}{6\pi\eta D}$$

Equation 3.4

Where k_B, T and η are the Boltzmann's constant, absolute temperature and dynamic viscosity, respectively.

3.3.6. Purification of glycerol-based surfactants

Glycerol was removed from **C41V** by mixing the surfactant with **EAc** at a ratio of **C41V**:**EAc** of 70:30. After one day, the surfactant dissolved in **EAc** was separated from the precipitate and evaporated at low pressure to obtain glycerol free surfactant.

The surfactants with higher degree esterification were separated by using a chromatographic column packed with silica gel (20 cm of height and 4 cm diameter). The column was first packed with **$CHCl_3$**:**Acetone** (90:10) and then 40 mL of **C41V** diluted in 40 mL of eluent were seeded. The solvent was recovered in 20 mL samples and thin layer chromatography (**TLC**) was used to determine the components present. Traces from diglycerol di, tri and tetra isostearate appeared in volumes up to 600 mL. When nothing was detected on the **TLC**, **$CHCl_3$**:**MeOH** (90:10) was added and used as eluent. Again, 20 ml samples were recovered until no signal of the eluting fraction was observed on **TLC** (400 mL). Finally, 300 mL of **MeOH** were passed through the column to obtain the remaining retained product. Three different fractions were collected after evaporation of solvents under reduced pressure.

3.3.7. Water/oil interfacial tension determinations

Experiments were carried out by filling the measuring cell (rotating horizontal capillary) with water saturated with **EAc**, followed by injection of a drop of oil (**C41V**:**EAc** mixture). The capillary was rotated at different revolutions with the pinning axes parallel to the capillary. The interfacial tension was calculated by the Vonnegtu's expression:

$$\gamma = \frac{\Delta\rho\omega^2 r^3}{4}$$

Equation 3.5

Where γ, $\Delta\rho$, ω and r are the interfacial tension, difference in densities, angular velocity and radius of the droplet respectively

3.3.8. Preparation of liquid crystal dispersions

Hexosomes dispersions were prepared as follows: **C41V** (0.5 g) was dissolved in **EAc** (ratios **C41V**:**EAc** of 1:0, 7:3, 5:5 and 3:7). 9.5 g of an solution of **F127** in phosphate buffer (**PBS**, 0.16M) or water was added to the solution of **C41V** in **EAc**. The mixture was vortexed and the resultant emulsion was further dispersed with an ultrasonic homogenizer at different times (KE-76 probe, Bandelin Sonoplus, amplitude: 50 %). **EAc** was removed in a rotary evaporator for 1.5 h at 25 ºC and 40 psi.

3.3.9. Encapsulation of active compounds

The hexosomes loaded with ketoprofen were prepared by dissolving the drug on the organic phase (**C41V**:**EAc**) before adding the **F127** solution and then following the procedure described in subsection 3.3.8.

3.3.10. High performance liquid chromatography (HPLC) quantification

HPLC was used to quantify the amount of Ketoprofen (**KP**) released from a sample to a receptor solution. The mobile phase was composed of an Organic: Aqueous phase ratio of 55:45 (v/v).

- Organic phase: Acetonitrile
- Aqueous phase: Citric acid (7.3 g/L), sodium chloride (NaCl, 3.8 g/L) and sodium hydroxide (NaOH, 0.15 g/L)

20µL of sample were injected with a flux of 1 mL/min. The retention time at these conditions was 4.5 minutes. For calibrating the instrument, known concentrations of **KP** dissolved in **PBS** were measured. The concentration, [C], vs the total area under the **HPLC** response curve was plotted (Figure 3.15)

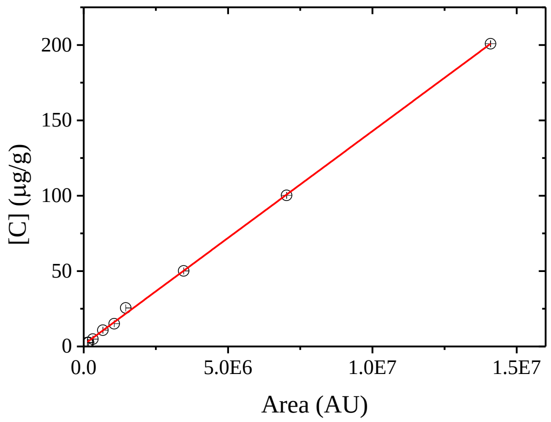

Figure 3.15. **HPLC** calibration curve of **KP** in **PBS**.

The fitted equation for the linear regression is:

$$[C] = 1.1892 + 1.4 * 10^{-5}[Area]$$

Equation 3.6

The fitting gave a R^2 of 0.9994.

3.3.11. Determination of Ketoprofen solubility

An excess of **KP** was added to a given solvent and stirred during 2 h. The resulting dispersion was passed through 0.2 µm filter and the concentration of **KP** in the filtrate was determined by **HPLC** analysis.

3.3.12. Encapsulation efficiency

The amount of encapsulated **KP** was determined indirectly by the filtration/centrifugation method. Three grams of the dispersion were placed in falcon tubes with a cellulose filter (molecular weight cut-off of 3000 Daltons) and were centrifuged at 5000 rpm for 1 h. The concentration in the filtrate was detected by **HPLC** analysis at a wavelength of 256 nm. The encapsulation efficiency is expressed as the percentage of **KP** incorporated in the carrier divided by the total amount of **KP** added into the dispersion:

$$Encapsulation\ Efficiency\ (\%) = \frac{KP_{total} - KP_{no-encapsulated}}{KP_{total}}$$

Equation 3.7

Where KP_{total} and $KP_{no\text{-}encapsulated}$ represent the concentration of **KP** in the system and the concentration of **KP** in the filtrate (non-encapsulated **KP**).

3.3.13. In vitro release assays

In the release assays of **KP**, a micellar and aqueous solutions of active compounds were also studied for comparison purposes.

Thermojacketted glasses were used to maintain the desired temperature (37 ºC). They were filled with 40 mL of different receptor solution: **PBS**, simulated stomach fluid and simulated intestine fluid. Spectra/Por Float-A-Lyzer G2 (Spectrum Labs) devices with a membrane composed of Biotech Grade Cellulose Ester with a molecular weight cut-off of 3.5 – 5 kDa were pre-wetted with 10 wt% **EtOH** in water for 20 minutes followed by a second wetting step of distilled water. Then, they were filled with 2 mL of sample and soaked into the receptor solution. Aliquots of 1 mL of the receptor solution were withdrawn from the experimental setup at different time intervals for analysis. The amount of **KP** was calculated so the final concentration in the receptor solution was 20 wt% of the total **KP** solubility in that media (Sink Conditions). These conditions were chosen to make the release rate independent from **KP** concentration.

The release profiles were fitted to the next mathematical models:

- **Higuchi model.[130]**

This model describes the release of an active compound through a polymeric matrix under Sink conditions. Higuchi model states that the amount of drug released, C, is proportional to the square root of experiment time, t:

$$C = K_H t^{1/2}$$

Equation 3.8

K_H is the Higuchi dissolution constant.

- **Korsmeyer-Peppas model.[131]**

This is a semi-empirical model that relates the amount of drug released in time as an exponential equation:

$$C = K_{KP} t^n$$

Equation 3.9

Where K_{KP} is a kinetic constant characteristic of the system, and n is the release exponent that is characteristic of the release mechanism (Table 3.2).

Table 3.2. Release mechanism at different release exponents, *n*, for the Korsmeyer-Peppas model.

Release exponent, *n*	Release mechanism
0.5	Fick diffusion
0.5<n<1.0	Anomalous transport
1.0	Transport type II
>1.0	Super transport type II

3.3.14. Estimation of the dye dimeric constant: The monomer-dimer model

The equilibrium between two dye molecules M and its dimer M_2 is written as:

$$2M \leftrightharpoons M_2$$

Therefore, the dimerization constant K_D is defined as:

$$K_D = \frac{C_{Dim}}{C_M^2}$$

Equation 3.10

With C_0 as the total dye concentration and considering the stoichiometry, the mass balance is:

$$C_0 = C_M + 2C_{Dim}$$

Equation 3.11

Considering equation (1) and (2) then

$$C_{\mathrm{M}} = \frac{\sqrt{8K_D C_0} - 1}{4K_D}$$

Equation 3.12

Considering Beer’s law the absorption spectra, $\varepsilon\ (\lambda, C_0)$, of the dyes will be the sum of the weighted contribution of monomer and dimer:

$$\varepsilon(\lambda, C_0) = \varepsilon_M(\lambda)C_1 + \varepsilon_{Dim}(\lambda)C_2$$

Equation 3.13

Combining (2), (3) and (4):

$$\varepsilon(\lambda, C_0) = \left(\varepsilon_M(\lambda) - \varepsilon_{Dim}(\lambda)\right)\frac{\sqrt{8K_D C_0} - 1}{4K_D} + \varepsilon_{Dim}(\lambda)$$

Equation 3.14

The spectra at different dye concentrations in water were fitted by assuming that the monomer spectra are similar to those obtained at high dilutions in **MeOH** and fitting the dimer spectra to a Lorentz function. The damped least-squares algorithm was used to solve the nonlinear fits with Origin 9.0 software.

The Gibbs energy of dissociation between two dye molecules, ΔG is calculated as:

$$\Delta G = -2 * k_B T * \ln K_D$$

Equation 3.15

Where k_B and T are the Boltzmann constant and temperature, respectively.

3.3.15. Scanning Electron Microscopy (SEM)

One drop of a sample dispersed in **EtOH** (concentration of ca. 1 mg/mL) was deposited on a silicon wafer in the case of high vacuum **SEM** equipment and on a carbon tape in the case of the low vacuum **SEM** equipment. Samples were dried at 80 ºC for at least 1 h.

3.3.16. Transmission Electron Microscopy (TEM)

A drop of sample dispersed in **EtOH** was deposited on a copper grid. For the JEOL JEM-2100 F copper grids were dried at 80 ºC for 24 h. For the TITAN ChemiSTEM instrument copper grids were dried under vacuum at room temperature. For ultra-microtone observations, the samples were dispersed in Spurr® epoxy resin and heated to 80 ºC for 48 h. Nano-meter thick cuts of the resin were obtained using a diamond cutter Ultra-microtome (ULTRACUT-E). These films were deposited on a copper grid. Samples were placed in a vacuum chamber for the observations.

3.3.17. Synthesis of dye-templated silica fibers

In a typical synthesis, 1 g of solution of dye (3.5 wt%) in aqueous ammonia (25%) was prepared. **TEOS**, the silica precursor, was added to the solution, and the mixture was stirred for 90 min at 25 ºC and then for 90 min at 70 ºC. The precipitate obtained from the sol-gel reaction was recovered by filtration and dried. The resulting powder was calcined in air at 550 ºC for 5 h (heating rate = 1 ºC/min).

The synthesis was scaled up as follows: a reaction mixture consisting of 3.5 g of pinacyanol acetate in 100 mL of concentrated ammonia (25 %) and 22 g of **TEOS** was stirred at room temperature for 2 h, followed by aging at 70 °C for 2 h. Samples were filtered and washed with water followed by calcination at 550 °C for 5 h (Heating rate = 1 °C/min).

3.3.18. Synthesis of carbon nanofibers

Carbon nanofibers (**CNF-PiC**) were synthesized following a procedure adapted from the literature using the silica fibers as hard templates and furfuryl alcohol as a carbon precursor.[132] To improve the carbonization of furfuryl alcohol, silica fibers (3 g) were stirred for 24 h in a solution of $AlCl_3$ (0.5 g) in **EtOH**. The resultant aluminated silica was collected by filtration, washed with **EtOH** and dried at 80 °C for 12 h. Silica fibers were soaked with furfuryl alcohol by the incipient wetness technique. Furfuryl alcohol (2.1 mL) was added to silica (3 g, total pore volume 0.7 cc/g). The sample was then carbonized in nitrogen atmosphere at 150 °C for 3 h at a heating rate of 1 °C/min from 80-150 °C, followed by a temperature increase from 150 to 300 °C at a rate of 1 °C/min. Temperature was finally increased to 850 °C at a rate of 5 °C/min and maintained at this temperature for 4 h. Silica was etched with a 1 M NaOH solution at 90 °C. The fibers were dried at 100 °C for 24 h. For graphitization, the carbon fibers were heated to 1100 ºC, 1500 ºC and 2000 ºC under high vacuum in a FVHP-1-3, RTR-20-3VH furnace (Fujidempla Kogyo Co., Ltd, Osaka, Japan)

3.3.19. Determination of the supercapacitive performances

1 mg of carbon nanofibers (**CNFs**) was dispersed in water:**EtOH** mixture (70:30, 1 mL) and stirred during 24 h to form a homogeneous dispersion. While stirring, 5 µL of the dispersion were taken and added to a glassy carbon electrode and dried under vacuum at 80 °C during 2 h. 3 µL of **NAFION** solution (0.5 wt% in **EtOH**) were deposited onto the electrode that was then dried under vacuum at 80 °C during 2 h. The mass of the materials loaded on the glassy carbon electrode for electrochemical supercapacitive performance testing was estimated using a quartz crystal microbalance (**QCM**).

The specific capacitance C_s was calculated from cyclic voltammetry (**CV**) curves by:

$$C_s = \frac{1}{m * v * \Delta V} * \int_{V_1}^{V_2} I(V)dV$$

Equation 3.16

Where *m* is the active electrode mass (i.e. **CNFs** mass), *v* is the scan rate and ΔV is the potential window. Specific capacitance was also calculated from galvanostatic charge/discharge (**CD**) curves using the following equation.

$$C_s = \frac{I_m * t_d}{\Delta V}$$

Equation 3.17

Where I_m, t_d and ΔV are the current density, discharge time and potential window, respectively.

3.3.20. Determination of the sensing performance

Vapor sensing was studied by Quartz Crystal Micro-balance (**QCM**) technique. The frequency of the **QCM** gold resonator was measured as a function of time and was used to determine the exact mass deposited on the electrodes. The change in the frequency shift was assessed as a function of time in gold electrodes before and after depositing the sample. The frequency shift, Δf, is related to the total mass loaded in the electrode, *m*, by the Sauerbrey equation:

$$m = -\frac{\Delta f}{S_f}$$

Equation 3.18

Where S_f is the sensitivity factor (for a 9 MHz crystal $C_f \approx 0.90$ Hz/ng). 1 mg of **CNFs** was dispersed in water/**EtOH** mixture (1 mL, 80:20) and stirred during 24 h to form a homogeneous dispersion. While stirring, 3 µL of dispersion were taken and added to a **QCM** gold resonator followed by drying at 80 °C during 24 h under vacuum. The frequency shift was measured upon exposure of different vapors to the **CNFs-**modified **QCM** electrode in a sealed container. Between measurements, the solvent was desorbed from the electrode by exposure to air. The recovery of the initial frequency value was taken as an indication of complete desorption. A repeatability test was also performed by alternate exposure and removal of the guest vapor molecules. As the blank test, frequency shift of bare Au-resonator without loading any material was recorded upon exposing different solvent vapors (hexane, cyclohexane, benzene, toluene and pyridine) and corrected from the frequency shift of the **CNF-PiC** modified **QCM** sensors. These vapors caused small frequency shift of bare Au-resonator: hexane (-2.9 Hz), cyclohexane (-4.9 Hz), benzene (-12.0 Hz), toluene (-12.1) and pyridine (-20.5 Hz). All the **QCM** experiments were carried out at 25 °C.

4. RESULTS AND DISCUSSION

4.1. PHASE BEHAVIOR OF DI-GLYCEROL BASED TECHNICAL GRADE SURFACTANTS AND APPLICATIONS

The present section describes the hierarchical self-assembly of technical grade diglycerol-based surfactants in water. The influence of the impurities produced due to the synthetic approach has also been studied. The potential use of these self-assemblies as functional materials in drug encapsulation and release have been explored and described above.

4.1.1. Qualitative Phase Behavior: Surfactant Selection

A screening study with different diglycerol-based surfactants, all having the same fatty acid ester (iso-stearic acid, C_{18-1}) in ratios of diglycerol:C_{18-1} of 1:1 (**C41V**), 1:2 (**C42V**), 1:3 (**C43V**) and 1:4 (**C44V**) was performed by conducting a water diffusion assay at 25 ºC using Polarized Optical Microscopy (**POM**) (Figure 4.1) to detect any evidence of birefringent liquid crystal formation with concentration. The bulk properties (i.e. viscosity, turbidity etc.) of water/surfactant mixtures (at c.a. 50 wt% surfactant) were also assessed. Upon contact with water, **C41V** presented some birefringent tactoids (which are observed in some packed columnar mesophases) (Figure 4.1a), whereas **C42V** only formed a non-birefringent viscous coarse dispersion (probably due to self-emulsification) (Figure 4.1b). 50 wt% mixtures of both surfactants were viscous and turbid. **C43V** and **C44V** presented a sharp boundary in the contact between pure surfactant and water (Figure 4.1c,d), however, they did not form any birefringent liquid crystal. 50 wt% samples rapidly separated into two fluid, transparent and isotropic phases. **C41V** and **C42V** were then chosen for further self-assembly studies in water.

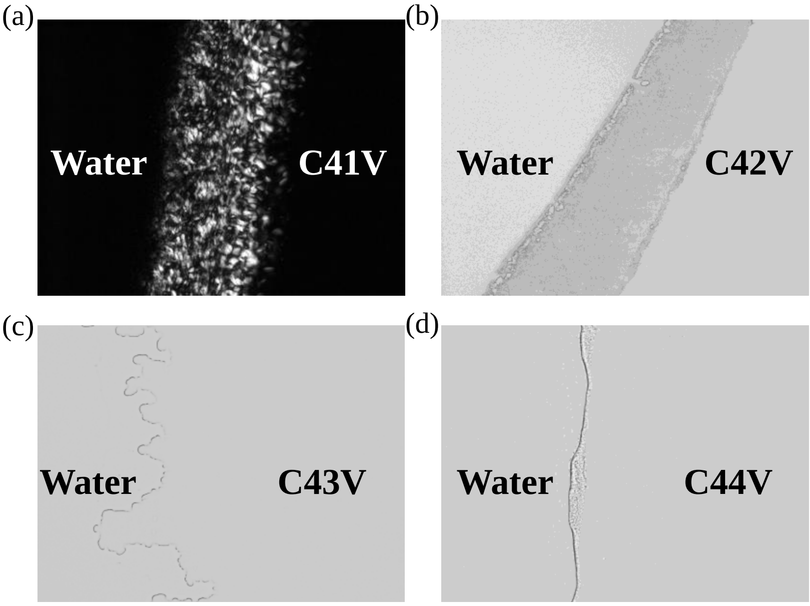

Figure 4.1. (a) **POM** of the contact region of the water/**C41V** system. Bright field microscope pictures of the contact between (b) water/**C42V**, (c) water/**C43V** and (d) water/**C44V**.

SAXS was performed on **C41V** and C42V samples with a surfactant concentration of 50 wt% (which for both surfactants was bi-phasic) to characterize the structure of the aggregates formed. The **SAXS** patterns are shown in Figure 4.2. While **C41V** self-assembled into cylindrical micelles packed in hexagonal structure (peak relative positions at 1:$\sqrt{3}$: $\sqrt{4}$), **C42V** formed a rather amorphous phase with a broad **SAXS** band that can be ascribed to a correlation distance between aggregates.

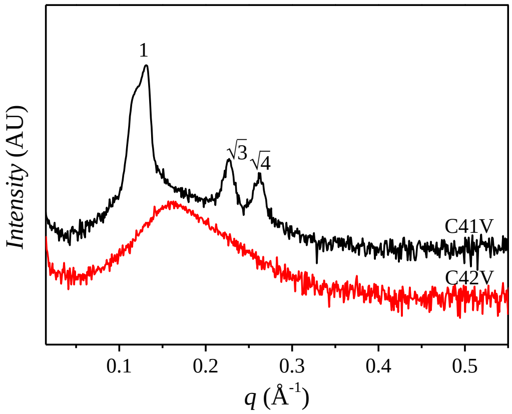

Figure 4.2. **SAXS** of 50 wt% of **C41V** and **C42V** samples in water at 25ºC.

C41V was considered the most suitable candidate for further studies since it forms a more ordered phase. In the next sub-sections the phase behavior of **C41V** in water will be described.

4.1.2. Phase Behavior of the Water/C41V System

4.1.2.1. **Water/C41V phase diagram determination as a function of concentration and temperature.**

The phase diagram of the water/**C41V** system was determined as a function of temperature and concentration (in wt %) and was built based on microscopic and macroscopic observations (Figure 4.3). This phase diagram is characterized by two multiphasic regions; one containing hexagonal liquid crystal at **C41V** concentrations lower than 0.5 wt% up to 95 wt% and below 70 ºC and the other above 70 ºC consisting in two liquid phases. Samples in the concentration range between 50 wt% and 95 wt% and at 25 ºC were turbid and highly viscous. A visible separation between a turbid viscous liquid and water was observed in samples with **C41V** content lower than 50 wt%. Generally, birefringent samples showed a smokey-like texture under **POM** (Figure 4.4a) which upon a cycle of heating and cooling changed into a fan shape conic texture characteristic of hexagonal liquid crystal (Figure 4.4b). The dimensions of the aggregates seem to exceed the wavelength of white light and thus cause the turbidity (backscattering). Due to the high turbidity of the samples, it was difficult to detect birefringence using a lamp and cross polarizers, therefore **POM** had to be used. At temperatures higher than 70 ºC there was a decrease in viscosity. All samples studied at temperatures higher than 70 ºC (up to 80 wt%) showed a macroscopic phase separation into two liquid and isotropic phases, resulting from the melting of the hexagonal liquid crystal. The melting temperature of the hexagonal phase is reduced in the range of concentrations from 80 wt% to 96 wt%. The complete loss of birefringence was considered as phase boundary between a liquid crystal and an amorphous structure.

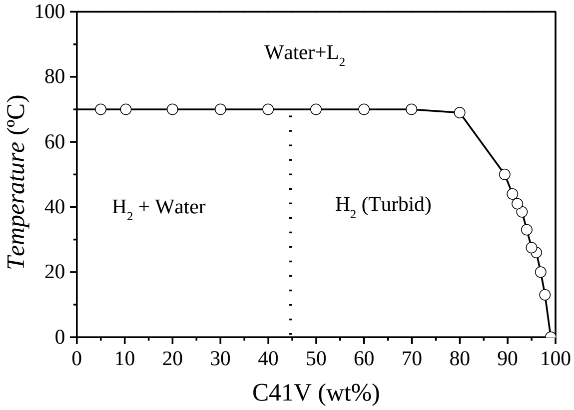

Figure 4.3. Phase diagram of **C41V** in water as a function of concentration and temperature. The dotted lines indicate a boundary where there is a visible phase separation. **H_2** and **L_2** denote inverse hexagonal and inverse micellar phases, respectively.

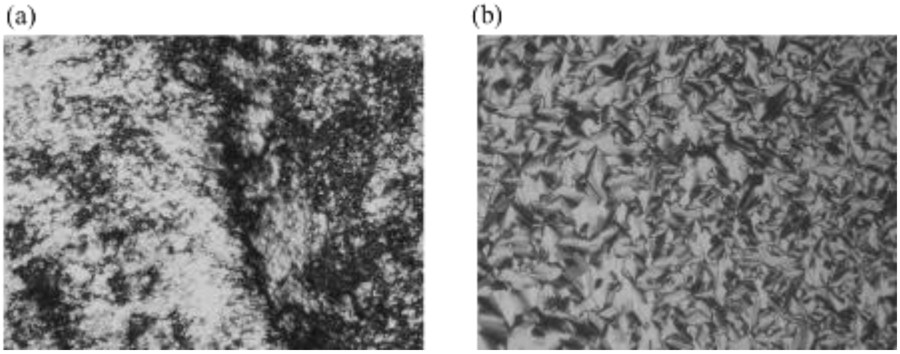

Figure 4.4. **POM** of a 30 wt% **C41V** sample at 25 ºC (a) without and (b) with a heating/cooling cycle.

4.1.2.2. **Structural characterization of the water/C41V mesophases**

SAXS patterns at 25 ºC, presented in Figure 4.5, with **C41V** concentrations up to 94 wt% showed 3 peaks with relative peak positions located at $1{:}\sqrt{3}{:}\sqrt{4}$, which can be assigned to a 2-dimensional hexagonal array of cylindrical aggregates. With the available techniques was not possible to infer the direct or inverse nature of this phase, however, an inverse hexagonal phase ($\mathbf{H_2}$) is expected considering the long hydrophobic chain of **C41V** (which favors a spontaneous negative curvature of the system and therefore its low solubility in water). Samples with **C41V** concentration higher than 94 wt% only showed a broad band that can be ascribed to an inverse micellar solution ($\mathbf{L_2}$). In fact, diglycerol isostearates are reported to form inverse micelles upon addition of small quantities of organic solvents.[133]

The Bragg distance, *d* (separation between planes), calculated from the first peak according to Equation 3.2 plotted as a function of concentration is presented in Figure 4.6. The Bragg distances increased (from 95 wt% to 40 wt % of **C41V**) due to swelling of the water channels in the $\mathbf{H_2}$ structure. At concentrations lower than 40 wt% of **C41V**, the Bragg distances remain constant indicating that the $\mathbf{H_2}$ mesophase is completely hydrated (the maximum swelling has been reached). This boundary coincides with the macroscopic observations (visible phase separation) and phase diagram presented in Figure 4.3. It can be considered that at concentrations lower that 40 wt% the $\mathbf{H_2}$ phase is in coexistence with excess water.

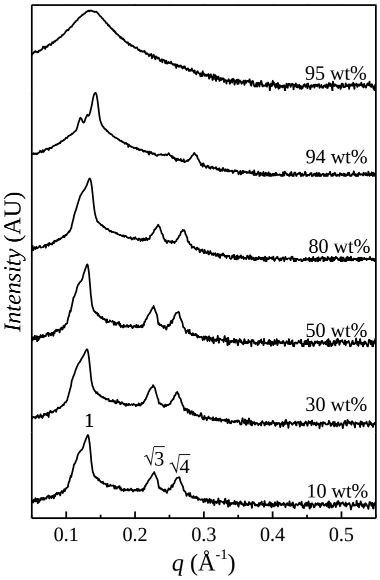

Figure 4.5. **SAXS** patterns of **C41V** samples at different **C41V** concentrations at 25 ºC.

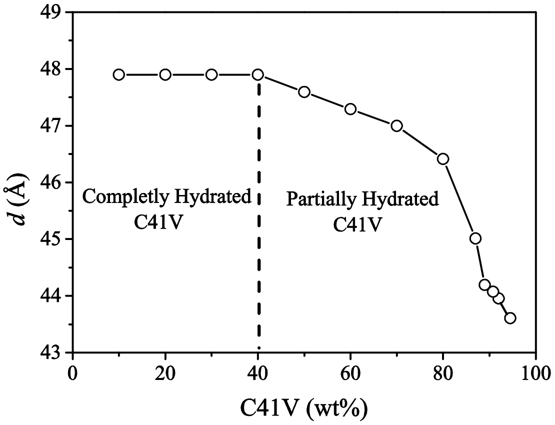

Figure 4.6. Bragg distances calculated from the first **SAXS** peak as a function of **C41V** concentration.

SAXS of samples at temperatures higher than 70 ºC presented only a broad band with a shoulder, which can be ascribed to an inverse micellar solution with strong inter-micellar interactions (Figure 4.7).

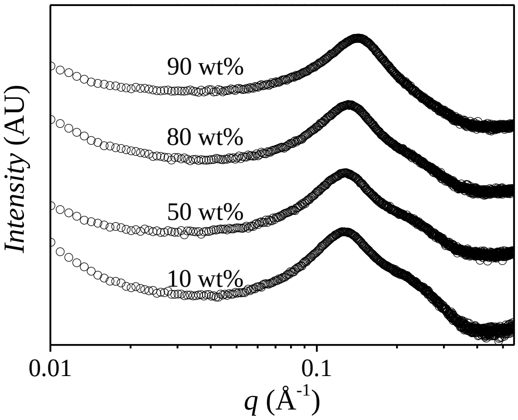

Figure 4.7. (a) **SAXS** patterns of **C41V** samples at different **C41V** concentrations at 75 ºC

In the water/**C41V** system no monophasic region (transparent phase) was found. No tie lines could be drawn since it is not really a binary system. This can be understood by considering Gibb's phase rule in Equation 1.10. The lack of monophasic region would imply that there are more than 2 components in the system. Considering that **C41V** is a mixture of many components (due to impurities produced in the synthetic procedure) ($c > 2$) and that in all regions of the phase diagram in Figure 4.3 are at least two phases present ($p \geq 2$), then $f > 2$. This means than more than 2 variables are needed to determine this multicomponent system. The phase diagram is a two-dimensional projection (temperature vs **C41V** wt%) of an n-dimensional system (pseudo-binary phase diagram).

4.1.3. Phase Behavior of water/C41V-NG (No Glycerol) system.

4.1.3.1. **Unreacted glycerol separation from C41V**

Glycerol was separated using ethyl acetate as described in subsection 3.3.6. The lack of methyl group proton signals on the **NMR** analysis of the separated fraction confirms that only glycerol is present (Figure 4.8). The surfactant with no glycerol is referred from now on as **C41V-NG**. For **C41V**, an equimolar ratio of di-glycerol and iso-stearic acid (1:1 esterification) is expected, but it is actually possible that more than one fatty acid molecule reacts with one di-glycerol molecule (in 1:2, 1:3 or 1:4 glycerol to fatty acid ratio). This would result in a complex mixture of diglycerol poly-isostearate surfactant molecules and excess glycerol, as in the present case.

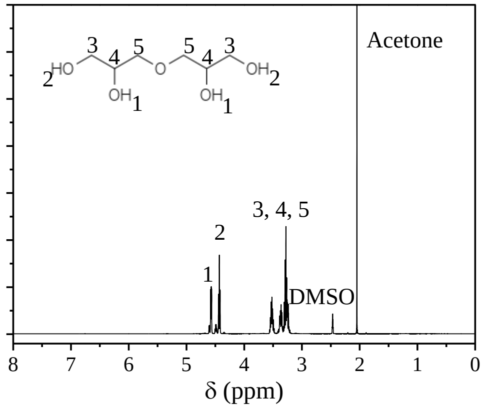

Figure 4.8. ^{1}**H-NMR** spectra of separated fraction from **C41V**.

4.1.3.2. Water/C41V-NG phase diagram determination as a function of concentration and temperature

The phase diagram of **C41V-NG** in water as a function of temperature and surfactant concentration is shown in Figure 4.9. In contrast to the water/**C41V** system, a single-phase (translucent) region is found at high **C41V-NG** concentrations (from 85 wt% to 96 wt% of **C41V-NG**) and below 70 ºC. Similar to the water/**C41V** system, an **H_2** phase is present from concentrations lower than 10 wt% up to 96 wt% and below 70 ºC. At 25 ºC these samples presented the same broken fan-shaped conic texture under **POM** (Figure 4.10a). At high surfactant concentrations (>85 wt%) there is a narrow region in which two phases coexists. **POM** images of this region show the presence of small birefringent tactoids (Figure 4.10b) that correspond to a sample of 90 wt% of **C41V** at 50 ºC) which was ascribed to an **H_2** phase dispersed in excess of surfactant. At temperatures higher than 70 ºC two fluid and isotropic phases are present. This bi-phasic region is ascribed to an inverse micellar solution in excess water (**L_2**+water). Comparing these results with those in Figure 4.3 seems that it is the presence of glycerol that conceals the monophasic region.

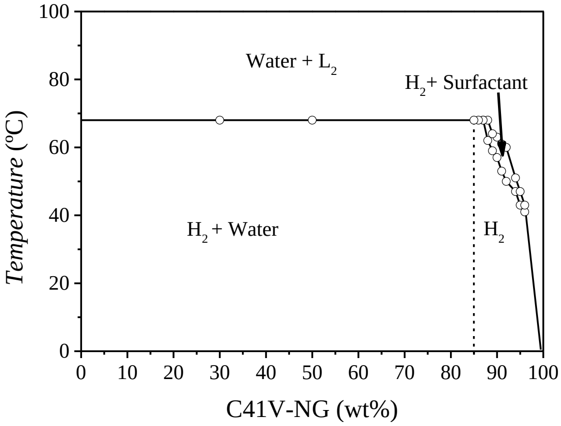

Figure 4.9. Phase diagram of **C41V-NG** in water as a function of concentration and temperature. The dashed lines indicate that no sharp phase transition could be detected. $\mathbf{H_2}$ and $\mathbf{L_2}$ denote inverse hexagonal and inverse micellar phases, respectively.

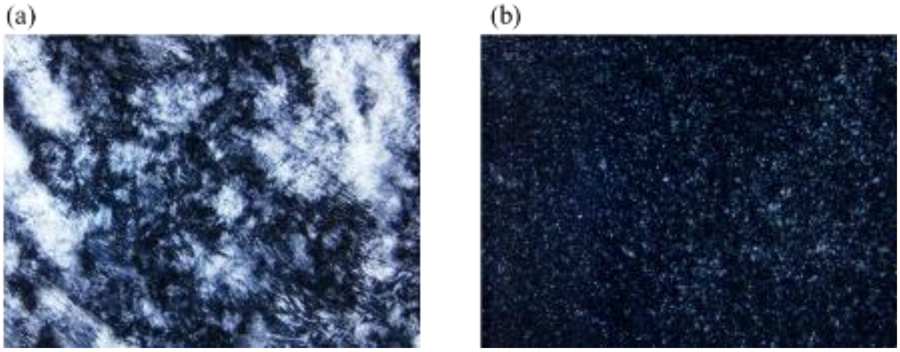

Figure 4.10. **POM** image of a 90 wt% **C41V-NG** sample at (a) 25 ºC and (b)50 ºC.

4.1.3.3. **Structural characterization of the water/C41V-NG mesophases**

At 25 ºC **SAXS** patterns of samples with different **C41V-NG** concentration showed 3 peaks with position ratios of $1{:}\sqrt{3}{:}\sqrt{4}$ characteristic of hexagonal liquid crystals (Figure 4.11).

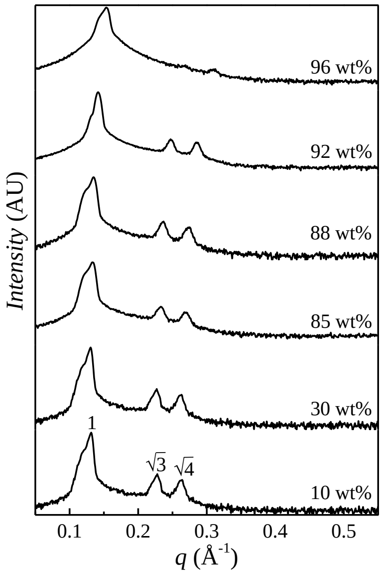

Figure 4.11. **SAXS** patterns for samples with different **C41V-NG** concentrations in water at 25 ºC.

The distances between planes, *d* (calculated from Equation 3.2), also increase with water content due to swelling of the $\mathbf{H_2}$ channels (Figure 4.12) but it becomes constant at **C41V-NG** concentrations lower than 80 wt%, which indicates that at this concentration the maximum swelling capacity of the aggregates has been reached (at 20 wt% of water). In contrast the maximum swelling is reached at 60 wt% of water in the water/**C41V** system. It has been reported for poly glycerol-based surfactants that a significant part of the ability to swell is due to the presence of the unesterified hydroxyl groups present in the poly glycerol head group.[134] However, most nonionic lipids, which undergo lyotropic mesomorphism, have a finite capacity to swell, as an example, in the case of pure monoglycerides the equilibrium interlayer spacing, resulting from the force balance between attractive long-range van der Waals forces and osmotic repulsion forces, amounts to approximately 20 Å in the $\mathbf{L_\alpha}$ mesophase.[134] At high **C41V** concentration where glycerol amount is significantly high the Bragg distance is considerably smaller than those in the water/**C41V-NG** system. Interestingly, at high water content (where glycerol concentration is almost negligible), the Bragg distance is similar for **C41V-NG** and **C41V** systems. The presence of glycerol has a dehydration effect on liquid crystal structure. These results also show that both systems (water/**C41V** and water/**C41V-NG**) have similar swelling capacity. It is likely that when water is added to **C41V** and $\mathbf{H_2}$ phase is formed some glycerol becomes insoluble, causing a macroscopic phase separation, which is observed in the water/**C41V** system. Glycerol would act as a chaotropic agent, namely, it will hydrate taking some of the free water. This would explain why the water/**C41V** needs more water content to completely swell than the water/**C41-NG** system.

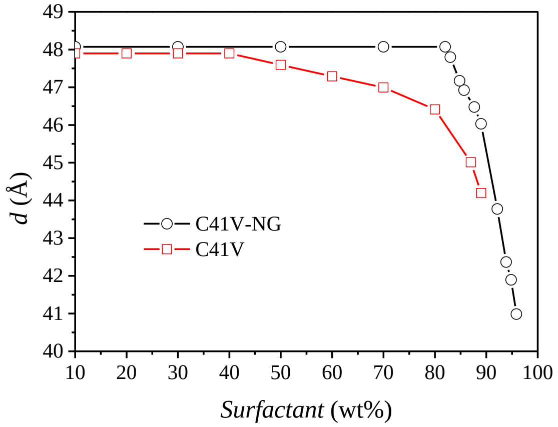

Figure 4.12. Bragg distances, *d*, calculated from the first **SAXS** peak as a function of surfactant concentration for **C41V-NG** and **C41V** systems at 25 ºC.

4.1.4. Phase Behavior of the Water/Diglycerol-Monofatty Acid/Diglycerol-Polyfatty Acids System.

4.1.4.1. **Separation of higher degree esterified surfactants.**

Diglycerol fatty acids with higher degree of esterification (diglycerol: fatty acid ratio of 1:2, 1:3 and 1:4) are probably one of the main impurities of **C41V**. Studying the effects of these impurities is of great interest for industry since it could provide a path to a better quality control and opens the possibility to have a versatile family of products with different properties produced from the same reactants but at different ratios. The separation of the higher degree esterified surfactants was performed as described in subsection 3.3.6. Three different fractions were obtained at 95 % yield:

- 1º fraction 60 % in weight (**F1**)
- 2º fraction 30 % in weight (**F2**)
- 3º fraction 10 % in weight (**F3**)

F1 consists of the more hydrophobic components of **C41V**, namely, diglycerol di, tri and tetra isostearate. A water contact experiment showed a sharp boundary between water and **F1**, similar to those in Figure 4.1c and d. **F2** consisted of the more hydrophilic molecules, namely, diglycerol mono-fatty acids of **C41V** and was obtained as a viscous semi-solid sample that showed birefringence and oily streaks textures under **POM** characteristic of lamellar liquid crystal, $\mathbf{L_\alpha}$ (Figure 4.13a). **SAXS** patterns from this dry sample phase (Figure 4.13b) featured two peaks with relative positions of 1:2, corresponding to a $\mathbf{L_\alpha}$ liquid crystal phase, with a distance between layers of 3.8 nm (note that there are no reflections in the **WAXS** region in the inset in Figure 4.13b). Considering that there is no water in the surfactant the surfactant monolayer the thickness is about 1.9 nm. The formation of the $\mathbf{L_\alpha}$ phase in

F2 can be attributed to the hydrocarbon chain length distribution (C_{14}, C_{16} and C_{18}) and corresponding di-glycerol fatty acid isomers present. These impurities can intercalate within the hydrophobic isostearate chain reducing their effective intermolecular interaction, avoiding the crystallization of the surfactant.

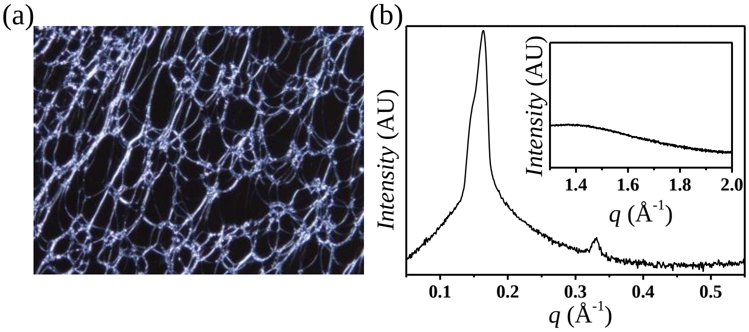

Figure 4.13. (a) **POM** of **F2** at 25 ºC and (b) **SAXS** pattern of **F2** at 25 ºC; the inset shows the **WAXS** region.

NMR spectra of **F3** showed similar spectra as the one shown in Figure 4.7 confirming that **F3** is unreacted glycerol.

4.1.4.2. **Pseudo-ternary phase diagram determination and phase characterization at 25 ºC**

The ternary phase diagram was constructed at 25 ºC by preparing samples with different water/**F2**/**F1** compositions. Visual observations of bulk properties (birefringence, viscosity, turbidity, etc.) were used to determine the phase boundaries and microscopy and **SAXS** for determining the structures of the phases. The resulting phase diagram is shown in Figure 4.14. Two single and birefringent phase regions were found at water contents lower than 30 wt%, one fluid at high **F2** content (ϕ_1, **F2**:**F1** ratios of 10:0 to 8:2) and one considerably more viscous as the **F1** content is increased (ϕ_2 ,**F2**:**F1** ratios of 6:4 to 4:6). ϕ_1 phase presented oily streaks under **POM** (Figure 4.15a). As the water content is increased (to contents >30 wt%) this texture is still observed in excess water, together with some multi-lamellar vesicles (Figure 4.15b). $\mathbf{L_\alpha}$ structure was confirmed by the presence of two peaks in the **SAXS** pattern with a *q* ratio of 1:2 (Figure 4.16a). ϕ_2 samples showed a broken fan-shape texture under **POM** (Figure 4.15c), which is characteristic of certain columnar mesophases. The texture of this phase was also observed in excess water on samples with **F2**:**F1** ratios of 6:4, 5:5 and 4:6 and water contents higher than 30 wt%. Hexagonal arrangement was confirmed by the appearance of three peaks in the **SAXS** pattern with *q* ratios of $1:\sqrt{3}:\sqrt{4}$ (Figure 4.16b). Again, an inverse hexagonal phase, $\mathbf{H_2}$ was ascribed due to the long hydrophobic chain of the surfactant. After a few days of equilibration samples with **F2**:**F1** ratios of 8:2 and 7:3 and with water content less than 10 wt% (region ϕ_3) showed two birefringent phases. These samples presented a mixture of oily streaks and broken fan shape textures under **POM**

(Figure 4.15d). **SAXS** clearly showed the presence of $\mathbf{H_2}$ and $\mathbf{L_\alpha}$ liquid crystals (Figure 4.16c). A transparent, no birefringent and no-fluid phase appeared in samples with **F2**:**F1** ratio of 8:2 and a water content of 50 wt% (region ϕ_4). This region only exists in a narrow range of compositions and could not be well defined. **SAXS** patterns from this phase in Figure 4.16d feature three sharp peaks that could be assigned to a cubic liquid crystal with Pn3m structure ($\mathbf{I_{Pn3m}}$). The **SAXS** pattern also shows a broad band in a *q* range between 0.1 and 0.3 Å^{-1}, which could be an indication that its actually a multiphasic region. With the techniques used we can not differenciate if this cubic liquid crystal has a micellar or bicontinous structure. The $\mathbf{I_{Pn3m}}$ structure is retained in excess water. Samples with **F2**:**F1** ratio of 8:2 and water contents from 10 wt% to 50 wt% (between ϕ_3 and ϕ_4 regions) showed two viscous phases, one of them birefringent. These samples presented oily streak texture under **POM** (Figure 4.15e), nevertheless, they were considerably more viscous than the $\mathbf{L_\alpha}$ phase in this system. **SAXS** patterns of this region, such as the one shown in Figure 4.16e presented several peaks that could not be asigned. At high **F1** content (ϕ_5, **F2**:**F1** ratios lower than 40:60) a multiphasic non-birefringent and fluid region was found. It is possible that at high **F1** contents is too hydrophobic and immiscible in water. This region was not further studied.

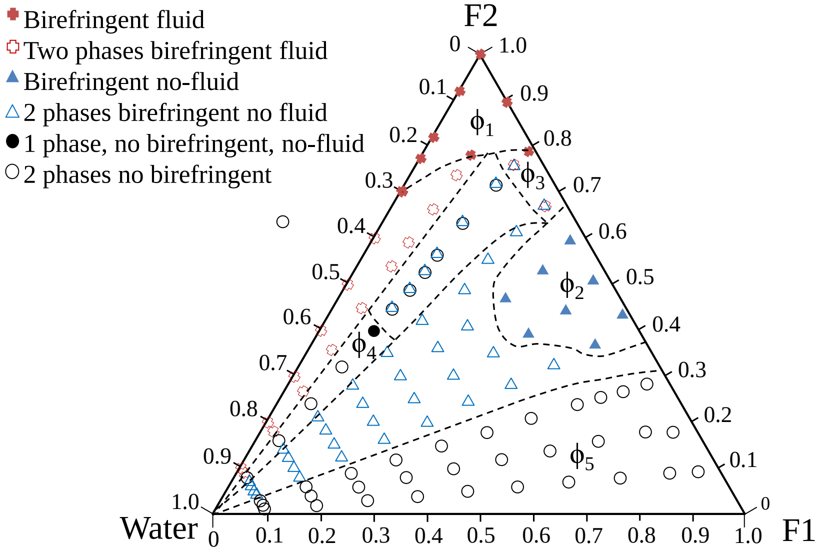

Figure 4.14. Ternary phase diagrams of the water/**F1**/**F2** system at 25 ºC. ϕ represent a region with similar properties.

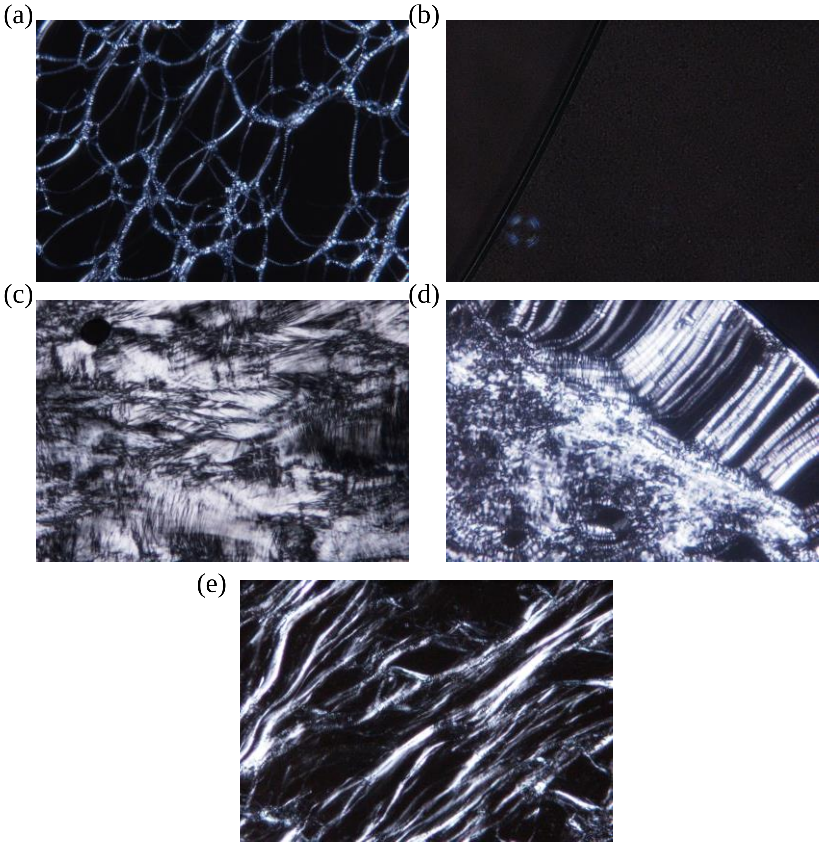

Figure 4.15. Representative **POM** for samples of the water/**F2**:**F1** system at 25 ºC: (a) L_α (**F2**:**F1** of 9:1 and 10 wt% water), (b) **L_α** in excess water (**F2**:**F1** of 9:1 and 95 wt% water), (c) **H_2** (**F2**:**F1** of 6:4 and 20 wt% water), (d) **H_2** + **L_α** (**F2**:**F1** of 7:3 and 30 wt% water) and (e) mixture of liquid crystals (**F2**:**F1** of 8:2 and 60 wt% water)

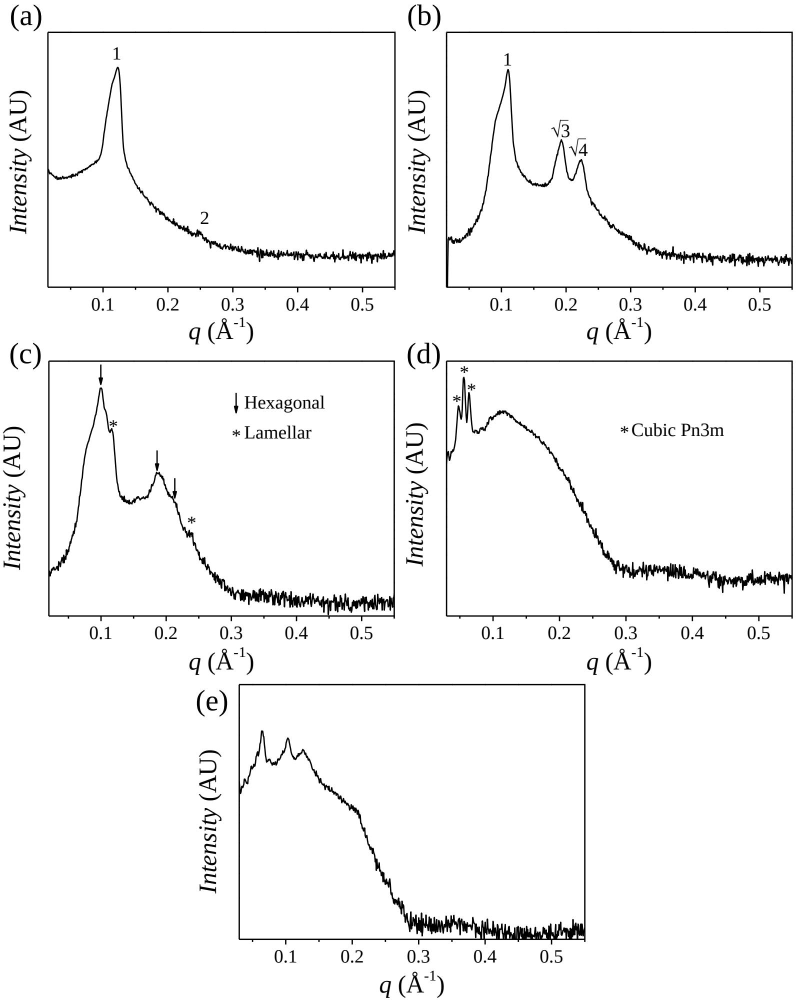

Figure 4.16. Representative **SAXS** patterns of the water/**F2**/**F1** system at 25 ºC: (a) L_α (**F2**:**F1** of 9:1 and 10 wt% water), (b) $\mathbf{H_2}$ (**F2**:**F1** of 6:4 and 20 wt% water), (c) $\mathbf{H_2}$ + $\mathbf{L_\alpha}$ (**F2**:**F1** of 7:3 and 30 wt% water), (d) Cubic **Pn3m** (**F2**:**F1** of 8:2 and 50 wt% water) and (e) Mixture of liquid crystals with unresolved structures (**F2**:**F1** of 8:2 and 40 wt% water).

Based on the visual observations and the structural characterization a ternary phase diagram can be drawn considering the Gibbs´phase rule, although this diagram is only for guidance (Figure 4.17).

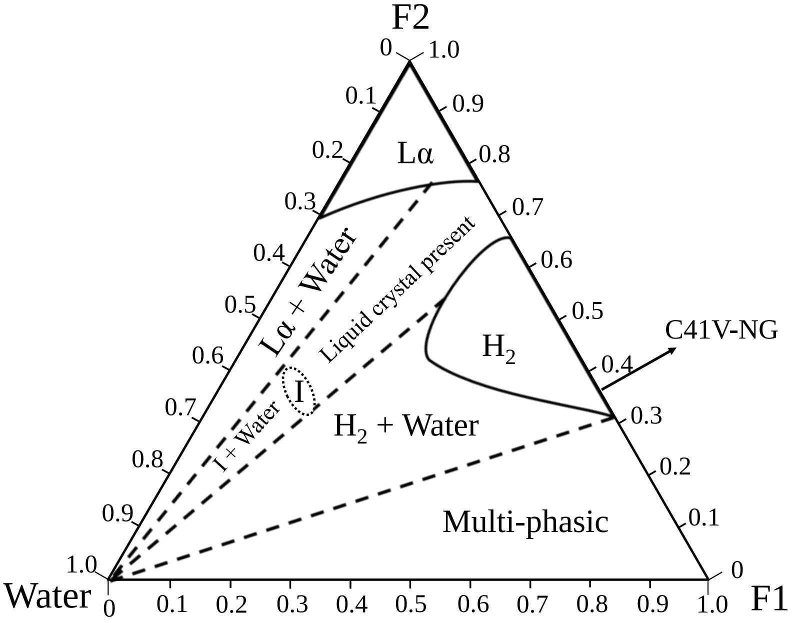

Figure 4.17. Representation of the phase diagram of the Water/**F2**/**F1** system at 25 ºC considering the Gibbs´ phase rule.

The self-assembly behavior of surfactants in solution into aggregated structures generally depends on the balance of intermolecular and inter-aggregate forces. In water, surfactants with a pronounced hydrophobic part and relatively small head groups have tendency to assemble into liquid crystals rather than micelles.[10] The ability of a pure surfactant to form a specific liquid crystal structure can be predicted by the packing parameter, *N*, (in Equation 1.7) which only considers the molecular geometry of the amphiphiles. For surfactant mixtures, as in the present case, the packing parameter represents an average calculated from the weighted *N* of all molecules present in the mixture.[135] Considering that the bilayer thickness of dry **F2**, determined by **SAXS** in Figure 4.13 is 3.8 nm, half of this value (1.9 nm) can be used as a good approximation for the alkyl chain length, l_c. Values for the cross sectional area of the head group of di-glycerol fatty acids have been reported and corresponds to 0.20 nm^2.[136] The average molecular volume of a hydrocarbon chain can be calculated using the Equation 1.8.

Considering the molecular structure of diglycerol mono-isostearate (17 carbons + 2 methyl groups), the volume of the hydrophobic tail, v_L, is 0.486 nm^3, then N= 1.3 (the *N* values for diglycerol fatty acid with more esterification degree are summarized in Table 4.1). This value is close to 1 (zero curvature) which favors the formation of flexible planar bilayers. Thus, it is possible that the reason for the morphology of the $\mathbf{L_\alpha}$ phase formed in the water/**F2** system can be explained by its molecular structure. For **F2**/**F1** mixtures (with a much higher degree of esterification and thus a higher degree of hydrophobicity) the packing parameter N would be greater than unity, and thus, inverted liquid crystalline structures, such as cubic or hexagonal are likely to form, as in the present case.

Table 4.1. Molecular parameters of Diglycerol (DG) Isostearate (C_{18-1}) with different degrees of esterification (1, 2, 3 and 4). $a_0 = 0.2$ nm^2 and l_c=1.9 nm

Surfactant	v_L (nm^3)	N
DG C_{18-1}	0.485	1.3
DG $2C_{18-1}$	0.970	2.7
DG $3C_{18-1}$	1.455	4.0
DG $3C_{18-1}$	1.940	5.4

Considering the weight fractions of the **F1** and **F2** obtained in the purification procedure, **C41V-NG** would be located around a **F2**:**F1** ratio of 40:60, which at 25 ºC would agree with the phases present in the water/**C41V-NG** system in

Figure 4.9.

From the phase behavior of **C41V** and their respective components. It can be concluded that in the water/**F2**/**F1** system three different liquid crystalline phases can be formed, namely, **$L_α$**, **H_2** and cubic **Pn3m**. The origin of these phase behavior can be attributed to the molecular structure of the surfactant molecules. As in many water/lipophilic polyglycerol-based surfactant systems, liquid crystalline phases can also coexist with excess water in a wide range of concentrations. These liquid crystals can be dispersed in water to form the so-called liquid crystalline nanoparticles (**LCN**), namely, vesicles (dispersions of **$L_α$**), hexosomes (dispersions of **H_2**) or cubosomes (dispersions of cubic liquid crystal).

4.1.5. Formation of Liquid Crystalline Nanoparticles (LCN)

As described in the subsection 4.1.2 an inverse hexagonal liquid crystal (**H_2**) can coexist with excess water in the water/**C41V** system even at low concentrations. This **H_2** phase coexisting with excess water can be dispersed to form **H_2** nanoparticles, the so-called, hexosomes. As these dispersions are not thermodynamically stable, the properties would largely depend on the dispersion method. Also, most of **H_2** phases need the presence of a stabilizer in order to facilitate their dispersion and increase stability. The effects of the dispersion method and stabilizers were studied in detail for the formation of hexosomes and are described in the sub-sections below.

4.1.5.1. **Preliminary studies: selection of a stabilizer and dispersion method**

Pluronic **F127** is one of the most used agents for dispersing and stabilizing liquid crystals.[137] Due to the high molecular weight and hydrophilicity of **F127** it is expected that its incorporation into inverse liquid crystals would be low, consequently the structure is maintained. However, the presence of **F127** has been reported to modify the structures of some cubic phases.[138, 139] For studying the behavior of **C41V** in presence of **F127**, the structure of the dispersed $\mathbf{H_2}$ phase (hexosomes) at 5 wt% of **C41V** as a function of **C41V**:**F127** ratio was assessed by **SAXS** in samples dispersed during 15 minutes using ultrasounds (Figure 4.18). No significant change was observed in the **SAXS** pattern up to a **C41V**:**F127** ratio of 60:40. Bragg distances in the samples with $\mathbf{H_2}$ structure remained unchanged. This indicates that **F127** does not penetrate the structure, but possibly it remains on the surface. At a **C41V**:**F127** ratio of 50:50 a transition to an amorphous liquid can be inferred from the lack of second and third order scattering peaks and broadening of the first order scattering peak.

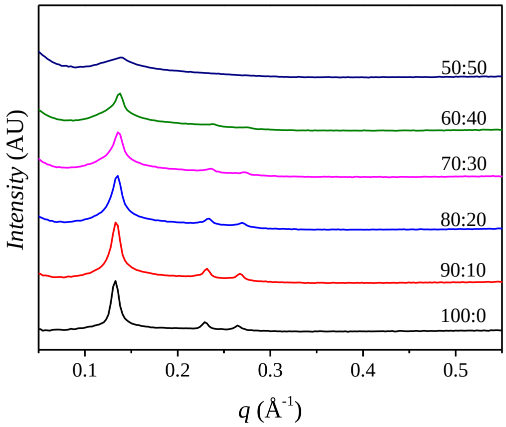

Figure 4.18. **SAXS** pattern of 5 wt% **C41V** samples in water with different **C41V**:**F127** ratios at 25 ºC.

In the literature, the most common and efficient dispersion methods for the formation of nanostructured dispersions are those employing high energy inputs (ultrasonication, microfluidization and homogenization).[90, 140, 141] Therefore, several high-energy dispersion methods were tested in order to find out the optimal for the water/**C41V**/**F127** system. Additionally, the presence of a volatile organic solvent has been reported to influence the final size of the dispersions,[142-144] therefore the addition of an organic volatile solvent on the dispersion was also considered. The particle size and stability of the final dispersion was used as characterization parameters and they are summarized in Table 4.2 for samples with 5 wt% of **C41V** and a **C41V**:**F127** ratio of 80:20. This ratio was selected since at this **F127** concentration (1.25 wt%) the dispersibility of the $\mathbf{H_2}$ phase was acceptable. All samples were prepared by adding **C41V** into a solution containing **F127** at 70 ºC and maintaining the mixture under magnetic stirring at room temperature for 24 h to assure the complete hydration of the **H_2** phase; the mixture was then dispersed using different methods.

Table 4.2. Hydrodynamic radius (R_H) of hexosome dispersions prepared with different methods for a sample with 5 wt% of **C41V** and a **C41V**:**F127** ratio of 80:20. Sizes were measured by **DLS** ($R_H < 1$ μm) and laser diffraction **DLS** ($R_H > 1$ μm).

Dispersion method	R_H/ μm	Stability at 25 ºC
Magnetic stirring at 70 ºC	50	Unstable
Ultraturrax at 70 ºC Up to 25 mins at 5000 RPMs	3.8	Unstable
Microfluidizer (70 ºC) Up to 10 cycles	2	Unstable
Film Hydration Ultrasound probe 15 mins (6.6 kJ/g of sample)	<0.1	Stable
Solvent Evaporation **EtOH** or **EAc** as organic solvent Ultrasound probe 15 mins (6.6 kJ/g of sample)	<0.1	Stable

The methods using shear (Ultraturrax) or high pressure homogenization to disperse the sample were not so efficient. Few minutes after finalizing the dispersion there was a macroscopic creaming. In addition, these methodologies also produced high amount of foam, which made it difficult the prolonged use of these techniques. The methods involving ultrasounds (with or without organic solvent) probed to be the most efficient for dispersing **H_2** phase in the water/**C41V**/**F127** system, so they were chosen for further studies. Although the temperature was not controlled in these methods the final temperature was always between 80 ºC and 90 ºC. The ultrasound method (with or without organic solvent) was also tried by placing the sample in an ice bath to control temperature but an unstable dispersion was obtained. It resulted obvious that higher temperatures are needed in order to form stable dispersions.

The influence of the stabilizer **F127** on the hexosome properties was studied for the different ultrasound methodologies (Figure 4.19). Similar results were obtained using the solvent evaporation method with **EtOH** (weight ratio of **C41V**:**EtOH** of 50:50) and the film hydration/ultrasound method. The effect of **EtOH** on the final dispersion does not seem to be significant on the dispersion properties, therefore this method was not further used. Nevertheless, the solvent evaporation method using ethyl acetate (weight ratio of **C41V**:**EAc** of 50:50) was more efficient to achieve smaller particle size. Interestingly, after 15 minutes of ultrasounds the size of the particles was considerable smaller (less than half) that those obtained by the film hydration/ultrasound method and solvent evaporation with **EtOH**.

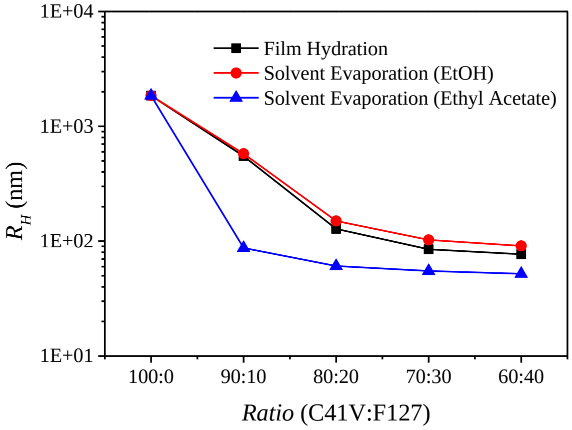

Figure 4.19. Hexosome hydrodynamic radius, R_H, as a function of the **C41V**:**F127** ratio for three different preparation methods. The **C41V**:**EtOH** and **C41V**:**EAc** was 50:50

4.1.5.2. **Optimization of the dispersion time**

The dispersion time needed to form hexosomes was studied in order to optimize their preparation. The dispersions were prepared as described in subsection 3.3.8 for samples with 5 wt% of **C41V** and a **C41V**:**F127** ratio of 80:20. The R_H of these dispersions is shown in Figure 4.20. Particles smaller than 1 µm were obtained only after 10 minutes with polydispersity indexes higher than 0.3 in the case of dispersions prepared by the film hydration/ultrasound method. Nevertheless, by preparing the hexosomes with the solvent evaporation method using **EAc** as organic solvent, comparable sizes were obtained in less than 1 minute. The amount of energy needed to form the hexosome dispersion (0.7 kJ/g of sample) was reduced in one order of magnitude in comparison with the film hydration/ultrasound method (7 kJ/mol). No significant changes in size were obtained for ultrasound times greater than 5 minutes. The hydrodynamic radius R_H of the particles in the dispersions after evaporation of the **EAc** was similar to those before the evaporation. This was not expected since 50 wt% of the total dispersed phase is ethyl acetate; its removal should result in a reduced particle size. This is an indication that after evaporation of the organic phase a hydration of **C41V** takes place and hexosomes are formed; water swells the particle, increasing their size.

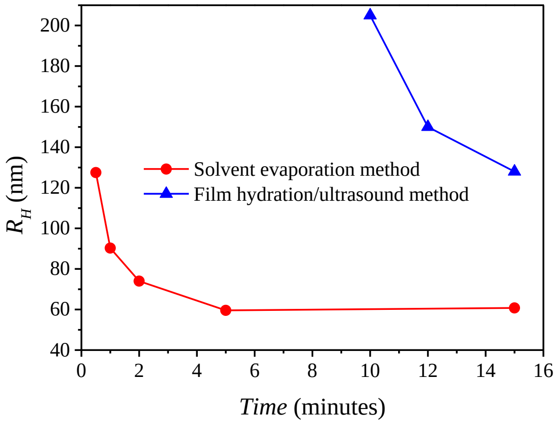

Figure 4.20. Hydrodynamic radius, R_H, of hexosomes prepared by the solvent evaporation method and conventional film hydration/ultrasound method as a function of ultrasound time for the dispersions for a sample with **C41V**:**F127** ratio of 80:20.

These results show that considerably smaller hexosomes can be obtained with the solvent evaporation method and using a shorter dispersion time (therefore, less energy). Since shorter ultrasound time is used, the sample is less likely to suffer a temperature increase. This is an advantage when thermolabile compounds have to be encapsulated into these dispersions. Two minutes was considered an optimal time for the preparation of hexosomes, since more time leaded to higher temperature increase. Unless stated, the results described in the following sections are prepared using the solvent evaporation method with **EAc** and dispersing during 2 minutes

4.1.5.3. **Effect of EAc and F127 concentration on the size of hexosome dispersions**

The effect of **EAc** initial content on the hexosome size was studied for different **C41V**:**F127** and different **EAc** amounts (Figure 4.21). Interestingly, the size is reduced as the **EAc** initial content is increased, up to a **C41V**:**EAc** ratio of 50:50. This could be attributed to **EAc** preventing the **C41V** aggregation into a bulk **H_2** phase. This allows the dispersed phase to retain low viscosity. In fact, **C41V** samples containing **EAc** can be emulsified easily by shaking the mixture.

It is to be noted that ultrasound dispersion is achieved via cavitation forces, namely, the sound waves propagate into the liquid media alternating high-pressure (compression) and low-pressure (rarefaction) cycles, with rates depending on the frequency of the ultrasounds. During the low-pressure cycle, high-intensity ultrasonic waves create small vacuum bubbles or voids in the liquid. When the bubbles attain a volume at which they can no longer absorb energy, they collapse violently during a high-pressure cycle. The higher the natural cohesive forces acting within a liquid (e.g. high viscosity and high surface tension) the more difficult is to attain cavitation; consequently, more energy would have to be applied to the dispersion in order to break the droplets. [145]

Also, it can be observed in Figure 4.21b that as the amount of **F127** stabilizer is increased there is a reduction of the final hexosome size. **F127** would possibly arrange on the surface of the liquid crystal particles and reduce the surface tension between the dispersed and continuous phase.[139, 146] At a **C41V**:**F127** ratio of 80:20 there is a plateau. This could indicate that at a ratio of **C41V**:**F127** of 80:20 the surface between **C41V** and water is already saturated with **F127** molecules.

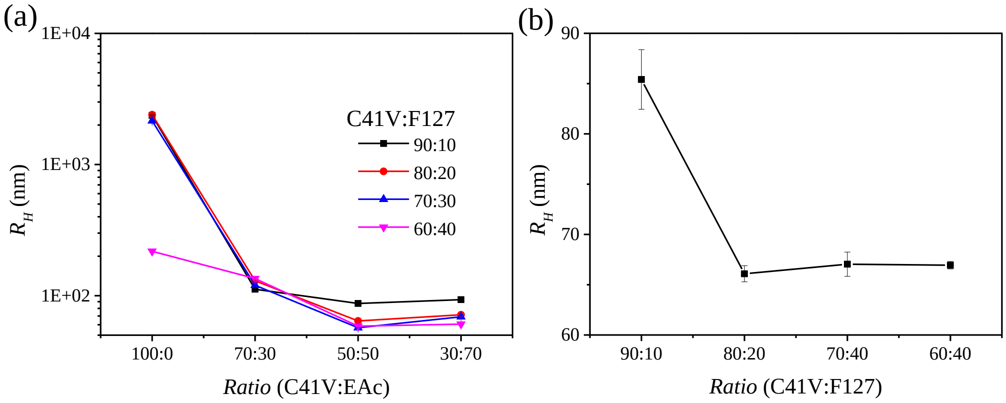

Figure 4.21. (a) Effect of the **C41V**:**EAc** ratio on the final hexosome size for samples with different **C41V**:**F127** ratios and (b) effect of the **C41V**:**F127** at a **C41V**:**EAc** of 50:50

Interfacial tension measurements between a solution of **C41V** in **EAc** (50 wt%) and water saturated with **EAc** as a function or **F127** concentration shown in

Figure 4.22 have similar tendency than Figure 4.21b. This could confirm that at a **C41V**:**F127** ratio of 80:20 the surface of the nanoparticles is already saturated with **F127** molecules.

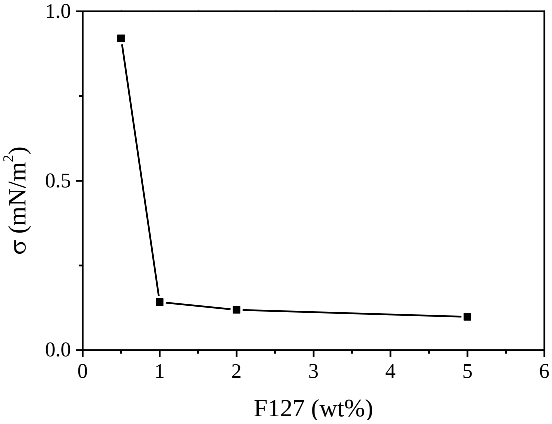

Figure 4.22. Interfacial tension measurements between water and **C41V**:**EAc** with a ratio of 50:50 as a function of **F127** concentration in wt%.

Therefore, **F127** acts as an agent for reducing the interfacial tension between the continuous/dispersed phases. **EAc** prevents the formation of liquid crystals, consequently the viscosity is reduced. These two effects allow ultrasound waves to reduce the particle size more efficiently.

These experiments show that **C41V**:**EAc** ratio of 50:50 is the optimal for the preparation of hexosomes via solvent evaporation/ultrasound method. Unless stated, the results described in the following subsections refer to this ratio and this preparation method.

4.1.5.4. **Structural characterization of the dispersions**

SAXS was used to determine the internal structure of the liquid crystal particles in these dispersions containing 5 wt% of **C41V** and different **C41V**:**F127** ratios. The **SAXS** patterns of the dispersions (Figure 4.23) showed three peaks corresponding to a hexagonal structure with Bragg distances identical to those in Figure 4.18 (approx. 4.8 nm), nevertheless there was a broadening of the peaks that made it difficult to resolve properly the second and third order refraction. This broadening is caused by the finite size of the hexosomes. The crystalline domain size (presented in Table 4.3) can be calculated using the Scherrer equation:

$$\tau = \frac{\lambda}{\beta \cos \theta}$$

Equation 4.1

Where τ is the mean size of the ordered crystalline domains which may be smaller or equal to the grain size. λ , β and θ are the wavelength (0.1542 nm), full width at half maximum in radians (FWHM) and Bragg angle, respectively. The crystalline domain is reduced with the **F127** concentration and the values are considerably smaller than the respective diameter. This difference could be caused by two different effects: one is that hexosomes could be of polycrystalline nature. The other one is that the hexosomes have also a **F127** shell and a hydration layer. However, if we consider that a **F127** shell thickness is around 20 nm (a **F127** micelle hydrodynamic radius is around 20 nm)[147] the hydrodynamic size is still bigger than the crystalline size. In any case, the reduction of the crystalline domain is in agreement with the reduction of the hydrodynamic radius, which gives evidence of the influence of the crystalline domain size on the hexosome size.

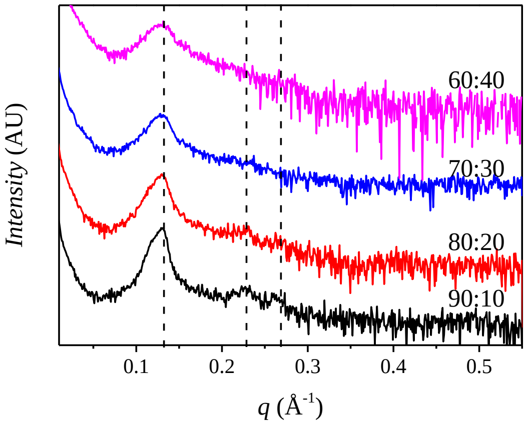

Figure 4.23. **SAXS** patterns for hexosome samples prepared by the solvent evaporation method at different **C41V**:**F127** ratios containing 5 wt% of **C41V**. The dotted lines indicate the peak positions for a hexagonal lattice.

Table 4.3. Crystalline domain size of hexosome dispersions prepared by the solvent evaporation method at different **C41V**:**F127** ratios containing 5 wt% of **C41V** calculated with Equation 4.1.

C41V:F127 ratio	Crystalline domain size (nm)	Hydrodynamic Diameter (nm)
90:10	20.8	170.8 ± 0.8
80:20	19.3	134.2 ± 0.4
70:30	18.3	132.1 ± 0.7
60:40	14.4	133.9 ± 0.9

4.1.5.5. **Influence of the continuous phase on hexosome dispersion properties**

One of the objectives of this thesis was the use of diglycerol-based surfactants as drug delivery systems. Therefore, the feasibility of preparing hexosome dispersions in a biological saline buffer (**PBS**, 0.16 M, pH=7.4) was studied. **PBS** was chosen as a continuous phase for dispersing the hexosomes since it has the same osmolality of blood (300 mOsm/kg). Figure 4.24 shows the hydrodynamic radius obtained as a function of the **C41V**:**F127** ratio. Interestingly, the size of the hexosomes was slightly smaller when prepared in **PBS**. This reduction in size could be caused by several effects. **EAc** is partially soluble in water, so it can diffuse from the dispersed to the continuous phase. This effect is enhanced when there is an increase of the osmotic pressure of the continuous media, which is proportional to the electrolyte concentration.[148, 149] Another effect that should be taken into account is that the presence of electrolytes has been reported to reduce the surface tension in water/surfactant/oil systems, which favor the formation of smaller droplets.[150]

The samples also showed a narrow size distribution (Polydispersity indexes or PDI < 0.2) in contrast with those prepared in water.

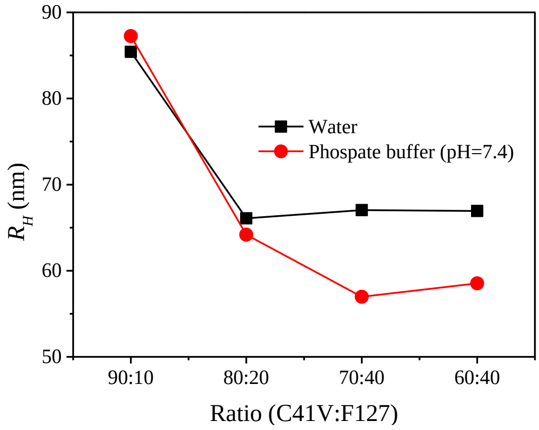

Figure 4.24. Hydrodynamic radius (R_H) for hexosomes with different **C41V**:**F127** ratios prepared in water and **PBS**.

SAXS patterns were similar to those of hexosomes prepared in water on Figure 4.23 (Bragg distance for the first peak: 4.8 nm); likesome, the second and third order peaks of a hexagonal lattice could not be clearly resolved. This can be caused by peak broadening arising from the finite size of the hexosomes. The hexagonal lattice can be assumed considering that the position of the first reflection peak is at the same position as the one in the bulk liquid crystal (in Figure 4.18) and dispersed samples in water (in Figure 4.23).

4.1.5.6. **Influence of hexosome concentration on dispersion properties**

Up to 20 grams of hexosomes in **PBS** were prepared using this procedure. It is worth noting that normal methods for preparing hexosomes (high shear, ultrasounds) only yield small volumes of sample. Only few reports have claimed the preparation of more than 100 g of dispersion in the same batch.[144] Recently, high volume fraction liquid crystalline dispersions were prepared in a lab-built dispersion equipment but high temperatures and pressures are needed.[151] Preparing high quantities, containing higher volume fraction of surfactant is of outermost importance for industrial applications. The feasibility of preparing more concentrated samples was studied. The size of the hexosomes as a function of **C41V** wt% for different **C41V:F127** ratios are shown in Figure 4.25. The increase of **C41V**:**F127** caused a visible increase of viscosity. Samples with 20 wt% of **C41V** and a **C41V**:**F127** ratio of 60:40 where too viscous (not fluid) and could not be dispersed. The hexosome sizes were reduced as the concentration of **C41V** increased. It is not clear how the increase in **C41V** concentration decreases the hexosome size. One probability would be that there is also an increase in **F127** concentration which could reduce more the interfacial tension, and therefore, reduce the hexosome size. Concentrated samples creamed after only 24 hours, but they could be diluted to 5 wt% to obtain up to 80 grams of sample with the same properties. These results suggest that this method have the potential for industrial production of hexosomes.

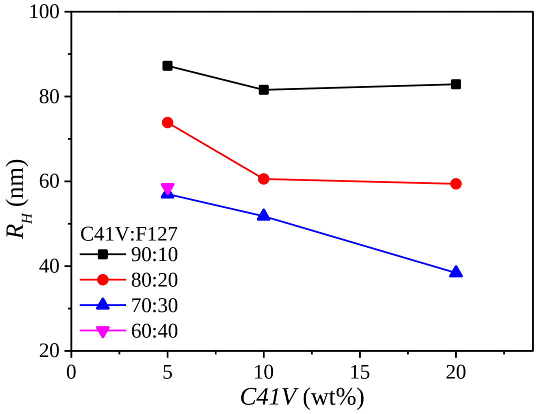

Figure 4.25. Hydrodynamic radius, R_H, of hexosomes as a function of the **C41V** concentration in samples with different **C41V**:**F127** ratio.

Inverse hexagonal liquid crystal of the water/**C41V** system could be dispersed in excess water in the form of nanoparticles stabilized by **F127**. The solvent evaporation method, using **EAc** as a volatile solvent proved to be the most efficient for obtaining hexosomes dispersions with smaller size and polydispersity. Short dispersion times (i.e. 1 min) and the possibility of preparing large volumes of dispersions show promise for the possible industrial applications of these systems. Hexosomes were prepared in **PBS** and considering that hydrophobic substances can be solubilized in the lipophilic domain of the nanoparticle, these dispersions can be used for drug delivery applications. A study of hexosomes as drug delivery vehicles will be described in the next section.

4.1.6. Encapsulation of Active Molecules in Hexosome Dispersions and Release Studies

Mono and diglycerol-based surfactant are widely used as food additives. They have unlimited acceptable Daily Intake.[23] Due to their molecular structure they can be sensitive to pH changes in the media (ester bond breaks) and can also be degraded by Lipase enzyme (present on the intestine) into glycerol and fatty acids. The degradation of the glycerol based surfactant would avoid the concentration of **LCNs** in specific parts of the body; additionally, it is known that fatty acids enhance drug absorption through the membranes in the gastrointestinal track.[152] This characteristics, together with their biocompatibility makes glycerol based **LCN's** appropriate for using them as drug delivery systems in oral administration of active compounds. It is known that lipophilic and hydrophilic molecules can be dissolved and encapsulated into the different domains of the liquid crystalline nanoparticles. Encapsulation is considered particularly advantageous for lipophilic active molecules, since it enables the incorporation of a higher amount of these compounds, a prolonged body circulation time, an increase on drug bioavailability, protection of the compound from their degradation, controlled release and reduction of the side effects; However, since **LCN's** are self-assembled materials, the incorporation of an active molecule could cause changes in their structure. In this work Ketoprofen (**KP**) was chosen as a model lipophilic drug. **KP** is an anti-inflammatory drug that is usually administered topically on the skin. **KP** topical patches are widely used in the treatment of muscular and bone pain. After 6 hours a peak of concentration is observed on muscular tissue. **KP** in oral dosage also shows the same concentrations in tissues after 14 hours; however, this oral dosage maintains 20 times more **KP** in the plasma than in the case when is applied topically, which could cause adverse reactions in the patient. Therefore, a more controlled release is then needed for oral delivery of **KP**.[153]

In the present work, **KP** was encapsulated in hexosomes with a composition of 5 wt% **C41V** and a **C41V**:**F127** ratio of 80:20. This formulation was used as drug delivery system for controlled release in aqueous media at different pH values to simulate the gastrointestinal track.

4.1.6.1. **Adjustment of Ketoprofen concentration on the hexosome dispersions.**

As described above, additives can cause changes in the internal structure of the hexosomes. **KP** was encapsulated in the hexosomes as described in subsection 3.3.9. Changes in the hexagonal structure as a function of total **KP** concentration were assessed by **SAXS** in samples with 5 wt% of **C41V** and a **C41V**:**F127** ratio of 80:20. Patterns are shown in Figure 4.26. The hexagonal structure was preserved in **KP** contents up to 0.5 wt% (**C41V**:**KP** of 10:1). At 1 wt% of **KP** only a broad band appeared, possibly due to an amorphous phase (Figure 4.26a). The Bragg distances of the first refraction peak of the hexagonal lattice increased with **KP** concentration (up to 0.5 wt% **KP**) (Figure 4.26b). This may be caused by the solubilization of **KP** in the lipophilic domain of the hexagonal lattice with the consequent swelling of the structure. The peaks also broaden, which suggests a reduction in the size of crystalline domains. At concentrations higher than 0.5 wt% the Bragg distance corresponding to the maxima of the band drops drastically, possible indicating a phase transition between a liquid crystal to an amorphous phase.

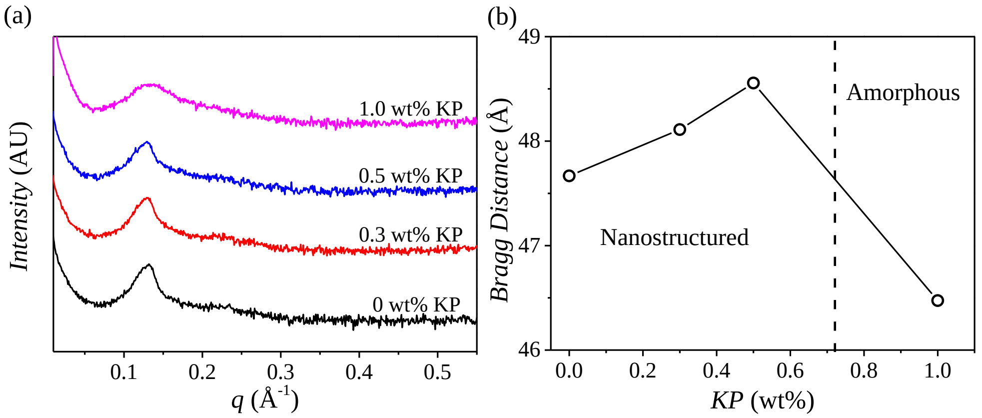

Figure 4.26. (a) **SAXS** patterns and (b) Bragg distances of the first reflection as a function of **KP** wt% for a sample with 5 wt% **C41V** and **C41V**:**F127** ratio of 80:20.

The hexosome sizes also decreased as the **KP** concentration increased (Figure 4.27a). This reduction could be associated to the shrinking of the crystalline domain caused by **KP**. It is worth also noting that **KP** can also reduce the interfacial tension between the liquid crystal and water. Therefore, it can favor the formation of smaller liquid crystal particles. The visual aspect of the samples stored at 25 ºC remained the same during long periods of time (i.e. 30 days). The stability of these samples at 25 ºC was assessed by **DLS** as a function of time (Figure 4.27b). The size of the hexosomes remained unchanged for at least 30 days.

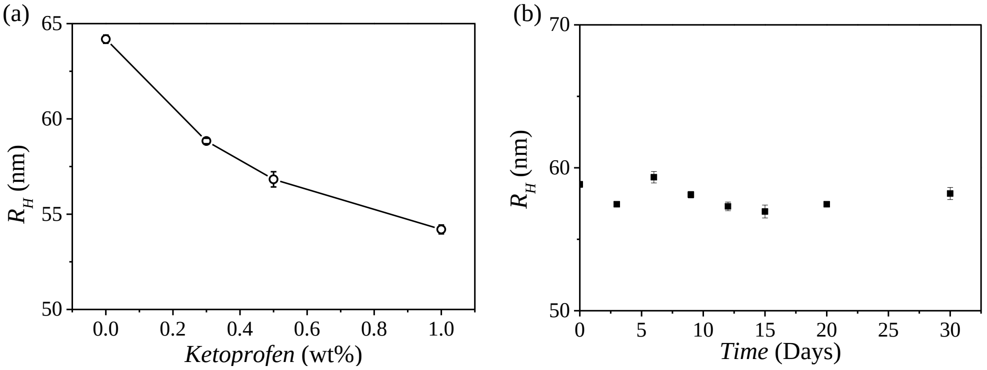

Figure 4.27. Hydrodynamic radius, R_H, of hexosome dispersions with 5 wt% **C41V** and **C41V**:**F127** ratio of 80:20: (a) As a function of **KP** concentration and (b) as a function of time for a sample containing 0.5 wt% **KP**.

4.1.6.2. **Efficiency of KP encapsulation and in-vitro drug release**

KP encapsulation efficiency was studied by the indirect filtration-centrifugation method (described in subsection 3.3.12). 0.5 wt% of **KP** encapsulated in 5 wt% **C41V** with **C41V**:**F127** ratio of 80:20 was chosen as the optimal formulation since it combined stability, small size, less concentration of **F127** and high drug loading. **HPLC** analysis was used to determine the amount of drug in the aqueous continuous phase. It was found that 86 % of drug was encapsulated in the hexosome dispersions.

A simulated gastric fluid receptor solution was used to resemble the stomach conditions (pH=1.3), and **PBS** at a pH of 7.4 was chosen as a control. Simulated intestinal fluids were also used, but growth of micro-biota in the media caused interferences in the **HPLC** methodology. In vitro **KP** release in the receptor solutions was studied using the hexosome dispersion and for comparison purposes, millipore water and **F127** micellar solutions loaded with the same drug concentration were also tested. The results are shown in Figure 4.28. All experiments were carried out at 37 ºC. Complete release of **KP** in aqueous solution was achieved after 9 h regardless of the pH of the receptor solution suggesting that **KP** could freely diffuse through the dialysis membrane. **KP** encapsulated in hexosomes and in **F127** micelles presented a more sustained release. It seems that **KP** is more retained in the hexosomes dispersions than in **F127** micelles. **F127** micelles presented almost the same release profile for all receptor solutions used, and complete release of **KP** was achieved after 25 hours. **KP** encapsulated in the hexosomes showed similar release profile during the first 9 hours independently of the pH of the receptor solution. However total release of **KP** in the hexosomes was reached after 25 h in the receptor solution with a pH value of 7.4. The release of **KP** encapsulated into the hexosomes to the receptor solution with pH value of 1.2 was incomplete in the same period of time. This difference could be caused by a crystallization of the lipids formed due to degradation of the ester bond of **C41V** at these acidic conditions.

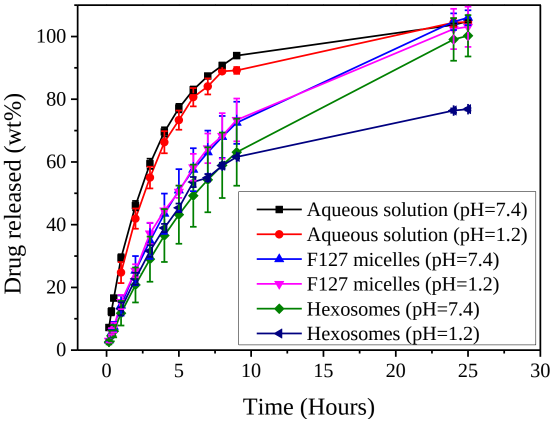

Figure 4.28. Release profiles of **KP** from an aqueous solution, **F127** micelles and from a hexosome dispersion with 5 wt% of **C41V** and **C41V**:**F127** ratio of 80:20 to receptor solutions at different pH values and at 37 ºC.

The release profiles were fitted to mathematical models in order to obtain more information about the release mechanism. Two models were considered, the Higuchi model and Korsmeyer-Peppas model (see subsection 3.3.13). The results are summarized in Figure 4.29, Table 4.4 and Table 4.5. The experimental data showed good fitting to both models (R^2 values higher than 0.94), although the fittings were better for the Higuchi model ($R^2 > 0.98$).

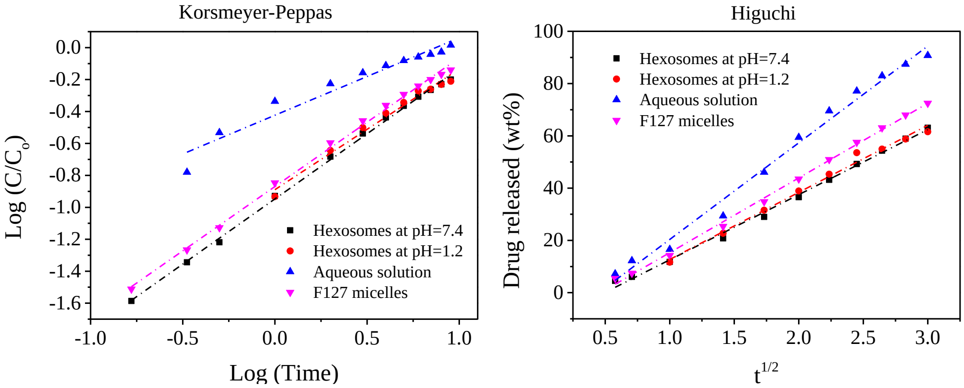

Figure 4.29. Fittings (lines) of release experimental data to the models of Korsmeyer-Peppas and Higuchi.

The fittings were performed on total drug release values lower than 60 % in the case of the Korsmeyer-Pepas model in order to obtain the diffusional exponent, *n*.[154] The **KP** aqueous solutions presented an *n* value close to 0.5, characteristic of a release mechanism under Fick's regime. For the encapsulated **KP** these *n* values were around 0.8. This means that the release mechanism follow an anomalous non-Fickian transport. This was observed for the hexosome dispersions and for the **F127** micelles. Since **F127** is adsorbed on the surface of the hexosomes it is possible that this release mechanism could be caused by the **F127** shell. In both systems, the kinetic, K_{KP}, (Korsmeyer-Pepas) or dissolution, K_H (Higuchi) constants for hexosomes were slightly lower than those for **F127** micelles.

Table 4.4. R^2, diffusional exponent (n) and kinetic constant K_{KP} of the Korsmeyer-Pepas model for different release experiments.

Sample	R^2	n	K_{KP} (h^n)
Aqueous solution	0.9413	0.49	0.42
F127 micelles	0.9954	0.82	0.94
Hexosomes (pH 7.4)	0.98156	0.76	0.89
Hexosomes (pH=1.2)	0.9983	0.81	0.87

Table 4.5. R^2, dissolution constant (K_H) of the Higuchi model for different release experiments.

Sample	R^2	K_H ($h^{1/2}$)
Aqueous solution	0.9876	37.00
F127 micelles	0.9975	28.58
Hexosomes (pH 7.4)	0.9955	25.67
Hexosomes (pH=1.2)	0.9876	24.92

Considering that liquids containing fats, such as milk, remains around 3 h in the stomach before going to the intestine, then more than 70 % of the **KP** encapsulated in the hexosomes will go to the intestine (see Figure 4.28). Additionally, lipases in the intestine can catalyze the cleavage of ester bond, which would produce glycerin and fatty acid. As these are edible surfactants, it is expected that after digestion these molecules would be expelled from the body, so no accumulation in organs is expected. These dispersions have the potential to be used as vehicles for encapsulating drugs for the delivery in the gastrointestinal track.

4.1.7. Summary

The phase behavior of the water/**C41V** system has been studied as a function of concentration and temperature. The phase boundaries of the phase diagrams were determined based on visual observations and **POM** textures. The structure of the mesophases was studied by **SAXS**. This system was characterized by a wide multiphasic region containing $\mathbf{H_2}$ liquid crystal.

Unreacted glycerol was separated from **C41V**. A $\mathbf{H_2}$ monophasic region was found in the water/**C41V-NG** which implies that glycerol produce a phase segregation in the water/**C41V** system. Diglycerol polyfatty acids were also separated from **C41V** and the influence of these separated impurities in the phase behavior were studied. It was found that the curvature of the diglycerol-monofatty acid fraction can be tuned by adding the diglycerol-polyfatty acid fraction, from a $\mathbf{L_\alpha}$ liquid crystal to a $\mathbf{H_2}$ phase.

$\mathbf{H_2}$ liquid crystal of the water/**C41V** system can be dispersed in excess water at low **C41V** concentrations to form nanometric size hexosomes. Pluronic **F127** is used as a stabilizer. The solvent evaporation method using ethyl acetate as an auxiliary solvent and dispersing with ultrasound is the most efficient for obtaining smaller sizes and narrow size distribution. Up to 80 *g* of hexosome dispersions can be obtained with this method.

Ketoprofen (**KP**) was encapsulated in the hexosomes dispersions. High encapsulation efficiencies were obtained (ca. 86 %). The encapsulated **KP** showed a sustained release to different receptor solutions, independently of the pH of the media in the 10 first h. The release profile (performed at acidic pH) changes after 10 h possible due to a degradation of **C41V** (breaking of ester bond).

4.2. PHASE BEHAVIOR AND SELF-ASSEMBLY OF DYES AND APPLICATIONS

Surfactant molecular self-assembly has been the subject of extensive studies. Little attention has been focused to the aggregation properties of other types of molecules. Chromonics are a class of molecules which self-assemble mainly as a result of $\pi - \pi$ interactions. Reported chromonics molecules are restricted to a few types of anionic dyes or polyaromatic planar molecules and only few systematic studies on self-assembly have been reported.[29, 35, 37] One of the main reasons is the low availability of these dyes and that their low purity, which can strongly modify their phase behavior.

This section describes how high purity cationic poly-aromatic dyes in water self-assemble into columnar aggregates. Cationic dyes with different molecular structures (but with flat aromatic backbones) were chosen for this study in order to understand better the correlation between molecular structure and phase behavior. Most of these molecules form aggregates in water that rearrange into more ordered structures as the dye concentration is increased. All of the dyes used in this work are readily available commercially. These commercial dyes are insoluble in water (with exception of Pyronin Y). According to the Hofmeister series, anions such as acetate and p-toluensulfonate get more hydrated than iodide, which could result in a higher solubility of the dye molecule. As the behavior of chromonics is not completely understood in terms of the effect of molecular architecture on their bulk properties it is hard to predict their liquid crystal formation. Water diffusion assays under **POM** were performed on different cationic dyes after counter-ion exchange and purification in order to observe liquid crystal evidence and proceed for further studies. Table 4.6 shows a summary of preliminary water contact tests for the different dyes used in this work.

In the next sections the self-assembly behavior, together with their respective structural characterization will be described in detail. First, the phase behavior study by means of phase diagram determinations of Quinaldine Red and Pyronin Y is reported. After understanding how they self-assemble, a systematic study of symmetric cyanine dyes (**TCC-C$_2$, TCC-C$_3$, TCC-C$_4$, TCC-C$_5$, OXA-3C, OXA-5C** and **PiC**) was carried out to get insight into the relation between molecular structure and bulk phase behavior. Finally, a preliminary and promising study about the chromonic self-assembly behavior of organometallic molecules (Alcian Blue) will be described.

Table 4.6 Summary of water contact experiments with different flat aromatic cationic dyes and their respective abbreviations.

Name	Abbreviation	Liquid Crystal Formation
Quinaldine Red Acetate	**QR-Ac**	Yes
Pyronin Y	**PyY**	Yes
3,3’-Diethylthiacarbocyanine Acetate	**TCC-C_2**	Yes
3,3’-Dipropylthiacarbocyanine Acetate	**TCC-C_3**	Yes
3,3’-Dibutylthiacarbocyanine Acetate	**TCC-C_4**	Yes
3,3’-Dipentylthiacarbocyanine Acetate	**TCC-C_5**	No
3,3’-Diethyloxacarbocyanine Acetate	**OXA-3C**	No
3,3’-Diethyldioxacarbocyanine Acetate	**OXA-5C**	Yes
Pinacyanol Acetate	**PiC**	Yes
Alcian Blue Acetate	**AB-Ac**	Yes
Alcian Blue p-Toluensulfonate	**AB-Toc**	Yes
Berberine Acetate	**Bb-Ac**	No

4.2.1. Phase Behavior of Quinaldine Red Acetate (QR-Ac)

QR is a relatively common dye, which interacts with many biological media; however, their aggregation properties remain unknown. To our knowledge, the aggregation properties of hemicyanine dyes have not been reported so far. The molecular structure or **QR-Ac** is shown in Figure 4.30.

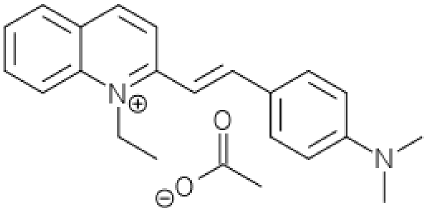

Figure 4.30. Molecular structure of **QR-Ac**.

Water contact experiment showed the presence of two different phases under **POM** (Figure 4.31). At high water content a Schlieren texture could be observed, which is characteristic of nematic (N) structures. At low water content a broken fan shape conic texture is shown, which is ascribed to closely pack columnar liquid crystals.

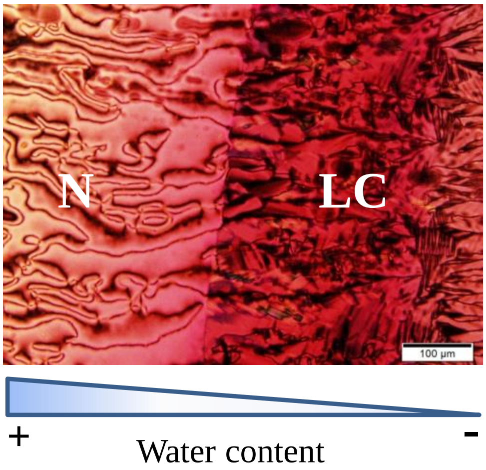

Figure 4.31. **POM** of the water contact experiment of **QR-Ac** at 25 ºC. N and LC represent Nematic and liquid crystalline structure with unresolved structure respectively.

4.2.1.1. **Determination of Water/QR-Ac phase diagram**

The partial phase diagram of **QR-Ac** (without purification) was first determined as a function of temperature and **QR-Ac** concentration in wt% (Figure 4.32a). The phase diagram was characterized mainly by a wide isotropic **I** region up to 55 wt% of **QR-Ac**. A coexistence region between nematic **N** phase and an isotropic phase (58 wt%, Figure 4.32b) was observed between 55 wt% and 60 wt% of **QR-Ac**. At concentrations from 60 wt% to 65 wt% of **QR-Ac** a crystalline solid **CS** coexist with the **N** and **I** phase (63 wt%, Figure 4.32c). A three-phase region is not compatible with the Gibbs phase rule for binary systems; therefore, more than 2 components must be present in the samples. At concentrations higher than 65 wt% of **QR-Ac**, a crystalline solid coexist with an isotropic phase (70 wt%, Figure 4.32d).

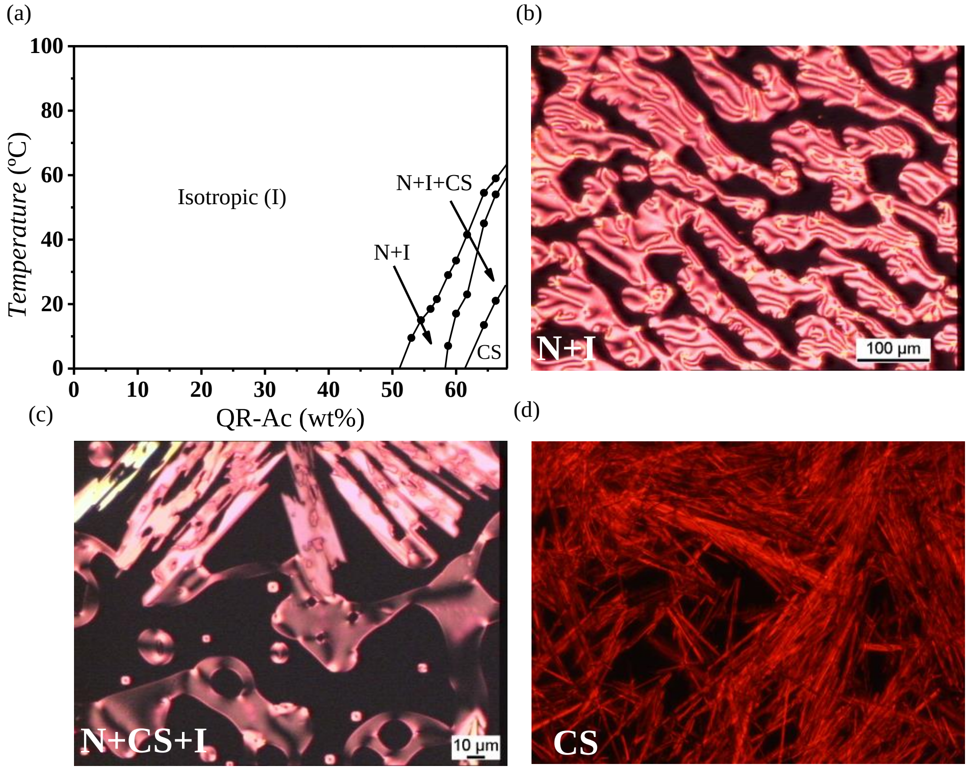

Figure 4.32. (a) Partial phase diagram of the water/**QR-Ac** (nonpurified) system as a function of temperature and **QR-Ac** wt% and **POM** textures of **QR-Ac** taken at 25 ºC for (b) nematic phase in coexistence with isotropic solution (58 wt% dye), (c) nematic phase in coexistence with isotropic solution and a crystalline solid (63 wt% dye) and (d) neddle like crystalline solid (70 wt% dye) . **I**, **N**, **CS** denote isotropic, nematic and cristalline solid respectively.

Although Quinaldine red iodide (**QR-I**) is commercially available at a relatively high purity (95 %), after counterion exchange it appears that this remaining 5 % influences the phase behavior significantly. Since **QR-I** is insoluble in water, the impurities can be separated by washing the solid with water and then performing the counterion exchange. A reduction in conductivity from 100 to 50 µS/cm was observed at the first washing step, probably due to a residual water soluble salt. After this first step, the conductivity remains constant after each washing step. This conductivity is caused by the small portion of **QR-I** dissolved into the water.

The partial phase diagram of purified **QR-Ac** in water as a function of temperature and concentration is shown in Figure 4.33. **QR-Ac** forms a nematic liquid crystal or **N** phase from 30 wt% to 57 wt% and bellow 45º C with a characteristic schlieren texture (Figure 4.34a); the **N** phase coexists with an isotropic liquid in a narrow concentration range. Melting of the **N** phase can be observed clearly under **POM** (Figure 4.34b). Above ca. 58 wt% and below 45 ºC, **QR-Ac** forms a chromonic rectangular phase or **O** phase (the structural characterization is given below), with a texture under polarized light characteristic of closely packed columnar mesophases (Figure 4.34c). Above 45 ºC the rectangular **O** phase transforms into a lamellar phase **Col$_L$**, inferred by the appearance of oily streaks (Figure 4.34d). This transition was not so sharp. It is noteworthy that lamellar phases have been only observed in chromonics at low concentrations,[42] whereas lamellar chromonic liquid crystals at high concentrations, as in the present case, are comparatively scarce. This transition, from **O** phase to **Col$_L$**, was confirmed by micro-differential scanning calorimetry (Figure 4.35) with a transition enthalpy of ca. 0.1 kJ/mol. Other high order transition at low temperatures could be observed but was not completely resolved, that could be attributed to crystallization (approx. enthalpy: 2 kJ/mol). The enthalpy values for the heating step for the **O** phase to **Col$_L$** transitions are summarized in Table 4.7. Above 70 wt% a liquid crystal coexists with a crystalline solid (**CS**). This two-phase region was not further studied.

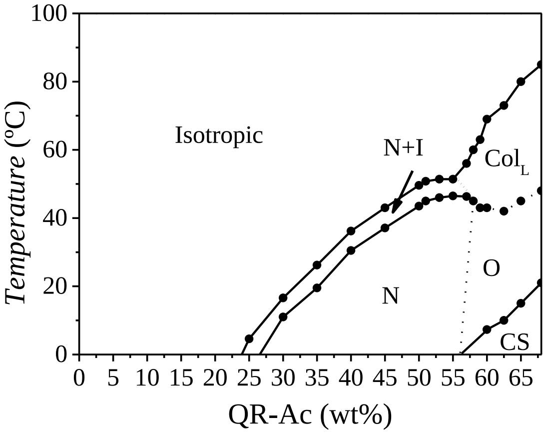

Figure 4.33. Partial phase diagram of purified **QR-Ac** in water as a function of concentration and temperature. The dotted lines indicate no sharp phase boundary. **N**, **O**, **I**, **Col$_L$** and **CS** denote nematic, columnar rectangular, isotropic, columnar lamellar and crystalline solid with unresolved structure, respectively.

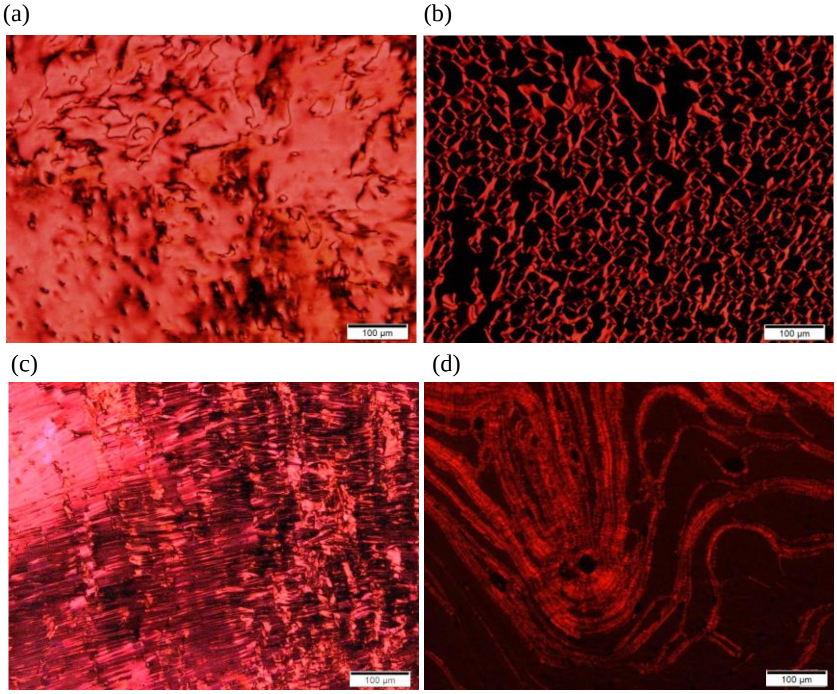

Figure 4.34. **POM** textures of **QR-Ac** in water samples for (a) nematic phase (55 wt% **QR-Ac**) at 25 ºC, (b) nematic phase in coexistence with isotropic solution (55 wt% **QR-Ac**) at 50 ºC, (c) fan shape conic texture (65 wt% **QR-Ac**) of an **O** phase at 25 ºC and (d) oily streaks (65 wt% **QR-Ac**) at 50 ºC.

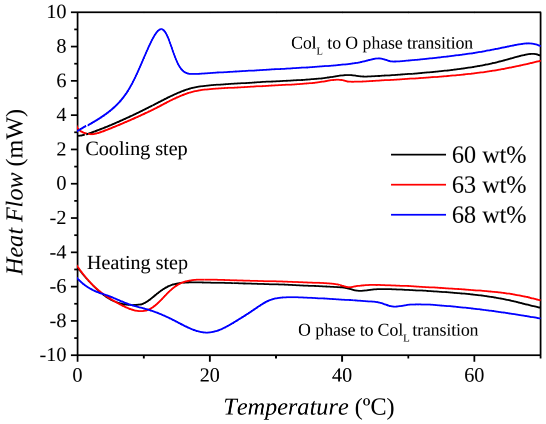

Figure 4.35. Micro-**DSC** curves for **QR-Ac** samples in water.

Table 4.7. Enthalpy values and transition temperatures for the transition from the **O** phase to **Col$_L$** phase of the water/**QR-Ac** system.

[C] (wt%)	Transition Temperature (ºC)	ΔH (kJ/mol)
60	42.65	0.0973
63	41.02	0.1563
68	47.79	0.1220

Comparing the phase diagrams of nonpurified **QR-Ac** in Figure 4.32a and the one for purified **QR-Ac** in Figure 4.33 it can be observed that the formation of the nematic, rectangular and lamellar mesophases is suppressed by impurities. Considering that one of the most common routes for synthetizing quinaldine red is achieved by condensation of 1-ethyl-2methylquinolinium iodide and the carbonyl of para-dimethylaminobenzaldehyde, then the main impurity in **QR-I** could be due to 1-ethyl-2methylquinolinium iodide. This is a weakly hydrated salt (chaotropic agent, on right side of the Hofmeister series) that can reduce the intermolecular interaction between the quinaldine red molecules, suppressing the liquid crystal formation. Although this aspect was no further studied, these results give some evidence of the possible influence of electrolytes into the phase behavior of **QR-Ac**.

Herein, all results will refer to purified **QR-Ac** unless otherwise stated.

4.2.1.2. **Characterization of isotropic region**

The molecular self-assembly of **QR-Ac** at low concentrations in the isotropic region was studied by **^{1}H-NMR** spectroscopy. The **^{1}H-NMR** in **D_2O** spectrum of **QR-Ac** was recorded at concentrations from $5x10^{-5}$ wt% to 5 wt% (Figure 4.36). Samples with **QR-Ac** with content lower than $5x10^{-5}$ wt% had a very poor signal-to-noise ratio. As it has been observed in chromonic systems, the continuous growth of molecular columns with increasing concentration causes shielding of the protons, which displace the chemical shifts upfield, the so-called ring-current effect.[33, 39, 40] **NMR** signals become wider above 5 wt%. This effect is caused by the reduction of the relaxation time of the aggregates as their size is increased.

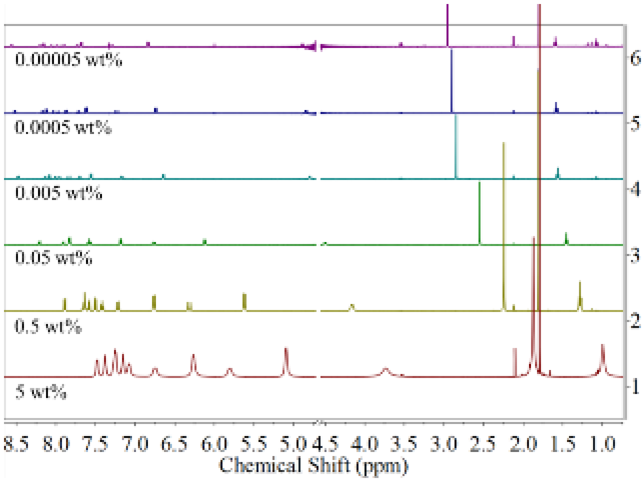

Figure 4.36. Recorded ^{1}**H-NMR** spectra of **QR-Ac** in **D_2O** at different concentrations.

The relative change of the chemical shift, *Δδ*, as a function of **QR-Ac** wt% is shown in Figure 4.37. No sign of leveling of the curve can be observed, and thus it can be inferred that aggregates and monomers coexist in the range of concentrations studied. Such coexistence is commonly found in chromonics.[36] The chemical shift of the phenylene ring protons (9 and 10 in Figure 4.37) decrease significantly (>1.4 ppm) with increasing concentration as comparison to the other protons, indicating that the phenylene ring undergoes efficient aromatic interaction within the aggregates.

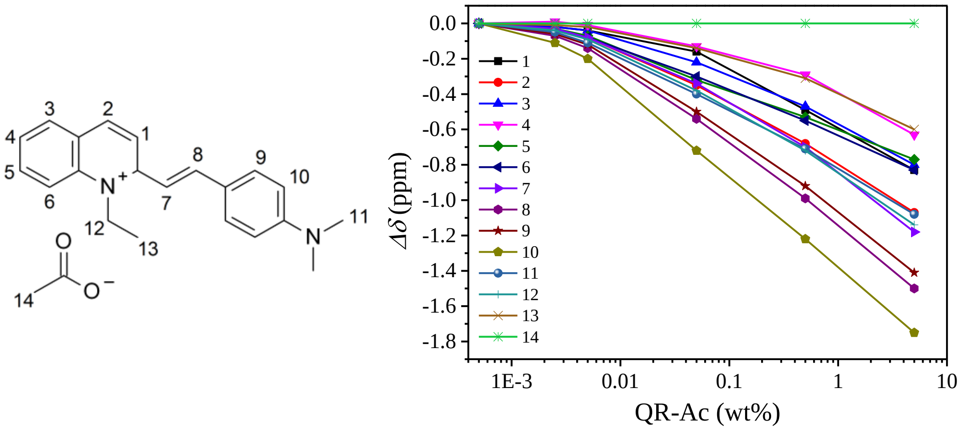

Figure 4.37. Relative change in the chemical shift, *Δδ*, at 25 ºC of the proton signals as a function of **QR-Ac** concentration in **D_2O** measured at 500 MHz. The molecular structure of **QR-Ac** with the corresponding numbering of protons is also indicated.

^{1}H-^{1}H nuclear Overhauser Effect spectroscopy (**NOEsy**) was used to get more insight into the aggregates conformation (Figure 4.38). **NOEsy** can provide information of proximity between protons from different molecules. **NOEsy** in **D_2O**

showed more signals that those recorded in **DMSO-d$_6$** which is an indication that more aggregation is taking place in aqueous media. In **D$_2$O**, ^{1}H-^{1}H correlation peaks of some of the protons of the quinolinium ring (H2, H3 and H4) with those of the dimethylamine moiety (H11) at the other end of the molecule were detected suggesting a parallel arrangement of **QR-Ac** in the stacks, with the electron-rich dimethylaniline in close proximity to the electron-deficient quinolinium moiety of another molecule.

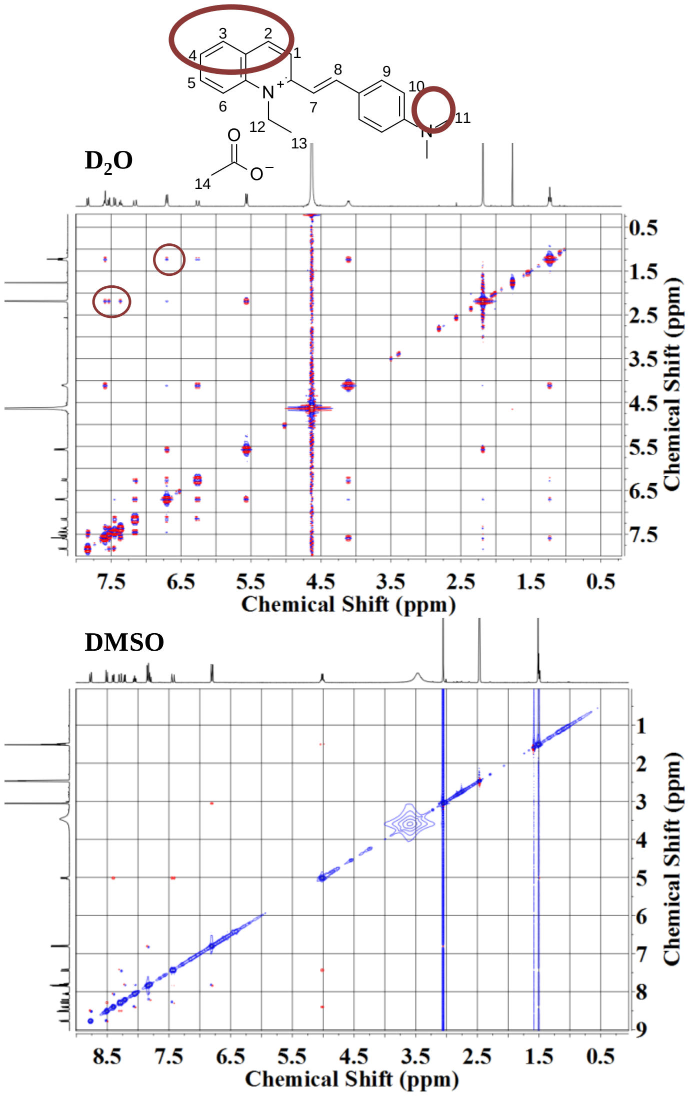

Figure 4.38. ^{1}H-^{1}H **NOEsy** spectra of 0.5 wt% of **QR-Ac** samples in **D$_2$O** and **DMSO-d$_6$**.

The molecular properties of **QR** are shown in Figure 4.39. The electrostatic potential map showed that the higher electron density is placed on the dimethyl alanine group.

QR also showed a high dipolar moment (6.2 Debyes) and approximate molecular dimensions of 8 Å x 16 Å.

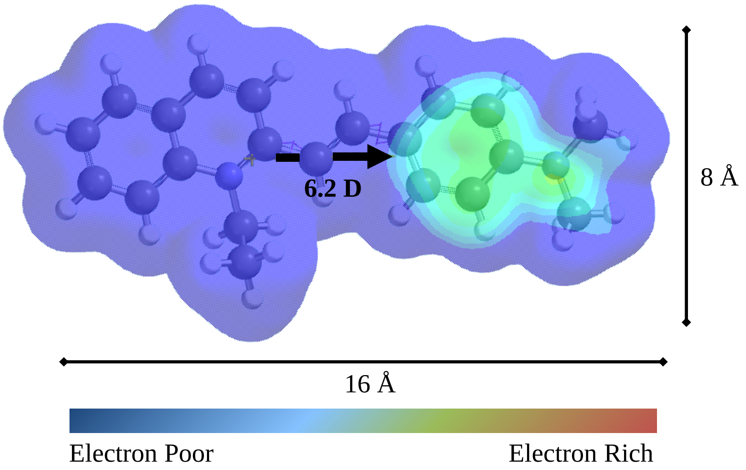

Figure 4.39. Molecular properties of **QR** molecule in water calculated using HF 6-31G in Spartan Pro (Wavefunction, inc.)

High dipolar moment molecules, such as **QR**, can lead to mutual alignment with another molecule. The energy of interaction, *w*, can be calculated as shown in Figure 4.40.[2] The calculations in Figure 4.40 appear to indicate that two dipoles always prefer to mutually orient themselves in line, but this is true only at the same value of d_m. Many dipolar molecules, like **QR**, are anisotropic in shape being longer in the direction of the dipole, so that in practice the center of such molecules can come significantly closer together when the align in parallel, making this interaction the more favorable one. Considering that the stacking distance of two molecules in chromonic systems is generally around 0.34 nm and considering that they interact through aqueous media (ε_{water} = 80.1ε_0), then the interaction energy calculated for two parallel arranged quinaldine molecules with a dipole of 6.4 *Debyes* at 300 K is of 0.4 k_BT, which is weaker than the thermal energy. It is noteworthy that the dielectric permittivity between two parallel stacked chromonic molecules should be different than ε_{water} since presumably there are no water molecules between the stacks. More interactions contribute for favoring the parallel stacking, such as electrostatic between the electronic distributions of molecules (π – π).

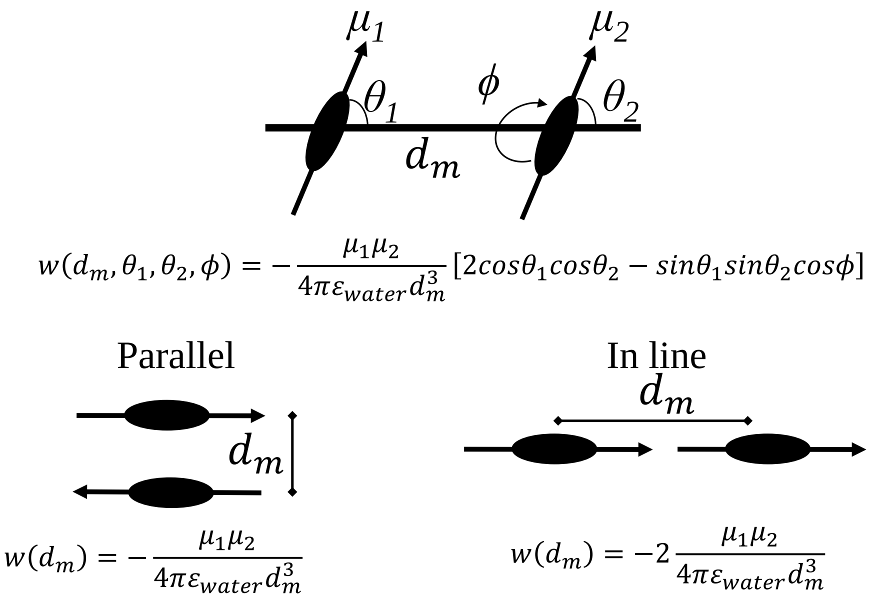

$$w(d_m, \theta_1, \theta_2, \phi) = -\frac{\mu_1\mu_2}{4\pi\varepsilon_{water}d_m^3}[2cos\theta_1cos\theta_2 - sin\theta_1sin\theta_2cos\phi]$$

$$w(d_m) = -\frac{\mu_1\mu_2}{4\pi\varepsilon_{water}d_m^3}$$

$$w(d_m) = -2\frac{\mu_1\mu_2}{4\pi\varepsilon_{water}d_m^3}$$

Figure 4.40. Common types of interaction, *w*, between two dipoles, μ_1 and μ_2, separated a distance d_m. ε_{water} is the dielectric permittivity of the water.

Recorded **UV-vis** spectra of **QR-Ac** aqueous solutions (

Figure 4.41) were similar to those of the iodide salt[155] with a main band at around 500 nm that shows a slight blue shift to shorter wavelengths as concentration increases, which is ascribed to exciton coupling between molecules in close proximity inside aggregates.

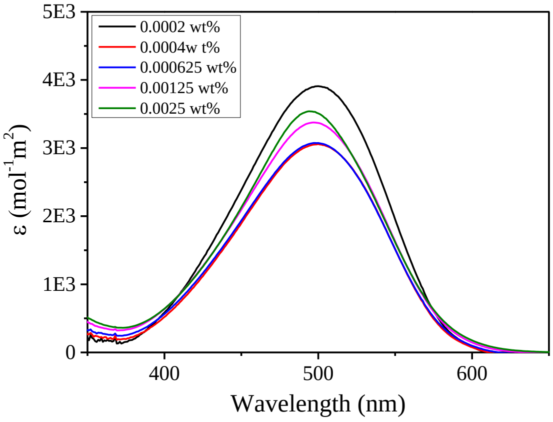

Figure 4.41. Recorded UV-spectra of aqueous solutions of **QR-Ac**.

4.2.1.3. **Structural characterization of the water/QR-Ac mesophases**

The structural features of chromonic liquid crystals (**CLCs**) in the water/**QR-Ac** system were analysed by **SAXS**/**WAXS**. The volume fraction, ϕ_f,of **QR-Ac** was calculated using Equation 3.3. The density was assumed to be 1.1 g/cm^3(density in solid state of the 1-ethyl-2-methylquinolinium iodide). Characteristic **SAXS**/**WAXS** patterns for the water/**QR-Ac** system are shown in Figure 4.42. All patterns feature a peak at $q \approx 1.8$ Å^{-1} Equivalent to a Bragg distance of 3.6 Å and corresponding to the stacking distance between the aromatic rings. This peak remains constant regardless of dye concentration.

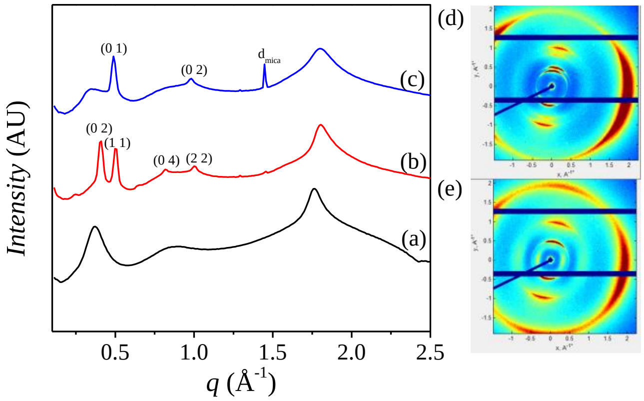

Figure 4.42. Characteristic **SAXS/WAXS** pattern of **QR-Ac** for (a) nematic phase at 50 wt% and 25 °C, (b) **O** phase at 65 wt% and 25 °C, and (c) lamellar phase (**Col**$_L$) at 65 wt% and 50 °C, d_{mica} is a reflection caused by the mica sample holder, (d) and (e) 2D patterns of rectangular **O** phase, and lamellar **Col**$_L$ phase, respectively.

For the nematic phase (Figure 4.42a) two other broad peaks are resolved, one at ca. 0.4 Å^{-1} that varies with concentration and temperature, and the other at ca. 0.9 Å^{-1} that remains constant regardless of the concentration and temperature. The q ratio between the second and third broad peaks (q_1:q_2= 1:2) agrees with a model of flat, stacked parallel sheets.[156] It is then possible that the cusp at 0.9 Å^{-1} which corresponds to a distance of 7 Å (i.e., twice the separation between aromatic moieties) results from longer range order within the molecular stacks, as it has been reported for Sunset Yellow and CI acid red 266.[40, 157] The broadness of the peaks may be attributed to a finite number of molecules in the aggregates; i.e., the columns continue growing as the concentration increases. The position of the first **SAXS** peak of the nematic phase indicates positional correlation between columns, *d*.

The *d* distance is reduced with increasing concentration, as the available aggregate space is reduced. The slope of double logarithm plot of the inverse of the distance between aggregates *1/d* vs the volume fraction, ϕ_f, for the **N** phase in Figure 4.43 gives a value of 0.55 which is characteristic of one dimensional columnar growing of aggregates (~0.5). The *d* distances remain constant with temperature for at the monophasic regions (nematic or isotropic), but experience a pronounced expansion in the biphasic region (**N+I**) (Figure 4.44).

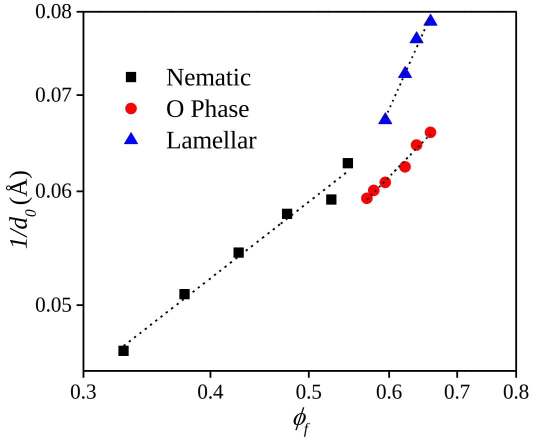

Figure 4.43. log-log plot of *1/d* vs volume fraction ϕ_f for the different **QR-Ac** mesophases at 25 ºC for Nematic and **O**-phase and 50 ºC for **Col$_L$**. The dashed lines correspond to linear data fittings.

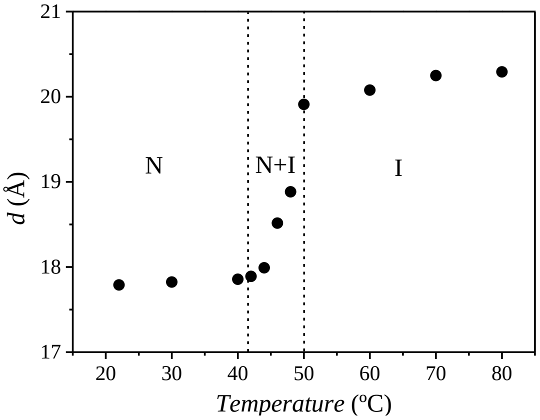

Figure 4.44.Variation of the mean distance between aggregates, *d*, with temperature for a 50 wt% **QR-Ac** sample.

At concentrations greater than 58 wt%, the **SAXS** pattern changes abruptly. Below 45 °C (Figure 4.42b) all patterns show four reflections, two of them sharp, corresponding to the planes with Miller indices of (02), (11), (04) and (22), which can be fitted to a 2D rectangular lattice (**O** phase). Nevertheless, the resolved reflections are not enough to unambiguously establish the symmetry of the phase (e.g., p6mm, p2gg or c2mm). The occurrence of the **O** phase indicates anisotropy of the cross section of the columnar aggregates, which is consistent with the parallel stacking predicted with **NOESy** at low concentrated samples in Figure 4.38.

The estimated cross-sectional area is around 130 Å^2 (Calculated with

Equation 1.6), which is slightly larger than the area of a single molecule (~110 Å^2) calculated with Spartan® (Wavefunction Inc.). The lattice parameters and peak positions are summarized calculated with Equation 1.5 in Table 4.8.

Table 4.8.Peak positions q and lattice parameters a and b for the **O** phase of the water/**QR-Ac** system at different concentration at 25 ºC.

[C] (wt%)	q_{02} (Å)	q_{11} (Å)	q_{04} (Å)	q_{22} (Å)	a (Å)	b (Å)
59.37	0.372	0.455	--	0.914	15.13	33.71
60.25	0.377	0.463	--	0.923	14.98	33.28
61.75	0.382	0.469	0.764	0.934	14.65	32.86
64.4	0.392	0.483	0.788	0.953	14.22	32.05
66	0.406	0.491	0.814	0.992	14.08	30.95
68	0.411	0.502	0.827	1.007	13.80	30.33

2D **SAXS** patterns showed a partial alignment that is characteristic of long anisotropic aggregates (Figure 4.42d). The axial arcs in the **WAXS** region are almost orthogonal to the equatorial **SAXS** reflections, evidencing that the stacking direction is perpendicular to the rectangular symmetry. As concentration increases, the Bragg distances calculated from the position of the first reflection peak in the **O** phase, d_O, becomes shorter as the concentration increases. The slope of double logarithm plot of $1/d$ vs the volume fraction ϕ_f for the **O** phase in Figure 4.43 gives a value of 0.7 which is compatible with one dimensional growth of aggregates.

Above 45 °C, **SAXS** patterns (Figure 4.42c) feature two well-defined reflections corresponding to the planes with Miller indices of (10) and (20), characteristic of a lamellar phase (**Col$_L$**) and a broad, rather diffuse reflection (hump) at lower q that varies with concentration (Bragg distance from 17 to 20 Å). Such reflection can be assigned to structural features within the lamellae, namely, of the columnar aggregates in the same layer with a characteristic separation distance. The pattern for the **Col$_L$** resembles that of mesh phases found positional correlation in surfactant systems.[158-160] However, the **Col$_L$** phase is different from lamellar phases usually found in surfactants and amphiphilic block copolymers systems.[161] In the **Col$_L$** mesophase, molecules are arranged in columns inside each layer. 2D patterns for the **Col$_L$** phase (shown in Figure 4.42e) again give evidence of a partial alignment, characteristic of anisotropic aggregates. The width of the molecular layer in a lamellar phase d_π can be calculated with Equation 1.4

The calculated width of the layers is about 8.5 Å, similar to those reported by Tiddy and co-workers for cyanine dyes in brick-wall unimolecular layers,[42, 44] and matching with the width of a single **QR-Ac** molecule. This width remains constant with temperature. Relevant structural parameters of this phase at 50 ºC are shown in Table 4.9.

Table 4.9. Peak positions q, distance between layers d and width of the layers d_π for the **Col$_L$** phase of the water/**QR-Ac** system at different concentration at 50 ºC

[C] wt%	q_{10} (Å^{-1})	q_{20} (Å^{-1})	d (Å)	d_π (Å)
62	0.4211	0.8422	14.9	8.9
64.5	0.4598	0.9196	13.7	8.5
66	0.4888	0.9776	12.8	8.2
68	0.4936	0.9872	12.7	8.4

From the gathered evidence, we cannot completely rule out the brick-wall lamellar structure proposed by Tiddy and coworkers but the proposed configuration would imply merely a rearrangement of the columns during the **O** phase−**Col$_L$** phase transition, which is more likely to occur than a simultaneous major change in molecular stacking. In fact, the layered structure with columnar organization is known to exist in certain discotic compounds[6] although to our knowledge, it has never been reported for chromonic systems. The slope of the double logarithm plot of the inverse of the distance between layers $1/d$ vs the volume fraction, ϕ_f, for the **Col$_L$** phase in Figure 4.43 gives a value of 1.6 which is characteristic of a two-dimensional swelling of layers.

The fact that the electronic distribution on the **QR-Ac** molecule is anisotropic gives rise to an anti-parallel arrangement between molecules. This type of arrangement allows **QR-Ac** to self-assembly into columns with anisotropic cross section. These columns rearrange to form a rich phase behavior, with two novel structures that has not been observed for other water/dye systems. Considering the collected data the proposed structures for the water/**QR-Ac** mesophases are summarized in Figure 4.45

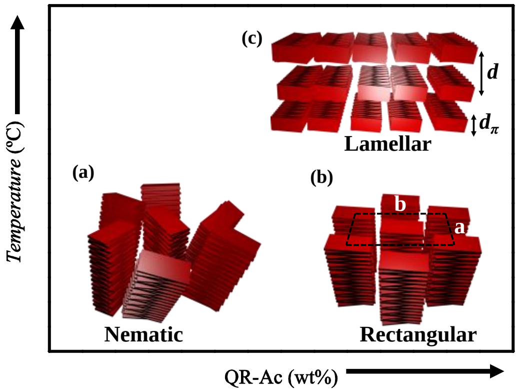

Figure 4.45. Representation of proposed structures for (a) Nematic **N** phase, (b) Chromonic columnar rectangular phase, **O** Phase and (c) Columnar lamellar Mesophase, **Col$_L$**, for the water water/**QR-Ac** system. Relevant structural parameters are also indicated

4.2.2. Pyronin Y (PyY) Phase Behavior

Pyronin Y (**PyY**, also called Pyronin G) is a cationic xanthene dye (Figure 4.46). It has been reported that **PyY** forms molecular stacks in dilute aqueous media.[162] Moreover, the liquid crystal formation of a similar family of molecules, xanthone dyes, has already been reported.[163] Xanthone dyes self-assembly into columns with multimolecular cross-section. Therefore, it is highly probable that **PyY** forms chromonic liquid crystal at high concentrations.

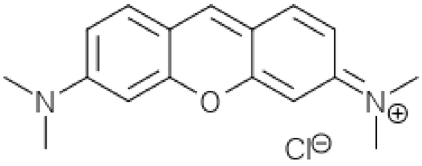

Figure 4.46. Molecular structure of **PyY**

Water contact experiments under **POM** showed the presence of a nematic phase (Figure 4.47). Similar to **QR-Ac**, at high water content a Schlieren texture could be observed, characteristic of nematic (N) structures. No other birefringent texture could be observed at low water contents.

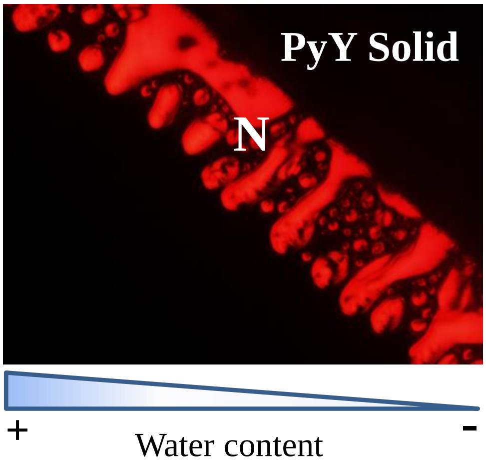

Figure 4.47. **POM** of the water contact experiment of **PyY** at 25 ºC. N represents Nematic liquid crystal.

4.2.2.1. **Determination of Water/PyY phase diagram**

The partial phase diagram of **PyY** constructed as a function of **PyY** concentration and temperature is shown in Figure 4.48. From 45 to 73 wt% **PyY** features an **N** phase at 25 ºC, as confirmed by the optical textures under the microscope (Figure 4.49a). The **N** phase coexists with an isotropic liquid in a wide range of concentrations which can be confirmed by **POM** (Figure 4.49b). This wide coexistence zone has been observed in other chromonic systems, such as in aqueous mixtures of Bordeaux dye and violet 20 dye [164, 165] Above 73 wt% the **N** phase coexists with a crystalline solid; this region was not further studied.

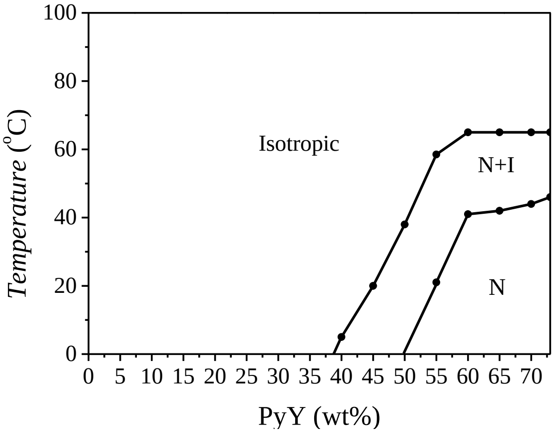

Figure 4.48. Partial phase diagram of **PyY** in water as a function of concentration and temperature. **N** and **I** denote nematic and isotropic, respectively.

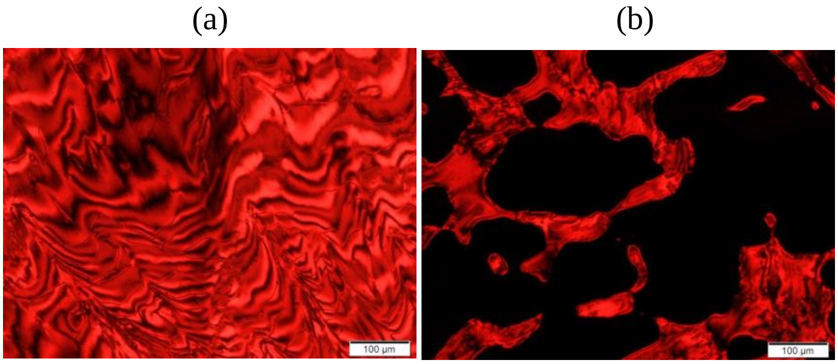

Figure 4.49. **POM** textures of **PyY** for (a) nematic phase (60 wt% dye) at 25 ºC and (b) the nematic phase in coexistence with isotropic solution (60 wt% dye) at 55 ºC.

Similar to **QR-Ac**, **PyY**, showed a non-cooperative melting from the **N** phase to the isotropic phase (i.e. a 60 wt% dye sample presented a coexistence region between nematic and isotropic phases from 37 ºC to 63 ºC). It is noteworthy that this coexistence region was wider for the water/**PyY** system. These types of transitions are thought to have activation of entropies, ΔH, near zero. Chromonic molecules in water are thought to go through an isodesmic aggregation process. In an isodesmic process, the addition or subtraction of a monomer to the growing aggregate is governed by a single equilibrium constant, K, regardless of the size or length of the aggregate. Consequently, a broad distribution in the degree of stacking is often observed for this type of process. It is known that the equilibrium constant is temperature-dependent, K=K(T), and so the aggregation may be promoted either by increasing the concentration or by varying the temperature.[166] An schematic process of an isodesmic and cooperative assembly (degree of aggregation vs concentration and temperature) is presented in Figure 4.50. Considering this, in a chromonic system, such as water/**PyY**, by increasing the temperature, the size of the aggregates is likely to decrease gradually causing a big coexistence region rather than a sharp transition at a certain temperature.

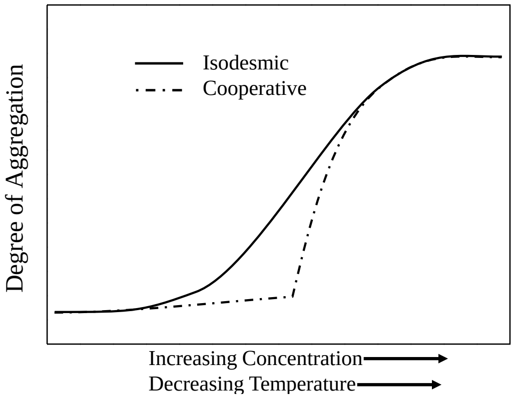

Figure 4.50. Schematic representation of the degree of aggregation versus concentration and temperature. Reproduced from [166].

4.2.2.2. **Characterization of Isotropic region**

^{1}H-NMR spectroscopy was performed on **PyY** at low concentrations to characterize the isotropic region and study the possible $\pi - \pi$ interactions. (Figure 4.51). The **^{1}H-NMR** spectrum of **PyY** was recorded in concentrations from 0.00275 wt% to 5 wt%. Samples with **PyY** with content lower than 0.00275 wt% showed a very poor signal-to-noise ratio. Similar to **QR-Ac**, it is expected that as the concentration is increased there is a shielding of the aromatic protons causing a displacement of the chemical shifts to higher fields (low ppm). **NMR** signals are broader above 5 wt% due to the reduction of the relaxation time of the aggregates as their size is increased.

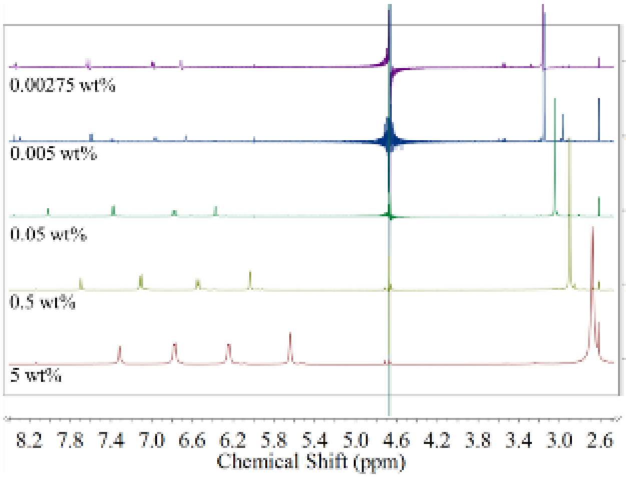

Figure 4.51. Recorded **^{1}H-NMR** spectra of **PyY** in **D_2O** at different concentrations.

The aromatic protons of **PyY** (1-4 in Figure 4.52) show pronounced decreases in chemical shifts with increasing concentration (Figure 4.52a) (changes between 0.8 and 1.2 ppm), whereas the protons of the dimethylammonium moieties shift much less (<0.5 ppm). This behavior is expected for molecules which self-aggregate into columns with the aromatic cores lying on top of each other.[33] Due to steric repulsions, the alkyl-ammonium substituents from adjacent molecules are expected to align in a staggered fashion. In contrast, as the temperature is increased the signals shifts displace to lower field (higher chemical shifts) (Figure 4.52b). The inter-molecular interactions are reduced as the temperature is increased. The relative change in chemical shift, $\Delta\delta$, varies almost linear with temperature with all concentrations. The slopes, *m*, of the graphs of $\Delta\delta$ vs temperature are summarized in Table 4.10. Considering the data collected by ^{1}**H-NMR** the size of the columnar aggregates formed would increase with concentration and decrease as the temperature increases. This lyotropic behavior with temperature and concentration is in agreement with those reported for chromonic systems.[26]

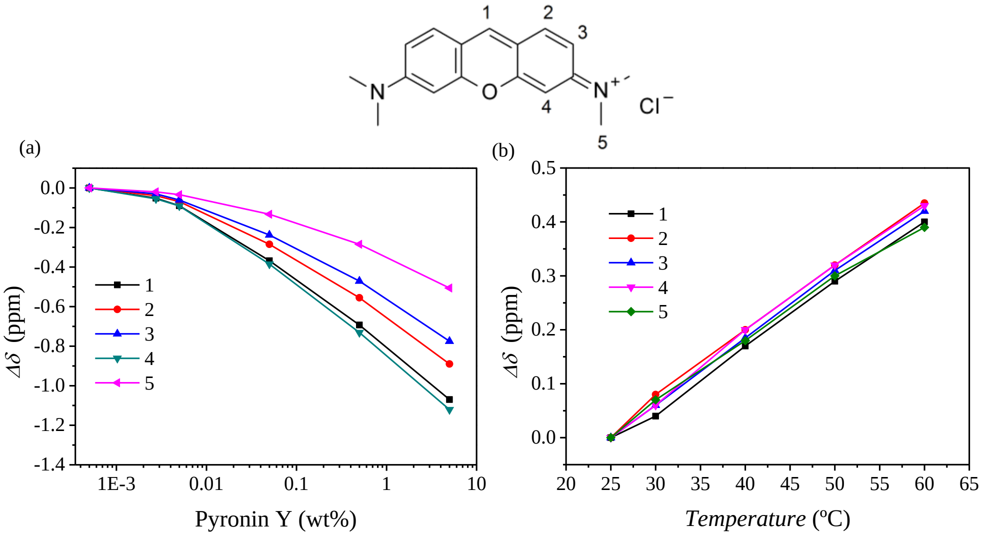

Figure 4.52. Relative change in the chemical shift, $\Delta\delta$, measured in **D_2O** at 500 MHz, $\Delta\delta$, of the proton signals as a function of (a) **PyY** concentration at 25 ºC and (b) Temperature (0.005 wt% sample). The molecular structure of **PyY** with the corresponding numbering of protons is also indicated.

Table 4.10. Slope values of the relative change in chemical shift, $\Delta\delta$, vs temperature plot for samples with different **PyY** concentration.

[C] wt%	*Slope* H1	*Slope* H2	*Slope* H3	*Slope* H4	*Slope* H5
0.00275	0.0119	0.0122	0.0110	0.0115	0.0110
0.005	0.0117	0.0123	0.0121	0.0124	0.0112
0.05	0.0127	0.0125	0.0124	0.0134	0.0115
0.5	0.0154	0.0152	0.0144	0.0154	0.0135
5	0.0140	0.0143	0.0136	0.0140	0.129

Additional evidence of **PyY** aggregation comes from the decrease in fluorescence intensity as the concentration is increasing (aggregation-induced quenching) (Figure 4.53). The non-fluorescent nature of aggregates can be explained by the exciton theory (see subsection 1.3.1). Two exciton states arise in the case of the face-to-face stacked dimer aggregates (the so -called H-aggregates), but only the transition to the higher energy exciton is allowed, and can be observed in the **UV-Vis** absorption spectrum as a blue shifted band. Rapid internal conversion of the excited state into the lower energy exciton state quenches the fluorescence as a result of the decreasing transition probably for a radioactive process from this state to the ground state. The fluorescence is quenched at relatively low **PyY** concentration (i.e. 0.08 wt%) which could indicate that the number density of dimers (aggregate) is high.

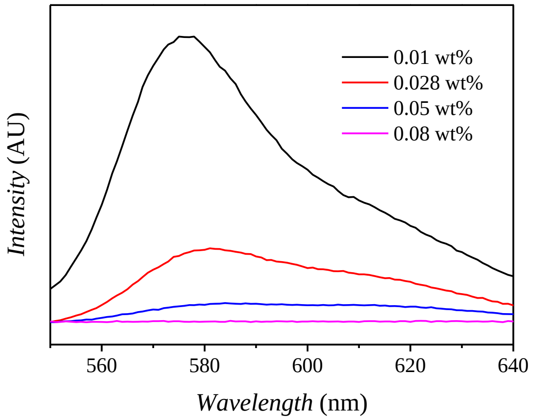

Figure 4.53. Fluorescence spectra of **PyY** (λ_{ext} = 530) at different concentrations in water at 25 ºC.

4.2.2.3. **Structural characterization of the water/PyY system.**

The structural analysis of **PyY** phases in water was carried out by **SAXS**/**WAXS** (Figure 4.54). The **SAXS** patterns of the **N** phase shows a broad band indicative of positional correlation between columns (Figure 4.54a). These bands were considerably broad. Some information on the ordering characteristic of the aggregates can be obtained from the widths of bands, *Δ(2θ)*. Considering the quadrature sum[167]:

$$\Delta(2\theta) = \lambda\left[\left(\frac{1}{n_m d_m}\right)^2 + \left(\frac{o^2\pi^2\beta^2}{2d_m^3}\right)^2\right]^{\frac{1}{2}}$$

Equation 4.2

Where λ is the X-ray wavelength (1.54 Å), *o* is the order of the diffraction (1 in this case), n_m is the number of molecules separated a distance d_m (in chromonics, *d* is aprox 3.4 Å) in the lattice and *δ* is the half width of an assumed Gaussian distribution in the parameter n_m. In this system δ is relative small since the molecules are closely packed together, then the first term in the equation determines the width of bands. Considering that in the nematic phase the number of molecules in an aggregate, n_m, varies with concentration and d_m is constant (0.36 nm), then, the more stacking molecules on each aggregate (increase in concentration), the thinner the band of the nematic phase.

Similar to **QR-Ac**, for **PyY** the distance between aggregates, *d*, within the nematic single-phase region decreases as the concentration increases (Figure 4.54b) whereas in the coexistence region it remains constant.

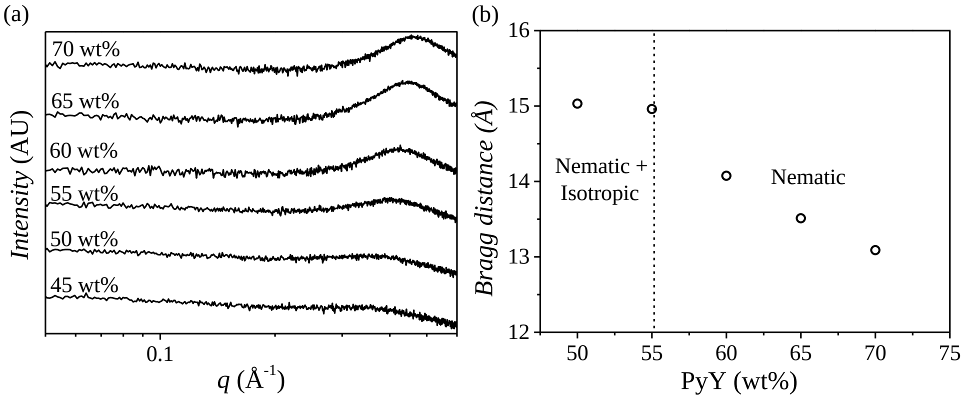

Figure 4.54.(a) **SAXS** patterns for the nematic phase of the water/**PyY** system at different dye wt%(b) Bragg distance calculated from the maximum of the band at 25 ºC as a function of **PyY** concentration.

The distance between aggregates, *d*, experience a slight expansion in the biphasic region as the temperature is increased (**N+I**) (Figure 4.55). The bi-phasic region width is calculated to be around ca. 27 ºC. *d* remained constant with temperature for at the monophasic regions (nematic or isotropic).

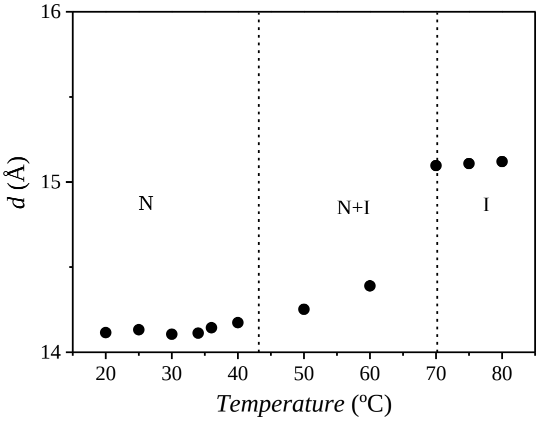

Figure 4.55. Variation of the mean distance, *d*, between aggregates for a 60 wt% **PyY** sample.

To estimate the cross-sectional area of the columns in the nematic phase, a hexagonal array of cylinders can be assumed as first approximation.[164] In fact, molecular simulations of the nematic phase formed by the dye Sunset Yellow show a loose hexagonal packing of the chromonic columns.[168] In a hexagonal array of cylinders, the square of the Bragg distance, d^2, varies with the inverse of the volume fraction, ϕ_f, following the equation:

$$d^2 = \frac{A_c\sqrt{3}}{2} * \phi_f^{-1}$$

Equation 4.3

Where A_c is the cross- sectional area of a cylindrical aggregate. The volume fraction was calculated by Equation 3.3 using the density of solid xanthene (1.2 cm^3). A_c can be determined from the slope of d^2 vs ϕ_f shown in Figure 4.56.

Within this approximation, a cross-sectional area of ca. 130 Å^2 is obtained. This value is slightly larger than the area for a **PyY** molecule, 100 Å, calculated with Spartan (Wavefunction Inc.). It is thus reasonable to say that **PyY** forms unimolecular stacks.

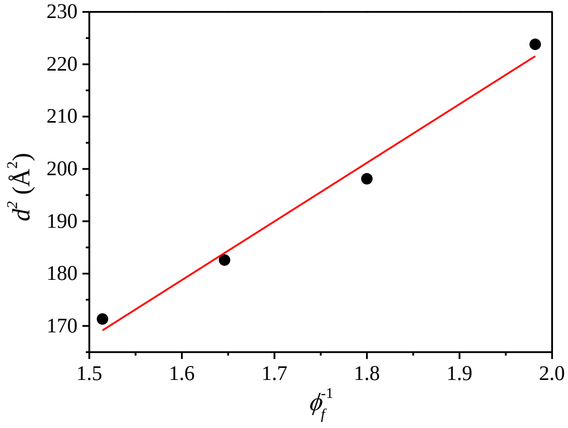

Figure 4.56. Variation of the square of the Bragg distance, d^2, with the inverse of **PyY** volume fraction ϕ_f, in the water/**PyY** system.

Another evidence of **PyY** having unimolecular aggregate can be inferred by **SAXS** data of a dilute sample (2 wt%) in Figure 4.57. No exact model could be adjusted, although, the cylinder model showed the best fit results. The aggregates cross-section radius was found to be around 5.4 Å which fits one of the dimensions of a **PyY** molecule calculated in Spartan Pro (Wavefunction Inc.) (ca. 6 Å). Considering a circular cross-section, the calculated area is 80 Å^2 also in agreement with a unimolecular cross-section.

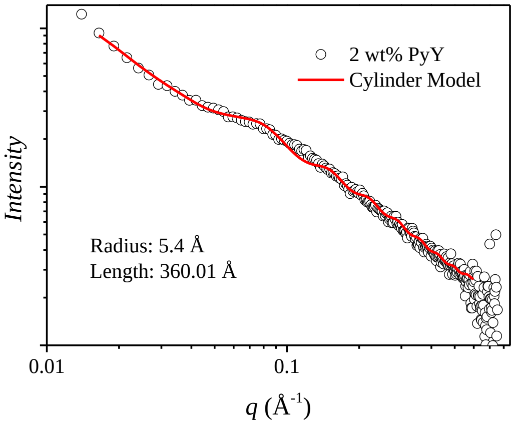

Figure 4.57. **SAXS** pattern for a 2 wt% **PyY** sample with the corresponding cylinder model fitting.

4.2.3. Self-Assembly of Cationic Carbocyanine Dyes

Cyanine dyes are planar molecules consisting in two heterocyclic units, which are linked by an odd number of methine groups. Attractive forces between these molecules induce self-assembly both in solution and on solid surfaces, causing changes in optical properties compared to those in the monomeric, non-aggregated state. The changes are reflected in a displacement of the bands in the absorption spectra: blue or hypsochromic shifts to shorter wavelengths are referred to as H-bands while red or bathochromic shifts to longer wavelengths are referred to as J-bands (see subsection 1.3.1). At higher concentrations in water, cyanine dyes can also assemble into chromonic liquid crystals.[39-45, 169] Although this behavior has been observed in many dyes, little systematic studies have been performed. Herein, in the next section the self-assembly and occurrence of chromonic liquid crystal in series of the acetate salts of thiacabocyanines, oxacarbocyanines and other cyanines (Pinacyanol Acetate and Alcian Blue) will be described.

4.2.3.1. **Thiacarbocyanines (TCC)**

The self-assembly of the acetate salts of thiacarbocyanines with different N-alkyl substituent (shown in Figure 4.58) in water was studied.

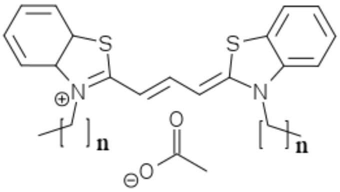

n=2 TCC-C_2
n=3 TCC-C_3
n=4 TCC-C_4
n=5 TCC-C_5

Figure 4.58. Molecular structure of **TCC** series of chromonic molecules.

Absorption spectra as a function of dye concentration are shown in Figure 4.59. From the absorption spectra of a **MeOH** solution (dashed lines in Figure 4.60) the monomer band for all molecules was identified with maxima at ~555 nm (the maxima is shifted 2 nm to lower energies in the case of **MeOH**). The absorptivity of the dyes is reduced as the n-alkyl chain length increases. Some spectral data of these dyes in **MeOH** are presented in Table 4.11. For all studied dyes, at a concentration below 0.0025 wt% in water, the monomer bands were found to be dominant. With increasing dye concentration, the intensity of a second band with a maximum around 510 nm increases, which were assigned to dimers. The positions of the maxima of monomer and dimer bands are similar to those reported for the iodide salts of thiacyanine dyes in water. A hypsocromic shift is observed which can be ascribed to H-aggregate (face to face stacking) formation.

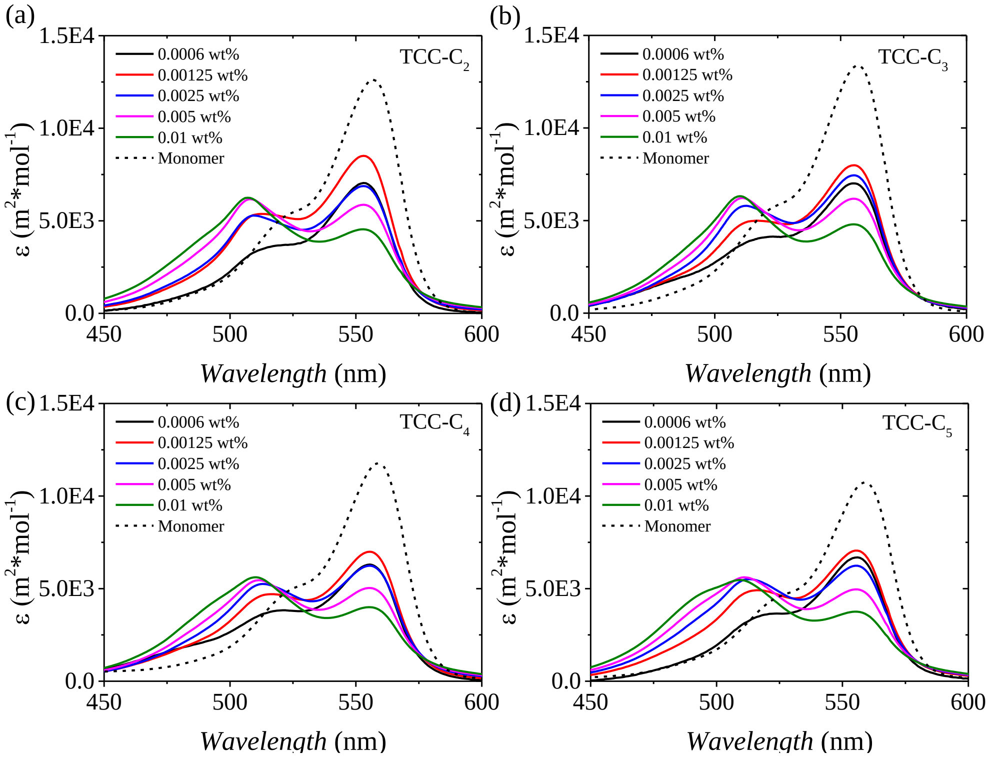

Figure 4.59.Absorption spectra at 25 ºC of (a) **TCC-C$_2$**, (b) **TCC-C$_3$**, (c) **TCC-C$_4$** and (d) **TCC-C$_5$** in water at different concentrations. The dotted lines correspond to the respective spectra of the dyes in **MeOH** measured at a concentration of ca. 0.0006 wt%.

Table 4.11. Spectral data of thiacarbocyanines.

N-Alkyl Thiacarbocyanine	Monomer λ_{max} (nm) H_2O/MeOH	Monomer ε_{max} in MeOH (m^2/mol)
TCC-C_2	555/557	12140
TCC-C_3	555/557	13299
TCC-C_4	555/557	11785
TCC-C_5	555/557	10747

To illustrate more clearly the monomer/dimer contributions to the absorption spectra, a deconvolution of the **UV-Vis** spectra was performed. The ratio $R_s = s_{dimer}/s_{monomer}$, ($s$ is the peak height from deconvoluted spectra) was plotted as a function of dye concentration $[C]_{dye}$ (Figure 4.60). R_s grow with $[C]_{dye}$, demonstrating that molecular self-assembly is favored with increasing dye concentration. For all studied dyes, the dimer contribution becomes dominant at a concentration of around 30 µM – 60 µM. There is no clear difference between R_s vs $[C]_{dye}$ plots for **TCC-C_2** and **TCC-C_3**, but R_s values of **TCC-C_4** and **TCC-C_5** appear to be higher suggesting a stronger tendency to aggregate. It seems that as the alkyl chain length is increased there is more interaction between the molecules. This could be a sign of a transition from a situation in which aggregation is purely induced by π – π interaction to one in which hydrophobic effect driven by the lateral alkyl chains starts to play a role.

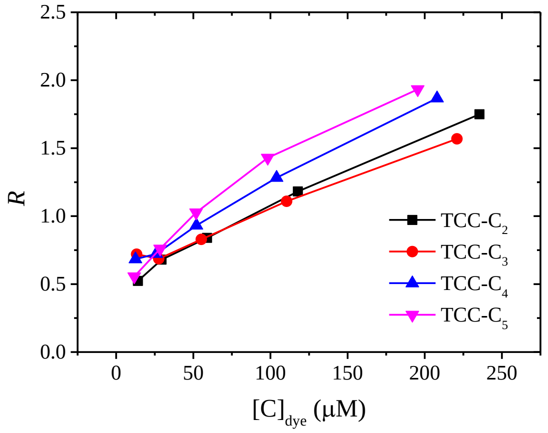

Figure 4.60.Change of ratio R_s with concentration at room temperature for **TCC-C_2**, **TCC-C_3**, **TCC-C_4** and **TCC-C_5**. $R_s = s_{dimer}/s_{monomer}$ (s is peak height from deconvoluted spectra with Origin 9.0. The Gauss method was used for concentrations < 100 µM, Lorentz for those > 100 µM).

If the separated absorption spectra of the monomer and dimer are known it would be simple to estimate the equilibrium constant of the monomer with dimers by applying a simple mass balance. However, the individual spectrum of the dimers cannot be obtained experimentally since as the concentration of dye is increased higher order aggregates are formed and the spectrum is more complex. The spectra of monomers can be measured, in principle, in highly diluted solutions, but some cationic dyes can absorb in the anionic glass cuvettes used for measuring and in most cases the spectra obtained is very noisy leading to considerable error in the analysis. The monomer spectra in water can be assumed to be similar to those in diluted solutions in a solvent in which aggregation is negligible, i.e. **MeOH**. Due to the small solvatochromic shift between **MeOH** and water solutions (ca. 2 nm, see Table 4.11) this seems a good approximation. The spectra were fitted to a model in which monomers and dimers are in equilibria to estimate the dimeric constant, K_D (see subsection 3.3.14). Table 4.12 shows the fitting parameters obtained. It seems that the energy of dissociation (calculated from Equation 3.15) increases with the number of carbon atoms of the N-Alkyl chain. The nonlinear fits are shown in Figure 4.61. As only the N-alkyl chain is varying, it is reasonable to infer that the extra interaction energy comes from hydrophobic interactions between the hydrocarbon chains. **TCC-C$_5$** K_D values were similar to those from **TCC-C$_4$**. It is noteworthy that the dimmer band of **TCC-C$_5$** appearing at ca. 510 nm is wider compared to the other thiacarbocyanines; consequently, the calculated K_D can be underestimated. This widening can be caused by the appearance of another band, corresponding to aggregates with larger aggregation number.

Table 4.12. Parameters obtained by fitting the **UV-Vis** spectra using the monomer/dimer model.

N-Alkyl Thiacarbocyanine	K_D (mol^{-1})	ΔG (k_BT)	Dimer max ε (m$_2$*mol^{-1})
TCC-C$_2$	15595 ± 926	19.30 ± 0.12	7420.2 ± 284.8
TCC-C$_3$	17746 ± 571	19.57 ± 0.07	7346.8 ± 93.9
TCC-C$_4$	25284 ± 917	20.27 ± 0.07	6735.4 ± 56.4
TCC-C$_5$	24932± 1374	20.24 ± 0.11	7318.5 ± 220.0

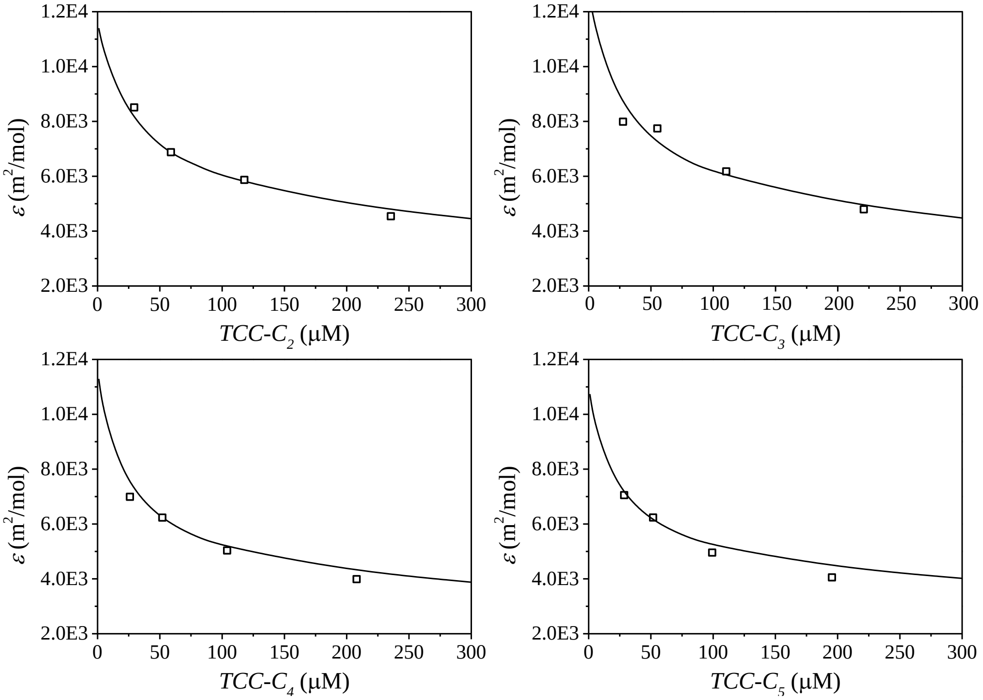

Figure 4.61. Theoretical absorption coefficients for **TCC** dyes (calculated using the dimer model)at 555 nm as a function of dye concentration. The squares are the experimental points.

To get further insight into the effect of aggregation on the optical properties, fluorescence spectra of **TCC-C$_{2–5}$** were also collected. The spectra of **TCC-C$_{2\text{-}5}$** at 0.0002 wt% features one band at 567 nm and a shoulder around 610 nm (Figure 4.62). The main, most intense band is ascribed to monomer emission. The monomer bands shift to longer wavelengths with increasing concentration. There is also a small red-shift in the maxima with increasing dye concentration. The plots of maximum fluorescence intensity against dye concentration (Figure 4.63) show that the most intense fluorescence can be achieved at ca. 25 μM; further increase in concentration produces aggregation-induced quenching. This again can be explained by the exciton theory (see subsection 1.3.1); the loss in fluorescence intensity as the concentration is increased is indication of the formation of face-to-face stacked dimer aggregates (the so called H-aggregates).

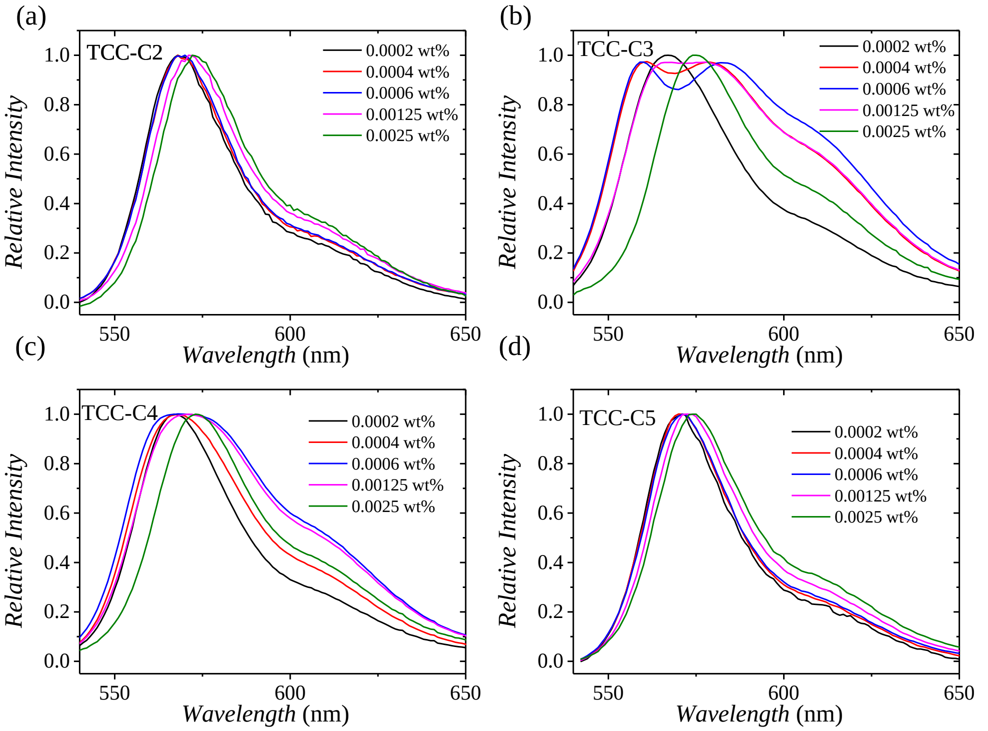

Figure 4.62. Concentration-dependent fluorescence spectra of **TCC-C$_2$** (a), **TCC-C$_3$** (b), **TCC-C$_4$** (c) and **TCC-C$_5$** in water at room temperature (λ_{ext}=535 nm). The signals have been normalized to 1.

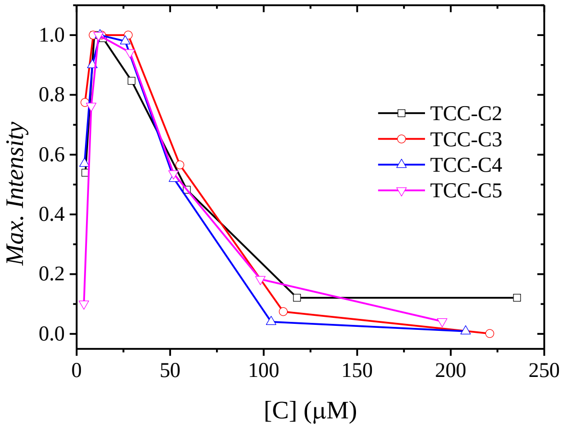

Figure 4.63. Maximum fluorescence intensity vs dye concentration, [C].

Figure 4.64 shows **POM** micrographs of water contact experiments of the four water/cyanine dyes systems. **TCC-C$_2$** and **TCC-C$_3$** show transformation from **N** to **M** phases with increasing concentration. This sequence is in agreement with the one described by Lydon.[26] Only an **N** phase could be observed for **TCC-C$_4$**. **TCC-C$_5$** did not show evidence of liquid crystal formation upon contact with water. The **N** phase for **TCC-C$_{2\text{-}4}$** exhibits schlieren texture characteristic of chromonic nematic phases, while the textures of the hexagonal or **M** phase of **TCC-C$_{2\text{-}3}$** shows a grainy texture.

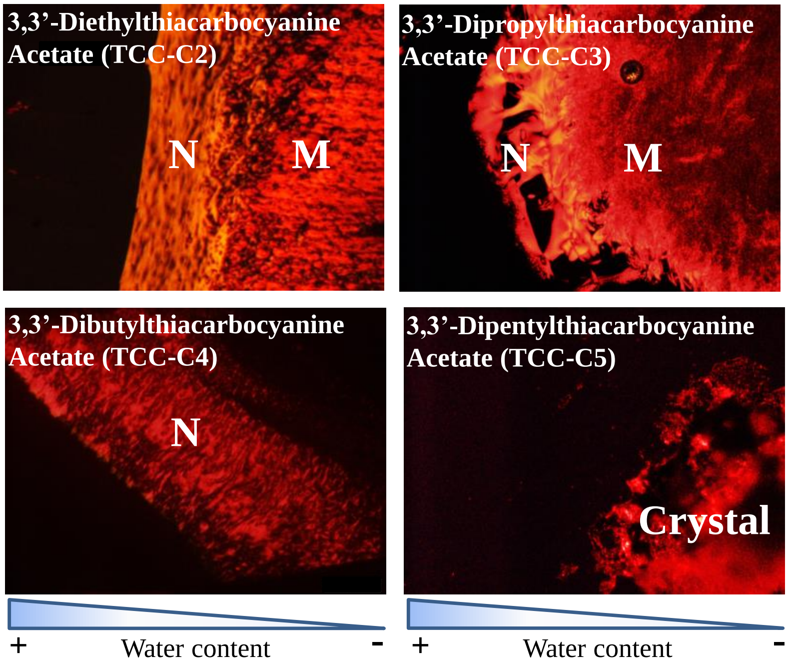

Figure 4.64. **POM** images of water contact experiments for **TCC-C$_{2\text{-}5}$**. **N** and **M** denote nematic and hexagonal phase respectively.

TCC-C$_2$ formed liquid crystals at concentrations as low as 1 wt%. **SAXS** of a more concentrated sample (4.5 wt% of **TCC-C$_2$** in Figure 4.65a) shows a peak at q_1 = 0.063 Å^{-1}. A weak reflection seen as an inflection appears at q_2 = 0.110 Å^{-1}. The q_1/q_2 ratio is ca. 1.7, corresponding approximately to a hexagonal arrangement; higher order reflections are not resolved. In a hexagonal arrangement of hollow cylinders, the radius can be calculated as:

$$R = \left(R_0 + \frac{2\phi d^2}{\pi\sqrt{3}} \right)^{1/2}$$

Equation 4.4

Where ϕ, d *and* R_o are the volume fraction, the Braggs distance calculated from the first refraction peak respectively and inner radio. Accordingly, for **TCC-C$_2$** at 4.5 wt% we obtain R=25 Å. A core-shell cylinder model only fitted well the SAXS pattern of a 1 wt% solution for q>0.25 Å^{-1} (see Figure 4.65b). This fitting resulted in a radius, r_{ext}, of 26.1 Å and a fixed shell thickness of 3 Å. This thickness is similar to the width of the quinaldine moiety.

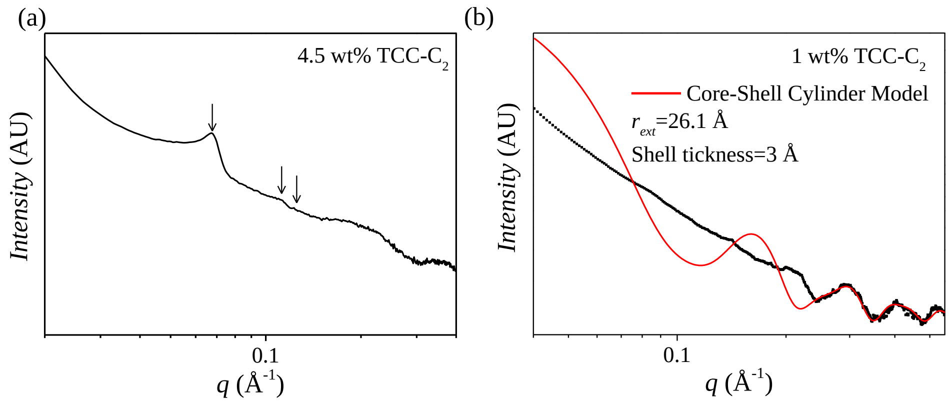

Figure 4.65. (a) **SAXS** curve for **TCC-C$_2$** at 4.5 wt% in water and (b) 1 wt% in water with the corresponding core-shell cylinder model. The arrows indicate the peak positions $(1:\sqrt{3}:\sqrt{4})$ corresponding to a hexagonal lattice

Considering that a single **TCC-C$_2$** has a molecular length of 17 Å, then, **SAXS** results give evidence of hollow aggregates with multimolecular cross section. Considering our model presented in Figure 4.66, around 9 molecules would be in the cross section.

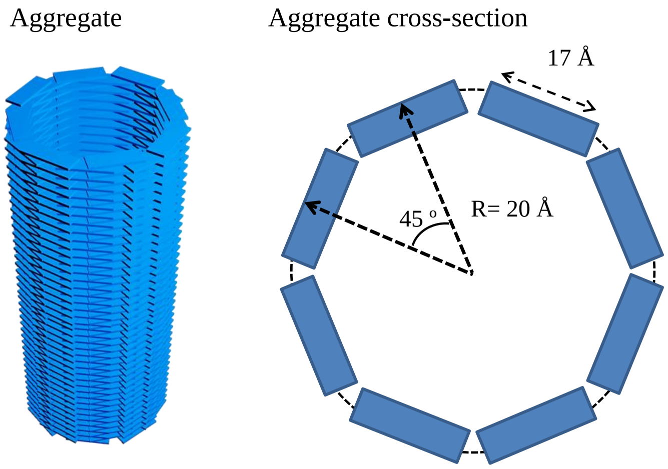

Figure 4.66. Schematic representation of our model for **TCC-C$_2$** aggregates.

In the present case it can be inferred by **UV-Vis** measurements that the intermolecular interactions increase as follow: **TCC-C$_2$**<**TCC-C$_3$**<**TCC-C$_4$**<**TCC-C$_5$**. As the only parameter changed in these molecules is the N-alkyl chain length, it seems reasonable that the gradual increase in intermolecular interactions is due to increase of the hydrophobic forces between the hydrocarbonated chains. **TCC-C$_5$** does not form liquid crystals, probably because its solubility in water is not enough to reach the critical concentration needed for structuration.

4.2.3.2. **Oxacarbocyanines (OXA)**

The self-assembly of the acetate salts of oxacarbocyanines containing 3 (**OXA-3C**) and 5 carbon (**OXA-5C**) atoms in the polymethine spacer chain (Figure 4.67) was investigated.

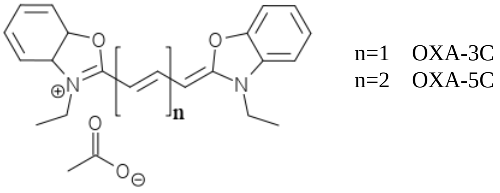

Figure 4.67. Molecular structure of Oxacarbocyanines.

The self-assembly of the **OXA** series in water was first studied by **UV-Vis** absorption spectroscopy (Figure 4.68). In contrast with the **TCC** series, the spectra of the **OXA** series did not change with concentration, showing lack of metachromasia (orthochromatic behavior). Their respective spectra are similar to those reported for the respective iodide dyes in **EtOH** with a band and a shoulder maxima located at 480 nm and 450 nm for **OXA-3C** (Figure 4.68a) and 576 nm and 530 nm for **OXA-5C** (Figure 4.68b).[170, 171] It is noteworthy that the absorption coefficient, ε, is reduced 30 % for **OXA-3C** and 80 % for **OXA-5C** (hypochromic effect) compared to those spectra in **EtOH**. Thus, it could be possible that the apparent lack of metachromasia is not because they are truly orthochromatic but because they are already fully aggregated in aqueous solution and the dimer spectra is similar to the monomer but with lower absorption coefficient. The spectra of these dyes would not be from single molecules but from an association of them. This ‘‘Apparent orthochromatic’’ behavior has been observed in other dye molecules such as Alcian Blue.[172] If we consider the exciton theory, explained in subsection 1.3.1, no exciton splitting occurs for the stacking angle of $\theta = 54.7$ º. This stacking configuration implies that the dimer’s **UV-Vis** spectrum is similar to the monomeric ones. It could be possible then that the oxacarbocyanines are stacked in two possible configurations depicted in Figure 4.69.

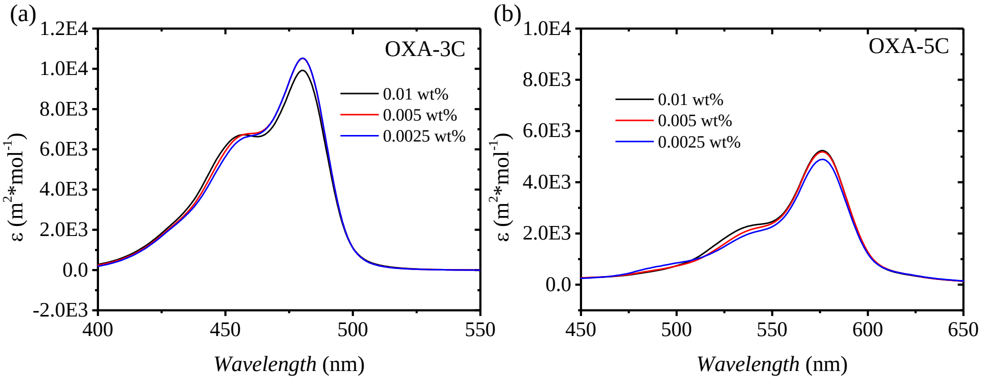

Figure 4.68. Absorption spectra at room temperature of (a) **OXA-3C** and (b) **OXA-5C** in water at different weight percentage.

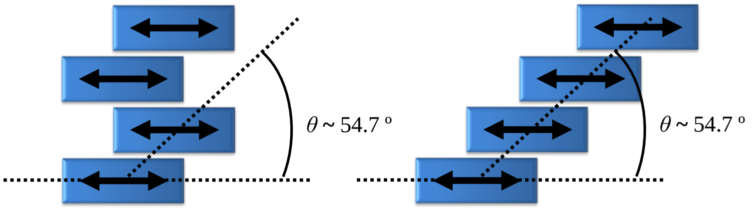

Figure 4.69. Schematic representation of two possible stacking of **OXA-3C** and **OXA- 5C** in water. The arrows represent the possible dipolar moments.

Fluorescence spectra of **OXA-3C** and **OXA-5C** were also collected (Figure 4.71). The fluorescence spectra of **OXA-3C** features one band at 500 nm and a shoulder around 525 nm (Figure 4.70a). **OXA-5C** spectra shows one band at 600 nm and a small shoulder at 630 (Figure 4.70b). In both cases there is a small red-shift in the maxima with increasing dye concentration. The plots of maximum fluorescence intensity against dye concentration (Figure 4.70c), show that the most intense fluorescence can be achieved at ca. 10 µM and 60 µM for **OXA-3C** and **OXA-5C** respectively; further increase in concentration produces aggregation-induced quenching. Similar to the **TCC** series, the loss in fluorescence intensity as the concentration is increased is indication of the formation of H-aggregates.

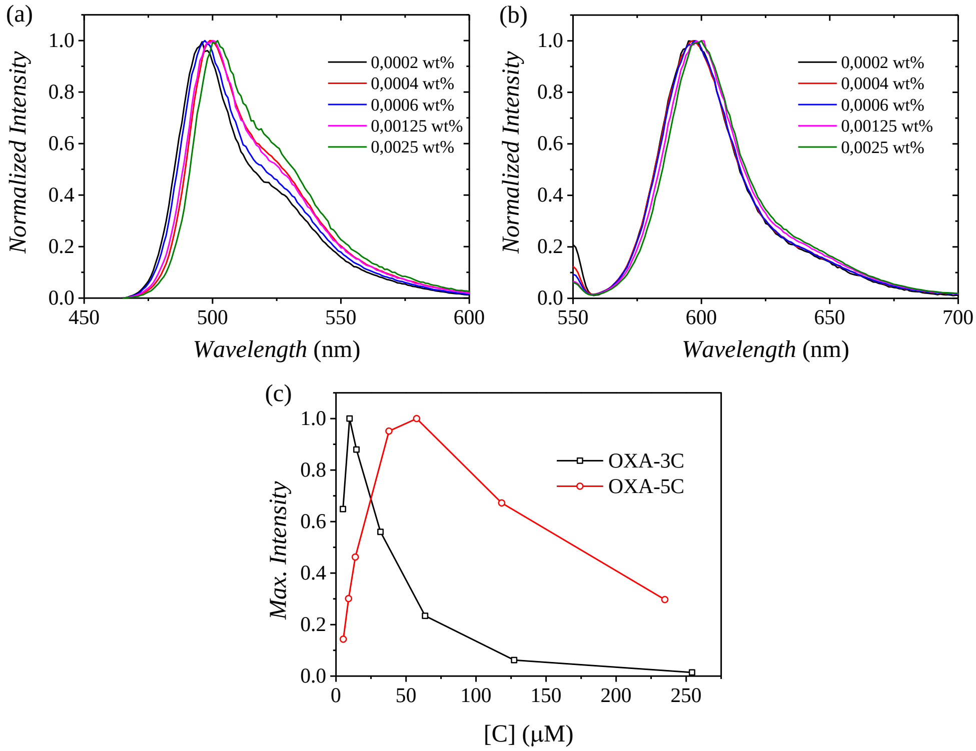

Figure 4.70.Concentration-dependent fluorescence spectra of (a) **OXA-3C** (λ_{ext}=460 nm) and (b) **OXA-5C** (λ_{ext}=550 nm) in water at room temperature. The signals have been normalized to 1. (c) Maximum intensity vs dye concentration, [C].

Figure 4.71 shows water contact experiments under **POM** of both oxacyanines. **OXA-3C** does not form liquid crystals. Samples containing up to 30 wt% of **OXA-3C** (maximum solubility) did not show birefringence or change in viscosity. Since **OXA-3C** does not form liquid crystals at low concentrations it is possible that the aggregates have unimolecular cross section (smaller effective volume). **OXA-5C** water contact experiment showed a schlieren texture that is characteristic of chromonic **N** liquid crystalline phases. More concentrated samples of **OXA-5C** could not be prepared because the solution rapidly precipitated due to the poor chemical stability of **OXA-5C** against nucleophiles, such as water. In fact cyanine dyes can get hydrolyzed in aqueous media (Figure 4.72). The hydrolysis is enhanced by the oxygen atom, since it subtracts electron density to itself, leaving the carbon atom (*) deficient in charge. Although no confirmed it is likely that **OXA-5C** forms multimolecular cross-section aggregates in aqueous solutions.

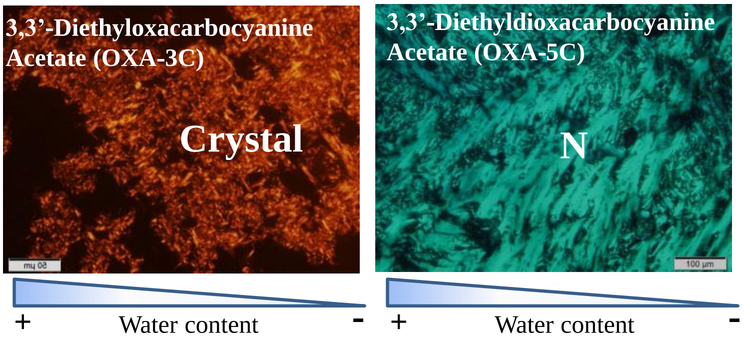

Figure 4.71.**POM** images of water contact experiments for **OXA-3C** and **OXA-5C**. **N** denote nematic phase.

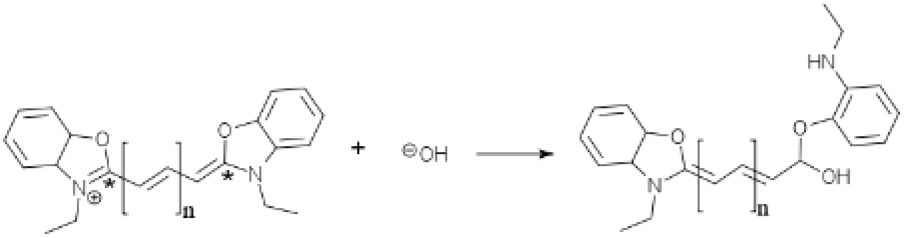

Figure 4.72. Oxacarbocyanines hydrolysis reaction that would take place in aqueous media.

4.2.3.3. **Pinacyanol Acetate (PiC)**

The chromonic self-assembly behavior of carbocyanines having 1 and 3 carbon atoms in the polymethine spacer (3-3' diethylcarbocyanine and 3-3' diethylisocyanine respectively) has already been reported.[39, 169, 173] In this work, the qualitative phase behavior and self-assembly was studied to compare with the other dyes previously described. **PiC** molecular structure is shown in Figure 4.73.

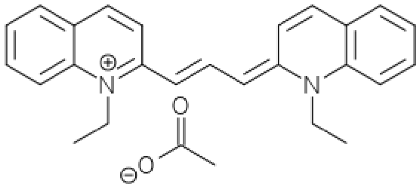

Figure 4.73. Molecular structure of **PiC**.

UV-Vis of **PiC** (Figure 4.74) shows a hypsochromic behavior that is characteristic of the formation of H-aggregates. At low concentrations (below 0.000675 wt) two bands appear, one at 600 nm, which can be ascribed to monomers, and other at ~550 nm which is caused by dimers. As the concentration is increased a third band appears at ~520 nm which is assigned to aggregates with a higher aggregation number.

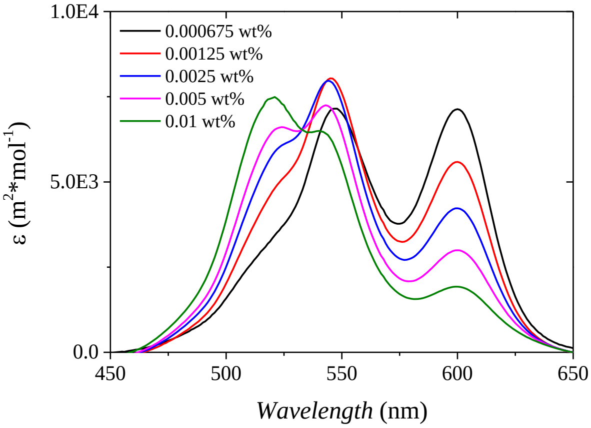

Figure 4.74.Absorption spectra at room temperature of **PiC** acetate at different weight percentage.

Water contact experiment observed in **POM** at room temperature (Figure 4.75) clearly shows the presence of two mesophases phases. At high water contents (left of Figure 4.75), a nematic, **N**, phase is found as inferred by the characteristic schlieren texture. As the water content is reduced, there is a sharp transition to a hexagonal, **M** phase.

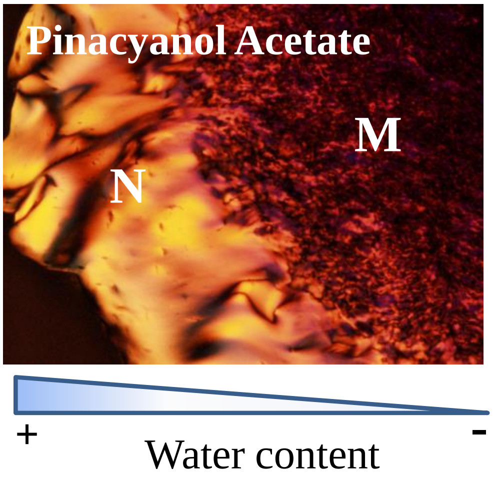

Figure 4.75. **POM** images of water contact experiments for **PiC**. **N** denote nematic phase.

SAXS was performed in selected samples of **PiC** in water at 25 ºC to obtain information of the structure of the mesophases and aggregates (Figure 4.76). Samples at concentrations up to 3 wt% showed only a broad band at low *q*'s which is ascribed to a nematic, **N** phase. This is in agreement with the schlieren texture observed in the water contact experiment Figure 4.75. A more concentrated sample (i.e. 5 wt%) showed two peaks in the ratio $1:\sqrt{3}$ that are characteristic of a hexagonal lattice (**M** phase). All samples studied showed several bands at high q values. These bands could be fitted with a core-shell cylinder model of 20 Å of radius and a shell thickness of 3 Å (which is the width of a quinaldine group) (Figure 4.76b). Since the length of a **PiC** molecule is only 17 Å the cylindrical aggregates must have many molecules in the cross section, probably similar to the model presented in Figure 4.66.

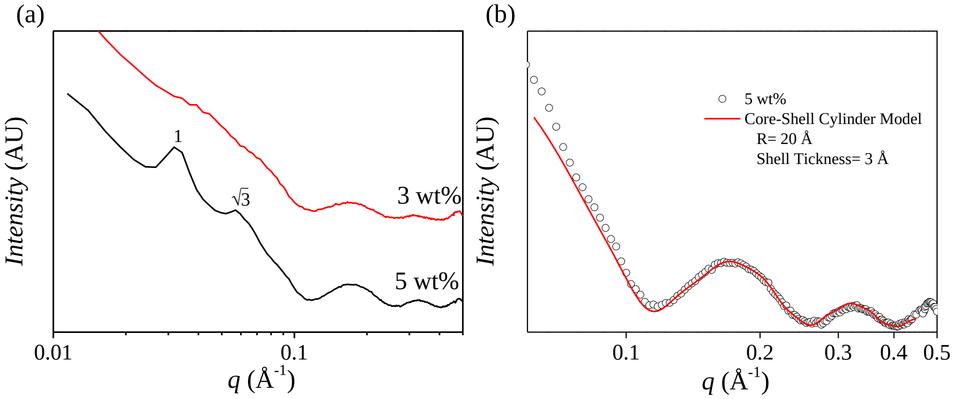

Figure 4.76. (a) **SAXS** curve for **PiC** at 3 wt% and 5 wt% in water and (b) the enlarged high *q* region with a cylinder core shell model plotted.

4.2.4. Self-Assembly of Alcian Blue (AB): Preliminary Results

Alcian Blue is the name of the family of metallorganic and aromatic basic dyes with the general molecular structure show in Figure 4.77.

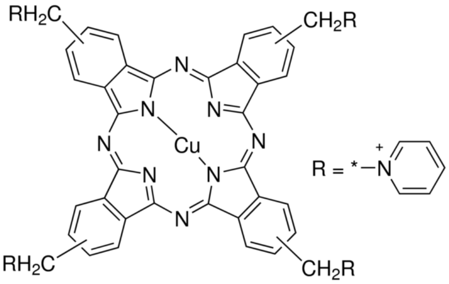

Figure 4.77. Molecular structure of Alcian Blue (tetrakis-methylpyridinium).

AB family of molecules is one of the most common and widely used cationic dyes for staining biological media. **AB** has the advantage that by incorporating it to biological media, the contrast in electron microscopy techniques increases due to the presence of copper. In aqueous solution large numbers of **AB** molecules stack together as aggregates of very large size, too large to be even dialyzed. Thus, even at a fairly high dilution, it has an absorption maximum at ~600–615 nm, which is actually not the absorption maximum of a dye monomer but that of the multimer. Only a very small shoulder of the absorption curve at 670–680 nm represents the monomeric dye, which is usually the minority and becomes even lesser minority ($<10^{-8}$M) in presence of salts. However when the solvent is **DMSO**, a non-protic solvent of moderately high dielectric constant, **AB** does not aggregate and a big monomeric absorption peak can be well visualized.[172] After purification and counterion exchange to acetate or p-toluensulfonate **AB** becomes more water soluble. In this section we describe the preliminary results obtained regarding phase behavior and self-assembly of **AB**.

4.2.4.1. **Alcian Blue chloride (AB-Cl)**

AB-Cl had limited solubility in water (< 5 wt%). The water contact experiment did not show evidence of liquid crystal formation. It has to be considered that **AB** molecules are basic dyes and they are poorly dissociated as the pH of the media is increased. Therefore, acidic solutions were also tested. When **AB-Cl** is put in contact with a 3 wt% aqueous solution of acetic acid, a liquid crystal texture was observed(Figure 4.78).

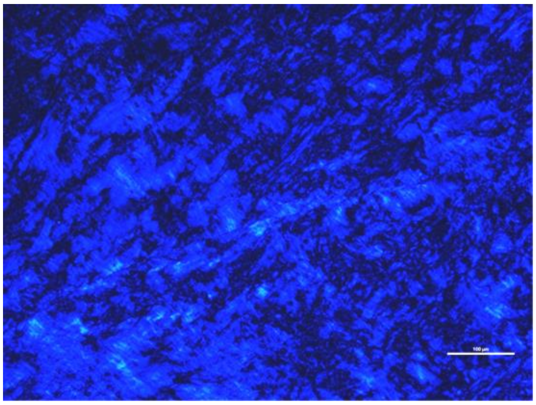

Figure 4.78. **POM** image of the water contact experiment of **AB-Cl** in contact with a 3 wt% solution of acetic acid.

4.2.4.2. **Alcian Blue acetate (AB-Ac)**

The water contact experiment of **AB-Ac** did not show evidence of liquid crystal formation; however, samples with concentrations from 5 wt% to 30 wt% were considerably viscous and isotropic. Samples containing more than ca. 30 wt% of **AB-Ac** showed some birefringence under **POM**. As an example, a sample containing 50 wt% of **AB-Ac** showed some birefringent dots under **POM** (Figure 4.79a) that is not common of any mesophase. A schlieren texture could be observed on the wall of the tube in which the sample was prepared (Figure 4.79b). It could be that a liquid crystalline phase coexists with an organogel. In fact, **SAXS** of this sample (Figure 4.80) showed a small decay with a shoulder at low *q* values; this shoulder could be attributed to a distance between aggregates in a nematic phase. A broad peak was also found at 3.4 Å, which is ascribed to the stacking distance between two **AB** molecules. Note that there are no crystalline peaks in the **WAXS** region. It is likely that **AB-Ac** in water is not completely dissociated and possibly forms a hydrated amorphous gel in coexistence with liquid crystal.

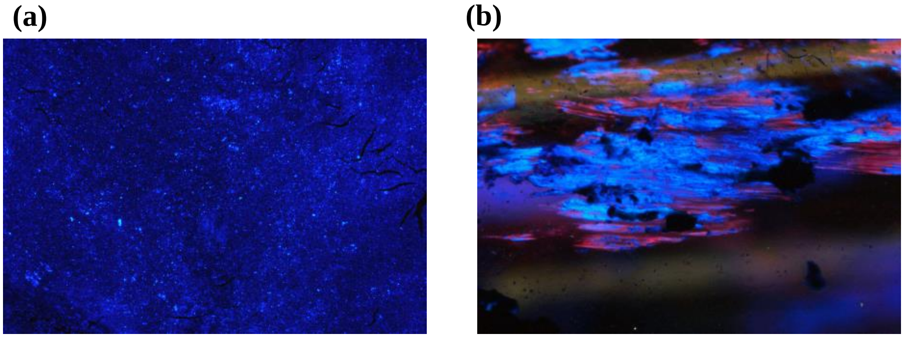

Figure 4.79. **POM** images of a 50 wt% **AB-Ac** sample in (a) between a microscope slide and a slid and (b) on the walls of the tube after centrifugation.

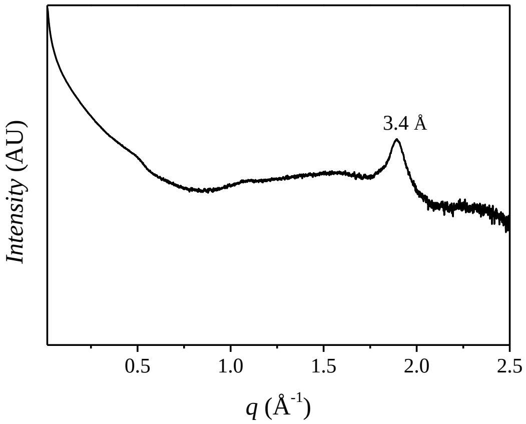

Figure 4.80. **SAXS** pattern of a 50 wt% **AB-Ac** sample at 25 ºC.

4.2.4.3. **Alcian Blue p-toluensulfonate. (AB-Toc)**

In contrast with the respective acetate salt**, AB-Toc** was not soluble in water. All **AB-Toc** samples showed a precipitate (from 90 wt% down to 1 wt% of **AB-Toc**). This precipitate was observed under **POM** (Figure 4.81). The samples showed birefringence after applying some pressure. At low magnification birefringent particles could be observed (Figure 4.81a). Higher magnification (Figure 4.81b) showed a texture that is similar to the one found in concentrated samples of the water/**QR-Ac** system, probably formed by a closely packed arrange of columns.

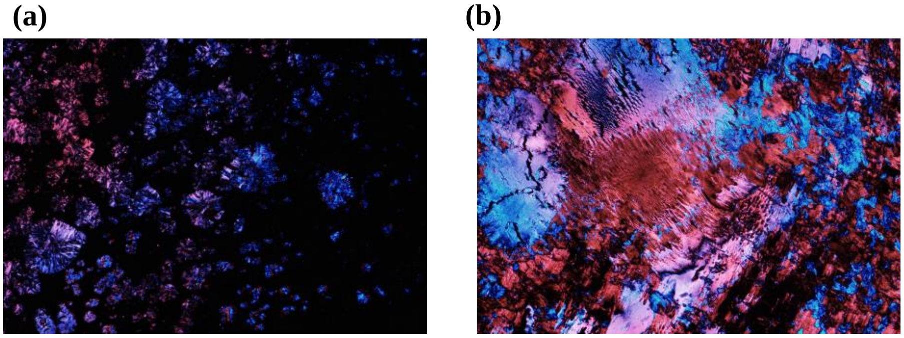

Figure 4.81. **POM** images of a 10 wt% **AB-Toc** sample at (a) low and (b) high magnification.

SAXS measurements were performed on the solid **AB-Toc** and the precipitate of the 10 wt% **AB-Toc** in water (Figure 4.82). The precipitate of the 10 wt% sample showed two peaks in the **SAXS** region with the ratios of $1{:}\sqrt{3}$ ascribed to a hexagonal arrange of cylinders (Figure 4.82a). Only one band was observed in **WAXS** (Figure 4.82b) which was located at q=2.0 Å^{-1} (3.1 Å that is attributed to the stacking distance between two **AB** molecules). The **AB-Toc** dry solid presented a broad band and two peaks with no characteristic peak ratio. The **WAXS** region presented many peaks that are generally caused by the presence of a crystalline solid (Figure 4.82b). The distance between aggregates calculated from the first refraction peak in the pattern of the precipitate of the 10 wt% **AB-Toc** is 23 Å. Considering that the length of a **AB** molecule is 19 Å, then, the aggregates would be poorly hydrated, even at high water content. This means that the structure has already reached their maximum swelling. Although there is a need for be further studies, this could be one of the first evidences of hexosome formation in chromonic systems.

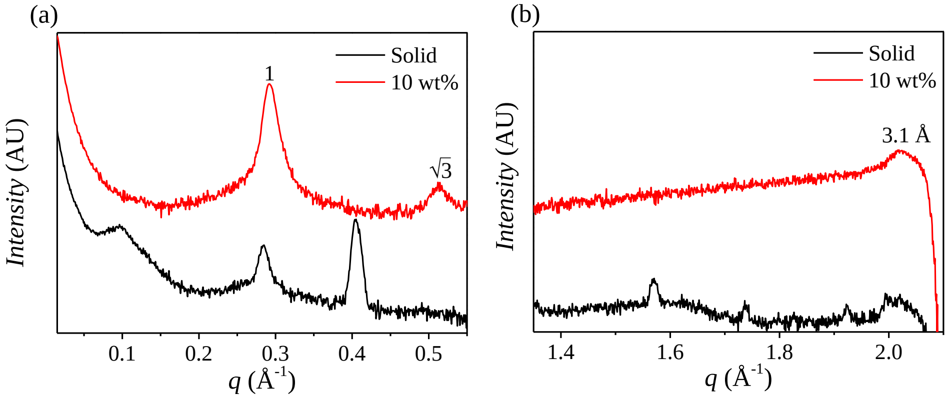

Figure 4.82. (a) **SAXS** and (b) **WAXS** patterns of a 10 wt% sample and a solid at 25 ºC.

4.2.5. Origin of chromonics self-assembly behavior

Chromonic liquid crystals form from the arising interactions between aggregates occurring at high concentrations. When we consider long-range interaction between aggregates, we find that the two most important forces are van der Waals and electrostatic. It is also worth noting that at shorter distances (below 1 to 3 nm) solvation and other types of steric forces may dominate over both. The free energy or interaction, W, between two parallel arranged identical cylinders is:

$$W = \frac{AL}{12\sqrt{2}{D_c}^{3/2}}\left(\frac{A_c}{4\pi}\right)^{1/4}$$

Equation 4.5

Where A, L, D_c and A_c are the Hamaker constant, length of the cylinders, distance between cylinders and cross-sectional area of the cylinders respectively. Typical values for the Hamaker constants of condensed phases, whether solid or liquid, are in the range of $(0.4\text{-}4)*10^{-19}$ J for interactions in vacuum. It is clear that as the length of the cylinders, L, is increased and the distance between aggregates, D_c, is decreased there is an increase in the free energy of interaction, W. We can argue that the formation of chromonic liquid crystals at a certain concentration will then be dominated by two main variables: D_c and L.

- **Distance between aggregates, D_c**

D_c at a constant concentration and temperature would depend on the effective volume of the aggregates, in the present case, the cross sectional area A_c (bigger cross section would mean higher effective volume, therefore the aggregates would be closer together). Comparing the cross-sectional areas of the molecules studied, then **QR-Ac** has bigger cross sectional area than **PyY**, so it is expected that at the same volume fractions, interactions between the aggregates will be stronger for **QR-Ac**. In the present case, this is manifested by the formation of liquid crystal at lower concentrations, in the case of **QR-Ac** (1 M) compared to **PyY** (1.5 M). **TCC** and **PiC** molecules form multimolecular cross section (one order of magnitude bigger than **QR-Ac** or **PyY**) and they form liquid crystals at considerably lower concentration (less than 5 wt%).

- **Length of the aggregates, L**

The length of the aggregates at a certain concentration and temperature would depend on the molecular interactions (more molecular interactions would mean higher degree of aggregation). Similar than in surfactant system, in order to form a liquid crystalline phase the molecular interactions must be equilibrated. Weak interaction energies would lead to a solution of disaggregated and hydrated molecules, while strong interactions would lead to big aggregates that would result in poor solubility. It is only when these interactions are equilibrated that liquid crystals can occur. These interactions can be tuned by changing the molecular structure.

As first observation cosmotropic counter-ions (such as acetate or p-toluensulfonate) increase the solubility of chromonic molecules and are more likely to form liquid crystals than their respective chaotropic iodide analogues. Acetate or p-toluensulfonate anions are more hydrated in solution than iodide. This would result in a weaker interaction between counter-ion and chromonic molecules in the case of acetate or p-toluene sulfonate, consequently, increasing the solubility. The electrostatic interaction between iodide and chromonic molecule would be stronger and lead to a poor solubility.

In the **TCC** series studied it is clear that as the N-alkyl chain is increased then the intermolecular interactions are increased. It seems that the interaction between alkyl chains contributes to the total interaction energy. Water dissociation forces cannot break **TCC-C$_5$** interactions, therefore this dye is less soluble in water.

If we compare **TCC-C$_2$** and **PiC** with **OXA-3C** in which only the heteroatom is changed (sulfur or methylene to oxygen) we find that, while **TCC-C$_2$** and **PiC** forms liquid crystals at low concentrations with a multimolecular cross section, **OXA-3C** is likely to form unimolecular aggregates and does not form liquid crystals at concentration lower than 30 wt%. While the sulfur atom has more or less the same electronegativity than carbon (~2.55) the oxygen is more electronegative (3.44), this would mean that in the case of **OXA-3C** the higher electron density will be located at the proximity of the oxygen rather than equally distributed around the molecule, like in the case of **TCC-C$_2$** or **PiC**. This could cause a more pronounced interaction between the electron rich regions of one molecule with the electron poor of other molecule, as it has been observed in **QR-Ac**. This would favor in this case the formation of unimolecular aggregates.

Increasing the length of the polymethine chain from 3 (**OXA-3C**) to 5 (**OXA-5C**) induces the formation of a liquid crystalline phase. The addition of two more carbons causes the increase in size in the π orbitals since there is more delocalization of electrons. The repulsion between π clouds of two different molecules causes a reduction in the intermolecular interactions, thus, increasing the probability of formation of liquid crystals.

4.2.6. Chromonics as templates for hard materials: Silica and Carbon Nanofibers

4.2.6.1. **Silica (SiO_2) Nanofibers**

As demonstrated in the previous section, **PiC** is a cyanine dye known to form chromonic nematic and hexagonal liquid crystalline phases in water, both formed by an arrange of hollow cylinders. It is reported that when silica precursor, such as **TEOS**, is added to a nematic liquid crystal of **PiC**, hydrolysis and condensation of silica species induces a hexagonal structure while maintaining the fiber-like morphology in the precipitated silica/pinacyanol composites.[39] The schematic representation of this process is shown in Figure 4.83. Experimental evidence suggests that anionic silicate oligomers binds electrostatically to the aggregates cationic surface and neutralize the long-range repulsions between them, leading to condensation into a more ordered intermediate (some sort of hybrid silica/**PiC** hexagonal liquid crystal) during silica polymerization, followed by co-precipitation of the silica/dye composite. However, it is not necessary for a chromonic molecule to be forming a nematic phase in order to produce silica fibers upon addition of **TEOS**. Perylene dyes, which self-assembly in water in unimolecular cylindrical aggregates also can produce nanostructured silica starting from an isotropic solution of the dye in aqueous ammonia.[33] In both cases the molecules were cationic showing that electrostatic interactions between charged silica and cationic molecules are important for this synthesis. Producing silica fibers by a one-pot, wet method is favorable from the occupational health point of view. Moreover, the synthesis of silica fibers using dyes is simple and not very depending on kinetic factors. In only 3 hours of synthesis, nanostructured fibers can be obtained.

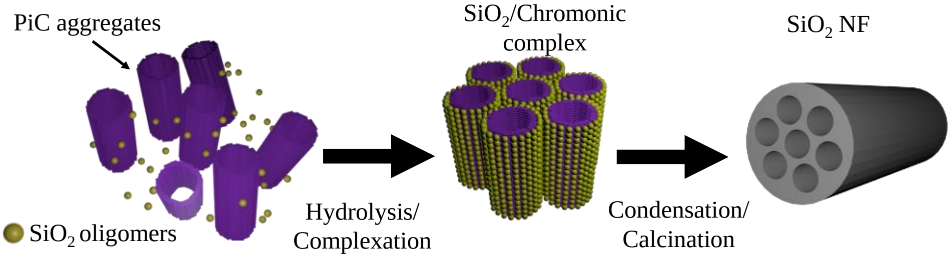

Figure 4.83. Schematic representation of silica nanofibers (**SiO_2NF**) using chromonics as templates.

With the aim of demonstrating a general route for this synthetic approach, we used the self-assemblies of the dyes studied in this thesis to produce silica materials. Silica was prepared following the synthetic procedure explained in subsection 3.3.17. Representative microscopic images of such materials are shown in Figure 4.84. Silica materials synthetized using **TCC-$C_{2\text{-}4}$** showed a fibrous morphology. Samples of mesoporous silica fibers obtained using surfactant templating usually have a considerable fraction of small particles.[174] In our case, samples are morphologically much pure as almost all silica is present in the form of fibers. This can be attributed to the fact that the silica sol-gel reaction takes place by direct templating of long, relatively rigid cylindrical aggregates, in contrast with conventional surfactant templates. **TCC-C$_3$** additionally formed some helicoidally fibers (Figure 4.85). This can be caused by direct templating of J-aggregates. In fact, some thiacyanine are known to form J-aggregates when they are in contact with a surface, such as silica or silver.[175, 176] **TCC-C$_5$** formed some fiber-like particles, nevertheless they were bigger that the ones compared with those prepared with **TCC-C$_{2-4}$**. It seems that **TCC-C$_5$** directly precipitates when mixed with silica oligomers instead of going through the cooperative self-assembly and only the **TCC-C$_5$** solid crystals are templated. Fibers obtained using **OXA-3C** had the same characteristics of **TCC-C$_5$**. In fact, the surface area of calcined **OXA-3C** silica fibers was approximately 30 m^2/g indicating that these fibers are probably non-porous. **OXA-5C** was too unstable in basic media, and after few minutes in aqueous ammonia, a precipitate appeared. Templating of silica with this dye was not successful.

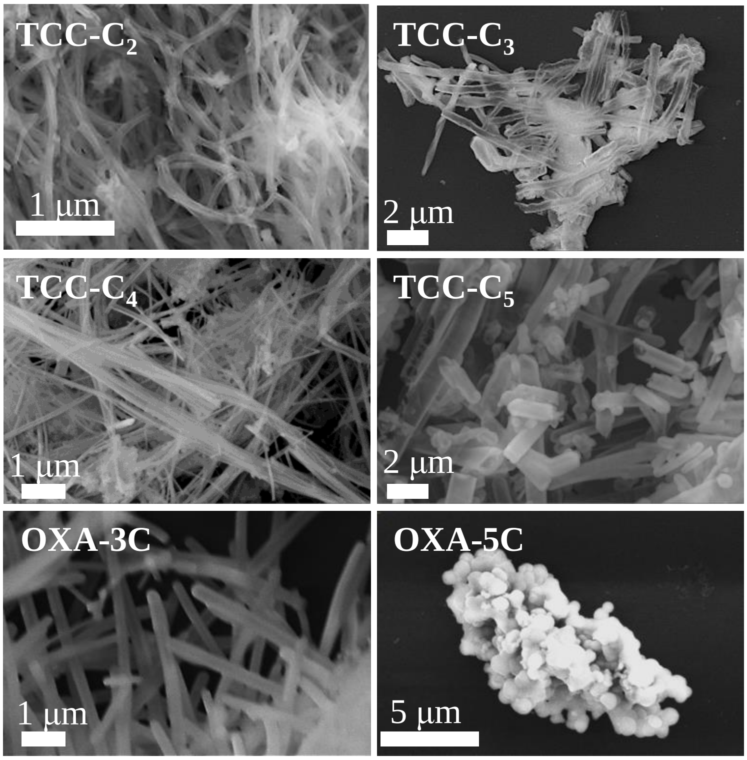

Figure 4.84. **SEM** images of silica nanofibers prepared from carbocyanines.

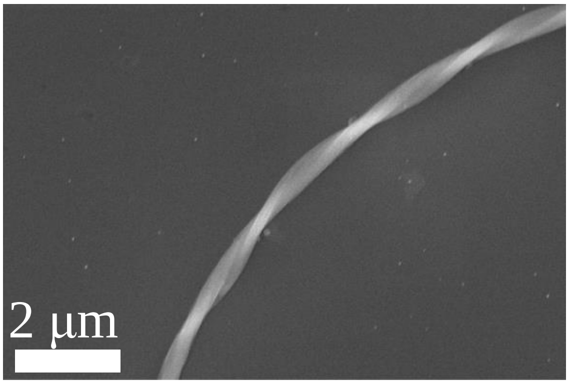

Figure 4.85. **SEM** image of a helicoidal fiber prepared using **TCC-C$_3$.**

Similar to the fibers obtained using **PiC** as template, **TCC-C$_{2\text{-}4}$** showed an inner structure of highly aligned channels that extend up to microns in length, as seen on the **TEM** images on Figure 4.86. **TEM** images of **TCC-C$_2$** showed that the cross-section of fibers is composed by circular pores arranged in a hexagonal fashion (Figure 4.86a-b). The pore diameter derived from the **TEM** images is around 3 nm, with a pore wall of ca. 1 nm. This pore size is in agreement with a multimolecular cross-section of the **TCC-C$_2$** aggregates that serve as silica templates (i.e. the model on Figure 4.66). The formation of aligned cylindrical nanopores with definite walls implies that the silica framework grows around the charged surface of the aggregates as a result of electrostatic interactions, which would be favored in a situation in which the majority of the ionic moieties reside on the outside of the columnar aggregates. This behavior has already been discussed.[44] The present case can also serve as an analytical tool to get insight into the structure of soft templates.

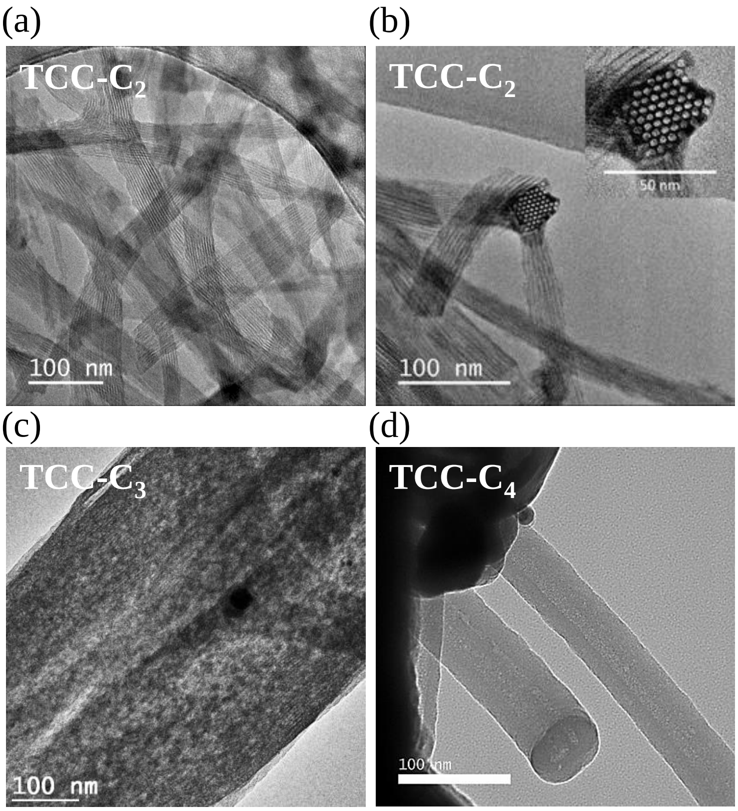

Figure 4.86.**TEM** images of silica nanofibers prepared from (a-b) **TCC-C$_2$**, (c) **TCC-C$_3$** and (d) **TCC-C$_4$.**

These fibers could also be obtained in the form of monoliths with different geometries. For instance, films (Figure 4.87) formed by nanofibers (Figure 4.87c) could be produced in one step (after the synthesis, the monolith is freeze dried and further calcined). Note that there is almost no shrinking after calcining the films. These films presented low density and relatively good mechanical properties. Although their preparation was not studied in detail, they show promising results. These monoliths can be used as supports for sensors or chemical reactions.

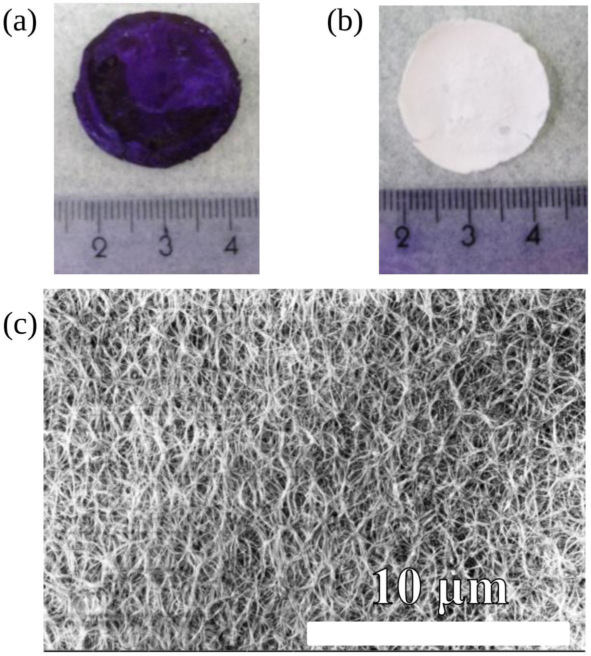

Figure 4.87. Photographs of self-standing films formed by silica nanofibers (a) before and (b) after calcination. A representative **SEM** image of the calcined film is shown in (c).

Moreover, monoliths can be casted into different shapes (Figure 4.88).

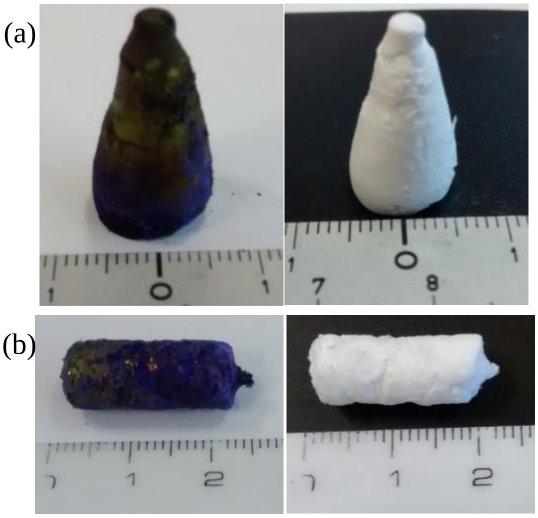

Figure 4.88. Monoliths formed by silica nanofibers, before (left) and after (right) calcination with (a) conic and (b) cylindrical shape.

In contrast with the carbocyanine dyes the other cationic dyes did not template silica fibers. **PyY** was not soluble in basic media. **QR-Ac** and **AB-Ac** were used to template silica but these experiments were not successful. It appears that **QR-Ac** and **AB-Ac** are only encapsulated on the amorphous silica network. Characteristic **SEM** images are shown in Figure 4.89. It is not clear why **QR-Ac** or **AB-Ac** cannot template silica into fibers. The most likely explanation is that these dyes only form liquid crystals at relatively high concentrations, as compared to other dyes reported to template silica fibers such as perylenes or cyanines. Other reason could be that these dyes are not completely dissociated at basic pH solutions in which the silica templating takes place since their pK_a value is too small. It could also be possible that the anionic silica oligomers cannot reduce sufficiently the repulsion between **QR-Ac** or **AB-Ac** aggregates and these would remain far from each other not condensing into a more ordered phase, as is the case of cationic carbocyanine dyes.

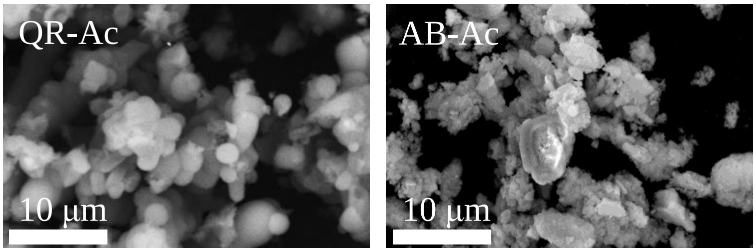

Figure 4.89. Characteristic **SEM** images of silica synthetized using **QR-Ac** and **AB-Ac**.

After calcination, nitrogen absorption/desorption curves for silica synthetized using **AB-Ac** show a type II isotherm that is characteristic of macroporous solid (Figure 4.90a). The surface area is ca. 600 m^2/g and a pore volume of 0.876 cm^3/g. BJH calculations showed a sharp pore size distribution located at 3.7 nm (Figure 4.90b) which is consistent with the approximate molecular length of one **AB** molecule, confirming that **AB-Ac** is successfully encapsulated on the silica framework.

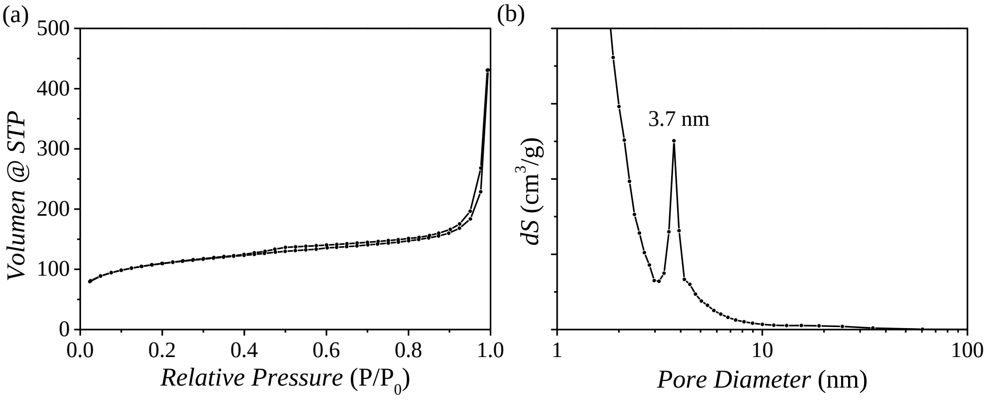

Figure 4.90. (a) Absorption/desorption isotherm and (b) the respective BJH pore size distribution for calcined silica prepared using **AB-Ac**.

Additionally, if the material is pyrolized under inert atmosphere (i.e. N_2 or Ar) a composite of metallic cupper encapsulated in carbon and silica can be obtained, as inferred from **XRD** measurements in Figure 4.91. This carbon/copper composite could be of interest in preparing heat sinks for high thermal conductivity applications.[177]

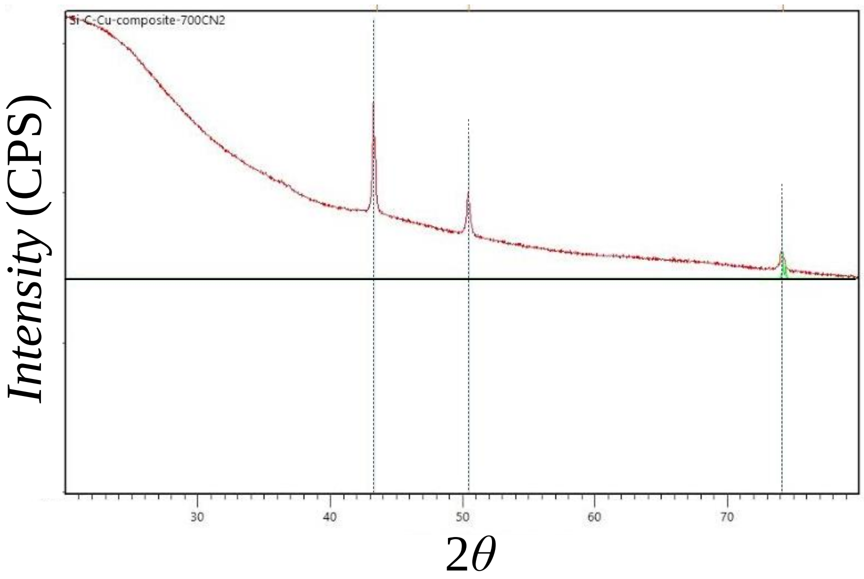

Figure 4.91. **XRD** of the carbonized **AB**/Silica composite under N_2 atmosphere. The lines indicate the face-centered-cubic (fcc) peak position of metallic copper.

In all cases the capacity of these dyes to direct silica growth seems to be related to their dissociation in basic media.

4.2.6.2. **Carbon Nanofibers**

Recently, considerable efforts have been devoted to the fabrication of porous carbon materials by using ordered mesoporous inorganic solids as templates.[132, 178-185] The templating method is a powerful approach to synthesize mesoporous carbon materials with tunable pore sizes and large specific surface areas. Silica provides an ideal template for carbon since its pore distribution and surface area can be finely tuned. Micro- and mesoporous carbons with high surface areas and controlled pore sizes can be obtained by embedding and carbonizing precursors in the silica nanochannels followed by removal of the silica by chemical etching (Figure 4.92). However, particle morphology is difficult to control using this approach since the most commonly used mesoporous silica templates do not usually have a well-defined particle shape. In the subsection 4.2.6.1, it was described how nanostructured mesoporous silica fibers with nanochannels growing along the fibers' long axis can be obtained using cationic chromonic molecules as templates.

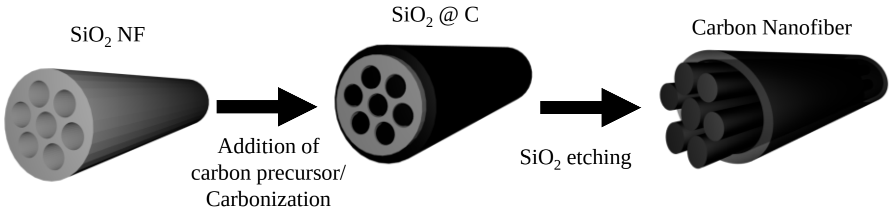

Figure 4.92. Schematic representation of carbon nanofiber synthesis using silica nanofibers as templates.

The synthesis of silica nanofibers (**SiO₂NF**) was scaled up using **PiC** as template (see subsection 3.3.17). The properties of the obtained fibers were similar to those reported in [39]. **SiO₂NF** have a width of around 50 nm and are several micrometers long (Figure 4.93a). Ultra-microtome cuts under **TEM** of these fibers in an epoxy resin (prepared as explained in subsection 3.3.16) reveal that these fibers are hollow (Figure 4.93b).

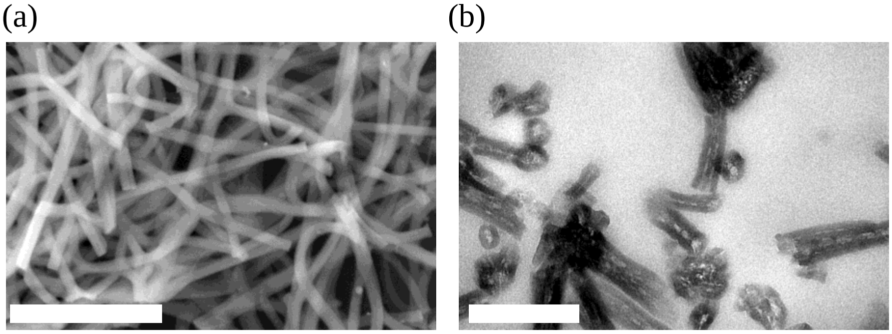

Figure 4.93. (a) **SEM** image of SiO_2NF and (b) **TEM** image of ultra-microtome cuts of **SiO_2NF** in epoxy resin. The scale bar is 200 nm.

Hexagonal arrangement of pores can be inferred by **SAXS** (Figure 4.94a), presenting two bands with the relative positions of $1:\sqrt{3}$. The distance between pores (calculated from the first peak on **SAXS** pattern using Equation 3.2) is 4.8 nm. Calcined **SiO_2NF** have a **BET** surface area of 230 m^2/g, a pore volume of 0.7 cm^3/g and an average pore size of ~3.4 nm (Figure 4.94b). The wall thickness, calculated as the difference between the pore size and distance between pores, is 1.4 nm.

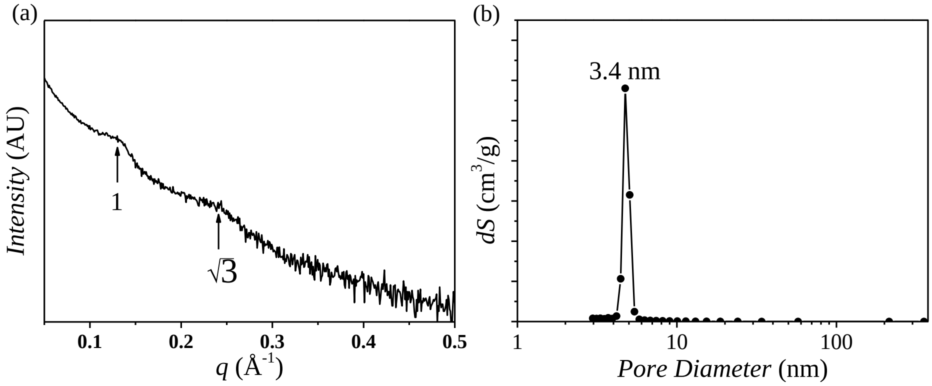

Figure 4.94.(a) SAXS patterns and (b) BJH pore size distribution for calcined **SiO_2NF** prepared using **PiC**.

Carbon nanofibers (**CNF-PiC**) were synthetized following the procedure described in subsection 3.3.18. Closer inspection shows that the fiber cross section is deformed (Figure 4.94a). Ultra-microtome films observed by **TEM** showed evidence that the carbon fibers are hollow, similar to their original **SiO_2NF** templates, but with thinner walls (ca. 7 nm, Figure 4.95b).

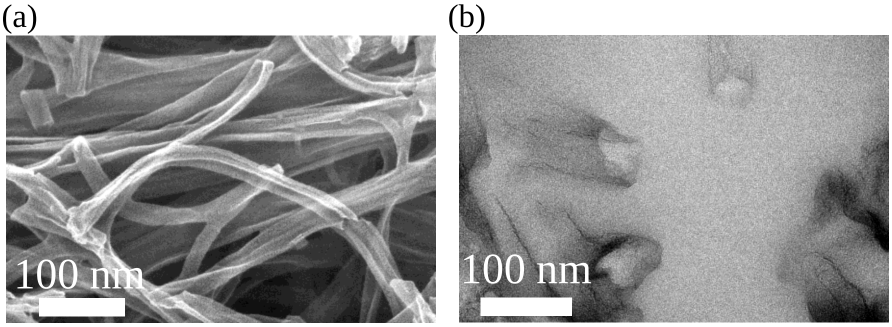

Figure 4.95. (a) **SEM** image of **CNF-PiC** and (b) **TEM** image of ultra-microtome cuts of **CNF-PiC** in epoxy resin.

The ordered nano-structure of the original template was lost, as inferred by the lack of peaks in the **SAXS** pattern. The loss of ordering of the pores may be attributed to the lack of pore interconnections in the silica template, which prevents the formation of carbon bridges that may serve as structural supports. This phenomenon has been observed in other templated carbons such as MCM-41.[179] Similar to **SiO_2NF** the adsorption/desorption isotherm (shown in Figure 4.96) of CNFs present a type II curve, characteristic of macroporous solids. The hysteresis is caused by nanometric pores. In **CNF-PiC** the surface BET area increased to 830 m^2/g and pore volume augmented to 2.7 cc/g compared to the original silica templates. The pore size distribution of **CNF-PiC** was sharp with a maximum at 3.8 nm (inset Figure 4.96), more than twice the **SiO_2NF** wall thickness; another peak appears with a maximum located at 1 nm, which can be caused by micropores. This difference demonstrates that a structural transformation of the carbon frameworks takes place upon removal of the silica wall, which can be attributed to strain in the carbon frameworks formed inside the silica pores.[182]

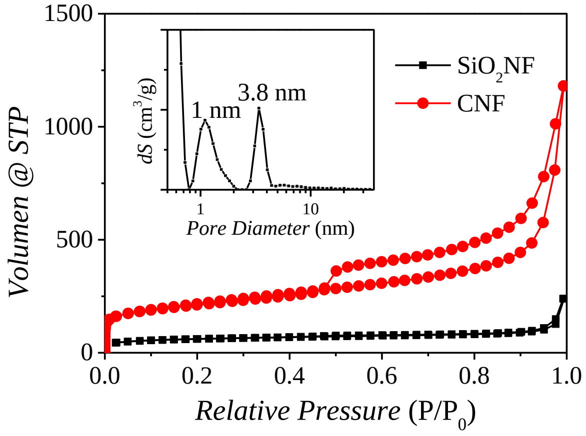

Figure 4.96. N_2 absorption/desorption isotherm for **SiO2NF** and their templated carbon nanofibers (**CNF-PiC**). The inset shows the DFT pore size distribution of **CNF**.

Investigations on the pyrolysis of carbon-rich precursors in carbonaceous particles have demonstrated the fact that there is a close relation between the starting precursor material and the product.[186] When using furfuryl alcohol as precursor, a high ratio of sp2 carbon is expected. This could increase the carbon conductivity which could be of interest in energy related applications. However, carbon obtained at relatively low temperatures usually gives disordered graphite layers and, therefore, poor conductivity. Furthermore, they are also thermally less stable compared to samples heat-treated at higher temperatures. The graphitization process comprises the ordering and stacking of graphite layers, which can be achieved by high-temperature heat treatment. Therefore, **CNF-PiC** were treated at 1100 ºC, 1500 ºC, 1800 ºC and 2000 ºC to obtain samples **CNF-1100**, **CNF-1500**, **CNF-1800** and **CNF-2000**, respectively. **SEM** (Figure 4.97) and **HR-TEM** (Figure 4.98) imaging techniques were used to determine the surface morphology and structure of the heat-treated **CNFs**. **CNF** morphology was preserved regardless of treatment temperature as inferred by **SEM** observations (Figure 4.97) being similar to those in Figure 4.95a.

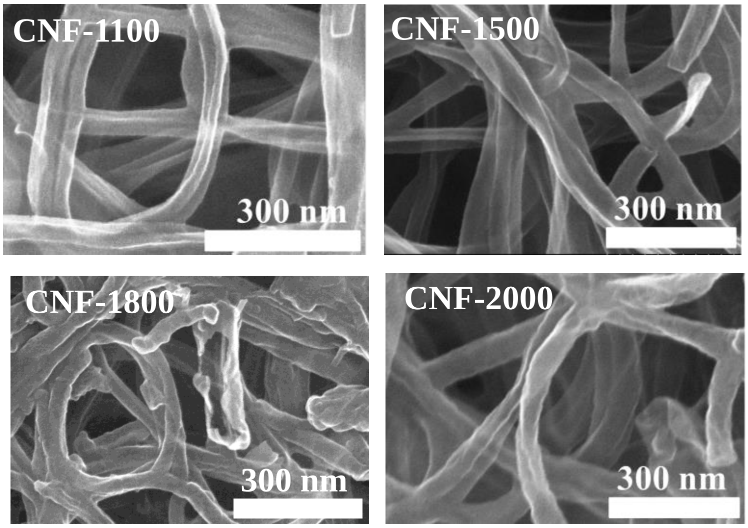

Figure 4.97. **SEM** images of **CNFs** after heat treatment.

HR-TEM imaging (Figure 4.98) of **CNF-PiC** shows randomly oriented graphite layers, while **CNF-2000** shows stacking of graphite layers (up to 7 sheets). As the temperature is increased there is a gradual ordering of the graphite layers. This shows that graphitization was achieved by the heat treatment.

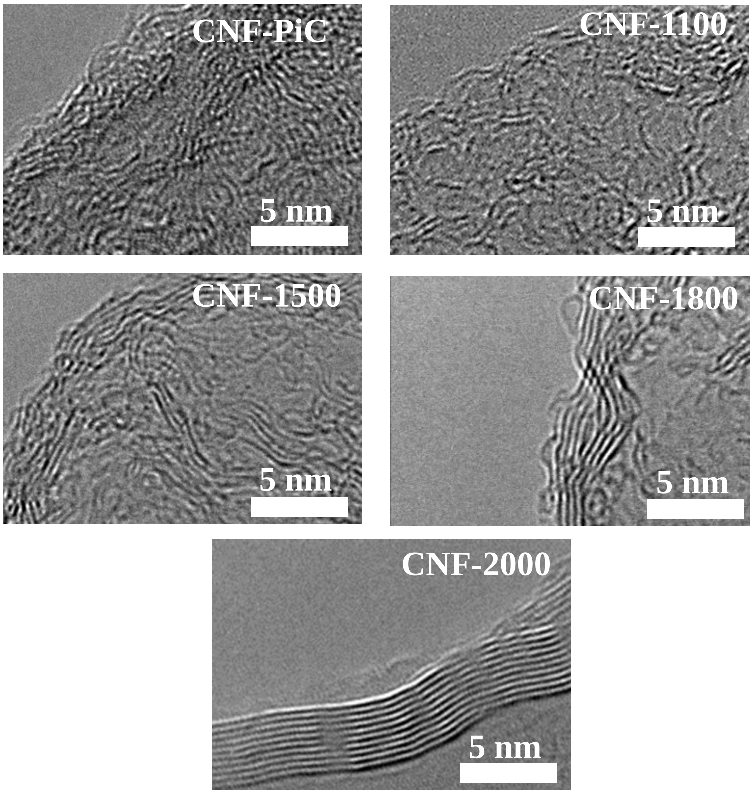

Figure 4.98. **HR-TEM** images of **CNFs** before and after heat treatment.

Powder X-ray diffraction and Raman scattering were used to investigate the evolution of the crystalline nature of **CNFs**. **XRD** of **CNFs** treated at temperatures lower than 2000 ºC shows two broad peaks that can be ascribed to disordered graphite (Figure 4.99a). In contrast to the fibers treated at lower temperatures, **CNF-2000** shows a sharp peak at 2θ ~ 26º (0.344 nm) that is indexed to the (002) crystalline plane (interlaying spacing between graphite sheets).

Raman scattering spectra from all the samples show two Raman bands at 1335 cm-1 and 1582 cm-1 corresponding to D and G bands of carbon materials (Figure 4.99b). The D band (also called defect-induced band) is ascribed to the existence of disordered carbon in the studied samples, while the G band is attributed to the stretching vibration mode of a graphitic structure. After heat treatment at temperatures higher than 1800 ºC, an additional Raman band (2D band) appears in the higher Raman frequency region indicating the formation of crystalline graphite.

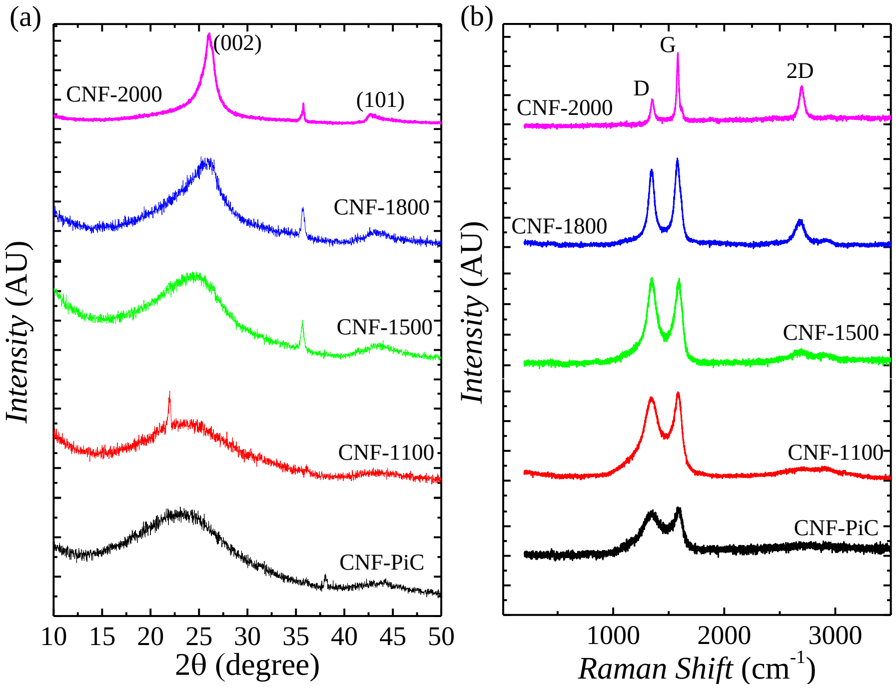

Figure 4.99. (a) **XRD** pattern and (b) Raman Spectra of **CNF** heat-treated at different temperatures. The asterisk-marked **XRD** peaks might be attributed to residual **SiO_2**.

Since graphitization increases the lattice order and produces smaller layer distances, it simultaneously leads to a considerable growth of ordered domains. These reduced lattice layer distances are macroscopically noted as a contraction in volume. This graphitization-shrinkage is approximately 3 to 5%.[187] Due to this shrinkage, density of the graphite increases. However, this shrinkage process depends on the structure and graphitization degree of the initial carbon. BET surface area of **CNFs** slightly increased with the heat treatment at 1100 °C from 826 m^2/g to 847 m^2/g (Table 4.13) but as the treatment temperature is increased, pores are disrupted, and the specific surface area is therefore reduced considerably. The pore size, calculated from DFT simulations, was 3.8 nm in diameter and remained unchanged after the heat treatment.

Table 4.13. Surface Area and Pore volume for **CNFs** treated at different temperatures.

Sample	BET Area (m^2/g)	Total Pore volume (cc/g)
CNF-PiC	826	2.7
CNF-1100	847	2.8
CNF-1500	580	2.7
CNF-1800	255	2.7
CNF-2000	271	2.3

XPS spectra of **CNFs** reveal the presence of C 1s and O 1s core level peaks (Figure 4.100a). Minute observation reveals that the O 1s **XPS** peak intensity of **CNF-1000**, **CNF-1500** and **CNF-2000** is lower compared to **CNF-PiC**. This demonstrates that oxygen functional groups disappear after the high temperature treatment. In fact, the relative intensities of the peaks are proportional to the amount of chemical groups on the carbon. Considering this, the oxygen content is estimated to be 4.7% for **CNF-PiC**, 3.0% for **CNF-1100**, 2.2% for **CNF-1500** and 0.2% for **CNF-2000**, respectively. As an example, on the C 1s and O 1s core levels were deconvoluted to obtain information about the chemical groups present on the surface of the carbon in **CNF-PiC**. The four deconvoluted peaks of the carbon 1s core level (Figure 4.100b) at 284.4, 285.5, 288.0 and 290.0 eV correspond to sp^2 carbon, sp^3 carbon, C=O and π–π shake up, respectively. Closer inspection on the oxygen core level (Figure 4.100c) reveals the presence of C=O (ca. 531 eV) and OH (536 eV) groups on the surface of the carbon.

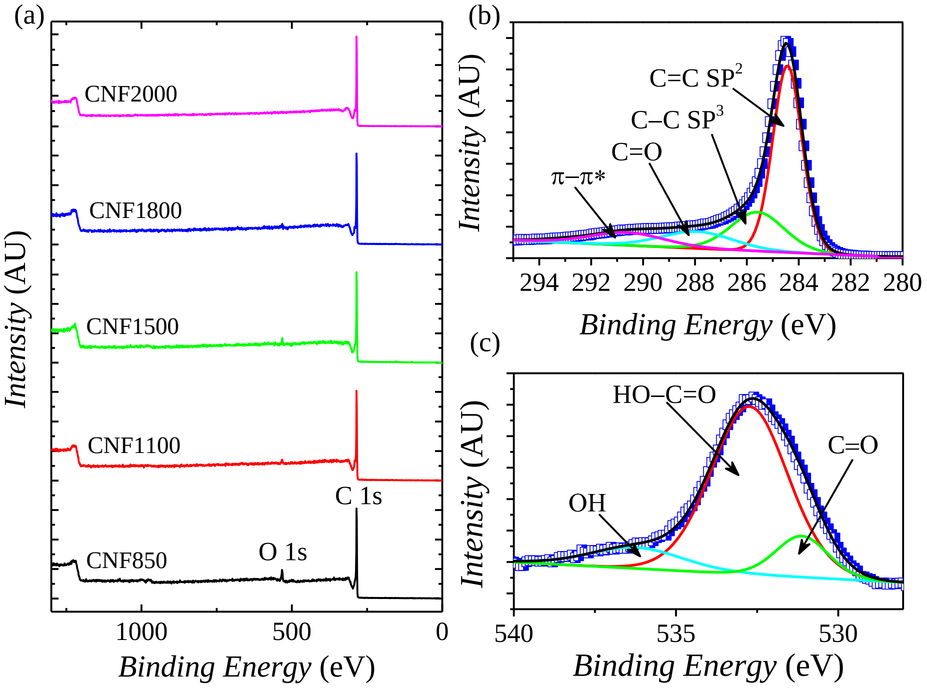

Figure 4.100.(a) **XPS** survey spectra of **CNFs**, (b) **XPS** C 1s core level spectrum with deconvoluted peaks of **CNF-1100** as representative example, and (c) the corresponding **XPS** O 1s core level spectrum with deconvoluted peaks.

- **Carbon Nanofiber Supercapacitor Behavior: Energy Storage on the Carbon Surface**

Electrochemical testing was carried out to study the supercapacitance performance of the **CNFs**. Cyclic voltammetry (**CV**) curves obtained for all samples exhibit approximately rectangular profile. As an example, **CV** curves at a scan rate of 50 mV/s is presented in Figure 4.101 for the different **CNF** samples. A rectangular **CV** curve corresponds to the ideal response for pure electrical double layer supercapacitors (low internal resistance).

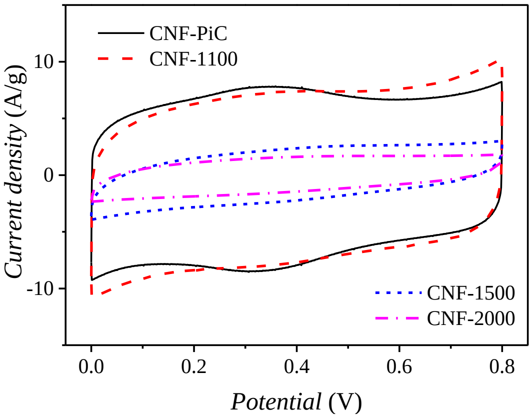

Figure 4.101. **CV** curves of **CNFs** at fixed scan rate of 50 mV/s.

When the scan rate is low, ions diffusion is slow, *i.e.*, ions have sufficient time for diffusion into the inner surfaces of pores or pore channels. Therefore, ion penetration distance and easily accessible pore channels are less important at low scan rates. However, at higher scan rates ion penetration is possible only on the surface of large pores (the small pores get obstructed), *i.e.*, less active surface area of the pores take part in the process (

Figure 4.102).[114] In general, the shape of **CV** curves deviates from the rectangular profile at increasing scan rate and, therefore, the capacitance decreases. **CV** curves of **CNF-PiC** and **CNF-1100** in Figure 4.103 maintained the rectangular shape even at high scan rates. **CNF-PiC** additionally shows a small deviation for the rectangular profile (*i.e.*, a bump at 0.3 V vs Ag/AgCl), that might be caused by oxygen surface functional groups present in the carbon sample.[119] The presence of mesopores, high pore volume (~2.7 cc/g) and morphology allows the fibers to easily adsorb guest electrolyte molecules even under high scan rates. Meanwhile, as the heat treatment temperature is increased (**CNF-1500** and **CNF-2000**), the shape deforms from the rectangular shape. This is expected, considering that the pore structure is collapsing due to a reduction in volume caused by the graphitization process.

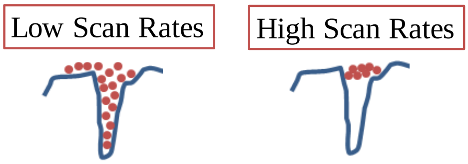

Figure 4.102. Schematic representation of capacitance loss due to high scan rates.

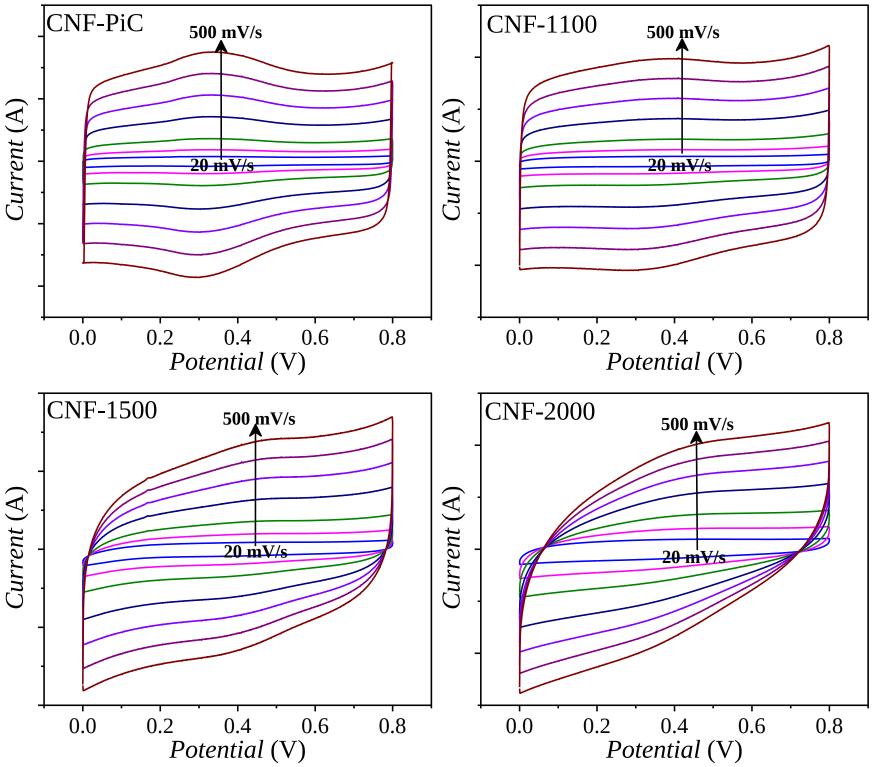

Figure 4.103. **CV** curves of **CNFs** at different scan rates (20, 50, 80,100, 200, 300, 400, 500 mV/s)

CNF-PiC and **CNF-1100** showed outstanding capacitance (307 F/g and 327 F/g at 5 mV/s, respectively, calculated from CV curves as explained in subsection 3.3.19) (Figure 4.104a). **CNFs** showed great capacitance retention to increasing scan rates and current densities among them, **CNF-PiC** showed superior capacitance retention (up to 79 % retention from 5 mV/s to 500 mV/s). This retention behavior could be attributed to the surface functional groups of **CNF-PiC**. Polar groups on the carbon surface increase wettability and could make the carbon surface more accessible to aqueous electrolytes,[107] allowing **CNF-PiC** to retain high capacitance even at high scan rates or currents. It is noteworthy that many methods exist for adding oxygen functionalization to carbon, such as chemical oxidation or plasma, but in the present case oxygen-containing groups result from the synthesis process without the need of an additional surface-treatment. As expected from the decrease in surface area, **CNF-1500** and **CNF-2000** capacitance was considerably lower, nevertheless, there is no linear correlation between capacitance and surface area (Figure 4.104b). Ordered graphitic carbon nanofibers are expected to have higher conductivity, which would lead to higher capacitance values. However, we have observed the opposite results. This demonstrates that the loss of surface area has greater influence on the capacitance value than the conductivity.

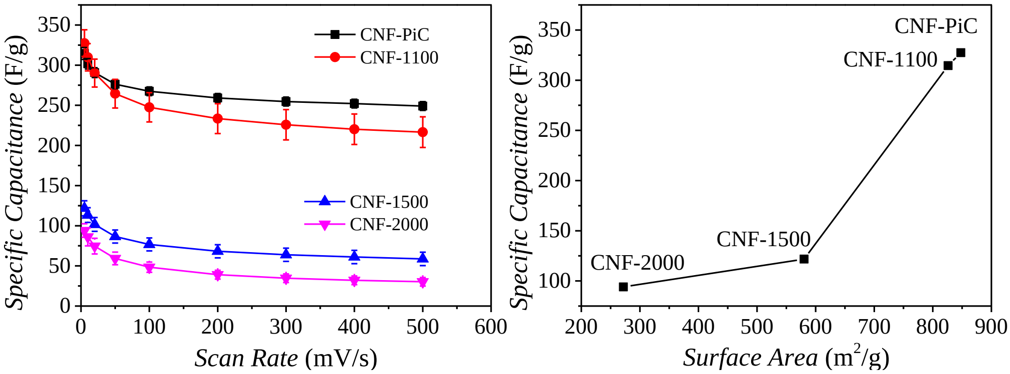

Figure 4.104. (a) Specific capacitance values for **CNFs** as a function of scan rate and (b) specific capacitance values for **CNFs** as a function of surface area at a scan rate of 5 mV/s.

Charge-discharge (**CD**) curves showed typical symmetric response (Figure 4.105a) corresponding to EDLC behavior. **CNFs,** particularly **CNF-PiC** and **CNF-1100** sustained high capacitance even at higher current density of 10 A/g (Calculated as explained in subsection 3.3.19, Figure 4.105b)

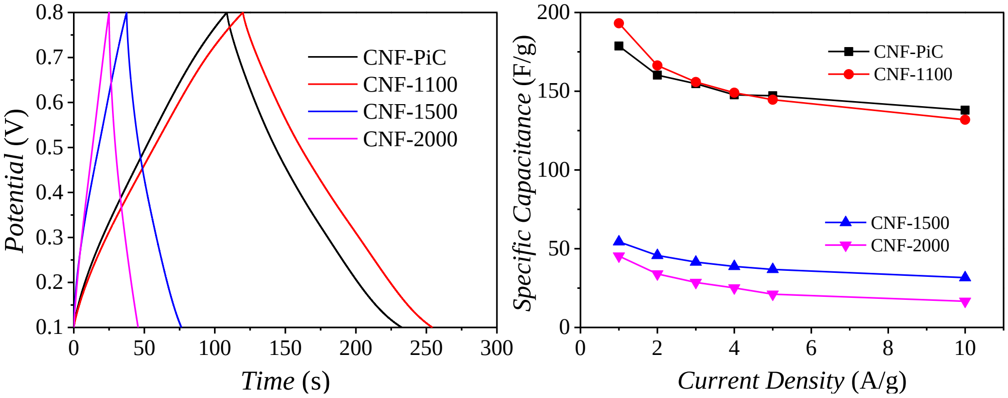

Figure 4.105. (a) **CD** curves for **CNFs** at fixed current density of 1 A/g and (b) Specific capacitance values for **CNFs** as a function of current density.

It is worth mentioning that the BET surface area of **CNFs** is rather low (~840 m^2/g) compared to other mesoporous carbon materials or commercially available conductive carbon black (1000-1500 m^2/g), so the high capacitance value must arise from other properties such as pore structure, surface chemistry or particle morphology. It should be noted that the electrode material design is one of the main parameters to enhance the capacitive properties of the **EDLCs**. A material with high porosity and that allows the electrolyte ions to easily access most of the surface is the suitable electrode material for high energy storage. In fact, other templated carbons such as CMK-3 show lower capacitance (~200 F/g at 1 mV/s) despite its high surface area (1200 m^2/g).[109] This suggests that some of the CMK-3 surface area is not accessible by the electrolyte. The hollow morphology of **CNF** could allow most of the area to be in full contact with the electrolyte solution. All of **CNF** exhibited excellent cyclic stability. The capacitance retention of **CNFs** after 1000 cycles of charging and discharging at 10 A/g was 92 % for **CNF-PiC** and 95 % for **CNF-1100**, **CNF-1500** and **CNF-2000**. **CNFs** have a capacitance similar to commercially available activated carbon that is already being used for supercapacitor electrodes (e.g. Maxsorb® with a capacitance of 330 F/g at 5 mV/s),[114] but additionally, **CNFs** capacitance retention at increasing scan rates (79 % retention from 5 to 500 mV/s) is considerable higher than that of activated carbon (< 20 % from 5 to 500 mV/s). Thus, the present **CNFs** could be of special interest for applications in which high currents are needed (i.e., faster charging).

- **Vapor Adsorption: Sensing Organics Compounds**

CNF-PiC can also be used as sensor material of industrial interest for sensing volatile organic compounds (**VOCs**), such as pyridine, benzene, and toluene. Vapor sensing properties of **CNF-PiC** were evaluated by the **QCM** technique explained in subsection 3.3.20. Solvents with similar molecular weight and vapor pressure were tested to study the selectivity of **CNF-PiC** (hexane, cyclohexane, benzene, toluene and pyridine). As the blank test, frequency shift of bare Au-resonator without loading any material was recorded upon exposing to the different solvent vapors and corrected from the frequency shift of the **CNF-PiC** modified **QCM** sensors. These vapors caused a small frequency shift of bare Au-resonator: hexane (-2.9 Hz), cyclohexane (-4.9 Hz), benzene (-12.0 Hz), toluene (-12.1) and pyridine (-20.5 Hz). Frequency shift of **CNF-PiC** modified **QCM** sensor was very quick upon exposure of solvent vapors (Figure 4.106). Adsorption of vapors of aromatic compounds such as benzene (-77 Hz), toluene (-82.7 Hz) and pyridine (-186 Hz) caused larger frequency shift compared to aliphatic hydrocarbons hexane (-5 Hz), and cyclohexane (-51 Hz) with almost similar molecular size and molecular weight. The sensing selectivity to **VOCs** decreases as follows: pyridine > toluene> benzene > cyclohexane > hexane. The higher sensing selectivity towards aromatic solvent vapors could be explained by constrain-free diffusion into the pores trough strong π–π interaction between aromatic guest molecules and sp2 carbon on the **CNFs** surface.[123, 124, 127, 129] Note that although the vapor pressure, molecular weight and structure of pyridine, benzene and toluene are more or less similar, pyridine caused a frequency shift more than twice in magnitude compared to benzene or toluene. This might be attributed to the basic nature of pyridine interacting with protonic Brønsted acid surface sites on **CNF-PiC** surface (i.e., OH, COOH as confirmed by **XPS** in Figure 4.100). In fact, the increase of acidic functionalities on carbon surfaces is known to improve the sensing capabilities towards specific basic molecules such as aniline or ammonia.[127]

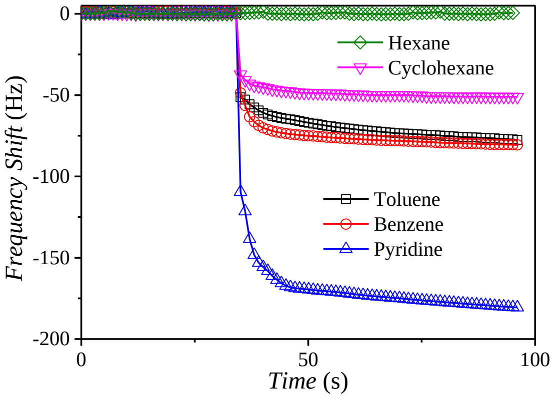

Figure 4.106. **QCM** frequency shifts upon exposure to different solvent vapors.

CNF-PiC also showed good cyclic stability against adsorption/desorption of solvent vapors. As it can be seen in Figure 4.107 the **QCM** response is immediate upon exposure to vapor. Also, the vapor quickly desorbs when the electrode is exposure to air.

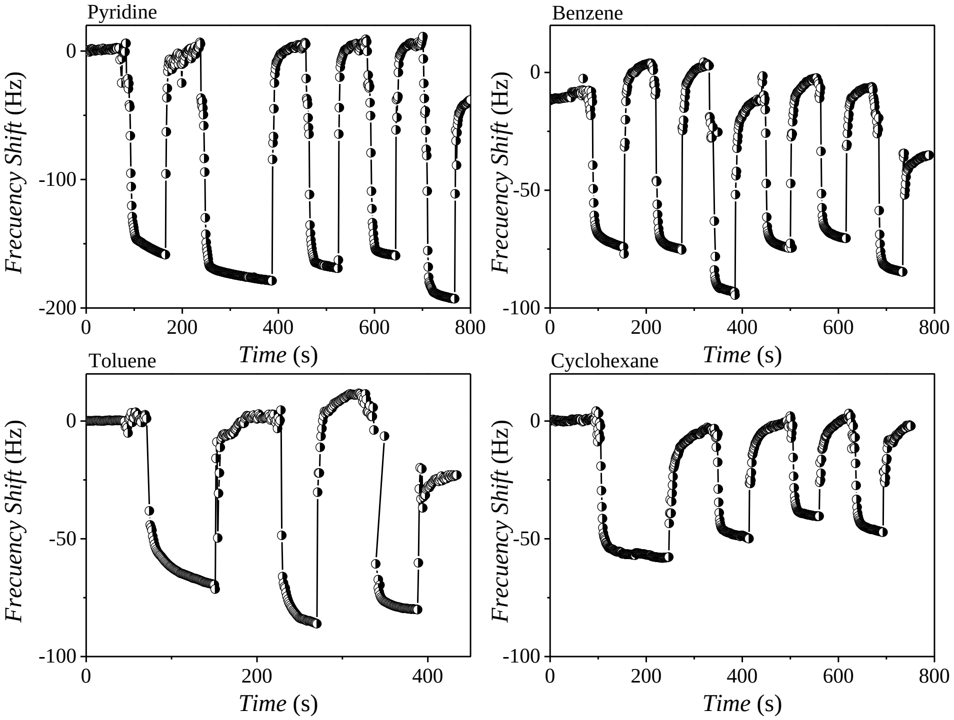

Figure 4.107. Repeatability test of **CNF-PiC** upon exposure and removal of different organic vapors.

These results demonstrate the potential use of **CNF-PiC** as a vapor sensors. These sensors would be of industrial importance. For example, pyridine is an organic compound used for the synthesis of many common products (i.e. agro-chemicals, pharmaceutics, dyes, adhesives, etc.). However, pyridine is a hazardous chemical; it is reported that reduces male fertility and is carcinogenic. Some foods emit this compound when grilled, so techniques that allow easy detection are of interest.[188] Toluene and benzene are also toxic and are used in many industrial syntheses or as solvents; therefore their detection is of interest for preventing health related injuries.

5. CONCLUSIONS

The phase behavior and self-assembly of diglycerol isostearate esters and cationic dye molecules has been studied in aqueous media as a function of concentration and temperature. The self-assemblies formed have been used as templates for novel nanostructured materials and some potential applications of the materials obtained as have been explored. The main conclusions of this thesis are summarized as follow:

Aqueous Phase Behavior of Technical Grade Diglycerol-Isostearate-Based Surfactants.

- The phase behavior of the water/**C41V** system as a function of **C41V** concentration and temperature is characterized by a wide multiphasic region with the presence of inverse hexagonal liquid crystal (**H_2**) at temperatures below 70 ºC. Two-liquid phases are formed at temperatures above 70 ºC. The absence of monophasic region was ascribed to the presence of impurities.
- Glycerol was separated from **C41V** by precipitation with ethyl acetate resulting in **C41V-NG** surfactant. Such a purification procedure allowed to obtain a single-phase **H_2**. It was also shown that glycerol dehydrates the **H_2** phase at high surfactant concentration but it does not have any effect on the **H_2** structure at low **C41V** concentrations.
- Separation of diglycerol fatty acids with higher esterification degree from **C41V** was achieved in good yield using a silica chromatographic column. The resulting diglycerol-monofatty acid fraction forms a lamellar liquid crystal (**L_α**) and the packing parameter was calculated to be near 1, which favors the formation of layered structures. The curvature of this system can be increased by adding the diglycerol polyfatty acids fraction; consequently, **L_α** and **H_2** phases could be obtained. Both phases can coexist and be dispersed in excess water to form vesicles and hexosomes.

Dispersion and Characterization of Inverse Hexagonal Liquid Crystal Nanoparticles (Hexosomes).

- The **H_2** phase of the water/**C41V** system could be dispersed in excess water in the form of nanoparticles stabilized by **F127**. The solvent evaporation method, using ethyl acetate as a volatile solvent followed by ultrasonic dispersion was found to be the most efficient for obtaining hexosome dispersions with small size and narrow size distribution. The dispersions remained stable at 25 ºC for at least one month.
- The size of the hexosomes can be controlled by varying the **C41V**:**F127** ratio. The interlayer distance in the hexagonal lattice of hexosomes did not change upon addition of **F127** (up to **C41V**:**F127** ratios of 60:40). This indicates that the stabilizer preferably goes to the interface between hexosome and water.
- Hexosome dispersion with smaller sizes and narrower distributions could be formed by dispersing the **H_2** phase in phosphate buffer instead of water. This

effect is ascribed to the increase of the osmotic pressure of the continuous media, which is proportional to the electrolyte concentration.

- Up to 80 g of hexosome dispersion (5 wt% C41V) could be prepared with the methodology presented in this work, showing potential for industrial applications.

Ketoprofen Encapsulation In Hexosome Dispersions and In-Vitro Drug Release

- Ketoprofen (**KP**) was successfully encapsulated in the hexosomes dispersions with high **KP** encapsulation efficiency (86 % at 10 wt% of **KP** in **C41V**). The encapsulation of **KP** changed slightly the structure of the hexosomes. The maximum loading without changing the $\mathbf{H_2}$ structure was achieved at a **C41V**:**KP** ratio of 90:10.
- The release rate of **KP** encapsulated in the hexosome dispersion to a receptor solution was sustained and independent of the pH of the receptor solution in the first 10 hours of release. After 10 hours, the hexosomes in contact with acidic media are degraded and consequently the release profile is changed. Therefore, these dispersions have the potential to be used as vehicles for encapsulating drugs for the delivery in the gastrointestinal track.
- The diffusional exponent, derived from the fitting of the release curves to the Korsmeyer-Pepas model, shows that the release mechanism follows an anomalous non-Fickian transport.

Aqueous Phase Behavior and Self-Assembly of Dyes

➢ Quinaldine Red Acetate (QR-Ac)

- The water/**QR-Ac** phase diagram is characterized by a wide liquid isotropic region at concentrations lower than 30 wt% of dye and 3 different liquid crystalline phase regions at high dye concentrations. With increasing concentration, a nematic, **N** phase, is formed, followed by a rectangular, **O** phase. The formation of a rectangular phase indicates that the aggregates cross-section is anisotropic. A rearrangement of the aggregates occurs in the **O** phase as the temperature is increased to form a columnar lamellar or $\mathbf{Col_L}$ phase presumably formed by layers composed of molecular stacks. **SAXS** and **WAXS** measurements confirm the presence of a **O** phase and $\mathbf{Col_L}$ phase. The calculated cross section area of the **QR-Ac** aggregates matches the molecular area confirming that the aggregates cross-sections are unimolecular.
- $\mathbf{^1H}$**-NMR** shows that the chemical shift of the phenylene group protons decrease strongly as the concentration is increased, evidencing the efficient intermolecular aromatic interactions. $\mathbf{^1H - {}^1H}$ **NOE** spectroscopy suggests that **QR-Ac** forms antiparallel stacks in $\mathbf{D_2O}$, with the dimethylaniline group (electron rich) interacting with the quinolinium moiety (electron poor).

- **Pyronin Y (PyY)**

- The water/**PyY** phase diagram is characterized by a wide isotropic region (up to 40 wt% of dye). With increasing concentration, a wide coexistence region between nematic liquid crystal and isotropic region and a monophasic nematic phase are found. **SAXS** calculations show that the cross-sectional area of the aggregates is close to the molecular area confirming that the cross-section of aggregates is also unimolecular.
- From **^{1}H-NMR** it can be inferred that aggregates and monomers coexist at all concentrations studied within the isotropic region. The protons from the aromatic core of the molecule show increasing chemical shifts with concentrations, in contrast to those in the dimethylamine groups. This behavior is expected for self-aggregation into stacks with aromatic cores lying on top of each other.

- **Thiacarbocyanines (TCC-$C_{2\text{-}5}$)**

- From **UV-Vis** spectroscopy it was estimated that the intermolecular interactions increase with the alkyl chain length. All studied dyes showed aggregation-induced quenching with maximum fluorescence at a concentration of ca. 25 μM.
- **TCC-$C_{2\text{-}4}$** formed chromonic liquid crystals upon contact with water. A multimolecular cross section can be inferred by **SAXS** measurements. In contrast **TCC-C_5** did not form liquid crystals in water because its low solubility.

- **Oxacarbocyanines (OXA-nC)**

- **UV-Vis** spectra remained identical with concentration (ortochromatic-like behavior). This could be attributed to the lack of exciton splitting due to the dyes stacking in angles close to θ = 54.7 º. Similar to thiacarbocyanines, oxacarbocyanines dyes showed aggregation-induced quenching with maximum fluorescence located at 10 μM and 60 μM for **OXA-3C** and **OXA-5C** respectively.
- **OXA-5C** formed chromonic liquid crystals upon contact with water in contrast to **OXA-3C**. **OXA-3C** samples up to 30 wt% of dye did not show evidence of liquid crystal formation. This suggests a low effective volume fraction of aggregates and thus, it is likely that this dye forms stacks with unimolecular cross-section.
- A complete characterization of these systems was not possible since both of oxacarbocyanines (**OXA-3C** and **OXA-5C**) show a fast degradation in water due to hydrolysis.

- **Alcian Blue (AB-Ac, AB-ToC, AB-Cl)**

- Alcian blue with different counterions showed evidence of molecular stacking, nevertheless, the dissociation of these molecules in water was rather small. **AB-**

Ac formed organogel-like structure containing birefringent particles. **AB-Toc** formed hexagonal liquid crystal upon addition of small quantities in water. This liquid crystal coexists in excess water at low **AB-Toc** concentrations. In contrast, **AB-Cl** was too insoluble in water and therefore did not form more structured phases.

- **AB-Cl** formed a liquid crystal with a possible nematic structure in acidic aqueous solutions (ca. 3 wt% of acetic acid). This is attributed to the increased dissociation of these dyes at acidic pH.

Chromonic Self-Assembly as Templates for Functional Materials

➢ Silica nanofibers

- **TCC-C$_{2\text{-}4}$** successfully directed silica growth into fibers with hierarchical structure consisting in cylindrical pores aligned along the fiber's axis, similar to those reported for Pinacyanol Acetate (**PiC**). The final silica product contained almost exclusively fibers. **TCC-C$_5$** formed a mixture between fibers and amorphous material. The capacity of these dyes to template silica can be associated to the formation of liquid crystals in solution. In contrast, **PyY**, **QR-Ac** and **AB** could not direct silica formation. It is noteworthy that cationic dyes are considered basic dyes and they are difficult to dissociate in basic media, thus, the capacity of cationic dyes to template silica growth as fibers is directly associated to the dissociation constant in basic media.
- Although **AB-Ac** could not direct silica growth, this dye was adsorbed into the silica due to electrostatic interactions. Calcination of this composite result in a high surface area material (ca. 600 m^2/g). If the material is calcined in an inert atmosphere, a **SiO$_2$**/Carbon composite containing metallic copper can be obtained.

➢ Carbon nanofibers

- Carbon nanofibers (**CNFs**) with a surface area of 830 m^2/g have been successfully synthesized using a hard templating approach with the mesoporous silica nanofibers as templates. Graphitized-wall **CNFs** were successfully obtained by heat treatment at 2000 ºC, however, the pore structure collapses at high temperatures leading to a reduction in the surface area.
- The **CNFs** showed excellent electrochemical performance (especially those containing disordered graphite walls), demonstrating their potential used as electrode material for supercapacitor applications. The maximum specific capacitance obtained (327 F/g at a scan rate of 5 mV/s) outperforms that observed for many activated carbons with a higher surface area. Furthermore, high capacitance retention at high current density and long cycle life makes this material a suitable candidate for use in advanced supercapacitor electrode designs. The low surface area, compared to other mesoporous or activated carbons, suggests that the high capacitance value, current and cycle stability

might be a consequence of the morphology, pore structure and surface chemistry. This allows the electrolytes to be in full contact with the entire available surface calculated by N_2 sorption measurements.

- Sensing measurements on the carbon nanofibers revealed selectivity for aromatic molecules caused by the free diffusion of these molecules into the pores of the electrode due to interaction with sp_2 carbon atoms. **CNFs** showed more sensitivity towards adsorption of pyridine. This can be attributed to acidic oxygen groups on the surface of **CNF** (detected by XPS) and from silica due to an incomplete template removal.

6. BIBLIOGRAPHY

1. Whitesides, G.M. and B. Grzybowski, *Self-Assembly at All Scales.* Science, 2002. **295**(5564): p. 2418-2421.
2. Israelachvili, J., *Intermolecular and Surface Forces*. Second Edition ed. 1998, California: Academic Press.
3. Feynman, R.P., *Forces in Molecules.* Physical Review, 1939. **56**(4): p. 340-343.
4. Lee, Y.S., *Self-Assembly and Nanotechnolgy: A Force Balance Approach*. 2008, New York: Wiley.
5. Luckhurst, G.R. and R. Poupko, *Molecular Organization Within Nematic and Smectic Phases of 4'-N-Octyloxy-4-cyanobiphenyl.* Molecular Physics, 1975. **29**(4): p. 1293-1296.
6. Laschat, S., et al., *Discotic Liquid Crystals: From Tailor Made Synthesis to Plastic Electronics.* Angewandte Chemie International Edition, 2007. **46**(26): p. 4832-4887.
7. Lughylin, R.G., *The Aqueous Phase Behavior of Surfactants*. 1994, San Diego: Academic Press.
8. Holmberg, K., et al., *Surfactants and Polymers in Aqueous Solution*. 2003, England: John Wiley & Sons, Ltd.
9. Rosen, M.J., *Surfactans and Interfacial Phenomena*. 3 ed. 2004, New York: John Wiley & Sons.
10. Tiddy, G.J.T., *Surfactant-Water Liquid Crystal Phases.* Physics Reports, 1980. **57**(1): p. 1-46.
11. Israelachvili, J.N., D.J. Mitchell, and B.W. Ninham, *Theory of Self-Assembly of Hydrocarbon Amphiphiles into Micelles and Bilayers.* Journal of the Chemical Society-Faraday Transactions Ii, 1976. **72**: p. 1525-1568.
12. Tanford, C., *The Hydrophobic Effect*. 1980, New York: Wiley.
13. Kunieda, H., G. Umizu, and Y. Yamaguchi, *Mixing Effect of Polyoxyethylene-Type Nonionic Surfactants on the Liquid Crystalline Structures.* Journal of Colloid and Interface Science, 1999. **218**(1): p. 88-96.
14. Seddon, J.M., *Structre of the Inverted Hexagonal (HII) Phase, and Non-Lamellar Phase-Transitions of Lipids.* Biochimica Et Biophysica Acta, 1990. **1031**(1): p. 1-69.
15. Forgiarini, A., et al., *Formation of Nano-Emulsions by Low-Energy Emulsification Methods at Constant Temperature.* Langmuir, 2001. **17**(7): p. 2076-2083.
16. Svensson, M., in *Surfactants from Renewable Resources*. 2010, John Wiley & Sons, Ltd: United Kingdom.
17. Izquierdo, P., et al., *Phase Behavior of Pentaglycerol Monostearic and Monooleic Acid Esters in Water.* Journal of Dispersion Science and Technology, 2006. **27**(1): p. 99-103.
18. Ishitobi, M. and H. Kunieda, *Effect of Chain Length Distribution on the Phase Behavior of Polyglycerol Fatty Acid Ester in Water.* Colloid and Polymer Science, 2000. **278**(9): p. 899-904.
19. Ai, S. and M. Ishitobi, *Effects of the Number of Fatty Acid Residues on the Phase Behaviors of Decaglycerol Fatty Acid Esters.* Journal of Colloid and Interface Science, 2006. **296**(2): p. 685-689.

20. Kumar, T.N., Y.S.R. Sastry, and G. Lakshminarayana, *Preparation and Surfactant Properties of Diglycerol Esters of Fatty Acids.* Journal of the American Oil Chemists Society, 1989. **66**(1): p. 153-157.
21. Shrestha, L.K., et al., *Aqueous Phase Behavior of Diglycerol Fatty Acid Esters.* Journal of Dispersion Science and Technology, 2007. **28**(6): p. 883-891.
22. De Meulenaer, B., et al., *Combined Liquid and Gas Chromatographic Characterisation of Polyglycerol Fatty Acid Esters.* Journal of Chromatography A, 2000. **896**(1-2): p. 239-251.
23. Friberg, S., *Food Emulsions*. 1976, New York.
24. Duerr-Auster, N., et al., *Microstructure and Stability of a Lamellar Liquid Crystalline and Gel Phase Formed by a Polyglycerol Ester Mixture in Dilute Aqueous Solution.* Langmuir, 2007. **23**(26): p. 12827-12834.
25. Attwood, T.K., et al., *The Distinction Between Chromonic and Amphiphilic Lyotropic Mesophases.* Liquid Crystals, 1990. **7**(5): p. 657-668.
26. Lydon, J., *Chromonic Review.* Journal of Materials Chemistry, 2010. **20**(45): p. 10071-10099.
27. Attwood, T.K., J.E. Lydon, and F. Jones, *The Chromonic Phases of Dyes.* Liquid Crystals, 1986. **1**(6): p. 499-507.
28. Maiti, P.K., et al., *Isodesmic Self-Assembly in Lyotropic Chromonic Systems.* Liquid Crystals, 2002. **29**(5): p. 619-626.
29. Wu, L., et al., *Nonamphiphilic Assembly in Water: Polymorphic Nature, Thread Structure, and Thermodynamic Incompatibility.* Journal of the American Chemical Society, 2009. **131**(21): p. 7430-7443.
30. Attwood, T.K. and J.E. Lydon, *Lyotropic Mesophase Formation by Anti-Asthmatic Drugs.* Molecular Crystals and Liquid Crystals, 1984. **108**(3-4): p. 349-357.
31. Govindaiah, T.N., H.R. Sreepad, and Nagappa, *Mesophase Formation in Binary Mixtures of Berberine and Glacial Acetic Acid.* Molecular Crystals and Liquid Crystals, 2013. **570**(1): p. 101-108.
32. Govindaiah, T.N., et al., *Optical Characterization of Lyotropic Chromonic Liquid Crystals.* Molecular Crystals and Liquid Crystals, 2014. **593**(1): p. 43-50.
33. Rodriguez-Abreu, C., et al., *Characterization of Perylene Diimide Dye Self-Assemblies and Their Use As Templates for the Synthesis of Hybrid and Supermicroporous Nanotubules.* ACS Applied Materials & Interfaces, 2011. **3**(10): p. 4133-4141.
34. Huang, L. and S.-W. Tam-Chang, *Ionic Perylene-3,4-Dicarboximide as Chromonic Mesogens and the Use of a Fluorescence Technique in Determining Phase Transition Temperatures.* Liquid Crystals, 2010. **37**(5): p. 555-561.
35. Tam-Chang, S.W., et al., *Molecularly Designed Chromonic Liquid Crystals for the Fabrication of Broad Spectrum Polarizing Materials.* Chemistry of Materials, 2004. **16**(10): p. 1832-1834.

36. Chen, Z., et al., *Photoluminescence and Conductivity of Self-Asembled pi-pi Stacks of Perylene Bisimide Dyes.* Chemistry- A European Journal, 2007. **13**(2): p. 436-449.
37. Tam-Chang, S.W., J. Helbley, and I.K. Iverson, *A Study of the Structural Effects on the Liquid-Crystalline Properties of Ionic Perylenebis(Dicarboximide) Using UV-Vis Spectroscopy, Polarized Light Microscopy, and NMR Spectroscopy.* Langmuir, 2008. **24**(5): p. 2133-2139.
38. Tam-Chang, S.-W., J. Helbley, and I.K. Iverson, *A Study of the Structural Effects on the Liquid-Crystalline Properties of Ionic Perylenebis(dicarboximide)s Using UV-vis Spectroscopy, Polarized Light Microscopy, and NMR Spectroscopy.* Langmuir, 2008. **24**(5): p. 2133-2139.
39. Rodriguez-Abreu, C., C. Aubery Torres, and G.J.T. Tiddy, *Chromonic Liquid Crystalline Phases of Pinacyanol Acetate: Characterization and Use as Templates for the Preparation of Mesoporous Silica Nanofibers.* Langmuir, 2011. **27**(6): p. 3067-3073.
40. Alfutimie, A., et al., *Chromonic Liquid Crystals Formed by CI Acid Red 266 and Related Structures.* Liquid Crystals, 2015. **42**(8): p. 1169-1178.
41. Mercado, B.R., K.J. Nieser, and P.J. Collings, *Cooperativity of the Assembly Process in a Low Concentration Chromonic Liquid Crystal.* Journal of Physical Chemistry B, 2014. **118**(46): p. 13312-13320.
42. Tiddy, G.J.T., et al., *Highly Ordered Aggregates in Dilute Dye Water Systems.* Langmuir, 1995. **11**(2): p. 390-393.
43. Mills, E.A., et al., *Large Assembly Formation via a Two-Step Process in a Chromonic Liquid Crystal.* Journal of Physical Chemistry B, 2012. **116**(45): p. 13506-13515.
44. Harrison, W.J., D.L. Mateer, and G.J.T. Tiddy, *Liquid Crystalline J-Aggregates Formed by Aqueous Ionic Cyanine Dyes.* Journal of Physical Chemistry, 1996. **100**(6): p. 2310-2321.
45. Zhang, Y.-F., et al., *Multiple Hybridized Resonances of IR-806 Chromonic Molecules Strongly Coupled to Au Nanorods.* Nanoscale, 2015. **7**(18): p. 8503-9.
46. Lokesh and N. Suryaprakash, *Self-Assembly of Folic Acid: A Chiral-Aligning Medium for Enantiodiscrimination of Organic Molecules in an Aqueous Environment.* Chemistry- A European Journal, 2012. **18**(37): p. 11560-11563.
47. Motkar, G., et al., *Self-Assembly of Folic Acid in Aqueous Media.* Aiche Journal, 2013. **59**(4): p. 1360-1368.
48. Tam-Chang, S.-W. and L. Huang, *Chromonic Liquid Crystals: Properties and Applications as Functional Materials.* Chemical Communications, 2008(17): p. 1957-1967.
49. Yadav, Y.J., et al., *Chromonic-Like Physical Luminescent Gels Formed by Ionic Octahedral Iridium(III) Complexes in Diluted Water Solutions.* Advanced Optical Materials, 2013. **1**(11): p. 844-854.
50. Hartshorne, N.H. and G.D. Woodard, *Mesomorphism in Sytem Disodium Chromoglycate-Water.* Molecular Crystals and Liquid Crystals, 1973. **23**(3-4): p. 343-368.

51. Cox, J.S.G., G.D. Woodard, and W.C. McCrone, *Solid-State Chemistry of Cromolyn sodium (Disodium-Cromoglycate).* Journal of Pharmaceutical Sciences, 1971. **60**(10): p. 1458-&.
52. von Berlepsch, H., K. Ludwig, and C. Bottcher, *Pinacyanol Chloride Forms Mesoscopic H- and J-Aggregates in Aqueous Solution - a Spectroscopic and Cryo-Transmission Electron Microscopy Study.* Physical Chemistry Chemical Physics, 2014. **16**(22): p. 10659-10668.
53. Wurthner, F., T.E. Kaiser, and C.R. Saha-Moller, *J-Aggregates: From Serendipitous Discovery to Supramolecular Engineering of Functional Dye Materials.* Angewandte Chemie-International Edition, 2011. **50**(15): p. 3376-3410.
54. Haverkort, F., A. Stradomska, and J. Knoester, *First-Principles Simulations of the Initial Phase of Self-Aggregation of a Cyanine Dye: Structure and Optical Spectra.* Journal of Physical Chemistry B, 2014. **118**(29): p. 8877-8890.
55. Kasha, H., H.R. Rawls, and M. Sashraf El-Bayoumi, *The Exciton Model in Molecular Spectroscopy.* Pure and Applied Chemistry, 1965. **11**: p. 371-392.
56. Shiyanovskii, S.V., et al., *Lyotropic Chromonic Liquid Crystals for Biological Sensing Applications.* Molecular Crystals and Liquid Crystals, 2005. **434**: p. 587-598.
57. Shiyanovskii, S.V., et al., *Real-time Microbe Detection Based on Director Distortions Around Growing Immune Complexes in Lyotropic Chromonic Liquid Crystals.* Physical Review E, 2005. **71**(2).
58. Ariga, K., et al., *Research Update: Mesoporous Sensor Nanoarchitectonics.* Apl Materials, 2014. **2**(3).
59. Mann, S., et al., *Sol-gel Synthesis of Organized Matter.* Chemistry of Materials, 1997. **9**(11): p. 2300-2310.
60. Walt, D.R., *Nanomaterials - Top-to-Bottom Functional Design.* Nature Materials, 2002. **1**(1): p. 17-18.
61. Hecht, S., *Welding, Organizing, and Planting Organic Molecules on Substrate Surfaces - Promising Approaches Towards Nanoarchitectonics from the Bottom Up.* Angewandte Chemie-International Edition, 2003. **42**(1): p. 24-26.
62. Lu, W. and C.M. Lieber, *Nanoelectronics From the Bottom Up.* Nature Materials, 2007. **6**(11): p. 841-850.
63. Archibald, D.D. and S. Mann, *Template Mineralization of Self-Sssembled Anisotropic Lipid Microstructures.* Nature, 1993. **364**(6436): p. 430-433.
64. Mann, S., *Molecular Tectonics in Biomineralization and Biomimetic Materials Chemistry.* Nature, 1993. **365**(6446): p. 499-505.
65. Mann, S., et al., *Crystallization at Inorganic-Organic Interfaces-Biominerals and Biomimetic Synthesis.* Science, 1993. **261**(5126): p. 1286-1292.
66. Zhao, D.Y., et al., *Morphological Control of Highly Ordered Mesoporous Silica SBA-15.* Chemistry of Materials, 2000. **12**(2): p. 275-+.

67. Kruk, M., et al., *Characterization of the Porous Structure of SBA-15.* Chemistry of Materials, 2000. **12**(7): p. 1961-1968.
68. Boyd, B.J., et al., *Lyotropic Liquid Crystalline Phases Formed from Glycerate Surfactants as Sustained Release Drug Delivery Systems.* International Journal of Pharmaceutics, 2006. **309**(1-2): p. 218-226.
69. Mulet, X., B.J. Boyd, and C.J. Drummond, *Advances in Drug Delivery and Medical Imaging Using Colloidal Lyotropic Liquid Crystalline Dispersions.* Journal of Colloid and Interface Science, 2013. **393**: p. 1-20.
70. Angelova, A., et al., *Biocompatible Mesoporous and Soft Nanoarchitectures.* Journal of Inorganic and Organometallic Polymers and Materials, 2015. **25**(2): p. 214-232.
71. Angelova, A., et al., *Self-Assembled Multicompartment Liquid Crystalline Lipid Carriers for Protein, Peptide, and Nucleic Acid Drug Delivery.* Accounts of Chemical Research, 2011. **44**(2): p. 147-156.
72. Drummond, C.J. and C. Fong, *Surfactant Self-Asembly Objects as Novel Drug Delivery Vehicles.* Current Opinion in Colloid & Interface Science, 1999. **4**(6): p. 449-456.
73. Liu, M., et al., *Nanostructured Cubosomes as a Platform for Oral Drug Delivery.* Current Pharmaceutical Biotechnology, 2015. **16**(4): p. 313-321.
74. Mezzenga, R., et al., *Understanding foods as soft materials.* Nature Materials, 2005. **4**(10): p. 729-740.
75. Nishino, A., *Capacitors: Operating Principles, Current Market and Technical Trends.* Journal of Power Sources, 1996. **60**(2): p. 137-147.
76. Winter, M. and R.J. Brodd, *What are Batteries, Fuel Cells, and Supercapacitors?* Chemical Reviews, 2004. **104**(10): p. 4245-4269.
77. Ariga, K., et al., *A Layered Mesoporous Carbon Sensor Based on Nanopore-Filling Cooperative Adsorption in the Liquid Phase.* Angewandte Chemie-International Edition, 2008. **47**(38): p. 7254-7257.
78. Brudzewski, K., S. Osowski, and T. Markiewicz, *Classification of Milk by Means of an Electronic Nose and SVM Neural Network.* Sensors and Actuators B-Chemical, 2004. **98**(2-3): p. 291-298.
79. Williams, H.D., et al., *Strategies to Address Low Drug Solubility in Discovery and Development.* Pharmacological Reviews, 2013. **65**(1): p. 315-499.
80. Shah, J.C., Y. Sadhale, and D.M. Chilukuri, *Cubic Phase Gels as Drug Delivery Systems.* Advanced Drug Delivery Reviews, 2001. **47**(2-3): p. 229-250.
81. Malmsten, M., *Soft Drug Delivery Systems.* Soft Matter, 2006. **2**(9): p. 760-769.
82. Buchheim, W. and K. Larsson, *Cubic Lipid-Protein-Water Phases.* Journal of Colloid and Interface Science, 1987. **117**(2): p. 582-583.
83. Larsson, K., *Cubic Lipid-Water Phases: Structures and Biomembrane Aspects.* Journal of Physical Chemistry, 1989. **93**(21): p. 7304-7314.
84. Efrat, R., et al., *Solubilization of Hydrophobic Guest Molecules in the Monoolein Discontinuous Q(L) Cubic Mesophase and Its Soft Nanoparticles.* Langmuir, 2009. **25**(3): p. 1316-1326.

85. Kraineva, J., et al., *Kinetics of lamellar-to-cubic and intercubic phase transitions of pure and cytochrome c containing monoolein dispersions monitored by time-resolved small-angle X-ray diffraction.* Langmuir, 2005. **21**(8): p. 3559-3571.
86. Caffrey, M., *A lipid's eye view of membrane protein crystallization in mesophases.* Current Opinion in Structural Biology, 2000. **10**(4): p. 486-497.
87. Ai, X. and M. Caffrey, *Membrane protein crystallization in lipidic mesophases: Detergent effects.* Biophysical Journal, 2000. **79**(1): p. 394-405.
88. *Delivery System Handbook For Personal Care and Cosmetic Products*. 2006, New York: William Andrew.
89. *Handbook of Non-Invasive Drug Delivery Systems*. 2010: William Andrew.
90. Larsson, K., *Aqueous Dispersions of Cubic Lipid-Water Phases.* Current Opinion in Colloid & Interface Science, 2000. **5**(1-2): p. 64-69.
91. Shrestha, L.K., et al., *Aqueous Foam Stabilized by Dispersed Surfactant Solid and Lamellar Liquid Crystalline Phase.* Journal of Colloid and Interface Science, 2006. **301**(1): p. 274-281.
92. Shrestha, L.K., et al., *Foaming properties of monoglycerol fatty acid esters in nonpolar oil systems.* Langmuir, 2006. **22**(20): p. 8337-8345.
93. Qiu, H. and M. Caffrey, *The Phase Diagram of the Monoolein/Water System: Metastability and Equilibrium Aspects.* Biomaterials, 2000. **21**(3): p. 223-234.
94. de Campo, L., et al., *Reversible Phase Transitions in Emulsified Nanostructured Lipid Systems.* Langmuir, 2004. **20**(13): p. 5254-5261.
95. Esposito, E., et al., *Cubosome Dispersions as Delivery Systems For Percutaneous Administration of Indomethacin.* Pharmaceutical Research, 2005. **22**(12): p. 2163-2173.
96. Montis, C., et al., *Magnetocubosomes for the Delivery and Controlled Release of Therapeutics.* Journal of colloid and interface science, 2015. **449**: p. 317-26.
97. Meli, V., et al., *Docetaxel-Loaded Fluorescent Liquid-Crystalline Nanoparticles for Cancer Theranostics.* Langmuir, 2015. **31**(35): p. 9566-9575.
98. Chung, H., et al., *Self-Assembled "Nanocubicle" as a Carrier for Peroral Insulin Delivery.* Diabetologia, 2002. **45**(3): p. 448-451.
99. Lopes, L.B., et al., *Reverse Hexagonal Phase Nanodispersion of Monoolein and Oleic Acid for Topical Delivery of Peptides: in Vitro and in Vivo Skin Penetration of Cyclosporin A.* Pharmaceutical Research, 2006. **23**(6): p. 1332-1342.
100. Lopes, L.B., et al., *Liquid Crystalline Phases of Monoolein and Water for Topical Delivery of Cyclosporin A: Characterization and Study of in Vitro and in Vivo Delivery.* European Journal of Pharmaceutics and Biopharmaceutics, 2006. **63**(2): p. 146-155.

101. Bye, N., et al., *Nitroxide-Loaded Hexosomes Provide MRI Contrast in Vivo.* Langmuir, 2014. **30**(29): p. 8898-8906.
102. Boyd, B.J., et al., *Hexosomes Formed from Glycerate Surfactants - Formulation as a Colloidal Carrier for Irinotecan.* International Journal of Pharmaceutics, 2006. **318**(1-2): p. 154-162.
103. Adhikari, M.P., et al., *Nanoporous Activated Carbons Derived from Agro-Waste Corncob for Enhanced Electrochemical and Sensing Performance.* Bulletin of the Chemical Society of Japan, 2015. **88**(8): p. 1108-1115.
104. Balducci, A., et al., *HighTemperature Carbon-Carbon Supercapacitor Using Ionic Liquid as Electrolyte.* Journal of Power Sources, 2007. **165**(2): p. 922-927.
105. Demarconnay, L., E. Raymundo-Pinero, and F. Beguin, *A Symmetric Carbon/Carbon Supercapacitor Operating at 1.6 V by Using a Neutral Aqueous Solution.* Electrochemistry Communications, 2010. **12**(10): p. 1275-1278.
106. Gamby, J., et al., *Studies and Characterisations of Various Activated Carbons Used for Carbon/Carbon Supercapacitors.* Journal of Power Sources, 2001. **101**(1): p. 109-116.
107. Qu, D.Y., *Studies of the Activated Carbons Used in Double-Layer Supercapacitors.* Journal of Power Sources, 2002. **109**(2): p. 403-411.
108. Lei, Z., et al., *Platelet CMK-5 as an Excellent Mesoporous Carbon to Enhance the Pseudocapacitance of Polyaniline.* Acs Applied Materials & Interfaces, 2013. **5**(15): p. 7501-7508.
109. Li, N., et al., *Supercapacitors Based on Ordered Mesoporous Carbon Derived from Furfuryl Alcohol: Effect of the Carbonized Temperature.* Journal of Nanoscience and Nanotechnology, 2014. **14**(7): p. 5157-5165.
110. Liang, Y.Y., et al., *A Simple Approach Towards One-Dimensional Mesoporous Carbon with Superior Electrochemical Capacitive Activity.* Chemical Communications, 2009(7): p. 809-811.
111. Lufrano, F. and P. Staiti, *Mesoporous Carbon Materials as Electrodes for Electrochemical Supercapacitors.* International Journal of Electrochemical Science, 2010. **5**(6): p. 903-916.
112. Shrestha, L.K., et al., *Fullerene Crystals with Bimodal Pore Architectures Consisting of Macropores and Mesopores.* Journal of the American Chemical Society, 2013. **135**(2): p. 586-589.
113. Wang, K., et al., *Mesoporous Carbon Nanofibers for Supercapacitor Application.* Journal of Physical Chemistry C, 2009. **113**(3): p. 1093-1097.
114. Xing, W., et al., *Superior Electric Double Layer Capacitors Using Ordered Mesoporous Carbons.* Carbon, 2006. **44**(2): p. 216-224.
115. Zhou, H.S., et al., *Electrochemical capacitance of self-ordered mesoporous carbon.* Journal of Power Sources, 2003. **122**(2): p. 219-223.
116. Babel, K. and K. Jurewicz, *KOH Activated Carbon Fabrics as Supercapacitor Material.* Journal of Physics and Chemistry of Solids, 2004. **65**(2-3): p. 275-280.

117. Futaba, D.N., et al., *Shape-Engineerable and Highly Densely Packed Single-Walled Carbon Nanotubes and Their Application as Super-Capacitor Electrodes.* Nature Materials, 2006. **5**(12): p. 987-994.
118. Shrestha, L.K., et al., *Nanoporous Carbon Tubes from Fullerene Crystals as the pi-Electron Carbon Source.* Angewandte Chemie-International Edition, 2015. **54**(3): p. 951-955.
119. Oh, Y.J., et al., *Oxygen functional groups and electrochemical capacitive behavior of incompletely reduced graphene oxides as a thin-film electrode of supercapacitor.* Electrochimica Acta, 2014. **116**: p. 118-128.
120. Stoller, M.D., et al., *Graphene-Based Ultracapacitors.* Nano Letters, 2008. **8**(10): p. 3498-3502.
121. Wang, Y., et al., *Supercapacitor Devices Based on Graphene Materials.* Journal of Physical Chemistry C, 2009. **113**(30): p. 13103-13107.
122. Zhu, Y., et al., *Carbon-Based Supercapacitors Produced by Activation of Graphene.* Science, 2011. **332**(6037): p. 1537-1541.
123. Tang, J., et al., *Towards Vaporized Molecular Discrimination: A Quartz Crystal Microbalance (QCM) Sensor System Using Cobalt-Containing Mesoporous Graphitic Carbon.* Chemistry-an Asian Journal, 2014. **9**(11): p. 3238-3244.
124. Hu, M., et al., *Direct Carbonization of Al-Based Porous Coordination Polymer for Synthesis of Nanoporous Carbon.* Journal of the American Chemical Society, 2012. **134**(6): p. 2864-2867.
125. Ji, Q., et al., *Layer-by-Layer Films of Graphene and Ionic Liquids for Highly Selective Gas Sensing.* Angewandte Chemie-International Edition, 2010. **49**(50): p. 9737-9739.
126. Ji, Q., et al., *Layer-by-Layer Films of Dual-Pore Carbon Capsules with Designable Selectivity of Gas Adsorption.* Journal of the American Chemical Society, 2009. **131**(12): p. 4220-+.
127. Jia, L., et al., *A Facile Photo-Induced Synthesis of COOH Functionalized Meso-Macroporous Carbon Films and their Excellent Sensing Capability for Aromatic Amines.* Chemical Communications, 2012. **48**(72): p. 9029-9031.
128. Kong, J., et al., *Nanotube Molecular Wires as Chemical Sensors.* Science, 2000. **287**(5453): p. 622-625.
129. Mane, G.P., et al., *Preparation of Highly Ordered Nitrogen-Containing Mesoporous Carbon from a Gelatin Biomolecule and its Excellent Sensing of Acetic Acid.* Advanced Functional Materials, 2012. **22**(17): p. 3596-3604.
130. Higuchi, T., *Mechamism of Sustained-Action Medication - Theoretical Analysis of Rate of Release of Solid Drugs Dispersed in Solid Matrices.* Journal of Pharmaceutical Sciences, 1963. **52**(12): p. 1145-&.
131. Korsmeyer, R.W., et al., *Mechamism of Solute Release from Porous Hydrophilic Polymers.* International Journal of Pharmaceutics, 1983. **15**(1): p. 25-35.

132. Lu, A.H., et al., *Taking Nanocasting One Step Further: Replicating CMK-3 As a Silica Material.* Angewandte Chemie International Edition, 2002. **41**(18): p. 3489.
133. Shrestha, L.K., et al., *Structural Investigation of Diglycerol Polyisostearate Reverse Micelles in Organic Solvents.* Journal of Physical Chemistry B, 2009. **113**(38): p. 12669-12679.
134. Small, D.M., *Handbook of Lipid Research: From Alkanes to Phospholipids*. Vol. 4. 1986, New York: Plenum Press.
135. Kratzat, K., C. Stubenrauch, and H. Finkelmann, *Mixtures of Branched Nonionic Oligo-Oxyethylene Surfactants in Aqueous Solutions: The effect of Molecular Geometry on LC Phase Behavior.* Colloid and Polymer Science, 1995. **273**(3): p. 257-262.
136. Kawaguchi, M., et al., *Surface Properties of Mono-, Di-, and Triglycerol Monostearate Monolayers Spread at the Air-Water Interface.* Langmuir, 2001. **17**(15): p. 4677-4680.
137. Gustafsson, J., et al., *Submicron Particles of Reversed Lipid Phases in Water Stabilized by a Nonionic Amphiphilic Polymer.* Langmuir, 1997. **13**(26): p. 6964-6971.
138. Landh, T., *Phase Behavior in the System Pine Oil Monoglycerides-Poloxamer 407-Water at 20 Degrees.* Journal of Physical Chemistry, 1994. **98**(34): p. 8453-8467.
139. Amar-Yuli, I., et al., *Hexosome and Hexagonal Phases Mediated by Hydration and Polymeric Stabilizer.* Langmuir, 2007. **23**(7): p. 3637-3645.
140. Barauskas, J., et al., *Cubic phase nanoparticles (Cubosome): Principles for controlling size, structure, and stability.* Langmuir, 2005. **21**(6): p. 2569-2577.
141. Yaghmur, A. and O. Glatter, *Characterization and Potential Applications ofNanostructured Aqueous Dispersions.* Advances in Colloid and Interface Science, 2009. **147-48**: p. 333-342.
142. Martiel, I., et al., *Facile Dispersion and Control of Internal Structure in Lyotropic Liquid Crystalline Particles by Auxiliary Solvent Evaporation.* Langmuir, 2014. **30**(48): p. 14452-14459.
143. Spicer, P.T., et al., *Novel process for Producing Cubic Liquid Crystalline Nanoparticles (Cubosomes).* Langmuir, 2001. **17**(19): p. 5748-5756.
144. Kim, D.H., et al., *A Simple Evaporation Method for Large-Scale Production of Liquid Crystalline Lipid Nanoparticles with Various Internal Structures.* Acs Applied Materials & Interfaces, 2015. **7**(36): p. 20438-20446.
145. Mason, T.J. and D. Peters, *Practical Sonochemistry*. 2011, Philadelphia: Woodhead Publishing Limited.
146. Nakano, M., et al., *Dispersions of Liquid Crystalline Phases of the Monoolein/Oleic Acid/Pluronic F127 System.* Langmuir, 2002. **18**(24): p. 9283-9288.
147. Chen, L.C., et al., *Pluronic P105/F127 Mixed Micelles for the Delivery of Docetaxel Against Taxol-Resistant non-Small Cell Lung Cancer: Optimization and in Vitro, in Vivo Evaluation.* International Journal of Nanomedicine, 2013. **8**: p. 73-84.

148. Solans, C. and I. Sole, *Nano-Emulsions: Formation by Low-Energy Methods.* Current Opinion in Colloid & Interface Science, 2012. **17**(5): p. 246-254.
149. Fornaguera, C., G. Caldero, and C. Solans, *Electrolytes as a Tuning Parameter to Control Nanoemulsion and Nanoparticle Size.* Rsc Advances, 2016. **6**(63): p. 58203-58211.
150. Binks, B.P., et al., *Stability of Oil-in-Water Emulsions in a Low Interfacial Tension System.* Langmuir, 2000. **16**(3): p. 1025-1034.
151. Salentinig, S., et al., *Preparation of Highly Concentrated Nanostructured Dispersions of Controlled Size.* Journal of Colloid and Interface Science, 2008. **326**(1): p. 211-220.
152. Vine, D.F., et al., *Effect of Dietary Fatty Acids on the Intestinal Permeability of Marker Drug Compounds in Excised Rat Jejunum.* Journal of Pharmacy and Pharmacology, 2002. **54**(6): p. 809-819.
153. Sekiya, I., et al., *Ketoprofen Absorption by Muscle and Tendon after Topical or Oral Administration in Patients Undergoing Anterior Cruciate Ligament Reconstruction.* Aaps Pharmscitech, 2010. **11**(1): p. 154-158.
154. Costa, P., J. Manuel, and S. Lobo, *Modeling and Comparison of Dissolution Profiles.* European Journal of Pharmaceutical Sciences, 2001. **13**(2): p. 123-133.
155. Koyama, Y., et al., *Resonace Raman and Electronic Absoption Probe of Membrane Energization - Quinaldine Red in Cells of Streptococcus-Faecalis.* Journal of Biological Chemistry, 1979. **254**(20): p. 276-285.
156. Pizzey, C., et al., *Suspensions of Colloidal Plates in a Nematic Liquid Crystal: a Small Angle X-ray Scattering Study.* Journal of Physics: Condensed Matter, 2004. **16**(15): p. 2479-2495.
157. Edwards, D.J., et al., *Chromonic Liquid Crystal Formation by Edicol Sunset Yellow.* Journal of Physical Chemistry B, 2008. **112**(46): p. 14628-14636.
158. Minewaki, K., et al., *Small Angle X-Ray Scattering from the Lamellar Phase Formed in a Nonionic Surfactant (C16E7)-Water System. Analysis of Peak Position and Line Shape.* Langmuir, 2001. **17**(6): p. 1864-1871.
159. Funari, S.S., M.C. Holmes, and G.J.T. Tiddy, *Intermediate Lyotropic Liquid-Crystal Phases in the C16EO6/Water System.* Journal of Physical Chemistry, 1994. **98**(11): p. 3015-3023.
160. Fairhurst, C.E., M.C. Holmes, and M.S. Leaver, *Structure and Morphology of the Intermediate Phase Region in the Nonionic Surfactant C16EO6/Water System.* Langmuir, 1997. **13**(19): p. 4964-4975.
161. Aramaki, K., et al., *Miscibility of Block Copolymers and Surfactants in Lamellar Liquid Crystals.* Macromolecules, 2003. **36**(25): p. 9443-9450.
162. Arik, M. and Y. Onganer, *Molecular Excitons of Pyronin B and Pyronin Y in Colloidal Silica Suspension.* Chemical Physics Letters, 2003. **375**(1-2): p. 126-133.
163. Perahia, D., E.J. Wachtel, and Z. Luz, *NMR and X-Ray Studies of the Chromonic Lyomesophases Formed by Some Xanthone Derivatives.* Liquid Crystals, 1991. **9**(4): p. 479-492.

164. Tomasik, M.R. and P.J. Collings, *Aggregation Behavior and Chromonic Liquid Crystal Phase of a Dye Derived from Naphthalenecarboxylic Acid.* Journal of Physical Chemistry B, 2008. **112**(32): p. 9883-9889.
165. Nastishin, Y.A., et al., *Optical Characterization of the Nematic lyotropic Chromonic Liquid Crystals: Light Absorption, Birefringence, and Scalar Order Parameter.* Physical Review E, 2005. **72**(4).
166. Smulders, M.M.J., et al., *How to Distinguish Isodesmic from Cooperative Supramolecular Polymerisation.* Chemistry-a European Journal, 2010. **16**(1): p. 362-367.
167. Boden, N., et al., *Order-Disorder Transitions in Solutions of Discoid Micelles.* Journal De Physique, 1986. **47**(12): p. 2135-2144.
168. Chami, F. and M.R. Wilson, *Molecular Order in a Chromonic Liquid Crystal: A Molecular Simulation Study of the Anionic Azo Dye Sunset Yellow.* Journal of the American Chemical Society, 2010. **132**(22): p. 7794-7802.
169. von Berlepsch, H., C. Bottcher, and L. Dahne, *Structure of J-Agregates of Pseudoisocyanine Dye in Aqueous Solution.* Journal of Physical Chemistry B, 2000. **104**(37): p. 8792-8799.
170. Tredwell, C.J. and C.M. Keary, *Picosecond Time Resolved Fluorescensce Lifetimes of the Polymethine and Related Dyes.* Chemical Physics, 1979. **43**(3): p. 307-316.
171. Obrien, D.F., T.M. Kelly, and L.F. Costa, *Excited State Properties of Some Carbocyabnine Dyes and Energy-Transfer Mechanism of Spectral Sensitization.* Photographic Science and Engineering, 1974. **18**(1): p. 76-84.
172. Scott, J.E., *Alcian Blue. Now you see it, now you don't.* European Journal of Oral Sciences, 1996. **104**(1): p. 2-9.
173. Stegemeyer, H. and F. Stockel, *Anisotropic Structures in Aqueous Solutions of Aggregated Pseudoisocyanine Dyes.* Physical Chemistry Chemical Physics, 1996. **100**(1): p. 9-14.
174. Kleitz, F., et al., *Mesoporous Silica Fibers: Synthesis, Internal Structure, and Growth Kinetics.* Chemistry of Materials, 2001. **13**(10): p. 3587-3595.
175. Tani, K., et al., *Photophysical Property and Photostability of J-aggregate Thin Films of Thiacyanine Dyes Prepared by the Spin-Coating Method.* Journal of Physical Chemistry B, 2008. **112**(3): p. 836-844.
176. Laban, B., et al., *Mechanism and Kinetics of J-Aggregation of Thiacyanine Dye in the Presence of Silver Nanoparticles.* Journal of Physical Chemistry C, 2014. **118**(40): p. 23393-23401.
177. Silvain, J.F., et al., *Novel Processing and Characterization of Cu/CNF Nanocomposite for High Thermal Conductivity Applications.* Composites Science and Technology, 2009. **69**(14): p. 2474-2484.
178. Yang, H.F. and D.Y. Zhao, *Synthesis of Replica Mesostructures by the Nanocasting Strategy.* Journal of Materials Chemistry, 2005. **15**(12): p. 1217-1231.
179. Tian, B.Z., et al., *Novel Approaches to Synthesize Self-Supported Ultrathin Carbon Nanowire Arrays Templated By MCM-41.* Chemical Communications, 2003(21): p. 2726-2727.

180. Stein, A., Z. Wang, and M.A. Fierke, *Functionalization of Porous Carbon Materials with Designed Pore Architecture.* Advanced Materials, 2009. **21**(3): p. 265-293.

181. Ryoo, R., et al., *Ordered Mesoporous Carbons.* Advanced Materials, 2001. **13**(9): p. 677-681.

182. Ryoo, R., S.H. Joo, and S. Jun, *Synthesis of Highly Ordered Carbon Molecular Sieves via Template-Mediated Structural Transformation.* Journal of Physical Chemistry B, 1999. **103**(37): p. 7743-7746.

183. Mbileni, C.N., et al., *Synthesis of Mesoporous Carbon Supports Via Liquid Impregnation of Polystyrene Onto a MCM-48 Silica Template.* Carbon, 2006. **44**(8): p. 1476-1483.

184. Lu, A.-H. and F. Schueth, *Nanocasting: A Versatile Strategy for Creating Nanostructured Porous Materials.* Advanced Materials, 2006. **18**(14): p. 1793-1805.

185. Kim, S.S. and T.J. Pinnavaia, *A Low Cost Route to Hexagonal Mesostructured Carbon Molecular Sieves.* Chemical Communications, 2001(23): p. 2418-2419.

186. Zhi, L., et al., *From Well-Defined Carbon-Rich Precursors To Monodisperse Carbon Particles With Hierarchic Structures.* Advanced Materials, 2007. **19**(14): p. 1849-+.

187. Kuznetsov, D.M., *Shrinkage Phenomena in Graphitization of Preforms in Castner Furnaces.* Refractories and Industrial Ceramics, 2000. **41**(7-8): p. 279-282.

188. Gross, G.A., et al., *Heterocyclic Aromatic Amine Formation in Grilled Bacon, Beef and Fish and in Grill Scrapings.* Carcinogenesis, 1993. **14**(11): p. 2313-2318.

7. GLOSSARY AND ABBREVIATIONS

ABBREVIATIONS

6d-DMSO	Deuterated dimethyl sulfoxide
AB-Ac	Alcian Blue Acetate
AB-Cl	Alcian Blue chloride
AB-Toc	Alcian Blue p-toluensulfonate
C41V	Technical grade diglycerol monoisostearate
C41V-NG	Technical grade diglycerol monoisostearate with no glycerol
C42V	Technical grade diglycerol diisostearate
C43V	Technical grade diglycerol triisostearate
C44V	Technical grade diglycerol tetraisostearate
CAC	Critical aggregate concentration
CD	Charge/Discharge
CNF	Carbon nanofibers
CV	Cyclic voltammetry
CMC	Critical micellar concentration
D_2O	Deuterated water
DLS	Dynamic light scattering
DSC	Differential scanning calorimetry
DSCG	Disodium chromoglycate
EDLCs	Electrical double layer capacitors
EAc	Ethyl Acetate
EtOH	Ethanol
F127	Pluronic F127
FA	Furfuryl alcohol
NMR	Nuclear magnetic resonance
NOEsy	Nuclear overhaouser effect
HPLC	High pressure liquid chromatography

HR-TEM	High resolution electron microscopy
LCD	Liquid crystal display
LCN	Liquid crystalline nanoparticles
MeOH	Methanol
PBS	Phosphate buffer saline
PDI	Polydispersity index
PiC	Pinacyanol acetate
POM	Polarized optical microscopy
PyY	Pyronin Y
QCM	Quartz microbalance
QR-Ac	Quinaldine Red acetate
QR-I	Quinaldine Red Iodide
SAXS	Small angle X-ray scattering
SEM	Scanning electron microscopy
SiO$_2$NF	Silicon Oxide nanofibers
TCC-C$_n$	n-alkyl thiacarbocyanine
TEM	Transmission electron microscopy
TEOS	Tetraethylortosilicate
TLC	Thin layer chromatography
XPS	X-ray photoelectron spectroscopy
XRD	X-ray diffraction
UV-Vis	Ultraviolet and visible spectroscopy
WAXS	Wide angle X-ray scattering

ROMAN SYMBOLS

a	Dimension of a cell unit
A	Hamaker constant

A_c	Cross-sectional area
a_s	Cross sectional area of the hydrophilic head in a surfactant
b	Dimension of a cell unit
$[C]$	Concentration
c	Components present in a system
C_0	Total dye concentration
C_{Dim}	Concentration of dimer
Col_L	Columnar lamellar liquid crystal
C_s	Specific capacitance
C_M	Concentration of monomer
D	Diffusion coefficient
d	Spacing between planes
D_c	Distance between cylinders
d_L	Thickness of layers in a lamellar liquid crystal
d_π	Thickness of layers in a chromonic lamellar liquid crystal
d_m	Distance separating molecules
F1	First fraction obtained during a chromatography
F2	Second fraction obtained during a chromatography
F3	Third fraction obtained during a chromatography
f	Degrees of freedom
f_s	Oscillator strength
I	Current
I_m	Current density
J_1	First order Bessel cuntion
K	Constant
k_B	Boltzmann constant
K_D	Dimerization constant

K_H	Higuchi dissolution constant
K_{KP}	Kinetic constant of the Korsmeyer-Peppas model
L	Length of the aggregates
m	mass
n	Release exponent of the Korsmeyer-Peppas model
N	Packing parameter
n_C	Number of carbon atoms in a hydrocarbon chain
n_{CH3}	Number of methyl groups in a hydrocarbon chain
o	Order of diffraction
p	Number of phases present in a system
q	Scattering vector
r	radius
r_c	core radius
r_{ext}	exterior radius
R^2	Mean squared error
R_H	Hydrodynamic radius
R_s	Ratio between peak heights
S_0	Ground state
S_1	Excited state
s_{dimer}	Peak height from deconvoluted spectra corresponding to the dimer
S_f	Sensitivity factor of QCM electrodes
$s_{monomer}$	Peak height deconvoluted spectra corresponding to the monomer
T	Temperature
t_d	Discharge time
t	Time
t_s	Shell thickness
V	Voltage

V_{ex}	Exciton splitting
V_{cil}	Cylinder volume
V_c	Volume of the core, in a core-shell cylinder structure
V_s	Volume of the shell in a core-shell cylinder structure
v_L	Volume of the hydrophobic tail
w	Interaction energy
wt%	percentage in weight

GREEK AND OTHER SYMBOLS

β	Full width at half maximum
δ	NMR shift in ppm's
ε	Absorption coefficient
ε_{water}	Dielectric permittivity in water
ε_o	Dielectric permittivity in vacuum
ϕ_f	Volume fraction
μ_x	Dipolar moment of an X molecule
η	Dynamic density
λ	Wavelength
θ	Angle
ρ	Density
ρ_c	Scattering electron density of the core in a core-shell cylinder structure
ρ_s	Scattering electron density of the core in a core-shell cylinder structure
$\rho_{solvent}$	Scattering electron density of the core in a core-shell cylinder structure
τ	Mean size of the crystalline domain
ω	Angular velocity
$\Delta\rho$	Difference of scattering electron density between the scattered and solvent
Δf	frequency shift
ΔG	Change in Gibb's free energy between two states

ΔH	Change in enthalpy between two states
ΔS_{int}	Change in entropy between two states
ΔV	Potential window

8. APPENDIX

- Support Information

8.1. SAXS MODELS

8.1.1. Cylinder Model

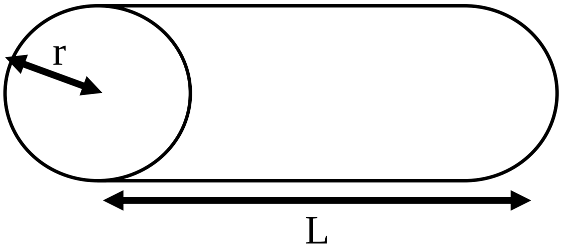

Figure 8.1. Representation of a cylinder with relevant structural parameters.

The form factor of a cylinder in a solution is defined as:

$$F(q) = (\Delta\rho) * V_{cil} \frac{\sin(0.5 * q * L * \cos(\alpha))}{0.5 * q * L * \cos(\alpha)} \frac{2J_1(q * r * \sin(\alpha))}{q * R * \sin(\alpha)}$$

Equation 8.1

α is the angle between the axis of the cylinder and q (scattering vector), V_{cil} is the volume of the cylinder, L is the length of the cylinder, r is the radius of the cylinder, and $\Delta\rho$ (contrast) is the scattering electron density difference between the scattered and the solvent. J_1 is the first order Bessel function.

8.1.2. Core-Shell Cylinder Model

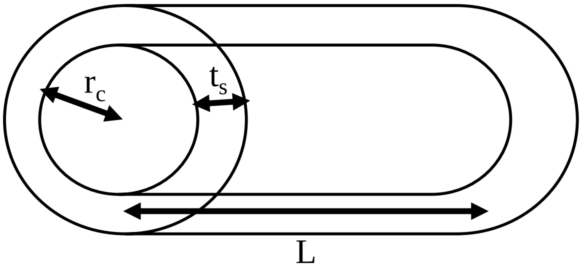

Figure 8.2. Representation of a core-shell cylinder with relevant structural parameters

The core shell cylinder form factor *F(q)* is defined as:

$$
\begin{aligned}
F(q) = (\rho_c - \rho_s) * V_c \frac{\sin(0.5 * q * L * \cos(\alpha))}{0.5 * q * L * \cos(\alpha)} \frac{2J_1(q * r_c * \sin(\alpha))}{q * r_c * \sin(\alpha)} \\
+ (\rho_s - \rho_{solvent}) \\
* V_s \frac{\sin(q(0.5L + t_s) * \cos(\alpha)}{q(0.5L + t_s) * \cos(\alpha)} \frac{2J_1(q(r_c + t_s)\sin(\alpha))}{q(r_c + t_s)\sin(\alpha)}
\end{aligned}
$$

Equation 8.2

The volume of the shell, V_s, can be calculated as:

$$V_s = \pi(r_c + t_s)^2(L + 2t_s)$$

Equation 8.3

α is the angle between the axis of the cylinder and q (scattering vector), V_s is the volume of the outer shell (i.e. the total volume, including the shell), V_c is the volume of the core, L is the length of the core, r_c is the radius of the core, t_s is the thickness of the shell, ρ_c is the scattering electronic density of the core, ρ_s is the scattering electronic density of the shell, $\rho_{solvent}$ is the scattering electronic density of the solvent. The outer radius of the shell is given by r_c+t_s and the total length of the outer shell is given by $L+2t_s$. J_1 is the first order Bessel function.